4. ZIRCALOY

Twenty seven materials properties of LWR fuel rod cladding (zircaloy-2 or -4) have been modeled for inclusion in the SCDAP/RELAP5 materials properties subcode package. Modeling approaches range from a choice of experimental data with linear interpolation or extrapolation or both to a semiempirical expression suggested by theory.

All 27 properties are modeled as a function of the cladding temperature. In addition, such variables as fast neutron flux, fluence, cold work, stress, time, and impurity content are used as arguments. Some of the subcodes are interconnected, employing in part identical or very similar correlations (for example, strain versus stress, stress versus strain, and cladding ultimate strength). Some subcodes call upon others, such as the physical properties subcode, PHYPRO; but all of the information needed to run a given subcode is contained in this report.

4.1 Melting and Phase Transformation Temperatures (CHYPRP)

To perform an accurate analysis of reactor behavior during an accident involving the core, it is necessary to know the melting and phase transformation temperatures of zircaloy. The subroutine CHYPRP calculates the zircaloy phase transition temperatures of interest for use in LWR analysis. The only input required in this subroutine is the excess weight fraction oxygen content of the zircaloy. From this input, the subroutine calculates the solidus temperature (appearance of lowest temperature liquid phase), the liquidus temperature (melting of the last solid phase), the alpha to alpha plus beta phase boundary, and the alpha plus beta to beta phase boundary for zircaloy.

4.1.1 Model Development

Four parameters are often used to describe the oxygen concentration in zircaloy. Table 4-1 shows the relationship between the one used in CHYPRP and the others. The first column gives the excess weight fraction oxygen content. The second column gives the corresponding values for the total weight fraction oxygen, assuming an as received oxygen concentration of 0.0012 by weight. The third column presents corresponding values for the atomic fraction of oxygen in the compound. The atomic fraction oxygen is related to the mass fraction oxygen in zirconium oxide by the equation

Table 4-1. Oxygen content parameters for zircaloy.

Excess mass oxygen fraction	Total mass oxygen fraction (WFOX)	Atomic oxygen fraction	Oxygen to metal ratio
O/kg Zr(O)	[kg O/kg Zr(O)]	(O/atoms compound)	Atoms O/ atoms metal
0.0000	0.0012	0.007	0.007
0.0100	0.0112	0.061	0.065
0.0200	0.0212	0.110	0.124
0.0300	0.0312	0.155	0.183

Table 4-1. Oxygen content parameters for zircaloy. (Continued)

Excess mass oxygen fraction	Total mass oxygen fraction (WFOX)	Atomic oxygen fraction	Oxygen to metal ratio
0.0400	0.0412	0.197	0.245
0.0500	0.0512	0.235	0.307
0.0600	0.0612	0.271	0.372
0.0657	0.0669	0.290	0.408

$$x = \frac{WFOX}{WFOX + \frac{GMWT(0)}{GMWT(Zr)}(1 - WFOX)} \quad (4\text{-}1)$$

where

x = the atomic fraction of oxygen in zircaloy containing oxygen (atoms of oxygen/ atoms of compound)

WFOX = mass fraction of oxygen in zircaloy containing oxygen (kg oxygen/kg compound)

GMWT(O)= molecular weight of an oxygen atom [16 kg (O)/kg• mole]

GMWT(Zr)= molecular weight of a zircaloy atom [91.22 kg (Zr)/kg•mole].

As-received zircaloy is presumed to have 0.0012 weight fraction oxygen.

The fourth column gives the corresponding values of the oxygen to metal ratio. This ratio is related to the atomic fraction oxygen by the following equation for zirconium oxide (which approximates zircaloy oxide):

$$YE = \frac{x}{1 - x} \quad (4\text{-}2)$$

where YE is the oxygen to metal ratio (atoms of oxygen/atoms of zirconium).

To convert the input excess weight fraction oxygen to an atomic fraction for oxygen in the zircaloy, the as received oxygen weight fraction for the zircaloy is added to the input weight fraction oxygen prior to calculating the atomic fraction of the oxygen in the zircaloy. From the calculated atomic fraction oxygen, the melting and phase transformation temperatures are calculated using equations from the PYHPRP,

PSOL, and PLIQ subcodes. To calculate the solidus temperature from the atomic fraction of oxygen in zircaloy, the following relationships are used:

For $x \leq 0.1$,

$$T_{sol} = 2098 + 1150\,x \quad . \tag{4-3}$$

For $0.1 < x \leq 0.18$,

$$T_{sol} = 2213 \quad . \tag{4-4}$$

For $0.18 < x \leq 0.29$,

$$T_{sol} = 1389.5317 + 7640.0748\,x - 17029.172\,x^2 \quad . \tag{4-5}$$

For $0.29 < x \leq 0.63$,

$$T_{sol} = 2173 \quad . \tag{4-6}$$

For $0.63 < x \leq 0.667$,

$$T_{sol} = -11572.454 + 21818.181\,x \quad . \tag{4-7}$$

For $x > 0.667$,

$$T_{sol} = -11572.454 + x(1.334 - x)\,21818.181 \tag{4-8}$$

where T_{sol} is the solidus temperature (K).

The liquidus temperatures are calculated using the following relationships:

For $x \leq 0.19$,

$$T_{liq} = 2125. + 1632.1637\,x - 5321.6374\,x^2 \quad . \tag{4-9}$$

For $0.19 < x \leq 0.41$,

$$T_{liq} = 2111.6553 + 1159.0909\ x - 2462.1212\ x^2 \ . \qquad (4\text{-}10)$$

For $0.41 < x \leq 0.667$,

$$T_{liq} = 895.07792 + 3116.8831\ x \ . \qquad (4\text{-}11)$$

For $x > 0.667$,

$$T_{liq} = 895.07792 + (1.34 - x)\ 3116.8831 \qquad (4\text{-}12)$$

where T_{liq} is the liquidus temperature (K).

The subcode CHYPRP also calculates the low and high temperature boundaries of the alpha plus beta phase region as a function of the total weight fraction oxygen in the compound. If the compound weight fraction oxygen is less than 0.025, then the low temperature boundary of the two-phase region is calculated as follows:

$$ctranb = 1094. + WFOX \cdot (-1.289 \times 10^3 + WFOX \cdot 7.914 \times 10^5\ ) . \qquad (4\text{-}13)$$

If the total weight fraction is greater than 0.025, then the low temperature boundary is calculated using the following equation:

$$ctranb - 1556.4 + 3.8281 \times 10^4 \cdot (WFOX - 0.025) \ . \qquad (4\text{-}14)$$

where ctranb is the low temperature boundary of the alpha plus beta phase region (K). If the lower alpha plus beta transition temperature is equal to or larger than the calculated solidus temperature, then the alpha plus beta lower boundary phase temperature is set equal to the solidus temperature.

The high temperature alpha plus beta phase region boundary temperatures are calculated using the following relationships, which use the input oxygen content rather than weight fraction. With an input oxygen content less than 4.7308937×10^{-3}, the upper phase boundary temperature is calculated using the following correlation:

$$ctrane = 392.46 \cdot [(100 \cdot WFOX)^2 + 3.1417] \ . \qquad (4\text{-}15)$$

If the oxygen content is greater than $4.7308937 \times 10^{-03}$, then the equation used to calculate the upper alpha plus beta phase boundary temperature is

$$ctrane = (100 \cdot WFOX) \cdot 491.157 + 1081.7413 \qquad (4\text{-}16)$$

where ctrane is the high temperature boundary of the alpha plus beta phase region (K). If the upper boundary temperature of the alpha plus beta phase region is greater than the calculated solidus temperature, then the upper boundary alpha plus beta phase temperature is set equal to the solidus temperature. The alpha plus beta boundaries expressions are based on data from Chung and Kassner.[4.1-1]

Figure 4-1 shows the calculated zircaloy solidus and liquidus temperatures and the calculated alpha plus beta phase region boundaries.

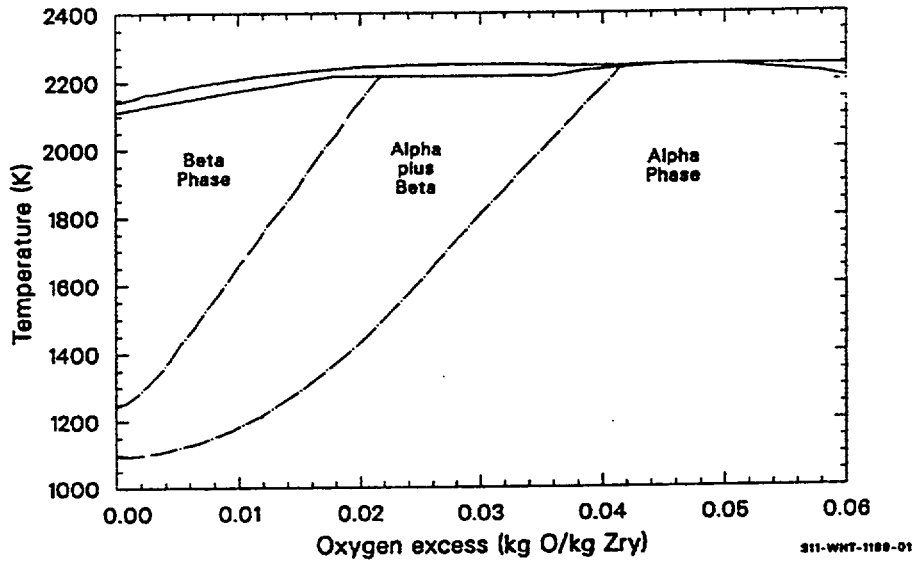

Figure 4-1. Zircaloy solidus and liquidus temperatures.

4.1.2 Reference

4.1-1 H. M. Chung and T. F. Kassner, "Pseudobinary Zircaloy Oxygen Phase Diagram," *Journal of Nuclear Materials, 84*, 1979, pp. 327-339.

4.2 Temperature Required to Prevent Hydriding of a Given Concentration of Hydrogen in Zircaloy (CTSOL)

An estimate of the temperature at which hydride precipitates begin to form in zircaloy cladding is useful for estimating when hydriding will begin to embrittle the cladding. The function CTSOL calculates the minimum temperature for complete solution of a given concentration of hydrogen. The expression used for the calculation is

$$\mathrm{CTSOL} = \frac{4401\mathrm{K}}{\ln\left(\frac{1.332\times10^{5}}{\mathrm{H}}\right)} \qquad (4\text{-}17)$$

where

CTSOL = minimum temperature for complete solution of a concentration of hydrogen in zircaloy (K)

H = hydrogen concentration (parts per million by weight).

The development of this equation is discussed in Section 4.3 in conjunction with the derivation of the model for the effect of hydride solution on zircaloy cladding specific heat.

4.3 Cladding Specific Heat, the Effect of Hydride Solution on Cladding Specific Heat, and Enthalpy (CCP, CHSCP, CENTHL)

Two function subcodes are used to describe the apparent specific heat of the zircaloys. The first, CCP, describes the true specific heat at constant pressures for the alloys. The second, CHSCP, describes the apparent addition to the specific heat because of energy used to dissolve the hydrides present in zircaloys. Uncertainty estimates have been determined and are returned by each function.

CCP requires only temperature as input, while CHSCP requires both temperature and the concentration of hydrogen. The hydrogen concentration may be supplied directly by the user or it may be calculated by the MATPRO function CHUPTK.

4.3.1 Specific Heat (CCP)

For the alpha phase of the zircaloys (temperature less than 1,090 K), CCP returns linear interpolations for the points listed in Table 4-2. (Linear interpolation is computed by the subcode POLATE described in Section 16.1.).

Table 4-2. Zircaloy specific heat capacities for CCP.

Temperature (K)	Specific heat capacity (J/kg · K)
300	281
400	302
640	331
1,090	375
1,093	502
1,113	590
1,133	615
1,153	719
1,173	816
1,193	770
1,213	619
1,233	469
1,248	356

Table 4-2 is based on precise data taken by Brooks and Stansbury[4.3-1] with a zircaloy-2 sample that had been vacuum annealed at 1,075 K to remove hydrogen. The standard error[a] of the CCP interpolation (that is, the precision of the fit to the data) was based on the 90 points in the data base and was found to be temperature dependent. For the 57 data points between 300 and 800 K, the standard error is 1.1 J/kg · K. Between 800 and 1,090 K, it is 2.8 J/kg · K.

For temperatures from 1,090 to 1,300 K (where Brooks and Stansbury do not report results), values of specific heat proposed by Deem and Eldridge[4.3-2] are adopted by MATPRO. The Deem and Eldridge values, shown in Table 4-3, are based on measurements of enthalpy and temperature which provide considerably less precise specific heat data than the results of Brooks and Stansbury.[4.3-1]

a. The standard error is estimated for a data set by the expression: [sum of squared residuals/number of residuals minus number of constants used to fit the data)]$^{1/2}$.

Table 4-3. Specific heat as a function of temperature--beta phase.

Temperature (K)	Specific heat (J/kg · K)
1,093	502
1,113	590
1,133	615
1,153	719
1,173	816
1,193	770
1,213	619
1,233	469
1,248	356

The standard error as estimated by the Deem and Eldridge data in the region 1,090 through 1,310 K is 10.7 J/kg · K. Again, this standard error is a measure only of the precision of the fit, since only a single data source is employed.

The specific heat as calculated by CCP is shown in Figure 4-2. Figure 4-3 and Figure 4-4 also show the CCP prediction, using an expanded scale at lower temperatures and illustrating the base data from Brooks and Stansbury as well as alpha phase (300 to 1,090 K) data from Deem and Eldridge that were not used in constructing CCP.

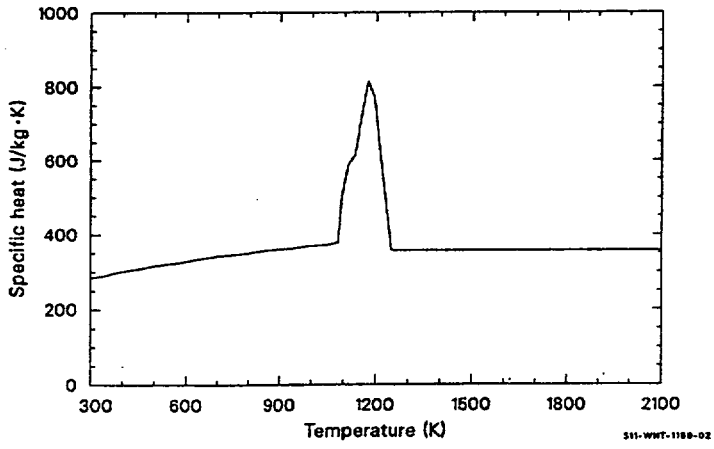

Figure 4-2. Specific heat of zircaloys as calculated by CCP for alloys without hydrides.

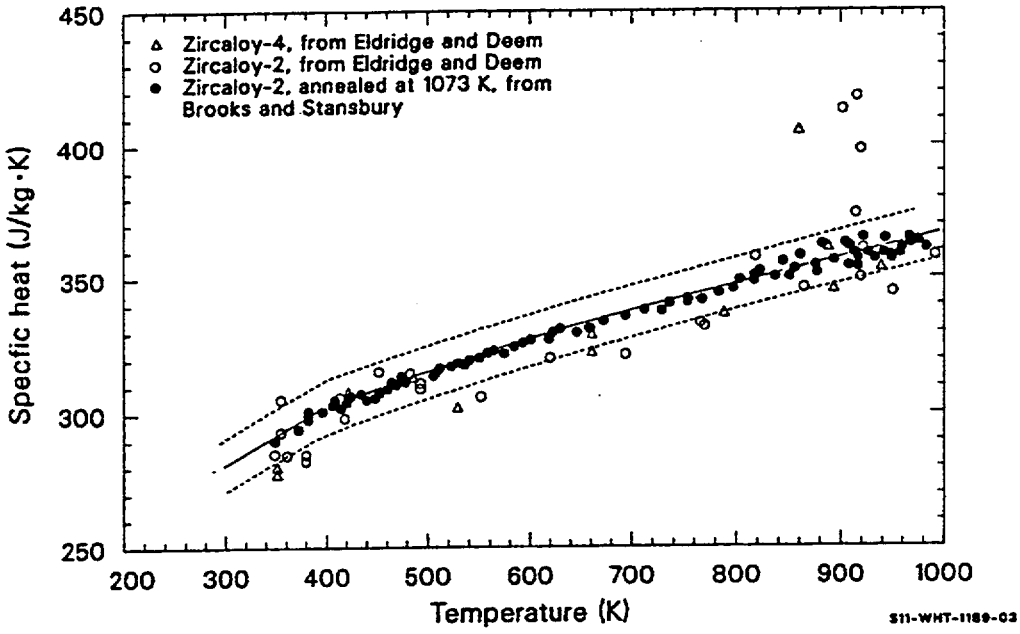

Figure 4-3. Available data, MATPRO expressions for specific heat, and estimated uncertainty of the MATPRO expression for temperatures from 300 to 1,000 K.

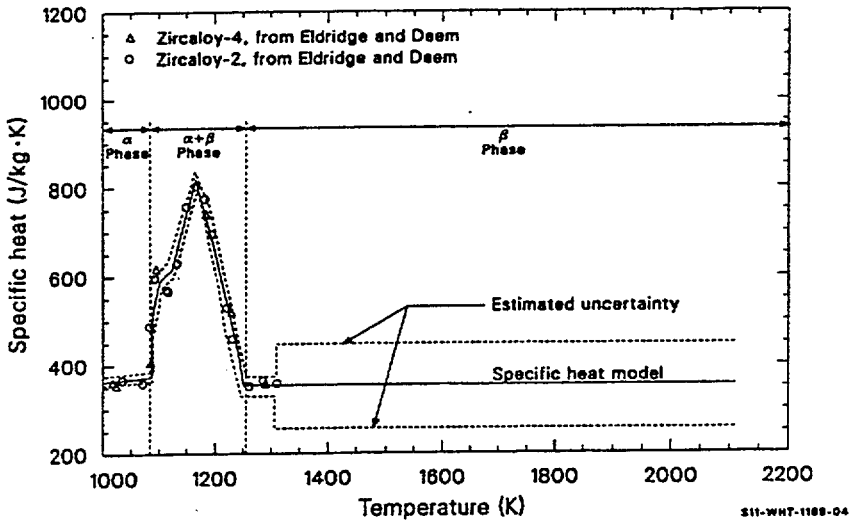

Figure 4-4. Available data, MATPRO expressions for specific heat, and estimated uncertainty of the MATPRO expression for temperatures from 1,000 to 2,000 K.

At temperatures up to 900 K, the Brooks and Stansbury data agree with the Deem and Eldridge data within 3%. Above the alpha plus beta to beta transformation temperature (about 1,250 K) and up to about 1,320 K, a constant value of 355.7 J/kg K was reported by Deem and Eldridge. This value agrees well with a value of 365.3 reported by Coughlin and King[4.3-3] for pure beta zirconium.

The estimated standard error of CCP for data consisting of a random sample from all zircaloy-2 and zircaloy-4 claddings is also shown in Figure 4-3 and Figure 4-4. This standard error is discussed in Section 4.3.3 after the discussion of the effect of hydride solution.

4.3.2 Effect of Hydride Solution (CHSCP)

Values returned by the function CHSCP for the addition to the specific heat due to energy used in solution of hydrides are:

$$CHSCP = \frac{ABC}{T^2}\left[\exp\left(-\frac{B}{T}\right)\right]\left[\exp\left(\frac{T-TSOL}{0.02TSOL}\right)+1\right]^{-1} \quad (4\text{-}18)$$

where

CHSCP = addition to true specific heat due to hydride solution (J/kg · K)

T = cladding temperature (K)

TSOL = minimum temperature for complete solution of the hydrogen concentration, as determined with Equation (4-19) (K)

A = 1.332×10^5 (ppm hydrogen)

B = 4.401×10^3 (K)

C = 45.70(J/kg ppm hydrogen).

TSOL, the minimum temperature required for complete solution of the hydrogen in the cladding, is determined from the expression

$$TSOL = \frac{B}{\ln\left(\frac{A}{H}\right)} \quad (4\text{-}19)$$

where

A and B = constants given in conjunction with Equation (4-18)

H = hydrogen concentration (ppm by weight).

A value of H can be determined with the function CHUPTK (Section 4.16).

Equations (4-18) and (4-19) are based on data reported by Scott[4.3-4] for zirconium with and without intentional additions of hydrogen. For temperatures below 830 K, Scott (Figure 16 of Reference 4.3-4) finds the logarithm of the terminal solubility of hydrogen in zirconium to be proportional to temperature. Below the temperature TSOL, when hydrides are not completely dissolved,

Energy to dissolve hydride = constant x exp(negative constant/temperature). (4-20)

It is assumed in this expression that the terminal solubility will be attained as long as undissolved hydrogen is present. The heat of solution per gram atom of hydrogen may be taken as the average of two values given by Scott (Table VII of Reference 4.3-4). Equation (4-18) results from differentiation of this expression with respect to temperature and multiplication by the empirical factor

$$\left[\exp\left(\frac{T-TSOL}{0.02TSOL}\right)+1\right]^{-1}$$

to express the fact that the data do not show an instant termination of hydride solution with increasing temperature.

Figure 4-5 illustrates Scott's data for two samples of zirconium iodide and a single sample of zirconium intentionally doped with approximately 300 ppm of hydrogen. The two zirconium iodide samples apparently contained some hydrogen and were fit by the MATPRO correlation [Equation (4-19)], assuming they contained 28 ppm hydrogen. Figure 4-5 also shows the MATPRO correlation assuming 300 ppm hydrogen and the curve recommended by Scott for pure zirconium.

4.3.3 Uncertainties in Specific Heat Predictions

The systematic error (the estimated variation between values obtained with different samples) is larger than the imprecision in the base data of CCP and CHSCP.

The standard error of CCP, reflecting the systematic error for a random sample of cladding zircaloys, is estimated to be ± 10 J/kg · K (± 3%) in the alpha phase. This value is based on the difference between values of specific heat estimated by Deem and Eldridge from their data[4.3-2] and the more precise data from one sample of zircaloy-2 used by MATPRO. In the alpha beta phase region and the beta region to 1,300 K, a roughly estimated standard error of 25 J/kg · K is assigned to CCP, based on the decreased precision of the measurements and on the lack of confirming data in this temperature range. Above 1,300 K, the only basis for the assumed constant value of specific heat is the prediction of the Debye model of heat capacity for temperatures above the Debye temperature. Since no data are available, a standard error of ± 100 J/kg · K is listed.

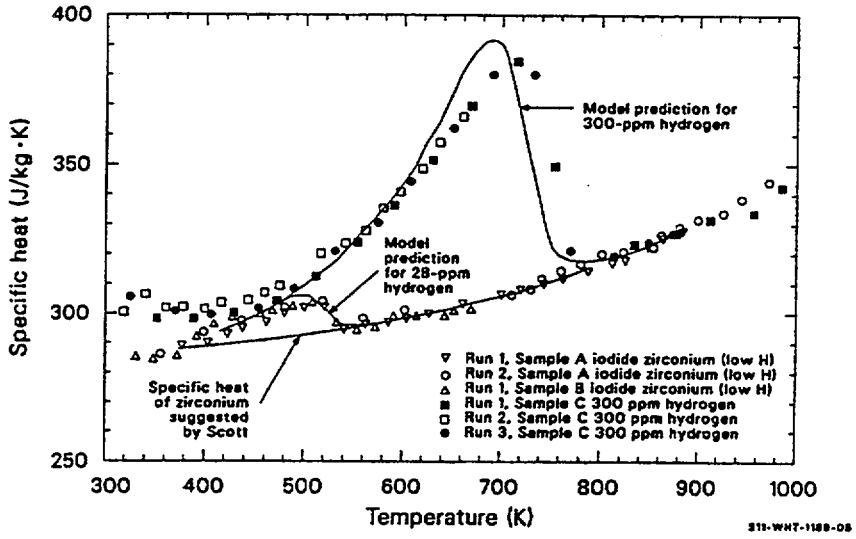

Figure 4-5. Data base for MATPRO prediction of the effect of hydride solution on specific heat, Scott's proposed curve for the specific heat of zirconium, and the MATPRO predictions for the effect of 28 and 300 ppm of hydrogen on the specific heat curve.

The basis for the estimate of the standard error of CHSCP over a random sample of cladding zircaloy is shown in Figure 4-6, which compares MATPRO predictions for several concentrations of hydrogen with a curve published by Brooks and Stansbury[4.3-1] for the specific heat of zircaloy-2 tested without prior heat treatment. The unpublished data are reported to be within 1% of this curve, and the MATPRO prediction is as far as 3% (10 J/kg · K) below the reported curve. Since the prediction of CCP in this temperature range is based on precise data (± 1.1 J/kg · K) taken with vacuum annealed samples of the same alloy, shown by a dashed line in Figure 4-6, most of the discrepancy (between the dashed line and the 28 ppm H solid line) is presumed to be due to errors inherent in the application by CHSCP to the zirconium data of Scott for zircaloy. A standard error of 50% in the hydrogen induced increment to apparent specific heat is, therefore, assigned to the model.

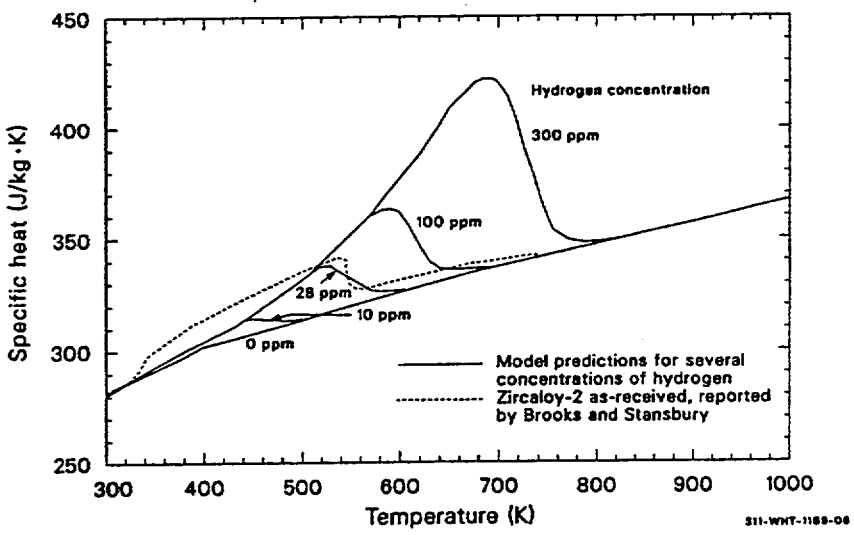

Figure 4-6. MATPRO predictions for apparent zircaloy specific heat for several hydrogen concentrations compared with the curve measured with as-received zircaloy-2.

The uncertainties in CCP are summarized in Table 4-4.

Table 4-4. Uncertainties in specific heat of zircaloy.

Temperature range	Standard error in CPP
$300 < T < 1{,}090$ K	± 10 J/kg · K
$1{,}090 < T < 1{,}300$ K	± 25 J/kg · K
$T < 1{,}300$ K	± 100 J/kg · K

4.3.4 Zircaloy Enthalpy (CENTHL)

The function CENTHL provides zircaloy enthalpy for temperatures above 300 K. The CENTHL enthalpy subcode requires a temperature and a reference temperature for which the enthalpy will be set equal to zero.

Zircaloy enthalpy is modeled by integrating the expressions used in the cladding specific heat subcode, CCP. Since CCP utilizes linear interpolation on the set of points reproduced in Table 4-2, the CENTHL routine uses the expression

$$H(T) - H(300) = \sum_{j=1}^{i} \Delta H_j + C_{p_i}(T - T_i) + \frac{(T - T_i)^2}{2(T_{i+1} - T_i)}(C_{P_{i+1}} - C_{p_i}) \qquad (4\text{-}21)$$

where

$H(T)$	=	enthalpy of zircaloy at temperature T (J/kg)
T_i	=	i-th temperature in Table 4-2 (K)
C_p	=	specific heat capacity at T_i (J/kg · K)
ΔH	=	change in enthalpy of zircaloy between T_{i-1} and T_i
T	=	temperature (K).

To find the enthalpy at a temperature greater than or equal to T_i, but less than T_{i+1}. Equation (4-21) can be derived by inspection of Figure 4-7. The first term is the enthalpy between T_1 and T_i, that is the area under the line segments which connect $C_{p_{i+1}}$ to C_{p_i}. The second term is the area of rectangle B, and the third term is the area of triangle A. The sum of these two areas is the enthalpy between T_i and T. Table 4-5 lists values of $\varepsilon\Delta H_j$ corresponding to the values of C_p in Table 4-2. The entries for 2,098 and 2,099 K incorporate the heat of fusion for melting zircaloy. The melt temperature and heat of fusion were taken from the MATPRO-11, Revision 2, PHYPRP subcode, and do not include the effect of oxidation on these quantities.

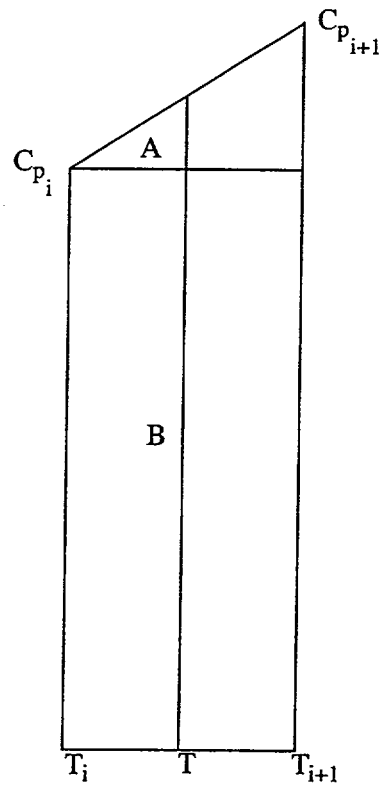

Figure 4-7. Derivation of Equation (4-21).

Table 4-5. Values of mass for zircaloy.

Temperature (K)	$\sum_{j=1}^{i-1} \Delta H_j$ (10^4J/kg)
300	0.000
400	2.915
640	10.511
1,090	26.396
1,093	26.52755
1,113	27.61955
1,133	28.82455
1,153	30.15855
1,173	31.69355
1,193	33.27955
1,213	34.66855
1,233	35.67655
1,248	36.29530
2,098	66.5553
2,099	89.0909

For temperatures greater than 2,099 K, an enthalpy consistent with a constant specific heat capacity above 2,099 K is calculated by omitting the third term on the right-hand side of Equation (4-21). Table 4-6 lists engineering estimates for the expected standard error of the enthalpy predicted by CENTHL with a reference temperature of 300 K.

Table 4-6. Uncertainty of zircaloy enthalpy.

Temperature range (K)	Expected standard error of CNTHL (fraction of predicted value)
$300 \leq T \leq 1{,}090$	0.03
$1{,}090 \leq T \leq 2{,}656.67$	$3 \times 4\ 10^{-4}\ (T - 1{,}090) + 0.03$
$2656.67 \leq T$	0.5

A code generated plot of zircaloy enthalpy change as a function of temperature is presented in Figure 4-8.

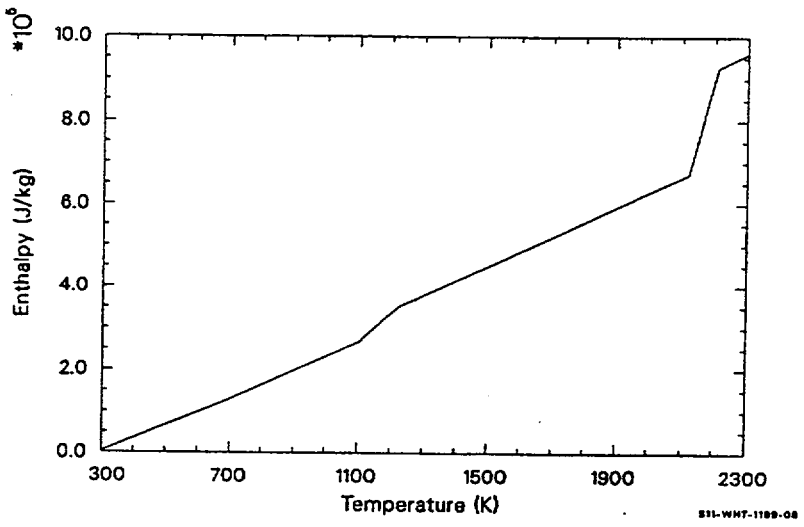

Figure 4-8. Zircaloy enthalpy as a function of temperature.

4.3.5 References

4.3-1 C. R. Brooks and E. E. Stansbury, "The Specific Heat of Zircaloy-2 from 50 to 700 °C," *Journal of Nuclear Materials, 18*, 1966, p. 223.

4.3-2 H. W. Deem and E. A. Eldridge, *Specific Heats and Heats of Transformation of Zircaloy-2 and Low Nickel Zircaloy-2*, USAEC BM1-1803, May 31, 1967.

4.3-3 J. P. Coughlin and E. G. King, "High Temperature Heat Contents of Some Zirconium Containing Substances," *Journal of the American Chemical Society, 72*, 1950, p. 2,262.

4.3-4 J. Scott, *A Calorimetric Investigation of Zirconium, Titanium, and Zirconium Alloys from 60 to 960 °C*, Ph.D. Thesis, University of Tennessee, 1957.

4.4 Thermal Conductivity (CTHCON)

The transfer of heat from the fuel pellet to reactor coolant depends partly on the thermal conductivity of the cladding. Accurate predictions of fuel temperatures require knowledge of zircaloy thermal conductivities. An expression has been developed for the thermal conductivity of zircaloy-2 and -4 based on the pooled data from eight reports. This expression and the uncertainty in the correlation are presented in this section.

4.4.1 Summary

The thermal conductivity of alloys is primarily a function of temperature. Other characteristics, such as residual stress levels, crystal orientation, and minor composition differences (zircaloy-2 versus zircaloy-4, for example), may have a secondary influence on thermal conductivity. Considering only temperature as the defining parameter, the thermal conductivity of zircaloy for temperatures less than 2,098 K and its uncertainty are found to be:

$$k = 7.51 + 2.09 \times 10^{-2} T - 1.45 \times 10^{-5} T^2 + 7.67 \times 10^{-9} T^3 \quad (4\text{-}22)$$

$$\sigma_k = 1.01 \ . \quad (4\text{-}23)$$

For temperatures greater than or equal to 2,098 K, the thermal conductivity and uncertainty are:

$$k = 36 \quad (4\text{-}24)$$

$$\sigma_k = \pm 5 \quad (4\text{-}25)$$

where

k = thermal conductivity of zircaloy (W/m · K)

T = temperature (K)

σ_k = standard deviation (W/m · K).

This equation predicts k very well from room temperature to the data limit of about 1,800 K and may be extrapolated with some confidence to the melting point. The standard deviation (σ_k) of the data with respect to this correlation appears to be temperature independent over the data range (Figure 4-9). Least squares regression analysis indicates that the standard deviation for each of the constants in Equation (4-22) is 20 - 30% of the value of the constant.

The correlations for zircaloy thermal conductivity at high temperatures required only consideration of the effect of melting on thermal conductivity. No data for liquid zircaloy thermal conductivity have been found; but Nazare, Ondracek, and Schulz[4.4-1] have reported that the ratios of solid state conductivities to liquid state conductivities at the melting temperatures for metals like zircaloy with eight nearest neighbor atoms is 1.6 ± 0.2.[a] Since the solid state conductivity predicted by the CTHCON function is 58 W/m · K, the liquid state conductivity should be about 36 ± 5 W/m · K.

a. The body-centered cubic lattice of beta-phase zircaloy has eight nearest neighbors.

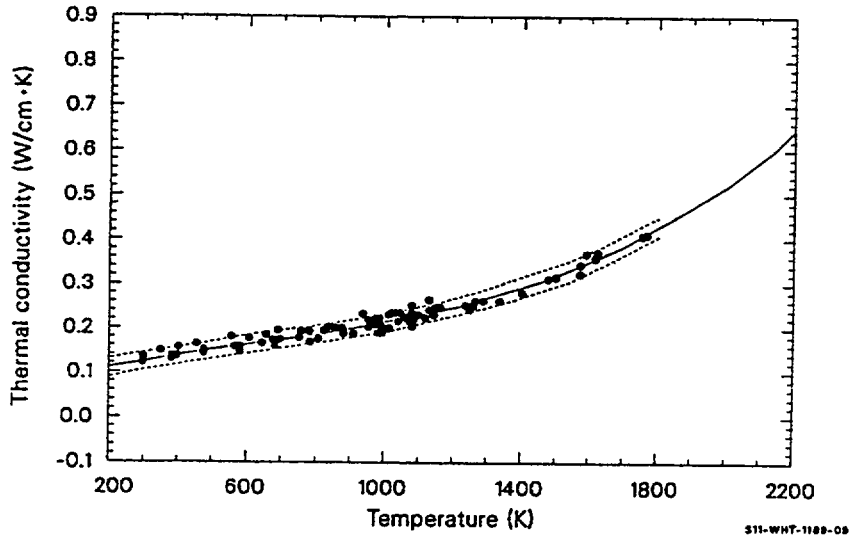

Figure 4-9. Thermal conductivity data, least squares fit, and the two standard deviation limits.

4.4.2 Literature Review

Anderson[4.4-2] reported thermal conductivity data for zircaloy-2 in the temperature range of 380 to 872 K. Chirigos et al.[4.4-3] reported thermal conductivity data for zircaloy-4 between 370 and 1,125 K. Feith[4.4-4] studied the thermal conductivity of zircaloy-4 between 640 and 1,770 K. Lucks and Deem[4.4-5] measured the thermal conductivity of zircaloy-2 in the temperature range of 290 to 1,075 K. Powers[4.4-6] reported three sets of thermal conductivity data for zircaloy taken from Battelle Memorial Institute (BMI) letter reports. These data cover both zircaloy-2 and -4 over temperature ranges of approximately 300 to 1,000 K. Scott[4.4-7] reported the thermal conductivity of zircaloy-4 between 400 and 1,060 K. Numerical values of his data were reported by Touloukian et al.,[4.4-8] These data are presented in Table 4-7.

Table 4-7. Zircaloy thermal conductivity data base.

Temperature (K)	Experimental thermal conductivity [W/(m · K)]	Calculated thermal conductivity [W/(m · K)]	Difference between calculated and experimental thermal conductivity	Reference	Material
380.4	13.50	13.78	-0.28	W. K. Anderson et al.	Zircaloy-2
469.3	14.43	14.92	-0.49		
577.6	15.68	16.22	-0.54		

Table 4-7. Zircaloy thermal conductivity data base. (Continued)

Temperature (K)	Experimental thermal conductivity [W/(m · K)]	Calculated thermal conductivity [W/(m · K)]	Difference between calculated and experimental thermal conductivity	Reference	Material
685.9	17.10	17.50	-0.40		
774.8	18.42	18.57	-0.15		
872.0	19.91	19.80	0.11		
373.2	13.60	13.69	-0.09	J. N. Chirigos et al.	Zircaloy-4
473.2	14.30	14.97	-0.67		
573.2	15.20	16.17	-0.97		
673.2	16.40	17.35	-0.95		
773.2	18.00	18.55	-0.55		
873.2	20.10	19.81	0.29		
973.2	22.50	21.19	1.31		
1,073.2	25.20	22.72	2.48		
1,123.2	26.60	23.56	3.04		
642.2	16.30	16.98	-0.68	A. D. Feith	Zircaloy-4
678.2	16.10	17.41	-1.31		
746.2	17.60	18.22	-0.62		
780.2	18.40	18.63	-0.23		
800.2	17.70	18.88	-1.18		
819.2	19.80	19.12	0.68		
833.2	20.10	19.29	0.81		
847.2	19.60	19.47	0.13		
850.2	20.00	19.51	0.49		
902.2	19.00	20.20	-1.20		
925.2	23.10	20.51	2.59		

Table 4-7. Zircaloy thermal conductivity data base. (Continued)

Temperature (K)	Experimental thermal conductivity [W/(m · K)]	Calculated thermal conductivity [W/(m · K)]	Difference between calculated and experimental thermal conductivity	Reference	Material
943.2	21.80	20.76	1.04		
946.2	20.40	20.80	-0.40		
960.2	22.10	21.00	1.10		
963.2	21.50	21.04	0.46		
969.2	21.40	21.13	0.27		
981.2	21.20	21.30	-0.10		
1,005.2	22.90	21.66	1.24		
1,012.2	23.60	21.76	1.84		
1,019.2	21.10	21.87	-0.77		
1,021.2	21.20	21.90	-0.70		
1,023.2	22.60	21.93	0.67		
1,025.2	23.20	21.96	1.24		
1,035.2	21.80	22.12	-0.32		
1,037.2	22.50	22.15	0.35		
1,040.2	22.90	22.19	0.71		
1,054.2	22.70	22.41	0.29		
1,063.2	24.00	22.56	1.44		
1,066.2	21.70	22.61	-0.91		
1,079.2	21.40	22.82	-1.42		
1,093.2	23.30	23.05	0.25		
1,122.2	22.50	23.54	-1.04		
1,128.2	24.50	23.65	0.85		
1,139.2	23.10	23.84	-0.74		
1,152.2	24.40	24.07	0.33		
1,161.2	24.20	24.24	-0.04		
1,232.2	25.30	25.60	-0.30		

Table 4-7. Zircaloy thermal conductivity data base. (Continued)

Temperature (K)	Experimental thermal conductivity [W/(m · K)]	Calculated thermal conductivity [W/(m · K)]	Difference between calculated and experimental thermal conductivity	Reference	Material
1,243.2	24.70	25.82	-1.12		
1,253.2	25.20	26.02	-0.82		
1,269.2	26.20	26.36	-0.16		
1,289.2	26.50	26.79	-0.29		
1,331.2	26.40	27.73	-1.33		
1,401.2	27.80	29.43	-1.63		
1,404.2	27.90	29.50	-1.60		
1,484.2	31.10	31.67	-0.57		
1,508.2	31.70	32.36	-0.66		
1,576.2	32.60	34.46	-1.86		
1,581.2	34.60	34.63	-0.03		
1,594.2	36.80	35.05	1.75		
1,624.2	36.30	36.07	0.23		
1,625.2	37.30	36.10	1.20		
1,755.2	41.40	41.00	0.40		
1,771.2	41.80	41.66	0.14		
293.2	12.60	12.58	0.02	C. F. Lucks and H. W. Deem	Zircaloy-2
373.2	13.40	13.69	-0.29		
473.2	14.50	14.97	-0.47		
573.2	15.60	16.17	-0.57		
673.2	17.00	17.35	-0.35		
773.2	18.40	18.55	-0.15		
873.2	19.90	19.81	0.09		
973.2	21.50	21.19	0.31		

Table 4-7. Zircaloy thermal conductivity data base. (Continued)

Temperature (K)	Experimental thermal conductivity [W/(m · K)]	Calculated thermal conductivity [W/(m · K)]	Difference between calculated and experimental thermal conductivity	Reference	Material
1,073.2	23.10	22.72	0.38		
373.2	14.11	13.69	0.42	A. E. Powers	Zircaloy-2
473.2	14.80	14.97	-0.17		
573.2	15.32	16.17	-0.85		
673.2	16.01	17.35	-1.34		
773.2	17.05	18.55	-1.50		
873.2	1.18	19.81	-1.63		
973.2	19.42	21.19	-1.77		
1,073.2	20.77	22.72	-1.95		
293.2	12.55	12.58	-0.03		
373.2	13.29	13.69	-0.40		
473.2	14.37	14.97	-0.60		
573.2	15.58	16.17	-0.59		
673.2	16.88	17.35	-0.47		
773.2	18.42	18.55	-0.13		
873.2	19.91	19.81	0.10		
973.2	21.52	21.19	-0.33		
1,073.2	23.02	22.72	0.30		
293.2	13.42	12.58	0.84		
373.2	13.67	13.69	-0.02		
473.2	14.16	14.97	-0.81		
573.2	15.13	16.17	-1.04		
673.2	16.39	17.35	-0.96		
773.2	18.00	18.55	-0.55		
873.2	20.17	19.81	0.36		

Table 4-7. Zircaloy thermal conductivity data base. (Continued)

Temperature (K)	Experimental thermal conductivity [W/(m · K)]	Calculated thermal conductivity [W/(m · K)]	Difference between calculated and experimental thermal conductivity	Reference	Material
973.2	22.55	21.19	1.36		
403.2	15.60	14.08	1.52	D. B. Scott, Y. S. Touloukian et al.	Zircaloy-4
452.1	16.30	14.70	1.60		
476.5	14.50	15.01	-0.51		
546.5	18.30	15.85	2.45		
557.6	15.80	15.99	-0.19		
602.6	17.60	16.52	1.08		
649.9	18.50	17.03	1.47		
682.1	19.20	17.45	1.75		
694.3	17.10	17.60	-0.50		
753.2	18.90	18.30	0.60		
770.3	18.90	18.51	0.39		
812.1	19.60	19.03	0.57		
826.5	20.10	19.21	0.89		
982.1	19.70	21.32	-1.62		
1,000.9	20.30	21.59	-1.29		
1,058.1	21.70	22.48	-0.78		

4.4.3 Model Development

The data reported in Section 4.4.2 refer to zircaloy-2 and zircaloy-4 having various textures and pretest histories. The alloy chemistry and heat transfer properties of zircaloy-2 and-4 are similar enough to consider them to be a single material. The differences in thermal conductivity between the materials appears to be of the same magnitude as the statistical scatter in the data.

Texture may have an effect in the alpha phase temperature region. Zircaloy is crystallized in a hexagonal, close packed configuration in the low temperature alpha phase; and there may be some difference in the thermal conductivity along the prismatic and basal directions. At higher temperatures, the material is body centered cubic and will not exhibit texture effects. In any case, contributions to the thermal conductivity due to texture are probably well within the scatter of the experimental data used to develop models for this property.

All of the available data for thermal conductivity of zircaloy-2 and -4 were combined and analyzed using a least squares polynomial fit of the third degree. The equation is:

$$k = 7.51 + 2.09 \times 10^{-2} T - 1.45 \times 10^{-5} T^2 + 7.67 \times 10^{-9} T^3 \quad . \tag{4-26}$$

where

k = zircaloy thermal conductivity (W/m•K)

T = temperature of cladding (K).

A comparison of calculated thermal conductivities and the data is shown in Figure 4-9.

The standard deviation of the data with respect to Equation (4-26) is 1.01 W/m• K. Thirty two of the points fall outside $\pm 1\sigma$ from the curve. Four points fall outside $\pm 2\sigma$ (Figure 4-9). The standard deviations of the coefficients of Equation (4-26) are about 20 - 30% of the absolute value of the coefficients.

The standard deviation is small enough so that the user may have considerable confidence in the model. Jensen[4.4-9] performed a parametric analysis of several variables involved in the estimation of fuel and cladding temperatures. Both steady-state and transient analyses showed that variations of $\pm$ 20% resulted in calculated cladding temperature variations of about 2.8 K. Fuel centerline temperatures are more sensitive to cladding thermal conductivity and showed variations of 28 K. Similar findings were reported by Korber and Unger.[4.4-10]

4.4.4 References

4.4-1 S. Nazare, G. Ondracek, and B. Schulz, "Properties of Light Water Reactor Core Melts," *Nuclear Technology, 32*, 1977, pp. 239-246.

4.4-2 W. K. Anderson, C. J. Beck, A. R. Kephart, and J. S. Theilacker "Zirconium Alloys," *Reactor Structural Materials: Engineering Properties as Affected by Nuclear Reactor Service*, ASTM-STP-314, 1962, pp. 62-93

4.4-3 J. N. Chirigos et al., "Development of Zircaloy-4," *Fuel Element Fabrication*, New York: Academic Press, 1961, pp. 19-55.

4.4-4 A. D. Feith, *Thermal Conductivity and Electrical Resistivity of Zircaloy-4*, GEMP-669, October 1966.

4.4-5 C. F. Lucks and H. W. Deem, *Progress Relating to Civilian Applications During June, 1958*, R. W. Dayton and C. R. Tipton, Jr., (eds.), BMI-1273, 1958, pp. 7-9.

4.4-6 A. E. Powers, *Application of the Ewing Equation for Calculating Thermal Conductivity from Electrical Conductivity*, KAPL-2146, April 7, 1961.

4.4-7 D. B. Scott, *Physical and Mechanical Properties of Zircaloy-2 and -4*, WCAP-3269-41, May 1965, pp. 5, 9.

4.4-8 Y. S. Touloukian, R. W. Powell, C. Y. Ho, and P. G. Klemens, *Thermophysical Properties of Matter, Volume 1, Thermal Conductivity*, NewYork: Plenum Press, 1970, pp. 888-889.

4.4-9 S. E. Jensen, *Parametric Studies of Fuel Pin Temperature Response*, IDO-17295, February 1969.

4.4-10 H. Korber and H. E. Unger, "Sensitivity Study on Core Heatup and Meltdown by Variation of Heat Conductivity and Thermal Emissivity," *Transactions of the American Nuclear Society, 18*, 1974, pp. 234-235.

4.5 Thermal Expansion, Density and Their Relation to Texture (CTHEXP, CDEN)

The model described herein calculates components of the thermal expansion strain for single crystal zircaloy. By use of pole figures to ascertain the average orientation of single crystals in a multicrystalline sample, such as zircaloy fuel rod cladding, these single crystal values may be applied to find the thermal expansion strain of any sample.

Thermal expansion strain, especially in the diametral direction, is important in safety analyses because it is a major factor in determining the pellet cladding gap, and thus the pellet temperature and its stored energy. Since zircaloy is an anisotropic solid, strains parallel and perpendicular to the basal pole direction of single crystal grains are needed to find the diametral strain in a multicrystalline sample. The subcode CTHEXP treats this strain as a tensor and uses pole figures to calculate the thermal expansion strain.

The subroutine CDEN returns the density of zircaloy from room temperature data and thermal expansion strains calculated with the CTHEXP subcode.

4.5.1 Summary (CTHEXP)

A total of six correlations that are functions of temperature only are used to find single crystal thermal strains. In addition, basal plane symmetry ($\varepsilon_{11} = \varepsilon_{22}$) is assumed. The model was developed for as fabricated zircaloy-4, but comparisons with zircaloy-2 and zirconium data also show good agreement for these materials.

The correlations for single crystal thermal strains are:

For $300 < T < 1{,}083$ K,

$$\varepsilon_{11} = 4.95 \times 10^{-6}\, T - 1.485 \times 10^{-3} \tag{4-27}$$

$$\varepsilon_{33} = 1.26 \times 10^{-5}\, T - 3.78 \times 10^{-3} \tag{4-28}$$

where

ε_{11} = circumferential thermal expansion (m/m)

ε_{33} = axial thermal expansion (m/m)

T = temperature (K).

For $1{,}083 \leq T \leq 1244$ K,

$$\varepsilon_{11} = \left[2.77763 + 1.09822\cos\left(\frac{T - 1083}{161}\pi\right)\right]\times 10^{-3} \tag{4-29}$$

$$\varepsilon_{33} = \left[8.76758 + 1.09822\cos\left(\frac{T - 1083}{161}\pi\right)\right]\times 10^{-3} \tag{4-30}$$

where the arguments of the cosines are in radians.

For $1{,}244\ K \leq T \leq 2098$ K,

$$\varepsilon_{11} = 9.7 \times 10^{-6}\, T - 1.04 \times 10^{-2} \tag{4-31}$$

$$\varepsilon_{33} = 9.7 \times 10^{-6}\, T - 4.4 \times 10^{-3}\ . \tag{4-32}$$

For temperatures > 2,098 K, consideration of the volume change associated with melting is required. Since no data have been found, a typical 2% volume increase at melt is assumed. The expressions used for the thermal strain in liquid zirconium (temperatures ≥ 2,098 K) are thus

$$\varepsilon_p = \frac{2}{3}\varepsilon_{11} + \frac{1}{3}\varepsilon_{33} + 0.0067 \tag{4-33}$$

where

ε_p = thermal expansion strain in liquid zircaloy (m/m)

ε_{11} = circumferential thermal expansion strain of a single crystal of zircaloy at 2,098 K (m/m)

ε_{33} = axial thermal expansion strain of a single crystal of zircaloy at 2,098 K (m/m).

Equations (4-29) and (4-30) are used to calculate ε_{11} and ε_{33}.

To obtain cladding strains from these single crystal strains, it is necessary to do a volume weighted averaging over the entire cladding section. Such an averaging requires a pole figure and is described in Section 16.2. The results are

$$\langle \varepsilon'_{11} \rangle = \langle \sin^2\phi \rangle \varepsilon_{11} + \langle \cos^2\theta \cos^2\phi \rangle \varepsilon_{22} + \langle \sin^2\theta \cos^2\phi \rangle \varepsilon_{33} \quad (4\text{-}34)$$

$$\langle \varepsilon'_{22} \rangle = \langle \cos^2\phi \rangle \varepsilon_{11} + \langle \cos^2\theta \sin^2\phi \rangle \varepsilon_{22} + \langle \sin^2\theta \sin^2\phi \rangle \varepsilon_{33} \quad (4\text{-}35)$$

$$\langle \varepsilon'_{33} \rangle = \langle \sin^2\theta \rangle \varepsilon_{22} + \langle \cos^2\theta \rangle \varepsilon_{33} \quad (4\text{-}36)$$

where primed strains refer to the laboratory system (cladding and unprimed strains to the single crystals),

θ = angle between the radial direction of the cladding and the c-axis of the single crystals

ϕ = angle between the circumferential direction of the cladding and the projection of the c-axis at a grain onto the circumferential--axial plane at the cladding.

As an example, the strains for a typical LWR cladding tube (zircaloy-4) are, for $T < 1{,}083$ K

$$\langle \varepsilon'_{11} \rangle = 6.48\times10^{-6}T - 1.95\times10^{-3} \quad (4\text{-}37)$$

$$\langle \varepsilon'_{22} \rangle = 5.63\times10^{-6}T - 1.69\times10^{-3} \quad (4\text{-}38)$$

$$\langle \varepsilon'_{33} \rangle = 1.04\times10^{-5}T - 3.11\times10^{-3} \quad . \quad (4\text{-}39)$$

Equations (4-37) through (4-39) are valid for $\langle \cos^2\theta \rangle = 0.71013$ and $\langle \sin^2\phi \rangle = 0.30822$.

Section 4.5.2 contains a review of the literature consulted. The model development is given in Section 4.5.3, and Section 4.5.4 contains a model data comparison with an uncertainty analysis.

4.5.2 Literature Review (CTHEXP)

The most important source is the model on cladding plastic deformation, Section 4.9, where the volume weighted averages of the direction cosines for typical LWR cladding are given. These averages were used with thermal expansion data from an EPRI report by Bunnell[4.5-1] to make the basic model. Since Bunnell does not report data in the beta phase (T > 1,244 K) for circumferential expansion, the data can be used only for an alpha phase model. The EPRI data do not show ε_{11} or ε_{22} equal to zero at 300 K, and therefore each point was shifted by an amount such that this requirement was met. To determine the validity of the resulting data, they were checked against the older data sources of Douglas,[4.5-2] Mehan and Wiesinger,[4.5-3] Scott,[4.5-4] and Kearns.[4.5-5] The correlations given here compare well with those of Douglass and Kearns, as shown in Figure 4-10 through Figure 4-13. The Mehan and Wiesinger data are for plates. To be compared with Equations (4-27) and (4-28), these equations must be converted from single crystal form to plate form. Since Mehan and Wiesinger give no detailed texture information, typical values for texture coefficients from Hann[4.5-6] were used. The results are shown in Table 4-8.

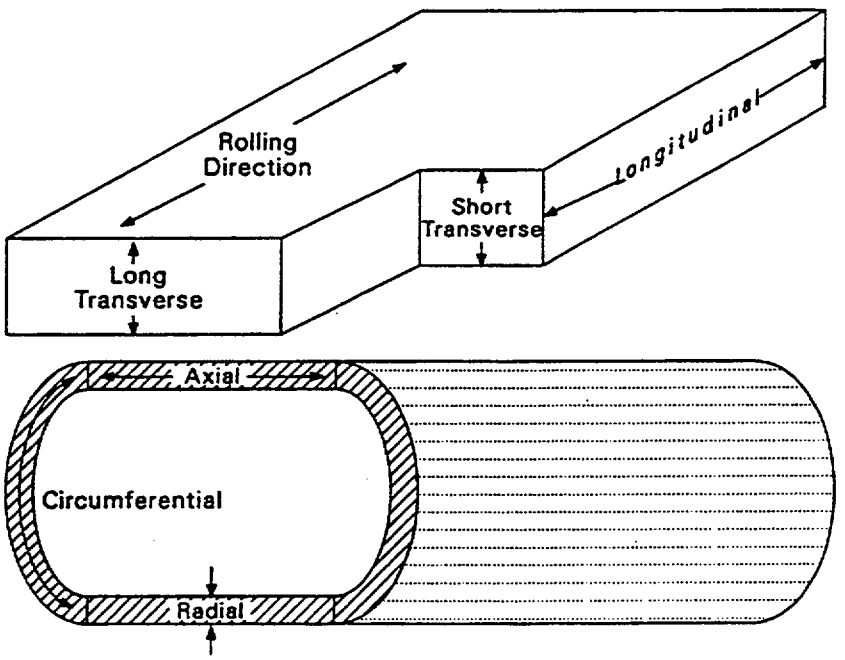

Figure 4-10. Comparison of CTHEXP prediction with Douglass' data in the axial direction.

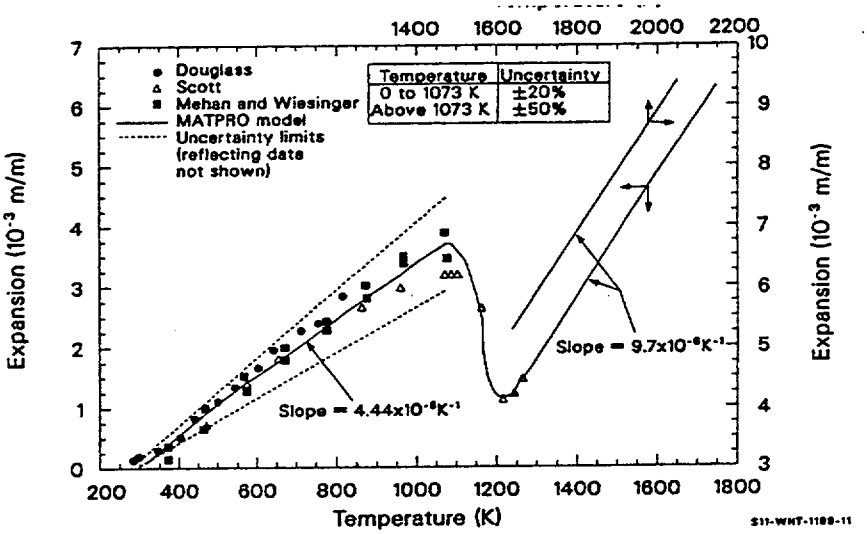

Figure 4-11. Comparison of CTHEXP prediction with Douglass' data in the circumferential direction.

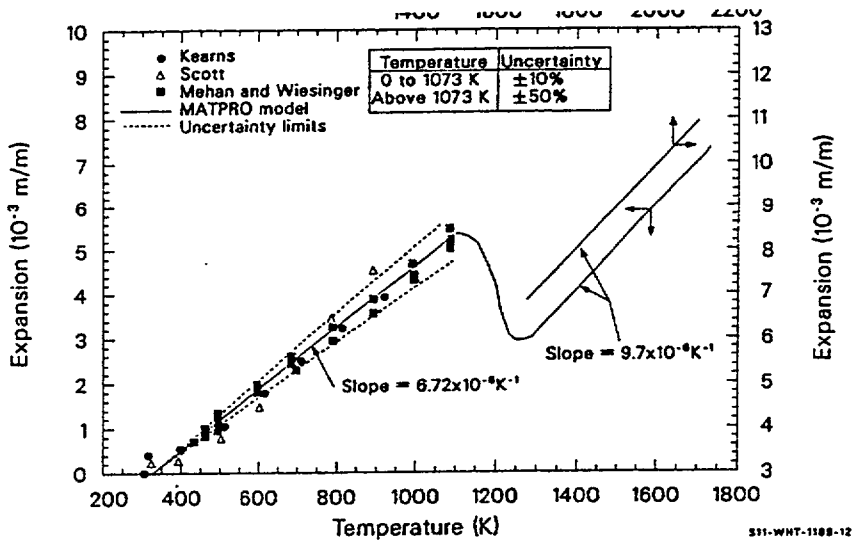

Figure 4-12. Comparison of CTHEXP prediction with Kearns' model in the axial direction.

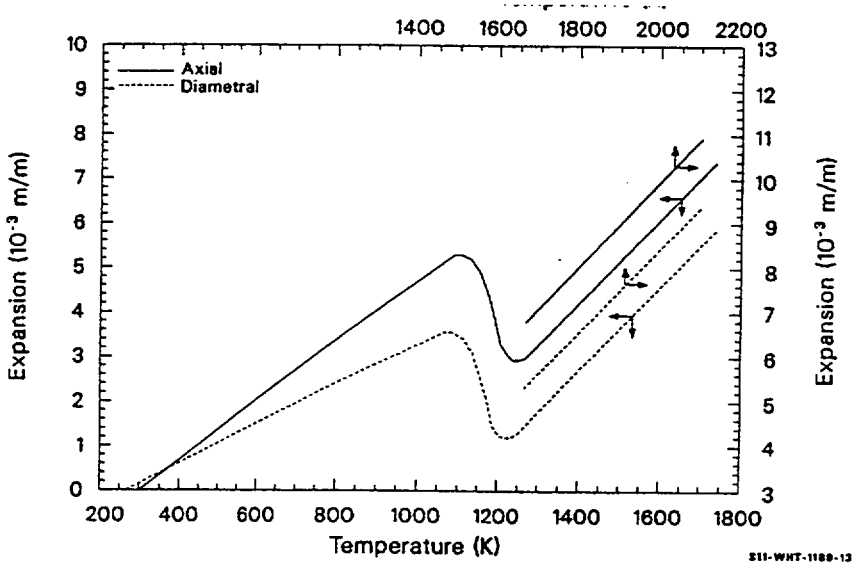

Figure 4-13. Comparison of CTHEXP prediction with Kearns' model in the circumferential direction.

Table 4-8. Comparison of Mehan and Wiesinger plate expansion with MATPRO model.

Direction	Mehan and Wiesinger	MATPRO model	Difference (%)
Longitudinal	4.62×10^{-6}	5.41×10^{-6}	-14.60
Transverse	6.58×10^{-6}	7.10×10^{-6}	-7.32

The differences shown in Table 4-8 can be easily explained by the unknown texture differences between the samples from which the data sets were derived.

All data sets had to be adjusted to give $\Delta L = 0$ at 300 K. This was done by adding or subtracting the strain at 300 K. This technique is not exact for engineering strains but results in negligible error when the strains are small, as in the case here.

These comparisons show that the Bunnell data are adequate in the alpha phase. Therefore, this data set is used as the data base in the low temperature ($T < 1{,}083$ K) range.

In the transition region between the alpha and beta phases ($1{,}083 \leq T \leq 1{,}244$ K), the volume strain was found using lattice constants for alpha zirconium from Douglass and for beta zirconium from Kittel.[4.5-7] This strain was divided by 3.0 to find an approximate linear strain, which was assumed to be equal in all three directions. A cosine function was fit to the strains to match the values at the end of the

alpha phase and the beginning of the beta phase. For the beta phase, the coefficient of expansion for zirconium from Skinner and Johnston[4.5-8] was used.

The correlations for T > 1,083 K are approximate. However, at these temperatures, the cladding is so soft that typical in-reactor stresses cause a significantly greater strain than the strain due to thermal expansion.

4.5.3 Model Development (CTHEXP)

The model development is divided into three sections, depending on the temperature: an alpha phase region, a transition phase region, and a beta phase region.

4.5.3.1 Thermal Expansion in the Alpha Phase. The basic equations used to model thermal expansion in the alpha phase are tensor transformation equations relating cladding strain components to single crystal strain components and parameters that describe the distribution of grain orientations in the cladding. The model is based on measured thermal strains in two directions for cladding with known texture. The inverse of the transformation is used to deduce single crystal thermal expansions from data.

Since strain is a second rank tensor, it is necessary to do a formal rotation of axes to describe single crystal strains viewed from a laboratory system. The rotation is shown schematically in Figure 4-14, which was taken from Section 4.6. To derive the various tensors, first consider the transformation necessary to obtain the laboratory unit vectors expressed in terms of the single crystal unit vectors. Since the single crystal is isotropic in planes perpendicular to the c-axis, assume for this transformation that the y-axis (single crystal) is in the same plane as the c-axis and the radial direction of the tube. Primed coordinates refer to those fixed in the laboratory system, and the unprimed coordinates refer to those fixed in the single crystals. The resulting transformation is

$$\hat{x}' = \sin\phi\hat{x} + \cos\theta\cos\phi\hat{y} + \sin\theta\cos\phi\hat{z} \tag{4-40}$$

$$\hat{y}' = -\cos\theta\hat{x} + \cos\theta\sin\phi\hat{y} + \sin\theta\sin\phi\hat{z} \tag{4-41}$$

$$\hat{z}' = -\sin\theta\hat{y} + \sin\theta\cos\theta\hat{z} \tag{4-42}$$

where θ and ϕ are defined in Figure 4-14.

Equations (4-40) through (4-42) show a first rank tensor transformation.

$$\hat{x}_i^j = c_{ij}\hat{x}_j \tag{4-43}$$

where c_{ij} is the transformation coefficient.

The corresponding transformations for strains (2nd-rank tensors) are

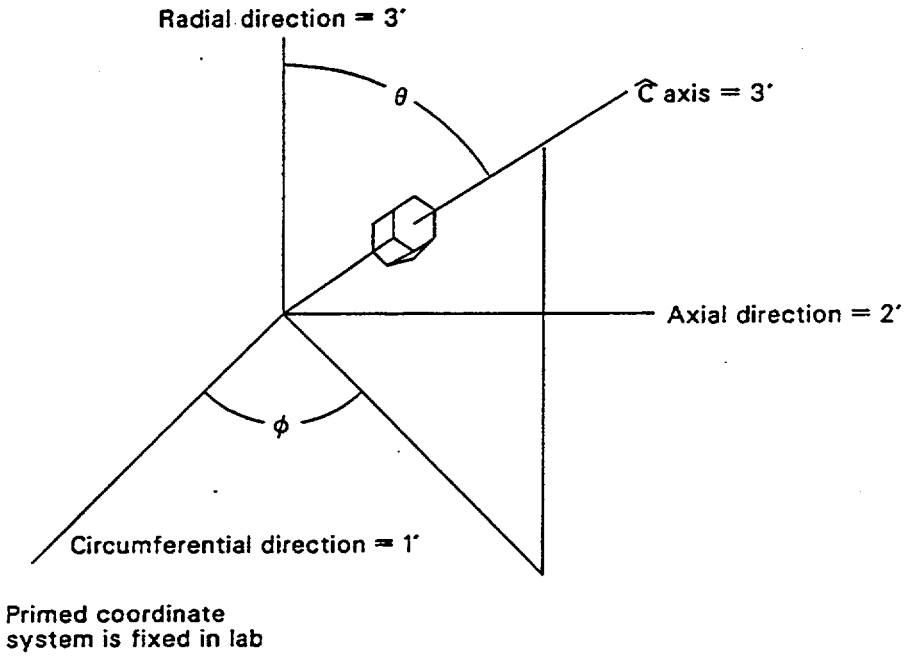

Figure 4-14. Angles and orientation of the unit cell of zircaloy relative to a system of coordinates fixed in the lab frame of reference.

$$\varepsilon'_{ij} = \sum_{s=1}^{3}\sum_{t=1}^{3} C_{is}C_{jt}\varepsilon_{st} \tag{4-44}$$

where C_{is} is the coefficient from the first order tensor transformation [Equations (4-40) through (4-42)]. For example, $C_{11} = \sin\phi$, $C_{12} = \cos\theta\cos\phi$, and $C_{13} = \sin\phi\cos\phi$.

Applying Equation (4-44) to find ε'_{11} gives

$$\begin{aligned}\varepsilon'_{11} = {} & (C_{11}C_{11}\varepsilon_{11} + C_{12}C_{11}\varepsilon_{21} + C_{13}C_{11}\varepsilon_{31}) + \\ & (C_{11}C_{12}\varepsilon_{12} + C_{12}C_{12}\varepsilon_{22} + C_{13}C_{12}\varepsilon_{32}) + \\ & (C_{11}C_{13}\varepsilon_{13} + C_{12}C_{13}\varepsilon_{23} + C_{13}C_{13}\varepsilon_{33}) \ .\end{aligned} \tag{4-45}$$

Substituting the appropriate C_{ij}'s into Equation (4-45) gives

$$\varepsilon'_{11} = \sin^2\phi\varepsilon_{11} + \cos\theta\cos\phi\sin\phi\varepsilon_{21} + \sin^2\theta\cos\phi 3\varepsilon_{31} + \sin\phi\cos\theta\cos\phi\varepsilon_{12} + \cos^2\theta\cos^2\phi\varepsilon_{22} + \sin^2\theta\cos\phi\varepsilon_{32} + \sin\phi\cos\phi\sin\theta\varepsilon_{13} + \cos\theta\cos\phi\sin\theta\varepsilon_{23} + \sin^2\theta\cos^2\phi\varepsilon_{33} \quad . \tag{4-46}$$

The volume weighted averages of the strain tensors are needed. These are given by

$$\langle\varepsilon'_{ij}\rangle = \int_0^{2\pi\pi}\int\varepsilon'_{ij}(\theta,\phi)\rho(\theta,\phi)\sin\theta d\theta d\phi \tag{4-47}$$

where

$\langle\varepsilon'_{ij}\rangle$ = volume fraction weighted average of e_{ij} (m/m)

$\varepsilon'_{ij}(\theta,\phi)$ = thermal expansion strain (m/m)

$\rho(\theta,\phi)$ = volume fraction of grains with their c-axis oriented in the region $\sin\theta\, d\theta\, d\phi$ about θ and ϕ.

Putting Equation (4-46) into Equation (4-47) gives

$$\langle\varepsilon'_{ij}\rangle = \varepsilon_{11}\int_{0\,0}^{2\pi\pi}\int\sin^2\phi\rho(\theta,\phi)\sin\theta d\theta d\phi + \varepsilon_{21}\int_{0\,0}^{2\pi\pi}\int\cos\theta\cos\phi\sin\phi\rho(\theta,\phi)\sin\theta d\theta d\phi\ldots \tag{4-48}$$

The integral $\int_{0\,0}^{2\pi\pi}\int\varepsilon_{11}\sin^2\phi\rho(\theta,\phi)\sin\theta d\theta d\phi = \langle\sin^2\phi\rangle$, the volume weighted average of $\sin^2\phi$. Similarly, the third integral

$$\varepsilon_{31}\int_{0\,0}^{2\pi\pi}\int\sin^2\theta\cos\phi\rho(\theta,\phi)\sin\theta d\theta d\phi = \langle\sin^2\theta\cos\phi\rangle = \langle\sin^2\theta\rangle\langle\cos\phi\rangle = 0.0 \tag{4-49}$$

because averaged over the 0 to 2π interval, $\cos\phi$ equals zero. In the same way, $\sin\phi$, $\sin\theta$, and $\cos\theta$ are zero. Only a squared function has a nonzero average. These averages may be found with the CTXTUR subcode of Section 16.2, using a pole figure for input texture information.

All nine of the tensor elements $\langle \varepsilon_{ij} \rangle$ may be found using Equations (4-44) and (4-47). The only nonzero ones are listed in Equations (4-34) through (4-36).

$$\langle \varepsilon'_{11} \rangle = \langle \sin^2\phi \rangle \varepsilon_{11} + \langle \cos^2\theta \cos^2\phi \rangle \varepsilon_{22} + \langle \sin^2\theta \cos^2\phi \rangle \varepsilon_{33} \quad (4\text{-}50)$$

$$\langle \varepsilon'_{22} \rangle = \langle \cos^2\phi \rangle \varepsilon_{11} + \langle \cos^2\theta \sin^2\phi \rangle \varepsilon_{22} + \langle \sin^2\theta \sin^2\phi \rangle \varepsilon_{33} \quad (4\text{-}51)$$

$$\langle \varepsilon'_{33} \rangle = \langle \sin^2\theta \rangle \varepsilon_{22} + \langle \cos^2\theta \rangle \varepsilon_{33} \quad . \quad (4\text{-}52)$$

From Section 4.9, the coefficients of the strains in Equations (4-34) through (4-36) may be found for the cladding used by Bunnell. Substituting these values into Equations (4-34) through (4-36), following equations are obtained.

$$\langle \varepsilon'_{11} \rangle = 0.18\varepsilon_{11} + 0.54\varepsilon_{22} + 0.28\varepsilon_{33} \quad (4\text{-}53)$$

$$\langle \varepsilon'_{22} \rangle = 0.82\varepsilon_{11} + 0.12\varepsilon_{22} + 0.06\varepsilon_{33} \quad (4\text{-}54)$$

$$\langle \varepsilon'_{33} \rangle = 0.34\varepsilon_{22} + 0.66\varepsilon_{33} \quad . \quad (4\text{-}55)$$

In a single crystal, the circumferential strain, ε_{11}, is equal to the diametral strain, ε_{22}, so Equations (4-53) through (4-55) reduce to

$$\langle \varepsilon'_{11} \rangle = 0.72\varepsilon_{11} + 0.28\varepsilon_{33} \quad (4\text{-}56)$$

$$\langle \varepsilon'_{22} \rangle = 0.94\varepsilon_{11} + 0.06\varepsilon_{33} \quad (4\text{-}57)$$

$$\langle \varepsilon'_{33} \rangle = 0.34\varepsilon_{22} + 0.66\varepsilon_{33} \quad . \quad (4\text{-}58)$$

Bunnell's data were taken in the laboratory frame. Therefore, Equations (4-56) through (4-58) must be inverted to find the single crystal strains in terms of the cladding strains

$$\varepsilon_{11} = -0.27\langle \varepsilon'_{11} \rangle + 1.27\langle \varepsilon'_{22} \rangle \quad (4\text{-}59)$$

$$\varepsilon_{33} = 4.27\langle \varepsilon'_{11} \rangle - 3.27\langle \varepsilon'_{22} \rangle \quad (4\text{-}60)$$

$$\varepsilon_{22} = \varepsilon_{11} \quad . \tag{4-61}$$

Bunnell's data, adjusted so the strain is zero at 300 K, are given in Table 4-9 and Table 4-10 for circumferential and axial thermal expansion, respectively.

Table 4-9. Bunnell's circumferential thermal expansion data.

Temperature (K)	ε_{11} x 10^{-3} (unitless)	Temperature (K)	ε_{11} x 10^{-3} (unitless)
394.15	1.806	616.15	2.326
398.15	1.136	620.15	2.516
401.15	1.266	625.15	1.916
405.15	0.716	627.15	2.926
439.15	1.336	663.15	2.636
444.15	1.516	667.15	2.826
444.15	2.206	671.15	2.226
447.15	0.926	673.15	3.396
481.15	1.616	708.15	2.986
485.15	1.786	712.15	3.126
488.15	1.196	716.15	2.516
488.15	2.196	718.15	3.736
523.15	1.876	751.15	3.266
528.15	2.016	755.15	3.456
531.15	1.416	759.15	2.856
532.15	2.516	761.15	3.916
568.15	2.096	794.15	3.646
572.15	2.216	797.15	3.756
577.15	1.626	802.15	3.166
579.15	2.776	804.15	4.346
836.15	4.026	964.15	4.806
840.15	4.096	969.15	5.026
844.15	3.476	972.15	4.376
846.15	4.396	975.15	4.676

Table 4-9. Bunnell's circumferential thermal expansion data. (Continued)

Temperature (K)	ε_{11} x 10^{-3} (unitless)	Temperature (K)	ε_{11} x 10^{-3} (unitless)
878.15	4.086	1008.15	5.006
881.15	4.436	1013.15	5.326
885.15	3.786	1017.15	4.656
888.15	4.506	1019.15	4.616
920.15	4.606	1044.15	4.736
925.15	4.716	1044.15	4.876
929.15	4.136	1044.15	5.646
931.15	4.706	1044.15	5.406

Table 4-10. Bunnell's axial thermal expansion data.

Temperature (K)	ε_{11} x 10^{-3} (unitless)	Temperature (K)	ε_{11} x 10^{-3} (unitless)
376.15	0.461	569.15	1.321
380.15	0.421	569.15	1.621
389.15	0.531	578.15	1.311
396.15	0.461	579.15	1.631
396.15	0.611	581.15	1.401
398.15	0.481	588.15	1.731
403.15	0.561	599.15	1.451
406.15	0.481	604.15	1.661
411.15	0.581	604.15	1.811
421.15	0.591	613.15	1.901
424.15	0.661	616.15	1.571
428.15	0.741	620.15	1.841
436.15	2.061	627.15	1.551
441.15	0.681	629.15	1.461
444.15	0.811	630.15	1.921
445.15	0.671	646.15	1.701

Table 4-10. Bunnell's axial thermal expansion data. (Continued)

Temperature (K)	ε_{11} x 10^{-3} (unitless)	Temperature (K)	ε_{11} x 10^{-3} (unitless)
449.15	0.691	646.15	2.031
456.15	0.901	651.15	1.851
462.15	0.941	653.15	2.111
466.15	0.801	663.15	1.841
468.15	0.901	663.15	2.031
477.15	1.031	671.15	2.151
482.15	0.901	673.15	1.831
489.15	1.121	675.15	1.871
490.15	0.911	686.15	2.221
496.15	1.201	691.15	1.991
504.15	1.201	694.15	2.271
506.15	1.021	697.15	2.221
511.15	1.181	704.15	2.061
512.15	1.251	707.15	2.111
523.15	1.111	711.15	2.351
524.15	1.351	718.15	2.101
531.15	1.451	721.15	2.111
532.15	1.101	726.15	2.401
535.15	1.131	833.15	2.511
540.15	1.141	734.15	2.251
548.15	1.481	738.15	1.051
550.15	1.211	740.15	2.481
557.15	1.441	749.15	2.531
563.15	1.581	750.15	2.381
760.15	2.351	930.15	3.281
763.15	2.321	932.15	3.221
764.15	2.631	932.15	3.471
771.15	2.691	946.15	3.431

Table 4-10. Bunnell's axial thermal expansion data. (Continued)

Temperature (K)	ε_{11} x 10^{-3} (unitless)	Temperature (K)	ε_{11} x 10^{-3} (unitless)
776.15	2.481	948.15	3.601
782.15	2.721	955.15	3.661
790.15	2.751	961.15	3.741
794.15	2.591	963.15	3.521
804.15	2.611	964.15	3.691
804.15	2.811	973.15	3.541
806.15	2.601	973.15	3.741
812.15	2.851	975.15	3.451
819.15	2.721	991.15	3.671
826.15	2.961	991.15	3.801
828.15	2.941	998.15	3.931
835.15	2.781	1003.15	3.581
843.15	3.031	1007.15	3.781
844.15	2.821	1007.15	3.851
848.15	2.761	1015.15	3.941
851.15	3.081	1017.15	3.081
862.15	2.961	1021.15	3.711
868.15	3.171	1032.15	3.901
869.15	3.191	1035.15	3.961
877.15	3.051	1042.15	4.181
878.15	3.181	1044.15	3.671
882.15	3.261	1047.15	3.821
886.15	3.061	1048.15	4.041
889.15	2.941	1052.15	4.071
890.15	3.321	1052.15	4.421
904.15	3.181	1052.15	4.161
908.15	3.401	1054.15	4.341
910.15	3.401	1084.15	4.461

Table 4-10. Bunnell's axial thermal expansion data. (Continued)

Temperature (K)	ε_{11} x 10^{-3} (unitless)	Temperature (K)	ε_{11} x 10^{-3} (unitless)
919.15	3.291	---	---
919.15	3.381	---	---
923.15	3.461	---	---

Using the data listed in these tables, the next step is to find the single crystal strains as a function of temperature. Since temperatures in the two tables do not always correspond, it was necessary to use Bunnell's correlations, which he used to fit those data, again adjusting them so the strains are zero at 300 K. A least squares fit was done, with the constraint that the strains are zero at 300 K. The results are given in Equation (4-27) and Equation (4-28).

Equations (4-27) and (4-28) are the models for the alpha phase of zircaloy single crystals. If one has a pole figure for cladding, Equations (4-47) through (4-49) may be used to find the cladding thermal expansion, remembering that $\varepsilon_{22} = \varepsilon_{11}$.

4.5.3.2 Thermal Expansion in the Transition Region. To obtain single crystal thermal expansion, both the axial and circumferential cladding thermal expansions are necessary. While axial data in the transition region are available, circumferential data are not. Due to this lack of data and the insignificance of thermal strain at these temperatures, an approximation was made.

For zirconium in the alpha phase at 1,123 K, the Douglass[4.5-2] correlation gives the lattice constants as c = 5.193 x 10^{-10} m and a = 3.245 x 10^{-10} m, giving a volume of 47.356 x 10^{-30} m^3. Kittel[4.5-7] gives the lattice constant for beta zirconium at the same temperature as 3.61 x 10^{-10} m, implying a unit cell volume of 47.046 x 10^{-30} m^3. This decrease in volume as the material changes from the alpha close packed structure to the generally more open beta body centered cubic is surprising, although it has been reported by many[4.5-2,4.5-4,4.5-8] The volume strain is ~0.66%, in good agreement with Skinner and Johnston.[4.5-8] To model the transition region, it is assumed that each dimension contributes equally to this volume strain

$$\frac{\Delta l}{l_0} = \frac{1}{3}\frac{\Delta V}{V_0} = \frac{1}{3}\frac{3.1\times10^{-31}}{(3.61\times10^{10})^3} = 2.196\times10^{-3} \qquad (4\text{-}62)$$

where

Δl = change in length (m)

l_o = reference length (m)

ΔV = change in volume (m^3)

V_o = reference volume (m^3).

At the start of the transition (T = 1,083 K), from Equations (4-27) and (4-28), $\varepsilon_{11} = 3.88 \times 10^{-3}$ and $\varepsilon_{33} = 9.87 \times 10^{-3}$; and at the end of the transition, $\varepsilon_{11} = 1.68 \times 10^{-3}$ and $\varepsilon_{33} = 7.67 \times 10^{-3}$. A simple pair of correlations fit these numbers.

For $1{,}083 \leq T \leq 1{,}244$ K,

$$\varepsilon_{11} = \left[2.77763 + 1.09822\cos\left(\frac{T - 1083}{161}\pi\right)\right]\times 10^{-3} \quad (4\text{-}63)$$

$$\varepsilon_{33} = \left[8.76758 + 1.09822\cos\left(\frac{T - 1083}{161}\pi\right)\right]\times 10^{-3} \quad (4\text{-}64)$$

where the arguments for the cosines are in radians. There are more significant figures in Equations (4-63) and (4-64) than in other parts of the model to avoid discontinuities, not to reflect more accurate data.

4.5.3.3 Thermal Expansion in the Beta Region. For the transition region, there are insufficient data to construct a detailed model for the thermal expansion in the beta region. However, the strain due to thermal expansion is relatively unimportant to the total strain at these high temperatures. The model for T > 1,244 K, based on the expansivity for zirconium reported by Skinner and Johnston,[4.5-8] is

$$\varepsilon_{11} = 9.7 \times 10^{-6}\, T - 1.04 \times 10^{-2} \quad (4\text{-}65)$$

$$\varepsilon_{33} = 9.7 \times 10^{-6}\, T - 4.4 \times 10^{-3} \ . \quad (4\text{-}66)$$

4.5.4 Model Data Comparison and Uncertainty (CTHEXP)

The only data to which the model is compared are from Bunnell's correlations in the alpha phase. The predictions of the model using Equations (4-27) and (4-28) are compared with the data predictions in Table 4-11 and Table 4-12 using Bunnell's correlations and Equations (4-67) and (4-68). The first table is for circumferential strain, and the second is for axial strain; both tables are for a single crystal.

Table 4-11. Comparison of model predictions and Bunnell's alpha phase data in the diametral direction.

Temperature (K)	Model (unitless)	(Bunnell) (unitless)	(Bunnell-model/ model
300	0	0	--
400	0.0007	0.0009	0.28
500	0.0014	0.0016	0.14
600	0.0021	0.0022	0.05
700	0.0028	0.0028	0.00
800	0.0035	0.0035	0.00
900	0.0043	0.0043	0.00
1,000	0.0050	0.0050	0.00
1,100	0.0057	0.0055	-0.04

Table 4-12. Comparison of model predictions and Bunnell's alpha phase data in the axial direction.

Temperature (K)	(Model)	(Bunnell)	
300	0	0	--
400	0.0005	0.0006	0.20
500	0.0011	0.0011	0.00
600	0.0016	0.0016	0.00
700	0.0022	0.0021	-0.05
800	0.0027	0.0027	0.00
900	0.0032	0.0032	0.00
1,000	0.0038	0.0038	0.00
1,100	0.0042	0.0045	-0.07

From these tables, the standard error of estimate is $\pm$ 12% for the circumferential direction and $\pm$ 8% for the axial direction. These uncertainties are somewhat artificial, since the model is compared to its own data base.

In the transition region and the beta phase, the uncertainty is expected to be much larger. An uncertainty of $\pm$ 50% was arbitrarily assigned to these regions until appropriate data are available for a better model.

4.5.5 Density (CDEN)

The CDEN function determines zirconium density from room temperature data and the thermal expansion strains calculated with the CTHEXP subroutine. By definition

$$\rho = \frac{m}{V} \tag{4-67}$$

where

ρ = density (kg/m^3)

m = mass of a sample of material (kg)

V = volume of the given mass of material (m^3).

Thermal expansion changes only the volume. The volume is related to a reference volume by

$$V = V_0 \exp(\varepsilon_x) \exp(\varepsilon_y) \exp(\varepsilon_z) \tag{4-68}$$

where

V_o = volume of the mass m when strains are zero (m^3)

$\varepsilon_x, \varepsilon_y, \varepsilon_z$ = true strains for any orthogonal coordinate system (m/m).

Substitution of Equation (4-68) into Equation (4-67) shows

$$\rho = \rho_0 \exp(-\varepsilon_x) \exp(-\varepsilon_y) \exp(-\varepsilon_z) \tag{4-69}$$

where ρ_0 is the density at any reference temperature (kg/m^3).

Since thermal strains are always much less than one,

$$\rho \approx \rho_0 (1-\varepsilon_x-\varepsilon_y-\varepsilon_z) \ . \tag{4-70}$$

The three orthogonal strains are provided by CTHEXP, and the reference density used is the value of 6.5510^3 kg/m^3 at 300 K reported by Scott.[4.5-4] This value is consistent with the high temperature value of 6,490 kg/m^3 often used in material properties subcodes. The predicted zircaloy thermal strains are

estimated in material properties subroutines to have an expected standard error near 10% of their predicted valves for temperatures below 1,090 K and 50% for higher temperatures.

4.5.6 References

4.5-1 L. R. Bunnell et al., *High Temperature Properties of Zircaloy Oxygen Alloys*, EPRI NP-524, March 1977.

4.5-2 D. L. Douglass, "The Physical Metallurgy of Zirconium," *Atomic Energy Review, 1*, 4, December 1963, pp. 73-74.

4.5-3 R. L. Mehan and F. W. Wiesinger, *Mechanical Properties of Zircaloy-2*, KAPL-2110, February 1961.

4.5-4 P. B. Scott, *Physical and Mechanical Properties of Zircaloy-2 and -4*, WCAP-3269-41, May 1965.

4.5-5 J. J. Kearns, *Thermal Expansion and Preferred Orientation in Zircaloy*, WAPD-TM-472, November 1965, pp. 17-18.

4.5-6 C. R. Hann et al., *Transient Deformation Properties of Zircaloy for LOCA Simulation*, NP-526, Volume 3, March 1978.

4.5-7 C. Kittel, *Introduction to Solid State Physics*, 3rd Edition, NewYork: John Wiley and Sons, Inc., 1966, p. 29.

4.5-8 G. B. Skinner and H. L. Johnston, "Thermal Expansion of Zirconium Between 298 and 1,600 K," *Journal of Chemical Physics, 21*, August 1953, pp. 1,383-1,384.

4.6 Elastic Moduli (CELMOD, CSHEAR, AND CELAST)

Elastic moduli are required to relate stresses to strains. The elastic moduli are defined by the generalized form of Hooke's law as elements of the fourth rank tensor that relates the second rank stress and strain tensors below the yield point. In practice, cladding is frequently assumed to be an isotropic material. In such a case, only two independent elastic moduli are needed to describe the relation between elastic stress and strain. These two constants, the Young's modulus and the shear modulus, are calculated by the functions CELMOD and CSHEAR. Elements of the tensor necessary to describe anisotropic cladding are calculated by the subroutine CELAST.

4.6.1 Summary

Cladding elastic moduli are affected primarily by temperature and oxygen content. Fast neutron fluence, cold work, and texture effects are also included in the models described herein; but they are not as important as temperature and oxygen content for typical LWR fuel rod cladding. The models are based primarily on data published by Bunnell et al.,[4.6-1] Fisher and Renken,[4.6-2] Armstrong and Brown,[4.6-3] and

Padel and Groff,[4.6-4] since these data include the best description of texture for the temperature range in which they were used. Data from several other sources[4.6-5 to 4.6-11] are used to evaluate the expected standard error of the CELMOD and CSHEAR codes and to estimate the effect of fast neutron fluence.[4.6-12] To calculate zircaloy elastic moduli at temperatures greater than the melting temperature of zircaloy (2,098 K), the moduli are set to zero. (Actually, 1.0×10^{-10} is used to avoid dividing by zero.)

The expressions used in the CELMOD subcode to calculate the isotropic Young's modulus are:

a. In the alpha phase,

$$Y = (1.088 \times 10^{11} - 5.475 \times 10^{7}\, T + K_1 + K_2)/K_3 \ . \quad (4\text{-}71)$$

b. In the beta phase,

$$Y = 9.21 \times 10^{10} - 4.05 \times 10^{7}\, T \quad (4\text{-}72)$$

where

Y = Young's modulus for zircaloy-2 and -4 with random texture (Pa)

T = cladding temperature (K)

K_1 = modification to account for the effect of oxidation (Pa)

K_2 = modification to account for the effect of cold work (Pa)

K_3 = modification to account for the effect of fast neutron fluence (unitless).

In the alpha plus beta phase, Y is the value obtained by linear interpolation of values calculated at the alpha to alpha plus beta and the alpha plus beta to beta boundaries.

The expressions used to model the effects of oxidation, cold work, and fast neutron fluence are

$$K_1 = (6.61 \times 10^{11} + 5.912 \times 10^{8}\, T)\, \Delta \quad (4\text{-}73)$$

$$K_2 = -2.6 \times 10^{10}\, C \quad (4\text{-}74)$$

$$K_3 = 0.88 + 0.12 \exp\left(-\frac{\Phi}{10^{25}}\right) \quad (4\text{-}75)$$

where

Δ = average oxygen concentration minus oxygen concentration of as-received cladding (kg oxygen/kg zircaloy). As-received oxygen concentrations are so small (0.0012 kg oxygen/kg zircaloy) that the exact magnitude of the as-received concentration will not affect the correlation predictions.

C = cold work (unitless ratio of areas)

Φ = fast neutron fluence (n/m^2).

The standard error of the CELMOD code is 6.4×10^9 Pa.

The expressions used in the CSHEAR subcode to calculate the isotropic shear modulus are:

a. In the alpha phase,

$$G = \frac{(4.04\times10^{10} - 2.168\times10^{7}T + K_1 + K_2)}{K_3} \quad . \tag{4-76}$$

b. In the beta phase,

$$G = 3.49 \times 10^{10} - 1.66 \times 10^{7}\, T \quad . \tag{4-77}$$

In the alpha plus beta phase, G is the value obtained by linear interpolation of values calculated at the alpha to alpha plus beta and the alpha plus beta to beta boundaries, where the other terms have been defined in conjunction with Equations (4-71) and (4-72).

The expression used to model the effect of oxidation for shear modulus is

$$K_1 = (7.07 \times 10^{11} - 2.315 \times 10^{8}\, T)\, \Delta \tag{4-78}$$

where the terms have been previously defined. The standard error of the CSHEAR code is 9×10^9 Pa.

The subcode CELAST calculates elastic compliance constants for isotropic cladding. This subcode is discussed in the model development Section 4.6.3 because it is the basis for the much simpler CELMOD and CSHEAR codes. The elastic moduli predicted by CELAST for typical textures are reasonably close to the moduli for isotropic cladding. Figure 4-15 illustrates this. The solid lines represent the Young's and shear moduli for isotropic (random texture) material. The six broken lines represent reciprocal compliance constants corresponding to diagonal elements of the traditional S-matrix. Three of these quantities may be interpreted as the apparent Young's moduli for stresses in the direction indicated, and the other three may

be interpreted as the apparent shear moduli for shears acting normal to the direction indicated. The only modulus which departs significantly from the isotropic moduli is the Young's modulus in the radial direction. It should be noted that this modulus was based on zirconium single crystal data because appropriate zircaloy data are not available. The axial and circumferential Young's moduli are based on zircaloy-4 data, and they are very similar to the isotropic Young's modulus. The increased Young's modulus in the radial direction is not expected to affect code predictions, even if zircaloy data do confirm the difference shown by the zirconium data.

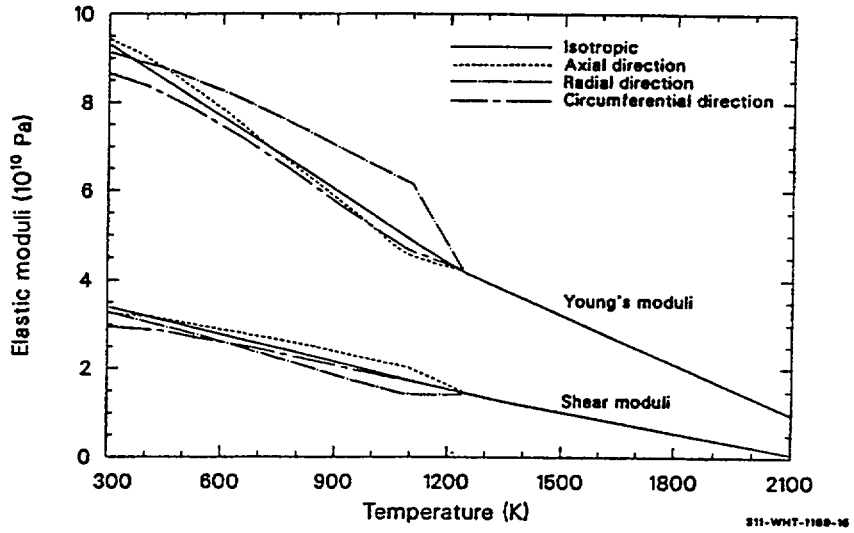

Figure 4-15. Elastic moduli for isotropic material compared to corresponding moduli for typical PWR cladding.

Details of the elastic modulus models are presented in the following sections. Section 4.6.2 is a review of available data, and Section 4.6.3 describes the model development. Section 4.6.4 is a comparison of the model and its data base. Uncertainties are discussed in Section 4.6.5.

4.6.2 Review of Available Data

Elastic moduli measurements may be classified as either static or dynamic. The static moduli are based on measurements of stress and strain under conditions which can, in principle, be representative of in-reactor cladding. However, the accuracy of the static moduli are typically limited by the accuracy of the measurement of the strain. Dynamic measurements avoid this difficulty by vibrating a sample of known dimensions in a resonant mode and inferring the moduli from accurate measurements of resonant frequency. The advantage in accuracy of the dynamic measurements is somewhat compromised by the fact that these measurements are made with the small cyclic strains associated with resonant modes. To date, static measurements have not achieved sufficient accuracy to show significant discrepancies with the dynamic measurements, so the dynamic measurements are used as a basis for the models discussed herein.

The most complete set of applicable elastic moduli measurements available are the dynamic measurements of zirconium single-crystal moduli by Fisher and Renken.[4.6-2] Measured values of the

stiffness moduli,[a] C_{11}, C_{33}, C_{44}, C_{13}, and C_{12}, are reported at 50 K intervals from 4 K to the alpha plus beta phase transition at 1,135 K. The C_{11}, C_{33}, C_{44}, and C_{13} moduli vary almost linearly with temperature between 300 and 1,135 K, while the C_{12} modulus is reported to increase in a nonlinear fashion with temperature. Least-squares polynomial fits to Fisher and Renken's data yield the following correlations when the data at 300 K or greater are used:

$$C_{11} = 1.562 \times 10^{11} - 4.484 \times 10^{7}\ T \tag{4-79}$$

$$C_{33} = 1.746 \times 10^{11} - 3.282 \times 10^{7}\ T\ . \tag{4-80}$$

$$C_{44} = 3.565 \times 10^{10} - 1.281 \times 10^{7}\ T \tag{4-81}$$

$$C_{12} = 6.448 \times 10^{10} + (3.1882 \times 10^{7} - 1.2318 \times 10^{4}\ T)\ T \tag{4-82}$$

$$C_{13} = 6.518 \times 10^{10} - 6.817 \times 10^{5}\ T \tag{4-83}$$

where C_{ij} are the five independent stiffness moduli for a hexagonal crystal (Pa). (The subscripts 1, 2, 3 refer to orthogonal coordinate axes arranged with the direction labeled 3 parallel to the c-axis. By basal plane symmetry, the 1 and 2 axes are any orthogonal axes in the basal plane.)

Single-crystal constants have not been determined for the high-temperature beta phase, so measurements on polycrystalline materials of unknown texture are used. The models are based on dynamic measurement of the Young's modulus[b] of zirconium by Armstrong and Brown[4.6-3] and by Padel and Groff.[4.6-4] The data from these two sources are reproduced in Table 4-13 and Table 4-14. The measurements differ by less than 5% at corresponding temperatures. As discussed in Section 4.6.3, compliance constants (elements of the inverse of the stiffness matrix) are obtained by assuming that the beta phase is isotropic.

Table 4-13. Beta-phase zirconium Young's Modulus measured by Armstrong and Brown.

Temperature (K)	Young's modulus (10^{10} Pa)
1,173	4.426
1,223	4.233

a. The definition of elastic stiffness moduli is reviewed in Section 4.6.3 in conjunction with the development of the model for the effect of texture variations.
b. Young's modulus is defined as stress in a given direction divided by strain in the same direction.

Table 4-13. Beta-phase zirconium Young's Modulus measured by Armstrong and Brown. (Continued)

Temperature (K)	Young's modulus (10^{10} Pa)
1,273	4.047
1,323	3.861
1,373	3.675
1,423	3.488
1,473	3.302

Table 4-14. Beta phase zirconium Young's Modulus measured by Padel and Groff.

Temperature (K)	Young's modulus (10^{10} Pa)
1,143	4.578
1,156	4.544
1,181	4.311
1,234	4.233
1,266	4.111
1,281	4.122
1,311	3.922
1,340	3.833
1,380	3.611
1,395	3.544
1,409	3.422
1,449	3.278
1,474	3.167

The alpha-phase data of Fisher and Renken do not help one to address three of the effects under consideration in this report-the effects of zircaloy-alloying elements, of oxidation, and of variations in texture. These considerations are addressed with the help of Young's moduli measurements in the axial and circumferential direction by Bunnell et al.[4.6-1] Bunnell's data provide important additional information because (a) they were taken with zircaloy cladding, (b) the samples contained various amounts of oxygen, and (c) an estimate of the initial texture of the material is available. Unfortunately, the texture information

is only available for the as-received samples and consists of a basal pole figure published by Chapman.[4.6-13]

Bunnell's data were analyzed using the model for the effect of texture developed in Section 4.6.3. The axial and circumferential Young's modulus data are used to establish correlations for the effect of temperature and oxygen on two of the five independent compliance constants. The correlations for as received and homogenized (annealed) cladding agree closely with the compliance constants obtained by inverting Equations (4-79) through (4-83) and lend confidence to the assumption that single crystal zirconium data are a good approximation to zircaloy data when oxygen concentrations are on the order of 0.001 weight fraction. The latter assumption is necessary because the data from zircaloy cladding are not sufficient to determine all five independent compliance constants.

Data relevant to modeling the effect of irradiation and cold work are limited both in quantity and in completeness. The Saxton CoreII Fuel Performance Evaluation[4.6-12] reports elastic moduli at 630 K for irradiated cladding. The moduli were measured with a static method in the axial direction, but no pole figure was provided so the effects of irradiation could not be separated from the effects of texture.

Data relevant to modeling the effect of cold work are contained (but not discussed as such) in the report by Bunnell et al.[4.6-1] The as-received material was cold-worked to about 0.75 and stress-relieved for 4 hours at 770 K.[4.6-13] The homogenized material was completely annealed. Unfortunately, the effect of cold work suggested by Bunnell's dynamic measurements of Young's modulus is opposite to the trend reported by Shober et al.[4.6-10] from static measurements. The dynamic measurements show a slight decrease in Young's modulus with cold work, and the static measurements show a slight increase in Young's modulus with cold work. Since neither source provides usable texture information, it is impossible to tell whether the change with cold work is due to associated changes in texture, to a separate effect associated with the cold work, or to a fundamental difference in the quantity that is being measured with the different techniques. The small decrease implied by Bunnell's data was tentatively included in the models for elastic moduli because of the greater precision of the dynamic data.

Several measurements of Young's and shear moduli were not used in constructing the models for elastic moduli because texture information was not available. The data are useful, however, as an independent test of the two approximate models for isotropic cladding. Busby[4.6-5] reported the axial Young's modulus for zircaloy-4 between 300 and 645 K for five combinations of cold work and heat treatment. Busby's data are reproduced in Table 4-15. Spasic et al.,[4.6-6] reported values of the static elastic modulus from room temperature to 675 K. Their data are reproduced in Table 4-16. The material used by Spasic et al., was not characterized as to cold work or texture. It is assumed that unirradiated material in the annealed condition was used in these tests. Mehan[4.6-7] and Mehan and Wiesinger[4.6-8] reported Young's modulus data from room temperature to 1,090 K. The data were taken with both static and dynamic techniques on unirradiated, vacuum annealed zircaloy-2 plates. Table 4-17 is a summary of Mehan's measurement. Northwood et al.[4.6-9] reported Young's modulus and shear modulus data from 293 to 773 K. The data were obtained with a resonance method and are accompanied by an excellent discussion of the effects of texture. The zircaloy-2 samples were machined from bar stock that had been annealed for 1 hour at 1,061 K. Table 4-18 is a summary of the zircaloy-2 data reported by Northwood et al.

Table 4-15. Young's modulus measurements by Busby.

Material	Temperature (K)	Young's modulus (10^{10} Pa)	Effective cold work predicted by the subcode CANEAL
78% cold work 922 K recrystallization for 5 hours	297	9.686	0%
78% cold work 922 K recrystallization for 5 hours	516	8.018	0%
78% cold work 922 K recrystallization for 5 hours	644	7.515	0%
15-20% cold work 783 K stress relief for 5 hours	297	10.031	5%
15-20% cold work 783 K stress relief for 5 hours	561	8.583	5%
15-20% cold work 783 K stress relief for 5 hours	559	8.349	5%
74% cold work 783 K stress relief for 5 hours	297	9.907	25%
73% cold work 783 K stress relief for 5 hours	644	7.708	25%

Table 4-16. Young's Modulus measurements by Spasic et al.

Temperature (K)	Young's modulus (10^{10} Pa)
300	10.10
373	9.25
423	8.78
473	8.52
673	7.70
673	7.40

Table 4-17. Young's Modulus measurement by Mehan.

Temperature (K)	Young's modulus (10^{10} Pa)	Method/direction
300	9.493	Static/not reported
300	9.473	Static/not reported
300	9.459	Static/not reported
300	9.500	Static/not reported
589	7.928	Static/not reported
589	7.790	Static/not reported
297	9.804	Dynamic/transverse
427	9.142	Dynamic/transverse
593	8.273	Dynamic/transverse
704	7.715	Dynamic/transverse
298	9.921	Dynamic/transverse
422	9.238	Dynamic/transverse
594	8.466	Dynamic/transverse
711	7.784	Dynamic/transverse
811	7.246	Dynamic/transverse
300	9.893	Dynamic/transverse
424	9.128	Dynamic/transverse
598	8.294	Dynamic/transverse
703	7.715	Dynamic/transverse
809	7.852	Dynamic/transverse
298	9.452	Dynamic/longitudinal
428	8.659	Dynamic/longitudinal
591	7.535	Dynamic/longitudinal
703	6.991	Dynamic/longitudinal
814	6.356	Dynamic/longitudinal
298	9.445	Dynamic/longitudinal

Table 4-17. Young's Modulus measurement by Mehan. (Continued)

Temperature (K)	Young's modulus (10^{10} Pa)	Method/direction
430	8.597	Dynamic/longitudinal
593	7.604	Dynamic/longitudinal
698	6.908	Dynamic/longitudinal
814	6.219	Dynamic/longitudinal
303	9.445	Dynamic/longitudinal
422	8.597	Dynamic/longitudinal
594	7.535	Dynamic/longitudinal
707	6.942	Dynamic/longitudinal
822	6.253	Dynamic/longitudinal

Table 4-18. Elastic moduli measurements by Northwood et al.[4.6-9]

Temperature (K)	Young's modulus longitudinal (10^{10} Pa)	Young's modulus transverse (10^{10} Pa)	Shear modulus torsional resonant mode (10^{10} Pa)
293	9.67	9.61	3.48
373	9.01	8.98	3.36
473	8.64	8.60	3.18
573	7.99	8.01	2.94
673	7.38	7.34	2.79
773	6.78	6.81	2.53

4.6.3 Model Development

The equations used in the CELMOD and CSHEAR subcodes are simplified forms of the more complex expressions used in the CELAST subcode. The quantities modeled by CELAST are elastic compliance coefficients. These coefficients, and the closely related elastic stiffness coefficients, are defined by the relations[4.6-14]

$$\varepsilon_i = S_{ij}\sigma_j \qquad (4\text{-}84)$$

$$\sigma_i = C_{ij}\varepsilon_j \tag{4-85}$$

where

ε_i = strain components

σ_i = stress components

S_{ij} = compliance matrix elements

C_{ij} = stiffness matrix elements.

Also, the usual tensor summation convention is assumed.

By inspection of Equations (4-84) and (4-85), it is clear that the compliance matrix is the reciprocal of the stiffness matrix. The author has elected to use compliance coefficients.

4.6.3.1 Effect of Texture Variations. Texture effects are modeled using techniques which have become fairly standard.[4.6-9,4.6-15,4.6-16] Macroscopic compliance matrix elements for polycrystalline materials are computed as the average of corresponding single-crystal values, weighted by the volume fraction of grains at each orientation.

$$\overline{S'_{ij}} = \iiint S'_{ij}(\theta, \phi)\rho(\theta, \phi)dv \tag{4-86}$$

where

S'_{ij} = macroscopic compliance constants (Pa^{-1})

$S'_{ij}(\theta, \phi)$ = single-crystal compliance constants defined relative to a fixed set of coordinates. Figure 4-16 defines the coordinates and the angles θ and ϕ.

$\rho(\theta,\phi)$ = volume fraction of grains with their c-axis orientated at angles θ and ϕ relative to the fixed set of coordinates.

The volume fraction of grains at angles θ and ϕ can be determined from c-axis pole figures.

$$\rho(\theta, \phi) = \frac{I(\theta, \phi)}{\int_0^{2\pi}\int_0^{\pi} I(\theta, \phi)\sin\theta d\theta d\phi} \tag{4-87}$$

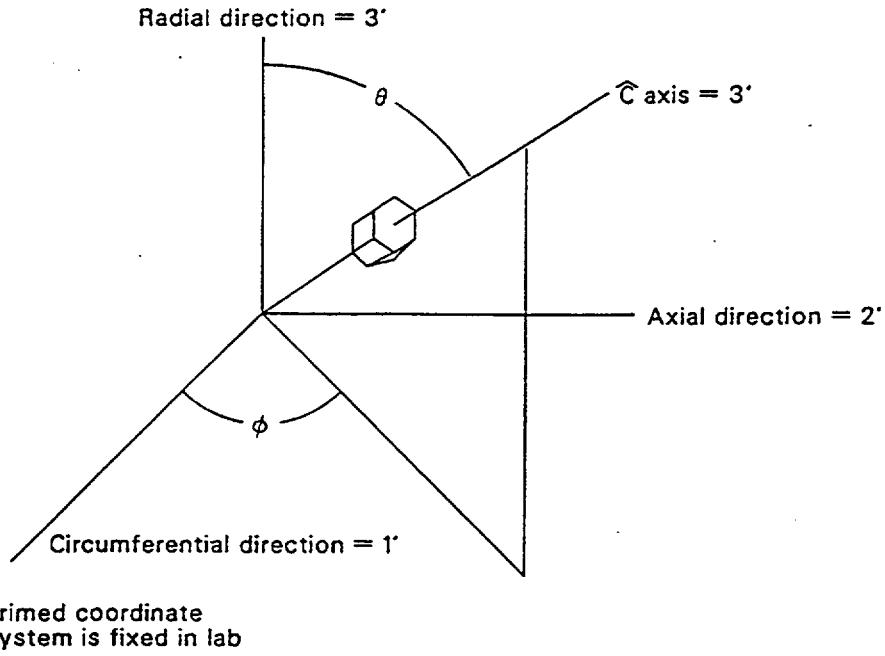

Figure 4-16. Reference directions selected for CELMOD/CSHEAR/CELAST analysis.

where $I(\theta,\phi)$ is the diffracted ray intensity of the basal planes as plotted in basal pole figures.

Expressions for the various single-crystal compliance constants, referred to a fixed coordinate system in $S'_{ij}(\theta, \phi)$ Equation (4-86), are obtained by applying standard tensor rotation techniques[4.6-17] to single crystal compliances defined relative to a set of coordinates attached to each grain, S_{ij}.[a] The traditional matrix notation is converted to a formal fourth-rank tensor using the relations listed in Table 4-19.[4.6-14] The coordinate system is rotated with the equation

$$S'_{ijke}(\theta, \phi) = C_{ir}C_{js}C_{kt}C_{eu}S_{rstu} \qquad (4\text{-}88)$$

where

$S'_{ijke}(\theta, \phi)$ = single-crystal compliance tensor elements measured with respect to the fixed (primed) coordinate system shown in Figure 4-16 (Pa^{-1})

a. In this section, primed compliance constants are referred to a system of coordinates that are fixed. Unprimed compliance constants are referred to a system of coordinates which are determined by the orientation of each grain, as shown in Figure 4-16.

S_{rstu} = single-crystal compliance tensor elements measured with respect to a coordinate system attached to each grain (Pa^{-1})

C_{ij} = elements of the rotation matrix

$$\begin{bmatrix} \cos\alpha & \sin\alpha\cos\theta & \sin\alpha\sin\theta \\ -\sin\alpha & \cos\alpha\cos\theta & \cos\alpha\sin\theta \\ 0 & -\sin\theta & \cos\theta \end{bmatrix}$$

α = complement of ϕ.

Table 4-19. Relations between fourth-rank tensor elements and traditional matrix elements.

Complete compliance tensor elements	Traditional matrix elements
$(S_{11ij}) =$	$\begin{bmatrix} S_{11} & (1/2)S_{16} & (1/2)S_{15} \\ (1/2)S_{16} & S_{12} & (1/2)S_{14} \\ (1/2)S_{15} & (1/2)S_{14} & S_{13} \end{bmatrix}$
$(S_{12ij}) =$	$\frac{1}{2}\begin{bmatrix} S_{61} & (1/2)S_{66} & (1/2)S_{65} \\ (1/2)S_{66} & S_{62} & (1/2)S_{64} \\ (1/2)S_{65} & (1/2)S_{64} & S_{63} \end{bmatrix}$
$(S_{13ij}) =$	$\frac{1}{2}\begin{bmatrix} S_{51} & (1/2)S_{56} & (1/2)S_{55} \\ (1/2)S_{56} & S_{52} & (1/2)S_{54} \\ (1/2)S_{55} & (1/2)S_{54} & S_{53} \end{bmatrix}$
$(S_{22ij}) =$	$\begin{bmatrix} S_{21} & (1/2)S_{26} & (1/2)S_{25} \\ (1/2)S_{26} & S_{22} & (1/2)S_{24} \\ (1/2)S_{25} & (1/2)S_{24} & S_{23} \end{bmatrix}$

Table 4-19. Relations between fourth-rank tensor elements and traditional matrix elements. (Continued)

Complete compliance tensor elements	Traditional matrix elements
$(S_{23ij}) =$	$\frac{1}{2}\begin{bmatrix} S_{41} & (1/2)S_{46} & (1/2)S_{45} \\ (1/2)S_{46} & S_{42} & (1/2)S_{44} \\ (1/2)S_{45} & (1/2)S_{44} & S_{43} \end{bmatrix}$
$(S_{33ij}) =$	$\begin{bmatrix} S_{31} & (1/2)S_{36} & (1/2)S_{35} \\ (1/2)S_{36} & S_{32} & (1/2)S_{34} \\ (1/2)S_{35} & (1/2)S_{34} & S_{33} \end{bmatrix}$
$(S_{rsij}) =$	S_{srij}

An equation relating the macroscopic elastic compliance constant S_{33} to the single-crystal compliance constants, resulting from combining the relations in Table 4-19 and Equations (4-87) and (4-88) follows:

$$\overline{S'_{33}} = (1 - 2\langle\cos^2\theta\rangle + \langle\cos^4\theta\rangle)S_{11} + (\langle\cos^2\theta\rangle - \langle\cos^4\theta\rangle)(2S_{13} + S_{44}) + \langle\cos^4\theta\rangle S_{33} \quad (4\text{-}89)$$

where

S'_{33} = macroscopic elastic compliance constant relating radial stress to radial strain (Figure 4-16) (Pa^{-1})

S_{11},S_{13}, = single-crystal compliance constants (Pa-1)

S_{33},S_{44} = elastic compliance constants for as-received zircaloy (Pa-1)

$\langle\cos^2\theta\rangle$ = volume fraction weighted average of the squared cosine of the angle θ (Figure 4-16)

$\langle\cos^4\theta\rangle$ = volume fraction weighted average of the fourth power of the angle θ.

4.6.3.2 Effect of Temperature. The effect of temperature on single-crystal elastic compliance constants is modeled separately for the alpha and beta phases of zircaloy.

Correlations for two of the five independent elastic constants, S_{11} and S_{44}, are developed from Bunnell's measurements of the axial and circumferential Young's modulus of unoxidized zircaloy-4.[4.6-14]

The other three single-crystal alpha phase constants, S_{33}, S_{12}, and S_{13}, are modeled by finding the matrix inverse of the stiffness moduli for zirconium [Equations (4-79) to (4-83)]. The expressions obtained from Bunnell's data are an improvement over the alternate expressions that could be obtained from the zirconium data because Bunnell's data were taken with zircaloy-4 cladding.

To use the zircaloy-4 data, the pole figure provided by Chapman is input to the MATPRO subcode CTXTUR to find the orientation angle averages relating single crystal elastic compliance constants to $\overline{S'_{11}}$ and $\overline{S'_{22}}$ for this cladding. The resultant expressions are:

$$\overline{S'_{11}} = 0.65106\, S_{11} + 0.09210\, S_{33} + (0.12842)(2\, S_{13} + S_{44}) \quad (4\text{-}90)$$

$$\overline{S'_{22}} = 0.88030\, S_{11} + 0.01900\, S_{33} + (0.05035)(2\, S_{13} + S_{44}) \quad (4\text{-}91)$$

where $\overline{S'_{11}}$, $\overline{S'_{22}}$ are the macroscopic elastic compliance constants (Pa^{-1}).

Inspection of the defining relation for the elastic compliance constant [Equation (4-75)] and the reference direction conventions used in the report (Figure 4-16) shows that $\overline{S'_{11}}$ is the reciprocal of Young's modulus measured in the circumferential direction of the cladding and $\overline{S'_{22}}$ is the reciprocal of Young's modulus measured in the axial direction of the cladding. Thus, Equations (4-86) and (4-87) can be used with Bunnell's measurements of the circumferential and axial Young's modulus of this cladding and the inverse matrix values of S_{33} and S_{13} to find least squares correlations for S_{11} and S_{44} as a function of temperature.

The correlations found from a least squares fit to Bunnells's data are:

$$S_{11} = 0.1028 \times 10^{-10} + T\,(-0.5417 \times 10^{-14} + T\, 0.1476 \times 10^{-16}) \quad (4\text{-}92)$$

$$S_{44} = 0.3904 \times 10^{-10} + T\,(-0.8118 \times 10^{-14} + T\, 0.2115 \times 10^{-16}) \quad (4\text{-}93)$$

where the terms of the equations have been previously defined.

Equation (4-92) predicts values of S_{11} which vary from zero to 10% below the value of S_{11} predicted by the zirconium data of Fisher and Renken.[4.6-2] Equation (4-93) predicts values of S_{44} which are about 20% above the value of S_{44} predicted by the zirconium data of Fisher and Renken.[4.6-2]

In the beta phase,[a] only two independent single crystal compliance constants are employed. The independent constants are S_{11} and S_{44}. By classical symmetry arguments, $S_{33} = S_{11}$ and $S_{23} = S_{13} = S_{12}$. A

correlation for one of the constants is obtained from a least squares fit to the beta phase zirconium Young's modulus data of Armstrong and Brown[4.6-3] and Padel and Groff.[4.6-4] The expression is

$$S_{11}^{-1} = Y = 9.21 \times 10^{10} - 4.05 \times 10^{7}\, T \qquad (4\text{-}94)$$

where

S_{11} = elastic compliance constant for beta phase zircaloy (Pa^{-1})

Y = Young's modulus for beta phase zircaloy (Pa).

Since no measurements of the shear modulus in beta phase zirconium are available, the second constant, S_{44}, is estimated by extrapolation of an approximate expression for the shear modulus of isotropic alpha phase zirconium to the higher temperatures of the beta phase.

The phase boundaries of the alpha, alpha plus beta, and beta phases are determined with correlations based on data from Figure III.33 of Reference 4.6-18. Compliance constants in the alpha plus beta phase region are obtained by interpolating between these constants at the boundaries of this region.

4.6.3.3 Effect of Oxygen. The only data available to model the effect of oxygen on the single-crystal compliance constants are Bunnell's measurements of axial and circumferential Young's moduli as a function of oxygen concentration.[4.6-1] The effect of oxygen on the alpha phase compliance constants is modeled in much the same way that Bunnell's data were used to correlate changes in the single crystal compliance constants S_{11} and S_{44} with temperature. The three-step procedure is outlined as follows:

1. Equation (4-91) is used with measured values of the axial Young's modulus ($1/S'_{22}$), approximate (zirconium) values of S_{33}, S_{13}, and S_{44} in the small terms containing these factors and the measured values of oxygen concentration to find a leas-squares fit correlation between S_{11} and the oxygen concentration.

2. Equation (4-90) is used with measured values of the circumferential Young's modulus ($1/S'_{11}$), the expression for S_{11} obtained in step (1), approximate (zirconium) values of S_{33} and S_{13}, and the measured values of oxygen concentration to find a least-squares fit correlation for S_{44} as a function of oxygen concentration. The correlations obtained are

$$1/S_{11} = 1/(S_{11})_o + (6.61 \times 10^{11} + 5.912 \times 10^{8}\, T)\Delta \qquad (4\text{-}95)$$

$$1/S_{44} = 1/(S_{44})_o + (7.07 \times 10^{11} + 2.315 \times 10^{8}\, T)\Delta \qquad (4\text{-}96)$$

a. The beta phase is body-centered cubic and has therefore been assumed isotropic.

where

S_{11}, S_{44} = elastic compliance constants for oxidized zircaloy (Pa^{-1})

$(S_{11})o$, $(S_{44})o$ = elastic compliance constants for as-received zircaloy (Pa^{-1})

Δ = average oxygen concentration minus oxygen concentration of as-received cladding (kg oxygen/kg zircaloy).

3. Equation (4-96) is assumed to apply to S_{13}, S_{33}, and S_{12}.

The effect of oxygen in the beta phase has been neglected because no relevant data are available and because an exact knowledge of elastic moduli at the high temperatures of the beta phase is not likely to be important to code applications.

4.6.3.4 Effect of Cold Work. Bunnell's measurements of the Young's modulus of cold worked, stress-relieved cladding were compared to his Young's modulus measurements of homogenized (annealed) cladding to estimate cold work effects. Measured values of the axial Young's modulus for the stress relieved material are related to S_{11} with Equation (4-91). The differences between $(S_{11})^{-1}$ in the cold worked material and (S_{11}) computed for annealed material [Equation (4-92)] are assumed to be proportional to the cold work (assumed = 0.5). The correlation resulting from an average of the six low temperature data on as-received cladding is

$$1/S_{11} = 1/(S_{11})_o - 2.6 \times 10^{10}\, C \qquad (4\text{-}97)$$

where

S_{11} = elastic compliance constant for cold worked zircaloy (Pa^{-1})

$(S_{11})_o$ = elastic compliance constant for annealed zircaloy (Pa^{-1})

C = cold work (unitless ratio of areas).

No modification of S_{44} was implied by Bunnell's measurements of the Young's modulus in the circumferential direction.

4.6.3.5 Effect of Irradiation. Data from the Saxton Core II Fuel Performance Evaluation[4.6-12] are used to estimate fast neutron fluence effects on elastic compliance constants. Since no pole figures for this material were found, measured values of the axial Young's modulus for the irradiated material are related to S_{11}, S_{33}, S_{13}, and S_{44} with Equation (4-95). The four compliance constants are assumed to decrease by a single factor due to the fluence, and the factor is determined by comparing the measured values of Young's modulus to the values predicted for unirradiated material. The factor which results from the

comparison is:

$$S_{ij}/(S_{ij})_o = 0.88 \quad (4\text{-}98)$$

where

S_{ij} = each of the compliance constants for the irradiated cladding (Pa^{-1})

$(S_{ij})o$ = each of the compliance constants predicted for unirradiated cladding (Pa^{-1}).

Measured values of fast neutron fluences received by the Saxton rods varied from 2.2 to 3.4 10^{25}n/m^2. No correlation using the fluence were found. The fluence dependence is therefore modeled by replacing Equation ((4-100)) with an assumed fluence dependent expression

$$H = 0.88 + 0.12 \exp(-\Phi/10^{25}) \quad (4\text{-}99)$$

where

H = ratio of compliance constants for irradiated material to compliance constants for unirradiated material

Φ = fast neutron fluence (n/m^2).

4.6.3.6 Derivation of the CELMOD and CSHEAR Codes from the CELAST Code. It has been mentioned in Section 4.6.3.2 that the compliance tensor contains only two independent constants for isotropic (random distribution of c-axes) cladding. Moreover, the definition of the compliance tensor implies that the constants may be interpreted as reciprocals of Young's modulus and the shear modulus

$$(\overline{S'_{ij}})_{isotropic} = \begin{bmatrix} Y^{-1} & a & a & 0 & 0 & 0 \\ a & Y^{-1} & a & 0 & 0 & 0 \\ 0 & 0 & Y^{-1} & 0 & 0 & 0 \\ 0 & 0 & 0 & G^{-1} & 0 & 0 \\ 0 & 0 & 0 & 0 & G^{-1} & 0 \\ 0 & 0 & 0 & 0 & 0 & G^{-1} \end{bmatrix} \quad (4\text{-}100)$$

where

$(S'_{ij})_{isotropic}$= compliance matrix for isotropic cladding (Pa^{-1})

Y = Young's modulus for isotropic cladding (Pa)

G = shear modulus for isotropic cladding (Pa)

a = $1/Y - 1/2G$ (Pa^{-1}).

Expressions for the isotropic Young's modulus and shear modulus in the alpha phase are obtained by computing S_{11} and S_{44} for the isotropic case with the CELAST code. Isotropic values of the several averages required by the code are computed by taking $I(\theta,\phi) = 1$ in Equation (4-87). The resultant values of the isotropic Young's and shear moduli decreased nearly linearly with temperature for temperatures above 450 K. The isotropic alpha phase Young's and shear moduli are therefore modeled with simple linear correlations obtained by fitting straight lines to their values at 623 and 1023 K. The resultant correlations are:

$$Y = 1.088 \times 10^{10} - 5.475 \times 10^{7}\ T \quad (4\text{-}101)$$

$$G = 4.040 \times 10^{10} - 2.168 \times 10^{7}\ T \quad (4\text{-}102)$$

where the terms have been defined in Equation (4-100).

Equation (4-102) is extrapolated to the high temperatures of beta phase zircaloy because no high temperature shear modulus data are available. The expression used in CELMOD for the Young's modulus of isotropic cladding is identical to the expression used in the CELAST code [Equation (4-72)].

Expressions for the change in Young's and shear moduli with increased oxygen, cold work, and fast neutron fluence are taken directly from the CELAST code. Expressions for the changes in the reciprocal of S_{11} are applied to Young's modulus, and changes in the reciprocal of S_{44} are applied to the shear modulus.

4.6.4 Comparison of Models and Data Base

Figure 4-17 and Figure 4-18 compare predictions obtained with the CELAST code to the axial and circumferential Young's moduli measured by Bunnell. Predicted moduli increase with increasing oxygen and decrease with increasing temperature. Both predicted and measured axial Young's moduli for homogenized (annealed) cladding at room temperature are larger than the corresponding circumferential Young's moduli, but the difference disappears at temperatures above 800 K. Even at room temperature, the difference is only slightly larger than the standard error of the model predictions. However, the low value of the circumferential Young's modulus is consistent with a minimum in predicted Young's modulus versus c-axis direction reported by Northwood.[4.6-9]

Figure 4-19 is a comparison of the Young's modulus predicted using the CELAST code with the beta phase zirconium data of Armstrong and Brown[4.6-3] and Padel and Groff.[4.6-4] The data show very little scatter, but are based on measurements of the Young's modulus of zirconium. The CELAST code has introduced a slight discontinuity in slope at 1,240 K, the alpha plus beta to beta phase boundary. For higher

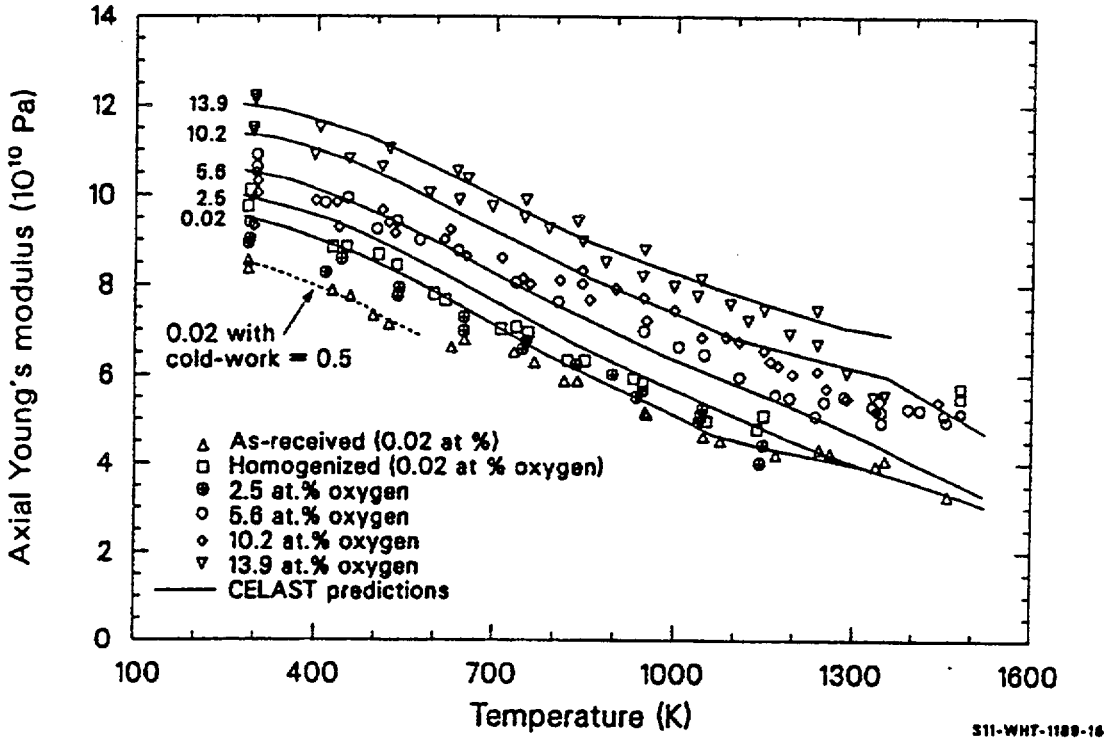

Figure 4-17. Measured values of axial Young's modulus compared to values predicted by the CELAST subcode for several oxygen concentrations and temperatures in the range of 300 to 1,500 K.

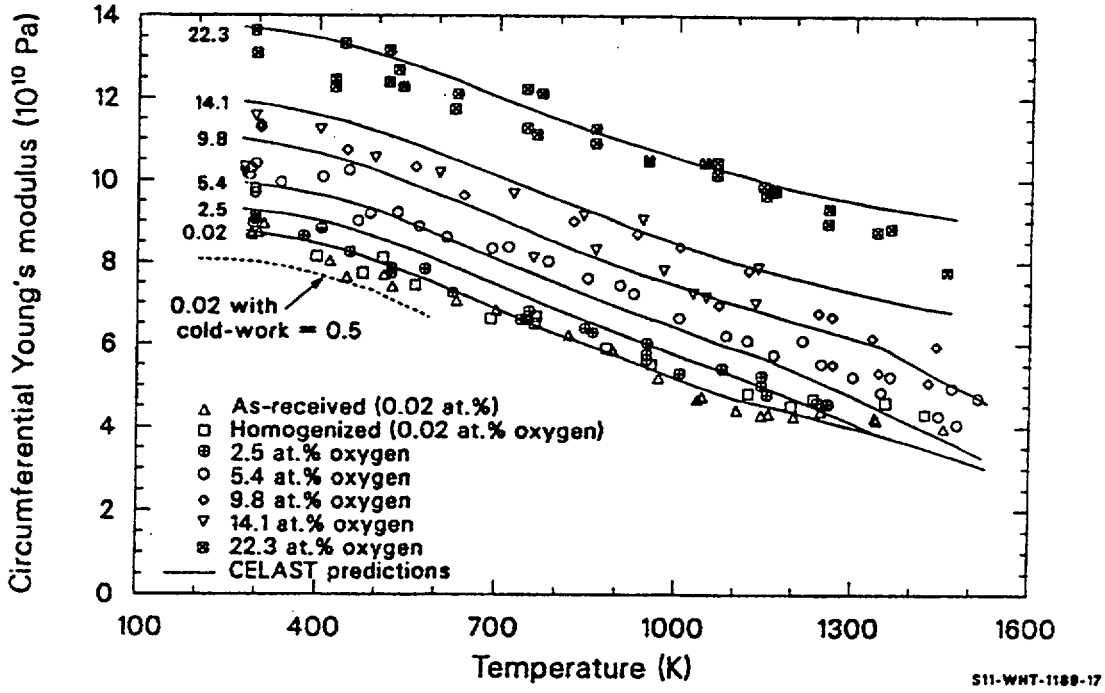

Figure 4-18. Measured values of circumferential Young's modulus compared to values predicted by the CELAST subcode for several oxygen concentrations and temperatures in the range of 300 to 1,500 K.

concentrations of oxygen, this discontinuity would appear at higher temperatures. The discontinuity is significant only in interpreting the physical meaning of the code predictions.

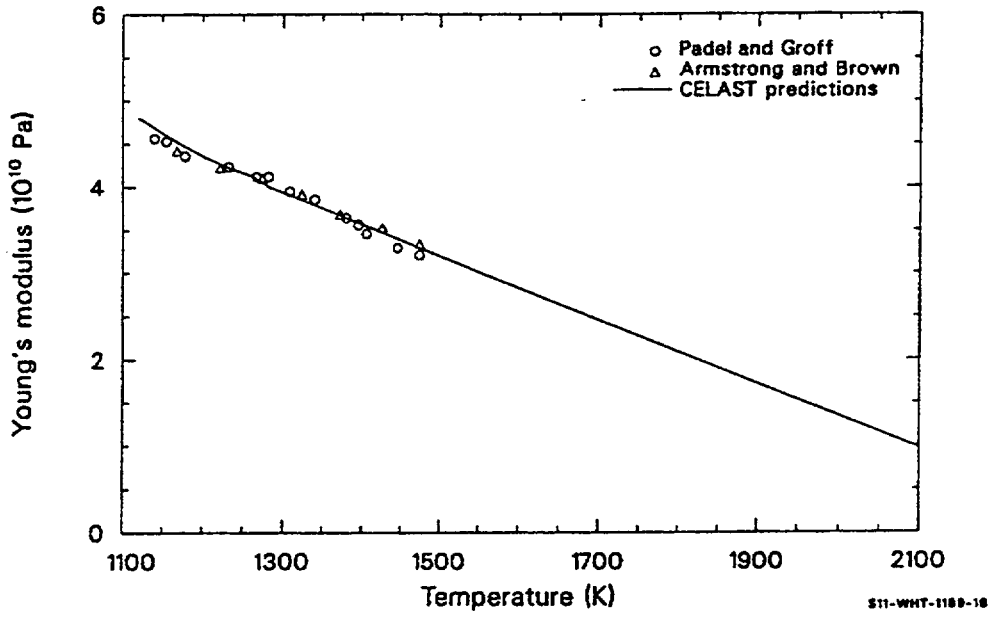

Figure 4-19. Comparison of the Young's modulus predicted with the CELAST code to the beta phase zirconium data of Padel and Groff, and Armstrong and Brown.

4.6.5 Expected Standard Error of the CELMOD and CSHEAR Codes

An estimate of the uncertainty of the CELMOD code is obtained by computing the standard error[a] of the code with the data of Table 4-15 through Table 4-18. For this calculation, the small effects of cold work are ignored. The standard error is 6.4 x 10^9 Pa. Since (a) the data used to estimate standard error are not used in the data base of the model; (b) the effects of texture, cold work, oxygen, and irradiation are not large compared to temperature effects; and (c) the residuals do not vary in any irregular fashion with temperature, this number is assumed to be a reasonable estimate of the expected standard error of the CELMOD code for in-reactor problems. At normal LWR temperatures, this standard error is 10% of the predicted value.

The uncertainty of the CSHEAR code is estimated by computing the standard error of the code with a large block of data (214 measurements) reported by Bunnell.[4.6-1] The data were not used in the development of the codes described here because the author was not able to interpret the effect of texture on the torsional wave used by Bunnell to measure shear modulus. The standard error, assuming the cladding was isotropic, is 9 x 10^9 Pa. At normal LWR temperatures, the standard error of the isotropic shear is 30% of the predicted value.

a. The standard error is estimated with a data set by the expression: [sum of squared residuals/(number of residuals - number of constants used to fit the data)]$^{1/2}$.

4.6.6 References

4.6-1 L. R. Bunnell et al., *High Temperature Properties of Zircaloy Oxygen Alloys*, EPRI NP-524, March 1977.

4.6-2 E. S. Fisher and C. J. Renken, "Single-Crystal Elastic Moduli and the HCP-BCC Transformation in Ti, Zr, and Hf," *Physical Review, 135 2A*, July 20, 1964, pp. A482-494.

4.6-3 P. E. Armstrong and H. L. Brown, "Dynamic Young's Modulus Measurements above 1000 °C on Some Pure Polycrystalline Metals and Commercial Graphites," *Transactions of the Metallurgical Society of AIME 230*, August 1964, pp. 962-966.

4.6-4 A. Padel and A. Groff, "Variation du Module de Young du Zirconium b en Function de la Temperature," *Journal of Nuclear Materials 59*, 1976, pp. 325-326.

4.6-5 C. C. Busby, *Properties of Zircaloy-4 Tubing*, WAPD-TM-585, December 1966, p. 65.

4.6-6 Z. Spasic et al., *Conference on the Use of Zirconium Alloys in Nuclear Reactors*, Marlanske Lanze, Czechoslovakia, USAEC CONF-681086, 1968, pp. 277-284.

4.6-7 R. L. Mehan, *Modulus of Elasticity of Zircaloy-2 Between Room Temperature and 1,000°F*, KAPL-M-RLM-16, July 1958.

4.6-8 R. L. Mehan and F. W. Wiesinger, *Mechanical Properties of Zircaloy-2*, KAPL-2110, February 1961, pp. 11-12.

4.6-9 D. O. Northwood et al., "Elastic Constants of Zirconium Alloys," *Journal of Nuclear Materials, 55*, 1975, pp. 299-310.

4.6-10 F. B. Shober et al., *The Mechanical Properties of Zirconium and Zircaloy-2*, BMI-1168, 1957.

4.6-11 C. L. Whitmarsh, *Review of Zircaloy-2 and Zircaloy-4 Properties Relevant to N. S. Savannah Reactor Design*, ORNL-3281, 1962.

4.6-12 W. R. Smalley, *Saxton Core II Fuel Performance Evaluation Part I: Materials*, WCAP-3385-56, September 1971.

4.6-13 R. H. Capman, *Characterization of Zircaloy-4 Tubing Procured for Fuel Cladding Research Programs*, ORNL/NUREG/TM-29, July 1976.

4.6-14 G. E. Dieter, *Mechanical Metallurgy*, New York: McGraw-Hill Book Company, Inc., 1976.

4.6-15 J. J. Kearns, *Thermal Expansion and Preferred Orientation in Zircaloy*, WAPD-TM-472, November 1965.

4.6-16 H. S. Rosenbaum and J. E. Lewis, "Use of Pole Figure Data to Compute Elasticity Coefficient of Zirconium Sheet," *Journal of Nuclear Materials, 67*, 1977, pp. 273-282.

4.6-17 R. B. Leighton, *Principles of Modern Physics*, New York: McGraw-Hill Book Company, Inc., New York, 1959.

4.6-18 H. M. Chung et al., "Mechanical Properties of Zircaloy Containing Oxygen," *Light-Water-Reactor Safety Research Program: Quarterly Progress Report for January-March 1976*, ANL-76-49.

4.7 Axial Growth (CAGROW)

A model for calculating the fractional change in length of zircaloy tubes due to irradiation induced growth is presented in this section. Effects of fast neutron fluence, tubing texture, cladding temperature, and cold work are included and apply equally well to zircaloy-2 and zircaloy-4. The change in length of commercial fuel rods due to irradiation growth is small; however, it can be a significant fraction of the clearance between the rod and the top and bottom assembly nozzles. Contact with the nozzles can cause rods to bow and possibly fail at points where rods contact each other.

4.7.1 Summary

The following equation has been developed to model the irradiation growth of zircaloy tubes at temperatures between 40 and 360 °C (the normal range of cladding temperatures in LWRs).

$$\Delta L/L = A\,[\exp(240.8/T)]\,(\Phi t)^{1/2}\,(1 - 3f_z)\,(1 + 0.02\,CW) \qquad (4\text{-}103)$$

where

$\Delta L/L$	=	fractional change in length due to growth
A	=	$1.407 \times 10^{-16}\ (n/m^2)^{1/2}$
T	=	cladding temperature (K)
Φ	=	fast neutron flux ($n/m^2 s$) ($E > 1.0$ MeV)
t	=	time (s)
f_z	=	texture factor[a] for the tubing axis

a. f_z is the effective fraction of cells aligned with their <0001> axis parallel to the tubing axis, as determined by ray diffraction analysis. A value of $f_z = 0.05$ is typical.[4.7-1]

CW = cold work (fraction of cross-sectional area reduction).

Axial growth for temperatures below 40 °C is approximated by using T = 40 °C in Equation (4-103), and growth above 360 °C is approximated by using T = 360 °C.

A comparison of values calculated by the CAGROW subroutine for fully annealed material with experimental results is presented in Figure 4-20. Comparison with the data shown from cold worked tubes was not possible because the exact amount of cold work was not reported.

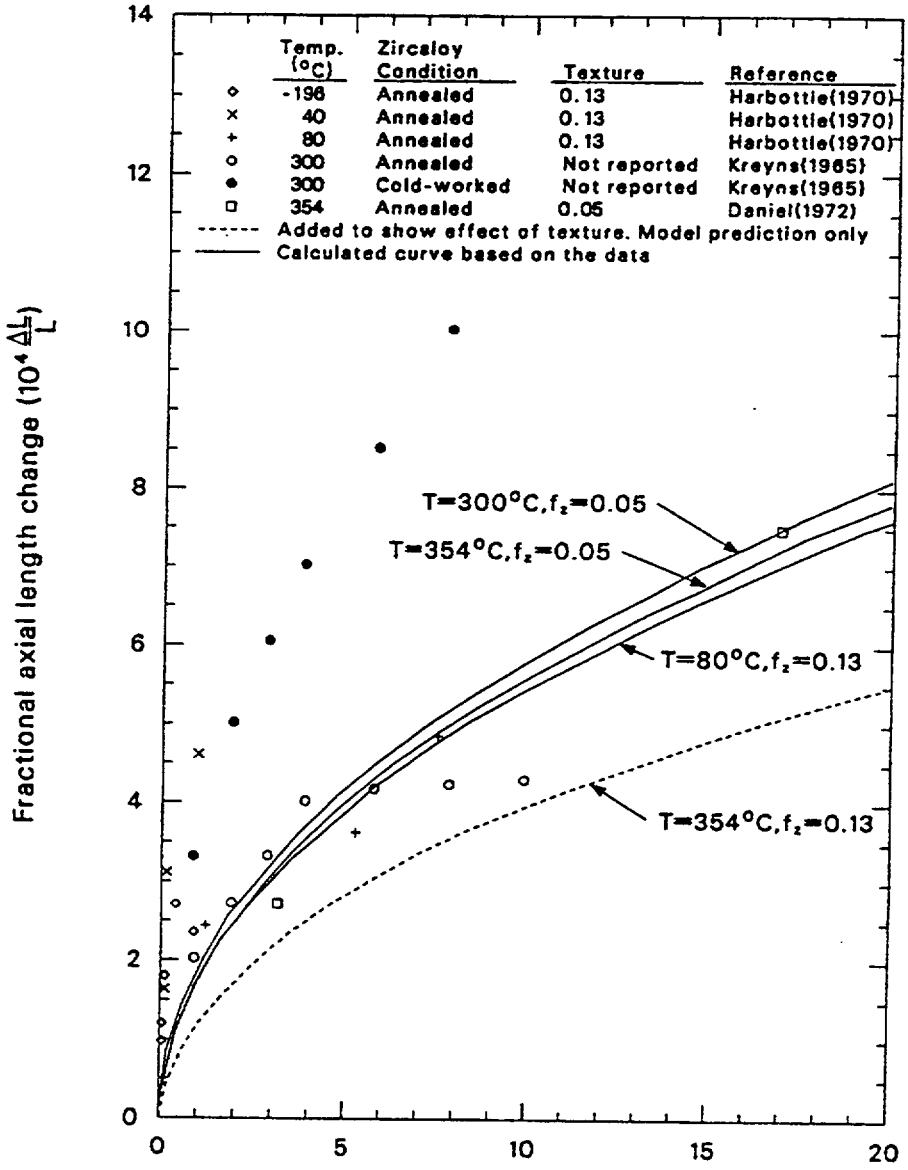

Figure 4-20. Model predictions and measured values of zircaloy tube axial growth as a function of fast neutron fluence, irradiation temperature, cold work, and texture coefficient, f_z.

4.7.2 Background and Approach

The irradiation growth of zircaloy cladding appears to be quite sensitive to texture; therefore, the effects of texture were considered first. The data were normalized to a standard texture ($f_z = 0.05$) before considering other effects on axial growth. The model was developed further by modeling the effects of fluence and irradiation temperature on the growth of annealed specimens. Finally, the effect of cold work was modeled after removing the effects of texture, fluence, and temperature from the cold worked specimen data, using the model based on annealed specimens. (The data were normalized to a texture of 0.05, a fluence of 2 x 10^{25} n/m2, and a temperature of 300 °C.) It should be noted, however, that the effect of cold work may not be treated completely, since the limited data base did not allow treatment of interactions between cold work and fluence, temperature, and texture.

In CAGROW, it is assumed that fast neutron flux and temperature both affect the growth rate by varying the concentration of interstitials which are free to migrate and cause growth. Since theoretical considerations imply a complex relation between temperature, fast neutron flux, time, and rate of growth, an empirical approach was used to approximate these effects. An empirical approach was also used to model the effect of cold work on zircaloy tube growth. The limited data were fit using an independent factor of the form (1 + constant x cold work), the least complex form consistent with the data available. The main conclusion is that cold work increases the rate of growth at low fluence. At higher fluences, the growth rate of annealed tubing may decrease rapidly. Cold-worked tubing continues to grow at higher fluences at nearly the rate established during early radiation.

4.7.3 Review of Experimental Data

Samples of zirconium, zircaloy-2, and zircaloy-4 irradiated in a fast neutron flux (E > 1 MeV) to fluences of 10^{25} n/m^2 show typical axial growth on the order of 0.1% of length or less. Since the effects of fuel-cladding mechanical interactions and pressure differentials across the cladding compete with the smaller effects of irradiation growth, the relatively plentiful data[4.7-2 to 4.7-4] are not directly useful in determining the change in cladding length due to irradiation growth. Data on thimble tubes or other structural elements relatively free of confounding effects would be useful. Table 4-20 summarizes the data used for development of the model.

Table 4-20. Measurements of growth in zircaloy tubing.

Source	ΔL/L (10^{-4})	Differential[a] ΔL/L (10^{-4})	Fast fluence (10^{22}n/m^{2}s)	Material	Fast Flux (10^{17}n/m^2·s)	Irradiation temperature (°C)
Kreyns[4.7-5]	2		100	Annealed zircaloy-4	(?)	300
	2.7		200			
	3.3		300			
	4.0		400			
	4.15		600			

Table 4-20. Measurements of growth in zircaloy tubing. (Continued)

Source	ΔL/L (10^{-4})	Differential[a] ΔL/L (10^{-4})	Fast fluence (10^{22}n/m^{2}s)	Material	Fast Flux (10^{17}n/m^2·s)	Irradiation temperature (°C)
	4.2		800			
	4.3		1,000			
	3.3		100	Cold worked zircaloy-4	(?)	300
	5		200			
	6		300			
	7		400			
	8.5		600			
	10		800			
Daniel [4.7-1] and [4.7-7]	2.7		310	Annealed zircaloy-4	12.5	354
	7.5		1700			
Harbottle[4.7-6]		1.2 ± 0.2	4.9	Annealed zircaloy-2	3	-196
		1.5 ± 0.3	9.7			
		2.3 ± 0.3	19			
		3.5 ± 0.5	50			
		3.0 ± 0.1	98			
		2.1 ± 0.2	8.2	Annealed	3	40
		4.0 ± 0.2	29	zircaloy-2		
		5.6 ± 0.4	100			
		3.1 ± 0.4	130	Annealed	12	80
		4.7 ± 0.4	54	zircaloy-2		
		6.3 ± 1.0	770			

a. Only the difference between longitudinal and transverse changes in length was reported.

Early data on irradiation-induced axial growth of zircaloy-4 tubing at 300 °C were obtained by Kreyns.[4.7-5] His experiments indicated that growth of cold-worked tubing is proportional to the square root of the fast neutron fluence up to its maximum fluence (10^{25} n/m^2). Growth of annealed tubing appeared to

saturate at a fluence of 4×10^{24} n/m^2 and a fractional length change of 4×10^{-4}. However, subsequent data taken by other investigators have indicated that saturation is not determined by fluence or net growth.

Harbottle[4.7-6] reported the difference in growth strains of transverse and longitudinal strips cut from zircaloy-2 pressure tubes. The strips were annealed and then irradiated at 196, 40, and 80 °C. The basal pole texture was found to be 13% in the direction of the tube axis and 36% in the circumferential direction, both before and after the cutting and annealing process. Harbottle's differential growth strains were converted to absolute values of axial growth strains by using the equation

$$\frac{1-3f_z}{1-3f_\theta} = \frac{\text{growth strain in axial direction}}{\text{growth strain in circumferential direction}} \quad (4\text{-}104)$$

where f_z and f_θ are the texture factors in the axial and circumferential directions, respectively.

A somewhat different approach was taken by Daniel[4.7-1,4.7-7] in a series of experiments that measured both diameter and length changes of fuel rods. The effects of fuel cladding interactions and pressure differentials across the cladding on measured changes in rod length could be separated from the effect of cladding growth, since no fuel cladding mechanical interaction was present in one experiment series. The separation was achieved by noting that the expected ratio of length-to-diameter changes is very different for fuel cladding interactions, creep due to pressure differentials across the rod, and irradiation-induced growth. In particular, the fractional change in diameter due to growth was predicted to be very small for typical cladding diameters and textures. Therefore, a plot of the measured change in length as a function of the measured change in diameter at a single fluence could be used to determine the change in length due to growth by simply extrapolating to zero changes in diameter with data that did not contain fuel cladding mechanical interactions. Daniel determined the fractional change in length at two values of fluence. His results[a] are particularly significant because they provide a measure of growth of annealed cladding at high fluence and do not show the saturation which Kreyns[4.7-5] observed.

4.7.4 The Effect of Texture on Axial and Circumferential Growth

Single-crystal texture effects are related to polycrystalline growth. Growth is pictured simply as a reduction of the c axis dimension of individual grains and an increase of the basal plane dimensions of the grains. The analysis is carried out with the help of an abstract picture of grains made up of schematic immobile unit cells, which decrease their c-axis length by a fraction and increase their a_1, a_2, and a_3 axis length by a fraction m. Although the picture of changing unit cell size does not represent atomic behavior within the grain, the growth of the grain is reproduced by the abstract picture.

Figure 4-21 illustrates the change in the axis lengths of the schematic unit cells. Growth of the three axes in the basal plane is assumed to be equal because of the symmetry of the lattice. The relation between the decrease of the c-axis dimension and the increase of the a axes is dependent on the details of the atomic

a. A growth component of strain equal to 7.5×10^{-4} at a fluence of 17×10^{24} n/m^2 and a growth strain of 2.7×10^{-4} at a fluence of 3.1×10^{24} n/m^2 were indicated by Daniel.[4.7-1,4.7-7]

model used to describe growth. For models that imply that the volume of the grain (and schematic unit cell) remains constant, $(1 + m) = (1 - n)^{-1/2}$. This value for 1 + m will be assumed at the last stage of the derivation of the effect of texture. It should be noted that the assumption is not made on the basis of a detailed atomic model. The constant volume assumption is made on the basis of experimental evidence,[4.7-8,4.7-9] and this evidence has been somewhat contradictory.

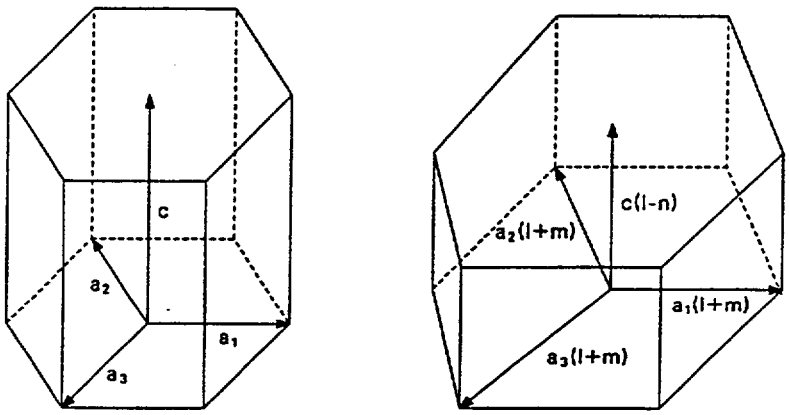

Figure 4-21. The growth of schematic unit cells in a grain.

4.7.4.1 Use of the X-ray Diffraction Orientations Parameter to Relate Single Crystal Models to Polycrystalline Results. The effective fraction of grains aligned with their c-axis parallel to a reference direction (axial, circumferential, or radial direction of the tube) is usually taken to be an orientation parameter[4.7-10] determined from ray diffraction studies. This parameter is formally defined as the average of the squared cosine of the azimuthal angle between the c-axis of individual grains and the reference direction, weighted by the volume fraction, V_i, occupied by cells at a given azimuthal angle, θ_i. That is,

$$F = \frac{\sum_i V_i \cos^2\theta_i}{\sum_i V_j} \quad . \tag{4-105}$$

It is shown in Reference 4.7-10 that polycrystalline bulk properties in a reference direction can be expressed as

$$P_{ref} = fP|| + (1-f)P_{\perp} \quad (4\text{-}106)$$

if the property has the following characteristics:

$$P_{\eta} = P||\cos^2\eta + P_{\perp}\sin^2\eta \quad (4\text{-}107)$$

where

P_{η} = the single-crystal property in a direction at an angle η to the axis

$P||$ = the single-crystal property along the c-axis

$P_{\perp}$ = the single-crystal property perpendicular to the c-axis.

The property in a reference direction of the polycrystalline sample is the volume weighted summation of this property in its individual crystals.

A property of the schematic unit cells that satisfies condition (a) is the square of the distance between two points imbedded in the schematic unit cell. That is, if (-x/2,-y/2,-z/2) and (x/2,y/2,z/2) are coordinates of two points in the cell relative to an origin at the middle of the cell, the squared distance between the points is

$$l^2 = Z^2 + X^2 + Y^2 \quad (4\text{-}108)$$

or

$$l^2 = l_o^2 (1 - n)^2 \cos^2 + l_o^2 (1 + m)^2 \sin^2\theta \quad (4\text{-}109)$$

where

l_o = the distance between the points

n and m = parameters that describe cell change

θ = the angle between the c-axis and the line between the points.

It is assumed here that condition (b) of the previous paragraph is also satisfied.

Equations (4-106) and (4-109) can be used to express the fractional change in the distance between two points of a polycrystalline sample. P|| and P$\perp$ of Equation (4-106) are identified as $l_o^2 (1 - n)^2$ and l_o^2

$(1 + m)^2$ in Equation (4-109) so that l^2 (the square of the distance between points of a polycrystalline sample) is

$$l^2 = f(1 - n)^2 l_o^2 + (1 - f)(1 + m)^2 l_o^2 \quad . \tag{4-110}$$

The fractional change in length along the reference direction of a polycrystalline sample will then be

$$\Delta l/l_o = (l - l_o)/l = [f(1 - n)^2 + (1 - f)(1 + m)^2]^{1/2} - 1 \quad . \tag{4-111}$$

The parameters n and m represent the average fractional growth of single crystals along the c and a axes. Since growth in zirconium alloys is typically less than 1%, n and m are small numbers and a Taylor series expansion of the radical about n = m = 0 is possible. The expansion yields

$$\frac{\Delta l}{l_0} \approx 1 + m - (n + m)f + \text{terms of order } n^2, \text{ and } mn^2 \tag{4-112}$$

If $(1 + m)$ is taken equal to $(1 - n)^{-1/2}$ to impose the restriction of a constant volume on the grain, the Taylor series expansion yields

$$\frac{\Delta l}{l_0} \approx \frac{n}{2}(1 - 3f) + \text{terms of order } n^2 \quad . \tag{4-113}$$

The assumption of constant volume is made here in lieu of a successful atomic level model for kinetics of growth.

4.7.4.2 Application of the Result of Section 4.7.4.1 ***to Measurements of Growth in Different Directions.*** Equations (4-112) and (4-113) have been derived without reference to any particular direction. Thus, for the axial component of growth, $\Delta l/l_0$ is measured along the tubing axis and f is the axial orientation parameter, f_z. If a change in tubing circumference (or diameter of the tube since the diameter is π-1 times the circumference) is being considered, $\Delta l/l_0$ is the fractional change in the tubing diameter or circumference and f is f_θ, the tangential orientation parameter.

4.7.5 Analysis of Irradiation-Induced Growth Factors Other Than Texture

The fast neutron flux (in addition to fluence) and the residual stress in the tubing may affect growth (Reference 4.7-6 and Reference 4.7-11), but no attempt has been made to include these effects due to lack of data. Also, no significant difference in the growth rates of zirconium, zircaloy-2, and zircaloy-4 has been reported, so no distinction between their growth rates has been incorporated into the model. As mentioned in Section 4.7.2, the first step in developing the model was to account for differences in growth

due to differences in texture. The factor (1 + 3f) of Equation (4-113) was used to adjust growth measured with arbitrary textures to values expected for f = 0.05. The results are illustrated in Figure 4-22.

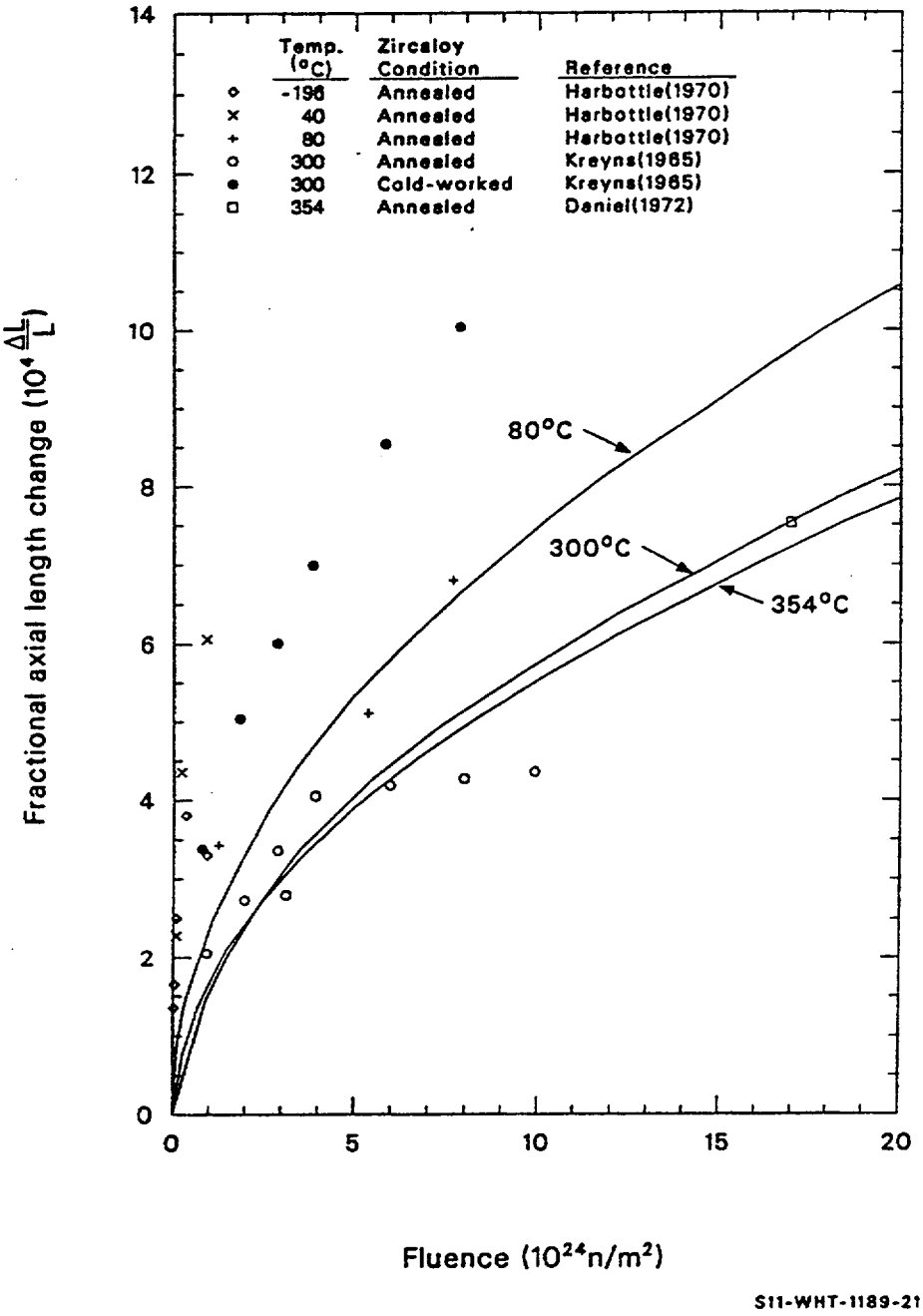

Figure 4-22. Model predictions and measured values of the growth of zircaloy tubes adjusted to a common texture coefficient of $f_z = 0.05$.

4.7.5.1 The Effect of Fast Neutron Fluence on Irradiation-Induced Growth. Many investigators have treated the effect of fast fluence by fitting in the empirical expression

$$\text{Growth strain} = (\text{fluence})^{q} \tag{4-114}$$

to the data,[4.7-6,4.7-8] with resultant values of q in the range from 0.3 to 0.8. Although good agreement can be obtained by allowing q to vary for each set of data, the results of such empirical fits are somewhat misleading. Hesketh[4.7-12] has derived a dependence on the square root of fluence [q = 0.5 in Equation (4-114)], and data from individual irradiations have not demonstrated a clear departure (other than saturation effects) from this rule. This point is illustrated in Figure 4-23 by showing a plot of axial growth as a function of the square root of the fluence.

Departures from q = 0.5 would be indicated by curvature of the data in Figure 4-23. Except for apparent saturation effects on annealed tubes at 300 °C, these departures are much less pronounced than differences due to different temperatures, fluences, and cold work. Moreover, there is a physical basis for expecting temperature and flux to modify the effect of given fluence. Therefore, the exponent in Equation (4-110) is fixed in the model at 0.5.

4.7.5.2 The Effect of Temperature on Irradiation-Induced Growth. It has been suggested by Harbottle[4.7-6] that growth is proportional to the instantaneous concentration of interstitials. This implies that growth should be directly proportional to the rate of interstitial production (which is proportional to neutron flux Φ) and inversely proportional to the rate of interstitial removal. Since interstitial removal is proportional to exp (interstitial migration energy/RT), the following expression for growth should apply.

$$\frac{\Delta L}{L} \propto \Phi \exp\left(\frac{E_M}{RT}\right) \tag{4-115}$$

where

E_M = interstitial migration energy

R = gas constant.

When Equation (4-115) is compared to data, E_M varies with temperature as expected; but any simple variation of E_M with temperature is not consistent with all experiments. A constant value for E_M has been used in the model, due to these inconsistencies and because it has been suggested that the dependence of E_M on temperature is too complex[4.7-13] to evaluate with existing data. E_M will actually change, in poorly defined steps, as the modes of interstitial migration change with increasing temperature. However, Figure 4-20, Figure 4-22, and Figure 4-23 indicate that there is a relatively small temperature dependence in the

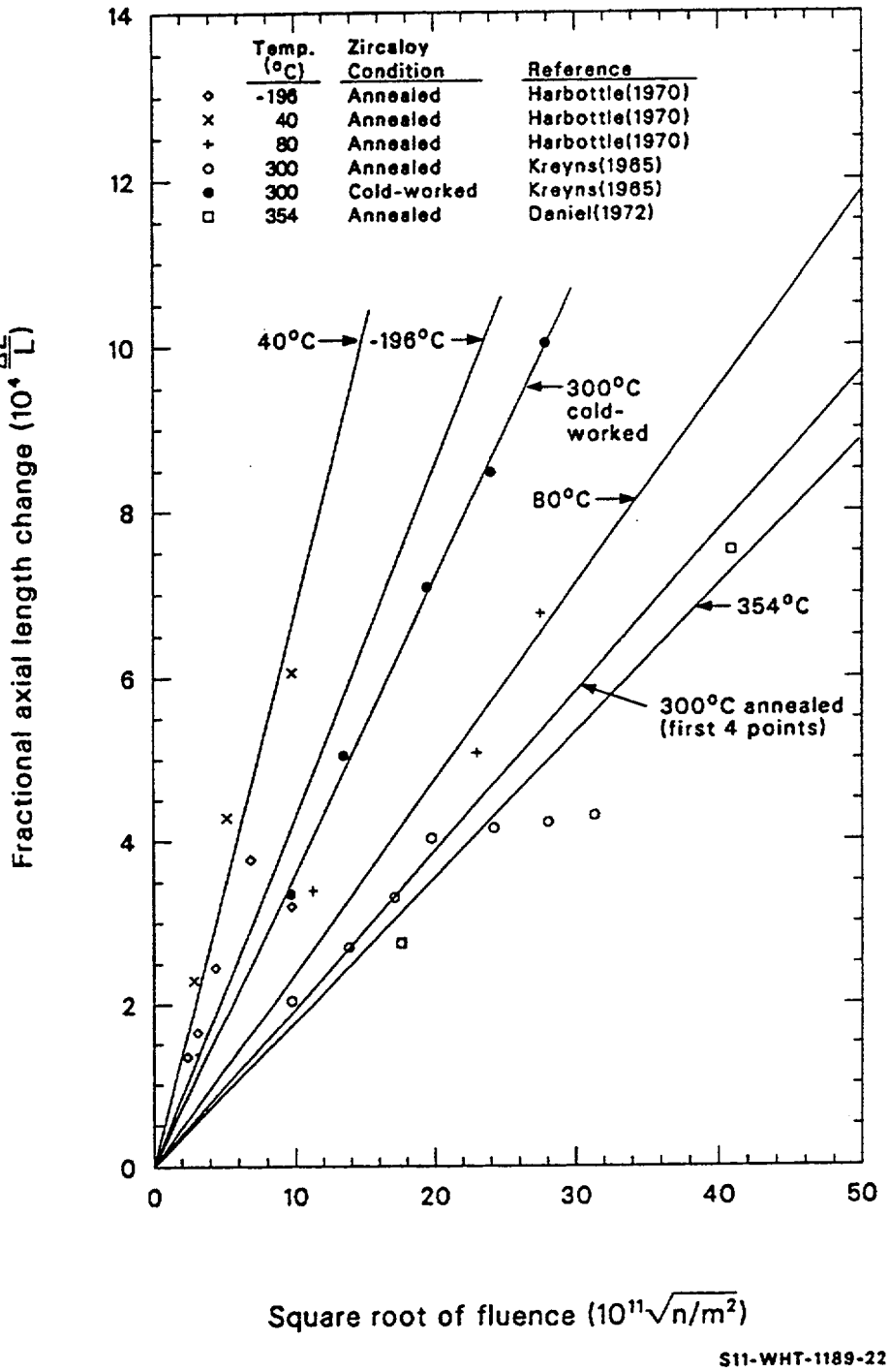

Figure 4-23. Zircaloy growth versus square root of fast neutron fluence for data adjusted to a common tube texture coefficient of $f_z = 0.05$ with linear least-squares fits superimposed.

normal operating temperature range for LWRs. Use of a small and constant value for E_M is therefore justified. A comparison of Equation (4-115) with the data shown in Figure 4-23 results in the following correlation:

$$\frac{\Delta L}{L} \propto \exp\left(\frac{240.8}{T}\right) . \qquad (4\text{-}116)$$

The fast flux factor of Equation (4-115) has been incorporated in the constant A of the full expression for growth, Equation (4-103).

The detailed data comparisons made while deriving Equation (4-116) provide justification for the functional dependence shown. When Harbottle's[4.7-6] data for growth under fast fluxes differing by a factor of two (at 40 and 80 °C, see Table 4-20) are compared, they are consistent with a value of E_M = 0.3 eV. This value of E_M is reasonable for atomic migration in that temperature range. When other data are examined, values of E_M = 0.075 eV result at -196 °C and of E_M = 0.157 eV at 354 °C. This range of values is also reasonable,[4.7-14] lending confidence to the functional dependence given by Equations (4-115) and (4-116).

4.7.5.3 The Effect of Cold Work on Irradiation Induced Growth. The observed effects of cold work have not been successfully explained in detail in the literature. For this model, general conclusions have been drawn from the available measurements and an empirical expression has been formed. The data taken by Kreyns[4.7-5] on cold worked zircaloy-4 tubes at 300 °C agree very well with a square root of fluence dependence, as shown in Figure 4-24. To compare these results with those for annealed tubes, the annealed data shown in Figure 4-23 were normalized to 300 °C using Equation (4-116). Figure 4-24 then indicates that the net effect of cold work is to increase the growth rate in the unsaturated range of fluence. Neither the dependence on the square root of the fluence nor the intercept at zero fluence are changed by cold work.

The only available data on the effect of varying the amount of cold work are reported in Figure 19 of Reference 4.7-8, which indicates the following approximate irradiation growth fractions in the longitudinal direction of zircaloy-4 plate specimens at 300 °C (Table 4-21). The data are reasonably consistent with a linear relationship between growth and cold work and have been incorporated into the model by assuming a factor of the form (1 + D x coldwork). Values of D determined from the data at three different fluences are listed in Table 4-22 where

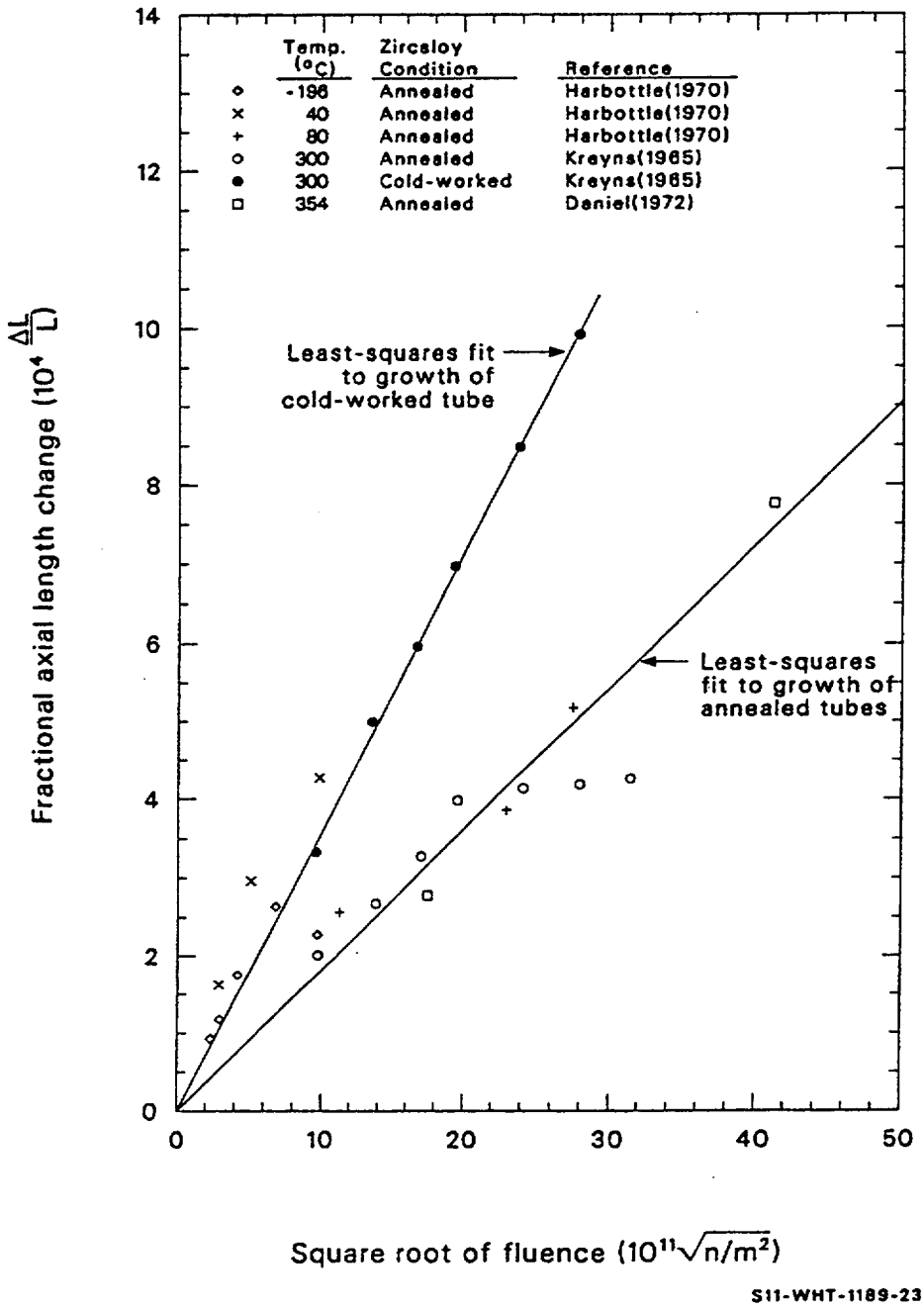

Figure 4-24. Zircaloy growth versus square root of fast neutron fluence for data adjusted to a common tube texture coefficient of $f_z = 0.05$ and to a common temperature of 300°C with linear least squares fits superimposed.

Table 4-21. Zircaloy growth data as a function of cold work and fluence.

	Cold work		
Fast fluence (10^{24}n/m^2)	**0%**	**20%**	**78%**
14	7.4×10^{-4}	7.8×10^{-4}	17.4×10^{-4}
20	8.2×10^{-4}	11.7×10^{-4}	24.4×10^{-4}
30	9.2×10^{-4}	17.3×10^{-4}	$35.7.3 \times 10^{-4}$

Table 4-22. Determination of cold work coefficient.

Fast fluence (10^{24}n/m^2)	**D**
14	1.7
20	2.0
30	3.8

$$D = \frac{1}{\text{cold work}}\left[\frac{\text{growth with cold work}}{\text{growth without cold work}} - 1\right] . \quad (4\text{-}117)$$

The value D = 2.0, given by the data at the lower fluences, is used in the model, since the measured growth with 0% cold work (Table 4-21) shows gross saturation effects similar to the effects apparent in the high fluence data of Kreyns. The model thus sacrifices a description of these gross saturation effects in order to fit the cold work data and the majority of annealed tubing data.

4.7.6 Evaluation of the Model and Its Uncertainty

The normalization of all the annealed data to identical conditions (texture coefficient f = 0.05, temperature at 300 °C), as shown in Figure 4-24, provides a test of the model. The model predicts irradiation-induced growth reasonably well except for data taken at fluences less than 10^{24} n/m^2 and except for greater-than-normal saturation effect seen in some annealed samples. Figure 4-20 leads to the same conclusion and also indicates the relative effects of the temperature, texture, and fluence variables as predicted by the model. [The factor A used in Equation (4-103) for these curves was derived from a linear least- squares fit to the data of Figure 4-24.]

Further refinement of the model to explain the relatively high growth measured at low fluence and to explain the gross saturation effects observed on some samples has not been attempted. In the low-fluence case, there are competing processes that may explain the high values sometimes found; and there is no way to distinguish between them without additional data. These effects are:

1. Stress relief causing additional length changes (Reference 4.7-11)

2. Variation in fast flux causing different growth rates (Reference 4.7-6)

3. Variation in interstitial migration energy with temperature, causing error in the temperature model (as discussed in Section 4.7.4.2).

Similar problems exist with attempts to model the gross saturation effects observed in some experiments by Kreyns, using tubing, and Fidleris,[4.7-8] using plate samples. There are sufficient data to indicate clearly that these saturation effects in growth are not simply a function of the fluence or the growth of the strain. However, few data are available to appraise correlations between saturation and other parameters.

An estimate of the uncertainty can be obtained by comparing predictions to the model with data not used in formulating the model. For example, the plate specimen data listed in Table 4-21 for 0% cold work (and 300°C) were not used to formulate the predicted growth of annealed tubes. When these data are compared with the model predictions for annealed growth at 300 °C, a discrepancy of approximately 10% is found. This 10% discrepancy is consistent with the scatter of the data at fluences above 10^{24} n/m^2 in Figure 4-24 and thus is a reasonable estimate of the model's uncertainty in the temperature range from 40 to 360 °C.

The uncertainty for temperatures outside of this range and for fluences less than 10^{24} n/m^2 may be substantially greater than 10%. In the low-fluence range, inspection of Figure 4-24 suggests uncertainties on the order of 100%. Such large discrepancies may be due to stress relief effects.[4.7-11] For temperatures much outside the range 40 to 360 °C, increased error will be caused by the presence of different modes of interstitial or vacancy migration, causing different rates of zircaloy growth.

4.7.7 References

4.7-1 R. C. Daniel, "In-Pile Dimensional Changes of Zircaloy-4 Tubing Having Stresses (Light Water Breeder Reactor Development Program)," *Nuclear Technology, 14*, May 1972, pp. 171-186.

4.7-2 W. R. Smalley, *Evaluation of Saxton Core III Fuel Materials Performance*, WCAP 3385-87, 1974.

4.7-3 J. B. Melehan, *Yankee Core Evaluation Program Quarterly Progress Report for the Period Ending September 1969*, WCAP-3017-6091, December 1969.

4.7-4 E. T. Laats and P. E. MacDonald, *Halden Project Fuel Behavior Test Program--Experimental Data Report for Test Assemblies IFA-226 and IFA-239*, NRC-OECD, March 1975.

4.7-5 P. H. Kreyns, quoted by E. Duncombe et al., *Comparisons with Experiment of Calculated Changes and Failure Analysis of Irradiated Bulk Oxide Fuel Test Rods Using the CYGRO-1 Computer Program*, WAPD-TM-583, September 1966.

4.7-6 J. E. Harbottle, "The Temperature and Neutron Dose Dependence of Irradiation Growth in Zircaloy-2," *Irradiation Effect on Structural Alloys for Nuclear Reactor Applications*, ASTM-STP-485, 1970, pp. 287-299.

4.7-7 R. Daniel, *In-Pile Dimensional Changes of Zircaloy-4 Tubing Having Low Hoop Stresses (LWBR Development Program)*, WAPD-TM-973, July 1971.

4.7-8 V. Fidleris, "Summary of Experimental Results on In-Reactor Creep and Irradiation Growth of Zirconium Alloys," *Atomic Energy Review, 13*, 1975, p. 51.

4.7-9 S. N. Buckley, "Discussion at Institute of Metals Spring Meeting," *Journal of the Institute of Metals, 97*, 1969, p. 61.

4.7-10 J. J. Kearns, *Thermal Expansion and Preferred Orientation in Zircaloy*, WAPD-TM-472, November 1965.

4.7-11 V. Fidleris, "The Effect of Cold Work and Stress Relieving on the Irradiation Growth Behavior of Zirconium Alloys," *Journal of Nuclear Materials, 46*, 1973, pp. 356-360.

4.7-12 R. V. Hesketh, "Nonlinear Growth in Zircaloy-4," *Journal of Nuclear Materials, 30*, 1969, pp. 217-222.

4.7-13 S. H. Bush, *Irradiation Effects in Cladding and Structural Materials*, NewYork: Rowman and Littlefield, 1965, p. 143.

4.7-14 A. Seeger and H. Mehren, "Analysis of Self Diffusion and Equilibrium Measurements," *Vacancies and Interstitials Metals*, A.Seeger (ed.), NewYork: American Elsevien Publishing Co., Inc., 1970, p. 892.

4.8 Creep (CCSTRN, CCSTRS, CABTP, CTP)

Cladding creep due to coolant pressure during steady-state operation is important in modeling the size of the fuel cladding gap and initial stored energy at the start of transients. For fuel rods with low internal pressure, the creep may be sufficiently rapid to also affect fuel relocation and effective conductivity of fuel pellets. Subroutines for finding creep strain as a function of stress and stress required to produce a given creep strain are presented in this section. The model used in these subroutines is based primarily on surface displacement data from the HOBBIE-1 test conducted by the U. S. Nuclear Regulatory Commission and the Energieonderzock Centrum Nederland (ECN).

4.8.1 Summary

The basic equation used in both the CCSTRN and CCSTRS subroutines is

$$\dot{\varepsilon}(t) = BA - \int_0^t B\exp\left[-(t-t')\left(\frac{\Phi}{\Psi}+\frac{1}{\gamma}\right)\right]\dot{\varepsilon}(t')dt' \quad (4\text{-}118)$$

where

$\dot{\varepsilon}(t)$ = tangential component of creep strain rate (s^{-1})

t = time since creep strain was zero (s)

t' = integration variable

B = rate constant (s^{-1}), Equation (4-118)

A = ultimate strain for infinite correlation (unitless), Equation (4-119)

Φ = fast neutron flux [$n/(m^2 \cdot s)$], E > 1 MeV

Ψ = correlation fluence, Equation (4-120) (n/m^2), E > 1 MeV

γ = zero flux correlation time, Equation (4-121) (s).

Correlations for the parameters A and B used in the CCSTRN and CCSTRS subroutines are contained in the CABTP and CTP subcodes. These correlations were obtained from out of pile creep strain versus time data. CABTP is called from CCSTRN, and CTP is called from CCSTRS. Both CABTP and CTP use the following expressions to calculate the needed parameters:

$$A = 3.83\times10^{-19}|\sigma|^r\frac{\sigma}{|\sigma|} \quad (4\text{-}119)$$

$$\begin{aligned} B &= 4.69\times10^{-6}|\sigma|^r\exp\left(-\frac{25100}{T}\right) \text{for } T \geq 615 \text{ K} \\ &= 1.9519804\times10^{-16}|\sigma|^r\exp\left(-\frac{10400}{T\sigma}\right) \text{for } T<615 \text{ K} \end{aligned} \quad (4\text{-}120)$$

where

σ = tangential component of stress (Pa)

T = temperature (K) (input temperatures are limited to the range 450 to 750 K)

r = 2.0 for stress between 0.2 and 0.75 times the strength coefficient of cladding

= 0.5 for stress between 0 and 0.2 times the strength coefficient of cladding

= 25.0 for stress less than 0.75 times the strength coefficient of cladding. The strength coefficient is approximated by the linear expression $1.5 \times 10^9 - 1.5 \times 10^6$ T, and the constants in Equation (4-120) are modified when stress is outside the range 0.2 to 0.75 times the strength coefficient to guarantee continuity at the boundaries of this range.

Expressions for the correlation fluence, Ψ, and zero flux correlation time, γ, were obtained from the slope of secondary creep rates versus temperature under tensile stress. These expressions are

$$\Psi = \begin{cases} 2.9\times10^{6}\exp\left(\frac{25100}{T}\right) & \text{for } T \geq 615 \text{ K} \\ 6.967795\times10^{16}\exp\left(\frac{10400}{T}\right) & \text{for } T < 615 \text{ K} \end{cases} \quad (4\text{-}121)$$

$$\gamma = \begin{cases} 8.6\times10^{-11}\exp\left(\frac{25100}{T}\right) & \text{for } T \geq 615 \text{ K} \\ 2.0663116\exp\left(\frac{10400}{T}\right) & \text{for } T < 615 \text{K}. \end{cases} \quad (4\text{-}122)$$

The CCSTRN subroutine calculates the tangential component of cladding creep strain at the end of a time step with constant cladding temperature, flux, and stress For time step intervals less than a time to steady-state, the infinite correlation approximation[a] is used to integrate Equation (4-118). The resultant expression for creep strain is

$$\varepsilon_{final} = [A - \varepsilon_{boundary}] [1 - \exp(B\Delta t)] + \varepsilon_{initial} \quad (4\text{-}123)$$

where

ε_{final} = tangential component of creep strain at the end of the time step (unitless)

a. The exponent in Equation (4-118) is approximated by a one.

$\varepsilon_{initial}$ = tangential component of creep strain at the start of the time step (unitless)

$\varepsilon_{boundary}$ = a boundary condition parameter used to force the creep rate to be continuous at the time step boundary when temperature and stress do not change (unitless); this parameter is zero for the first time step and is determined by Equations (4-146) and (4-147) for subsequent time steps

Δt = time step duration (s).

For time step durations longer than the time to steady-state, the steady-state approximation $[\ddot{\varepsilon}(t) \approx 0]$ is used to integrate Equation (4-118). The resultant expression for creep strain is

$$\varepsilon_{final} = (A - \varepsilon_{boundary})[1 - \exp(-B\Delta t_{ss})] + \frac{BA\left[\frac{\Phi}{\Psi} + \frac{1}{\gamma}\right](\Delta t - \Delta t_{ss})}{1 + \frac{\Phi}{\Psi} + \frac{1}{\gamma}} + \varepsilon_{initial} \quad (4\text{-}124)$$

where Δt_{ss} is the time to steady-state (s). The time to steady-state is defined to be the time when creep strain rates given by Equations (4-123) and (4-124) are equal

$$\Delta t_{ss} = -\frac{1}{B}\ln\left[\frac{A}{1 + \frac{B}{\frac{\Phi}{\Psi} + \frac{1}{\gamma}}}\frac{1}{(A - \varepsilon_{boundary})}\right] \quad (4\text{-}125)$$

or 0 if the argument of the log term is outside the range $0 <$ argument < 1.

Subroutine CCSTRS uses an interaction technique and trial assumptions to solve Equation (4-125) or (4-124) for stress when ε_{final}, $\varepsilon_{initial}$, and Δt are known. The procedure begins by solving Equation (4-125) with the implied assumption that Δt is $< \Delta t_{ss}$. In this case, the possible range of stresses is bounded and the function is monotonic. The range is cut in half in each of several iterations by testing stress at the midpoint of the possible range. f substitution of the trial solution into Equation (4-125) yields a Δt_{ss} that is $> \Delta t$, the trial solution is adopted.

A second trial solution is obtained by solving Equation (4-124) for $|\sigma|^r$ with the assumption that Δt_{ss} is zero. If this trial solution yields $\Delta t_{ss} = 0$ in Equation (4-125), it is adopted.

If neither of the two trial solutions are adopted, the technique used in CCSTRS employs the observation that the initial trial solution provides a maximum $|\sigma|^r$ and the second trial solution provides a

minimum initial slope. The implied range of possible stress is then cut in half in each of several iterations by testing in Equations (4-125) and (4-124) with stress at the midpoint of the range.

Uncertainty estimates for creep strain and stress are provided by CCSTRN and CCSTRS. Both estimates are based on the observation that the only creep data with compressive stresses are at a temperature of 644 K and stresses in the range 120 to 140 MPa. The expression used to estimate the uncertainty of the strain calculated in CCSTRN is

$$f_{\varepsilon+} = 1 + 0.3\left(1 + 2\left|\frac{\sigma + 130\times10^6}{130\times10^6}\right| + 5\left|\frac{T - 644}{644}\right|\right) \tag{4-126}$$

$$f_{\varepsilon-} = \frac{0.4}{\left(1 + 2\left|\frac{\sigma + 130\times10^6}{130\times10^6}\right| + 5\left|\frac{T - 644}{644}\right|\right)} \tag{4-127}$$

where $f_{\varepsilon\pm}$ are the upper and lower uncertainty estimates of the calculated creep strain increment magnitude.

The expression used to estimate the uncertainty of stress calculated in CCSTRS is

$$f_{\sigma+} = 1 + 0.075\left(1 + 2\left|\frac{\sigma + 130\times10^6}{130\times10^6}\right| + 5\left|\frac{T - 644}{644}\right|\right) \tag{4-128}$$

$$f_{\sigma-} = \frac{0.85}{\left(1 + 2\left|\frac{\sigma + 130\times10^6}{130\times10^6}\right| + 5\left|\frac{T - 644}{644}\right|\right)} \tag{4-129}$$

where $f\sigma\pm$ are the upper and lower uncertainty estimates of the calculated stress magnitude expressed as a function of the calculated stress magnitude.

The following subsections discuss available data and development of the model.

4.8.2 Survey of Available Data

Data that measure creep under tensile stress are being supplemented by data for creep with compressive stress in very limited ranges of temperature and stress. The available theories and data for creep under compressive stress are surveyed in this section.

Currently, there are no theories directed specifically at compressive stress; but Dollins and Nichols,[4.8-1] Piercy,[4.8-2] MacEwen,[4.8-3] and Nichols[4.8-4,4.8-5] have discussed similar physical models that

explain the general features of in-pile creep of cladding under tensile stress. For the temperature range 523 to 623 K, these authors believe the controlling mechanism for in-pile creep at stresses < 70 to 100 MPa is the preferred alignment of irradiation-induced dislocation loops during nucleation. At higher stresses, the effective stress at dislocations is thought to be sufficiently large to allow dislocation glide between the neutron produced depleted zones. The creep rate would then be controlled by combined rates of dislocation glide between depleted zones and climb out of these zones. Although some of Nichol's ideas have been challenged,[4.8-5,4.8-6,4.8-7] the predicted linear stress dependence of strain rate at low stress is supported by several authors;[4.8-8,4.8-9] and his prediction that the strain rate at high stress is proportional to approximately the one-hundredth power of stress in the 523 to 623 K temperature range is consistent with the MATPRO models for cladding plastic deformation at high stress (see Section 4.9). Unfortunately, Nichols predicts a complex relation between strain rate and stress for intermediate stress. The dependence of strain rate on stress is expected to vary from the tenth power of stress to the first power and then to the fourth power as stress increases. The physical model proposed by Nichols has been consulted but not used directly because the cost associated with the use of such a detailed model is not justified until compressive creep data confirm the model.

A similar, but less physically founded, stress dependence is proposed by Fidleris in his review of experimental data.[4.8-9] He reported that creep rate varies linearly with stress at temperatures around 570 K and stresses less than one-third the yield stress. With increasing stress, the strain rate is reported to be proportional to higher powers of stress, reaching a power of 100 at stresses of 600 MPa. The model for creepdown uses only the general features of the stress dependence reported by Fidleris because insufficient creepdown data exist to support detailed modeling.

The data referenced by Fidleris show that the in-reactor creep rate depends on material, flux temperature, and direction of testing, as well as stress. At temperatures below half the melting temperature (1,050 K) and stresses lower than the yield stress, the in-reactor creep reaches a constant rate, while the out of reactor creep rate becomes negligibly small with time. The steady-state creep rate is stated to be independent of test history or strain, at least for fast neutron fluences below 3×10^{24} n/m^2 (E > 1 MeV).

Below 450 K, temperature is reported to have little effect and, for stresses below the yield stress, the strain is < 0.001. The out-of-reactor creep data of Fidleris can be described by

$$\varepsilon = A \log t + B \qquad (4\text{-}130)$$

where

ε = strain

t = time (s)

A,B = constants.

In the range 450 to 800 K, Fidleris reports that the out-of-reactor creep strain is often represented by equations of the type

$$\varepsilon = At^m + B \qquad (4\text{-}131)$$

where ε, t, A, and B were defined in conjunction with Equation (4-130) and m is a constant between zero and one. Recovery of some of the strain is possible in this temperature range, and dynamic strain aging[4.8-10] frequently causes anomalously low creep strains and rates.

Equations (4-130) and (4-131) and other conclusions in Fidleris' review are based on his own extensive data for uniaxial, tensile creep of zirconium alloys, both in and out of reactor.[4.8-11] From these data, Fidleris concluded that the in-reactor creep is approximately proportional to the fast neutron flux for all temperatures. Other investigators treat the effect of fast neutron flux on creep in different ways.[4.8-12] Although most authors have treated in-reactor creep as the sum of the out-of-reactor creep and an additional irradiation-induced creep proportional to fast neutron flux to some power, a, there is disagreement about the magnitude of the exponent a. Ross-Ross and Hunt[4.8-8] report that creep rate is directly proportional to the fast flux, Wood[4.8-13,4.8-14] uses a = 0.85, Kohn[4.8-15] uses a = 0.65, and Gilbert[4.8-16] finds a = 0.5 for yielding creep at moderate stress levels. MacEwen[4.8-3] and Nichols[4.8-4] have resolved this apparent conflict by suggesting that the flux exponent can have values from 0 (Nichols) or 0.5 (MacEwen) to 1.0, depending on the flux and temperature.

The expressions for calculating creepdown models the effect of fast neutron flux on creep with an expression that is proportional to fast neutron flux for large fluxes but less dependent on flux for smaller fluxes. Equation (4-131), Fidleris' equation for creep strain versus time with tensile stress, has not been used because it is inconsistent with data obtained from tests with compressive stress.

The effects of grain size annealing and texture are addressed by several authors. Fidleris[4.8-9] finds that the zircaloy-2 creep rate increases continuously with grain size at 573 K. However, within the limited range of grain sizes formed in his recrystallized zircaloy-2 (6 to 20 μm), very little variation is reported. Stehle[4.8-17] reports creep strains in cold worked material that are more than twice as large as the creep strains in recrystallized cladding. He also reports that the short time creep strain of stress relieved tubes is larger than that of recrystallized tubes but that plots of creep strain versus time for stress relieved and recrystallized cladding intersect at about 6,000 hours. Kohn[4.8-15] reported that the biaxial creep rate of Zr-2.5 Nb fuel cladding is about 10 times higher than that of pressure tube material under similar conditions. He states that texture differences between the materials and the overaged precipitate structure in the as manufactured cladding can explain the difference in creep rates. The importance of texture is disputed by Stehle,[4.8-17] who reported that mechanical anisotropy (especially in longtime creep) is surprisingly low compared to the anisotropy in short time creep at room temperature. The effects of grain size, annealing, and texture have not been considered in the creepdown model because an explicit model for these effects on creepdown was premature at the time of model development.

Theories surveyed above may be misleading when applied to compressive creep because they are based primarily on tensile stress data. Picklesimer,[4.8-18] Lucas and Bement,[4.8-19] and Stehle[4.8-17] have pointed out that deformation with compressive stress differs from tensile deformation. Stehle has obtained data showing that the magnitude of creep strain of tubes under external pressure can be as small as half the creep strain of tubes under internal pressure.

The biaxial compressive stress data available include out-of-reactor measurements at three stresses and one temperature. Results from a single in-reactor experiment are also available. All experiments except one were conducted by Hobson using tubes from a shipment of typical pressurized water reactor cladding purchased specifically for use in fuel cladding research programs sponsored by the NRC.[4.8-20]

The only biaxial compressive strain data from a different lot of cladding were reported by Stehle.[4.8-17] His measurements of the tangential creep as a function of time for standard stress relieved tubing fabricated according to KwU (Kraftwerke Union) specifications are reproduced in Figure 4-25. The tangential stress in this test was 140 MPa, and the temperature was 643 K. The magnitudes of the measured creep strains are somewhat smaller than the out-of-pile strains computed from Hobson's out-of-pile data at the same temperature but are within the range of the scatter reported by Stehle for cladding with varying cold work and stress relief annealing histories. Since the details of the stress relief anneal on the lot of cladding used by Stehle are not reported, the data will be used only to assess the uncertainty of the creepdown model.

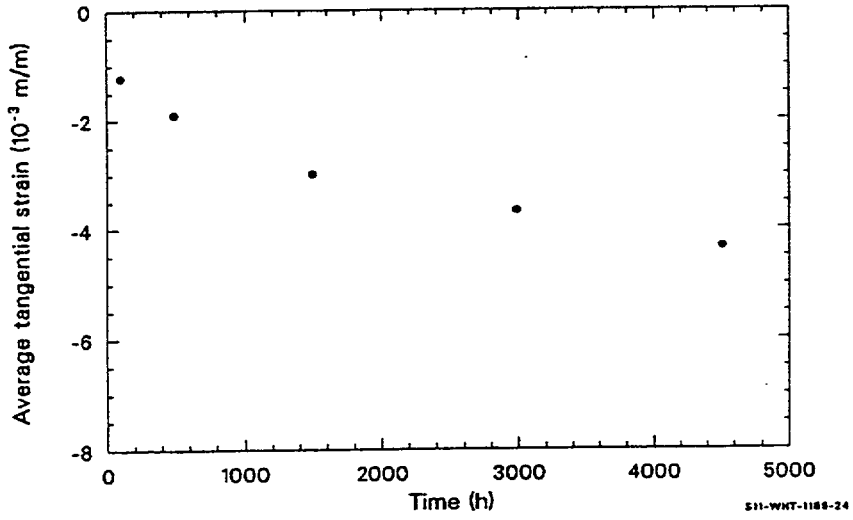

Figure 4-25. Average tangential creep strain as a function of time at 140 MPa and 643 K reported by Stehle.

The data reported by Hobson[4.8-21 to 4.8-24] are radial displacements of the cladding surface at various azimuthal angles and axial positions (6.34 mm apart). The 20 probes used to measure the displacement were arranged in a double helix pattern over a 50.8 mm length of cladding, as shown by probe number in Table 4-23. This table is arranged so that the location of the probes may be visualized by thinking of the cladding surface as split along the cylinder axis and rolled out in the plane of the page. Hobson has pointed out[4.8-23] that the exact shape of the cladding surface cannot be determined with point-by-point data from a few radial probes and that the exact stress state at any point in the sample is related to the geometry of the sample. In spite of these complications, the data can be analyzed to obtain the average tangential strain, as discussed in the next section of this report. Hobson data play a dominant role in the development of the creepdown model because the cladding is typical of LWR cladding, the stress is compressive, the cladding

displacement is reported as a function of time at 2-hour intervals, and the temperature is typical of the cladding temperatures predicted by the FRAPCON-2 code. The only atypical feature of the data is the magnitude of the stresses employed by Hobson, 125 and 135 MPa. These stresses are characteristic of low pressure rods, so extrapolation to smaller stress magnitudes is necessary to model current fuel rod prepressurization levels.

Table 4-23. Surface coordinates of probes which measure radial displacement.

Axial position	Azimuthal angle (degrees)							
(mm)	0	45	90	135	180	225	270	315
0.00	1	--	--	--	13	--	--	--
6.35	--	4	--	--	--	16	--	--
12.70	--	--	7	--	--	--	19	--
19.05	--	--	--	10	--	--	--	22
25.40	2	--	8	--	14	--	20	--
31.75	--	5	--	--	--	17--	--	
38.10	--	--	9	--	--	--	21	--
44.45	--	--	--	11	--	--	--23	
50.80	3	--	--	--	15	--	--	--

4.8.3 Model Development

It has been concluded that the most relevant data for modeling cladding creepdown under the compressive stress of steady-state LWR reactor conditions are the data of Hobson. Extensive theory and tensile creep data are useful only to provide a tentative extension of the model to stresses and temperatures where no creepdown data are available.

The first step in the analysis of Hobson's data was to estimate the average tangential strain from radial displacements measured by probes at the locations shown in Table 4-23. This was done by inspecting plots of the radial displacement measured for each test. Table 4-24 and Figure 4-26 are examples of the results. The table was constructed from Hobson's data for Test 269-4 (14.4 MPa pressure) at 200 hours, and the figure is a polar plot of the radial displacement as a function of the azimuthal angle of the probe. The plot exaggerates the radial displacement by a factor of 10 compared to the scale of the circle, which represents zero displacement. From an inspection of the figure, it can be seen that the radial displacements at 200 hours in Test 269-4 are consistent with the assumption that the cladding surface was an ellipse, with major axis between 0 and 45 degrees and the center displaced slightly toward the 180 to 270-degree quadrant. There is some variation with axial position, as shown by the scatter in the displacements with common azimuthal angles and different axial positions.

Table 4-24. Radial displacements at 200 hours in Hobson's Test 269-4 (10^{-3} mm).[a]

(mm)	0	45	90	135	180	225	270	315
0.00	4	--	--	--	12	--	--	--
6.35	--	6	--	--	--	12	--	--
12.70	--	--	48	--	--	--	12	--
19.05	--	--	--	-19	--	--	--	-29
25.40	31	--	-63	--	40	--	-58	--
31.75	--	3	--	--	--	31	--	--
38.10	--	--	-77	--	--	--	-60	--
44.45	--	--	--	-36	--	--	--	-38
50.8031	--	--	--	32	--	--	--	

a. 14.48 MPa pressure differential and 0.2127 mm pellet cladding gap.[4.8-23]

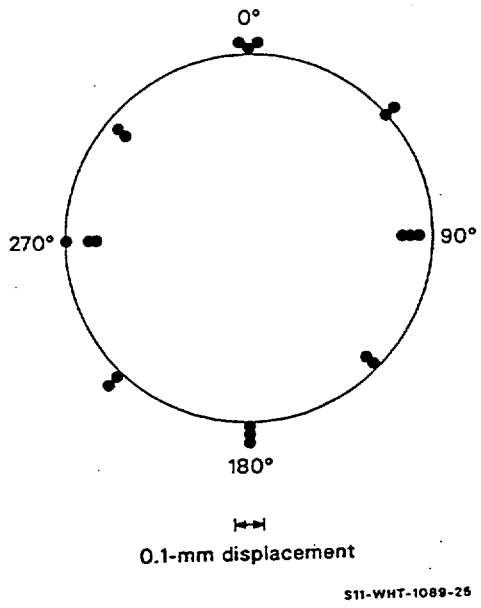

Figure 4-26. Radial displacement of cladding surface at 200 hours in Hobson's test 269-4.

The elliptical shape and gradual axial variations are also consistent with general descriptions of cladding surfaces after creepdown given by Stehle[4.8-25] and Bauer.[4.8-26] On the basis of several plots like Figure 4-26 and the general descriptions just mentioned, the author has concluded that (a) an ellipse is a

reasonable approximation for the cladding surface at any given height prior to extensive fuel cladding interaction and (b) the major and minor axes (length or orientation or both) vary slowly with axial position.

The assumption that the cladding surface at any axial position is an ellipse allows calculation of the average tangential strain, as outlined in the six steps below.

1. The circumference of the elliptical surface was related to the major and minor semi-axis lengths with the approximate expression

$$c = 2\pi\left[\frac{(a^2 + b^2)}{2}\right]^{1/2} \tag{4-132}$$

where

c = circumference (m)

a,b = semi-axis lengths (m).

2. The average tangential strain was defined as

$$\varepsilon_\theta = \int_{\text{circumference}} \frac{1}{s} ds \cong \frac{c_{final} - c_{initial}}{c_{initial}} \tag{4-133}$$

where

ε_θ = average tangential strain (unitless)

s = arc length

$c_{initial}$ = initial circumference (m)

c_{final} = final circumference (m).

3. Equations (4-132) and (4-133) were combined to obtain

$$\varepsilon_\theta = \left(\frac{a^2_{final} + b^2_{final}}{a^2_{initial} + b^2_{initial}}\right)^{1/2} - 1 \tag{4-134}$$

4. $a_{initial}$ and $b_{initial}$ were assumed equal to r_0, and a_{final} and b_{final} were set equal to the initial values plus Δa and Δb.

5. A Taylor series expansion to order $\Delta a/r_o$ and $\Delta b/r_o$ was used with Equation (4-134) and Step 4 above to find

$$\varepsilon_\theta \cong \frac{1}{2}\left(\Delta a + \frac{\Delta b}{r_0}\right) \tag{4-135}$$

where

r_o = initial radius of the outside (circular) surface of the cladding (m)

$\Delta a, \Delta b$ = change of the major and minor semi-axes lengths (m).

6. Measurements of the radial displacements at one axial position (25.4 mm) and azimuthal angles of 0, 90, 180, and 270 degrees are available from Hobson's data. If these four measurements happen to occur along the major and minor axes of the ellipse, Equation (4-135) is sufficient to convert the data to an expression for the average circumferential component of the strain. When the radial displacements at 25.4 mm are not measured along the major and minor axes of the ellipse, the derivation is more complex; but the result (to order $\Delta a/r_r$ in the Taylor series expansion) is an equation of the same form as Equation (4-135), with Δa and Δb replaced by the average radial displacements along any two axes at right angles to each other and at any angle to the major and minor axes of the ellipse. The expression then becomes

$$\varepsilon_\theta \cong \frac{1}{2}\left(\Delta a' + \frac{\Delta b'}{r_0}\right) \tag{4-136}$$

where $\Delta a'$ and $\Delta b'$ are the change of the cladding radius measured along any mutually perpendicular axes at one axial position (m).

The second part of the analysis of Hobson's data was to describe the average tangential strains obtained from the data and Equation (4-136). Figure 4-27 displays the calculated average tangential strain from two out-of-pile tests at 15.86 MPa differential pressure. During the first 600 hours, the strains are remarkably consistent. During the last 400 hours of the tests, the strain in Test 269-27 was noticeably larger than that of Test 269-8. Test 269-27 had a large simulated axial gap centered about the axial position of the four probes used to determine the strain. Test 269-8 had only a small axial gap. The difference in strain at long times is probably due to the effect of the different contact times with the simulated fuel.

Figure 4-28 illustrates the strain versus time results obtained from the 14.48 MPa out-of-pile test. The magnitude of the strain at any time is significantly smaller than the strains obtained with the 15.86 MPa tests.

In an effort to describe the strain-versus-time data shown in Figure 4-27 and Figure 4-28, the constants in Equations (4-130) and (4-131) for tensile creep were fit to selected strain-time pairs. Each equation was then tested by extrapolating to longer or shorter times and comparing the predicted strains to

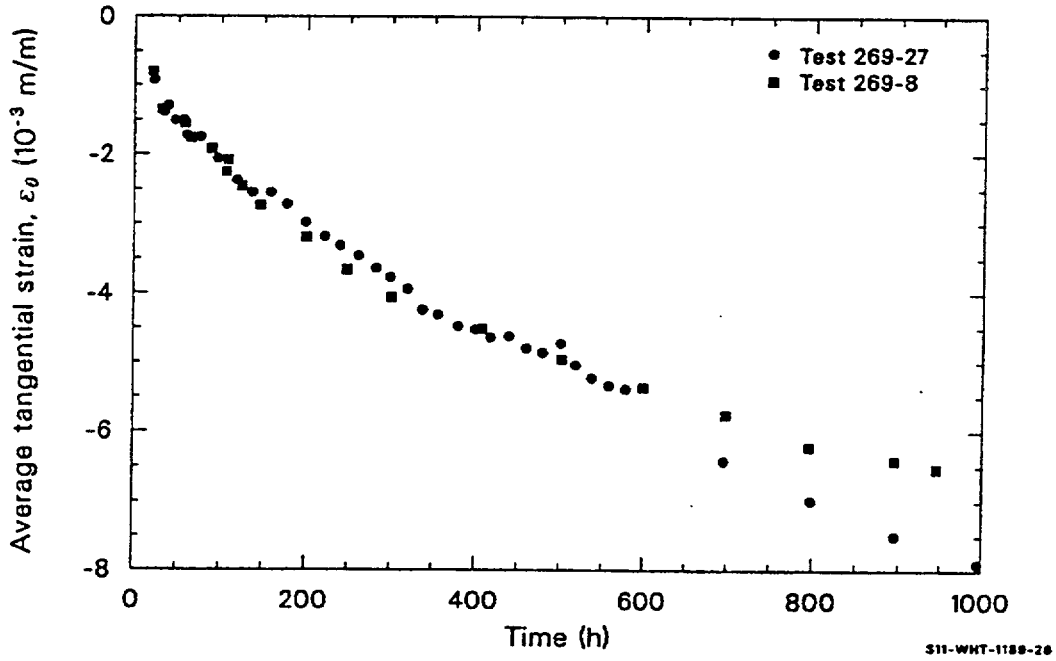

Figure 4-27. Average tangential creep strain as a function of time at 15.86 MPa differential pressure.

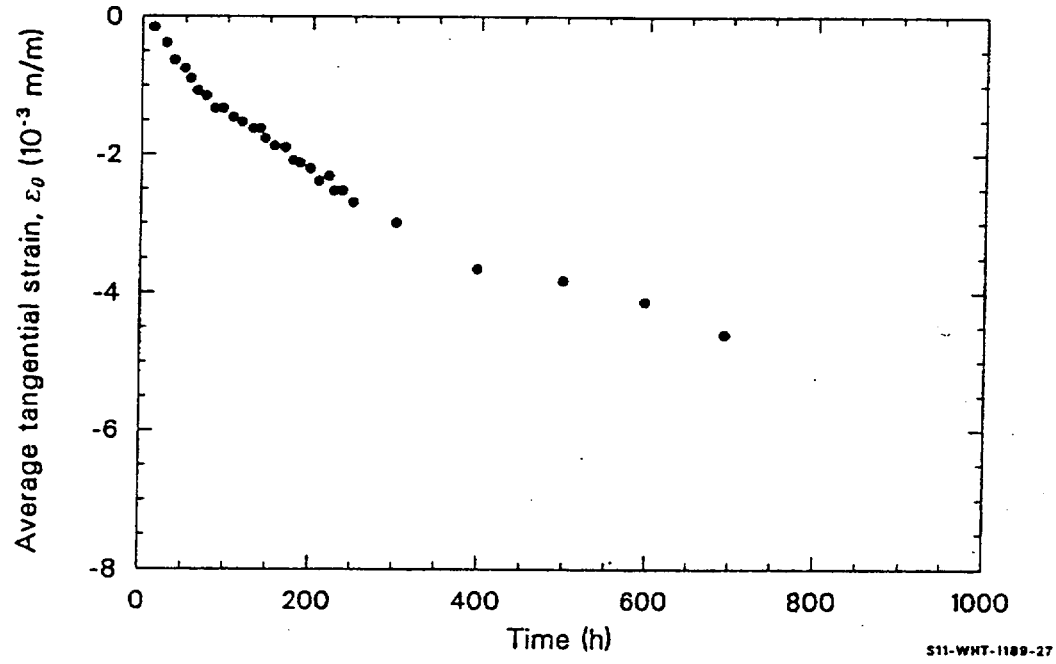

Figure 4-28. Average tangential creep strain as a function of time at 14.48 MPa differential pressure.

strain-time pairs not used in determining the constants A and B Neither equation passed this test. Equation (4-130) consistently had too much curvature,[a] and Equation (4-131) had too little curvature.

The equation finally adopted for short time out-of-pile tests was

$$\varepsilon_\theta = A[1 - \exp(-Bt)] \tag{4-137}$$

where

ε_θ = average tangential strain (m/m)

t = time (s)

A,B = functions of stress and temperature.

For the 14.48 MPa test, A = -5.32 x 10^{-3} and B = 7.64 x 10^{-7} seconds. For the 15.86 MPa tests, A = -6.32 x 10^{-3} and B = 9.17 x 10^{-7}seconds. The values of A and B for each stress were determined with a two step process:

1. A value of B was guessed and one strain time pair (ε_o,t_o) was selected as a reference. Other strain time pairs (ε_j, t_j) were then used to find an improved guess for B according to the relation

$$B_j = \ln\left(1 - \frac{\varepsilon_j[1 - \exp(-B_{guessed}t_0)]}{\varepsilon_0}\right) . \tag{4-138}$$

2. Once a single value of B that worked for several strain-time pairs was determined, a least-squares fit was carried out to determine A.

The two sets of values for A and B were used to estimate the effect of change in stress. A and B were assumed to be dependent on stress to some power, n; and n was calculated from A and B at the two stresses where they are known

$$n = \frac{\ln(A\text{at}15.86\text{MPa}/A\text{at}14.48\text{MPa})}{\ln\left(\frac{15.86}{14.48}\right)} = 1.89 \tag{4-139}$$

a. $(d^2\varepsilon_\theta)/dt^2$ too large.

$$n = \frac{\ln(\text{Bat}15.86\text{MPa}/\text{Bat}14.48\text{MPa})}{\ln\left(\frac{15.86}{14.48}\right)} = 1.89 \ . \qquad (4\text{-}140)$$

In view of the limited number of tests, both values of n were assumed to be 2. This result implies a strain rate proportional to the fourth power of stress,[a] a conclusion that agrees with one of the intermediate stress regions suggested by Dollins and Nichols[4.8-1] in Section 4.8.2.

The resultant expressions for the stress-dependence of A and B near 125 MPa and at a temperature of 644 K are

$$A = -5.32 \times 10^{-3} \{\sigma^2/[(1.245 \times 10^8)^2]\} \qquad (4\text{-}141)$$

$$B = 7.64 \times 10^{-7} \{\sigma^2/[(1.245 \times 10^8)^2]\} \qquad (4\text{-}142)$$

where σ is the tangential component of stress.

The data from Hobson's in-reactor experiment were converted to average tangential strains with the same technique used for the out-of-reactor experiment. Figure 4-29 displays the resultant average tangential strains as a function of time, along with the predicted out-of-reactor average strain from Equations (4-137), (4-141), and (4-142). The temperature during the in-reactor experiment was approximately the same as the temperature of Hobson's out-of-reactor experiments, but pressure varied from 13 to 13.5 MPa, so the tangential stress (116 MPa) was smaller in magnitude than stresses of the out-of-pile experiments.

Interpretation of the in-reactor data is complicated by absence of data for the first 80 hours, by reactor shutdown from 540 to 610 hours, and by the apparent positive average tangential strains from 80 to 200 hours. Hobson[4.8-24] has discussed the apparent positive average strains during the early part of the experiment and suggests that the positive readings come from the effects of a reactor scram at 50 hours on the experiment electronics.

The in-reactor strains shown in Figure 4-29 are consistent with a simple relation between the out-of-reactor strains and the in-reactor strains [for fast neutron flux of 5.4×10^{17} n/m^{2}s). The dashed line of the figure is the strain predicted by assuming that the initial out-of-reactor strain rate, AB, is maintained throughout the in-reactor experiment. The strains are described to within the experimental uncertainty by this line.

If this simple relation between initial out-of-reactor creep rates and in-reactor creep is confirmed by subsequent experiments with compressive stress, the implications for model development are significant. The result implies that irradiation-induced creep for compressive stress is not an independent additional

a. The time derivative of Equation (4-137) is proportional to A x B.

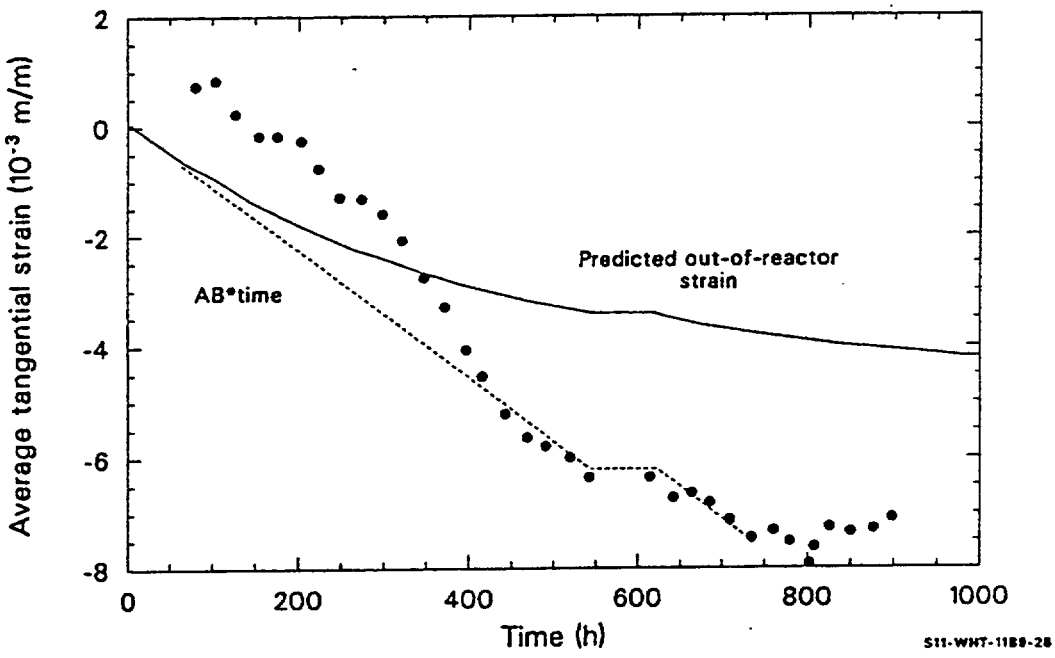

Figure 4-29. Average tangential creep strain as a function of time from Hobson's in-reactor experiment at 13 to 13.5 MPa differential pressure and 5.4 x 10^{17} fast neutrons (m^2/•s).

creep (as virtually all the models based on tensile deformation data have assumed) but simply the result of destruction of some effect associated with prior creep strain that impedes further creep strain. In the absence of any data other than those from Hobson's experiments, the assumption must be made that either (a) the in-reactor creep rate is related to the initial out of reactor creep rate for compressive stress at temperatures near 644 K or (b) the fast neutron flux, stress magnitude, and temperature are coincidentally at values that make the independent irradiation-induced creep rate equal to the initial out-of-reactor creep rate. The author has selected assumption (a) and has developed a model for cladding creepdown that is consistent with this assumption.

To be consistent with the assumption that some effect associated with prior creep strain impedes further creep strain, the independent variable in Equation (4-137) was changed from time to prior strain. The equation was then differentiated with respect to time, and the differentiated expression was used with Equation (4-137) to eliminate time, resulting in the expression

$$\dot{\varepsilon}_\theta = B(A - \varepsilon_\theta) \tag{4-143}$$

where $\dot{\varepsilon}_\theta$ is the time derivative of the tangential strain (s^{-1}).

If fast neutron flux destroys some effect associated with prior creep strain, the appropriate modification of Equation (4-143) to describe in-reactor creep will reduce or eliminate the term, $-B\varepsilon_\theta$, when a fast neutron flux is present. This was accomplished by adapting the idea of an auto-correlation function

from statistical mechanics.[4.8-27] The total strain in Equation (4-143) is replaced by the integral of the strain increment at a prior time, t', times a correlation function that approximates the rate of destruction of the effect of prior strain on the current strain rate. In the absence of detailed information, the correlation function is represented by an exponential. The resultant generalization of Equation (4-143) is

$$\dot{\varepsilon}_\theta = B\left(A - \int_0^t \exp\left[-(t-t')\left(\frac{\Phi}{\Psi}+\frac{1}{\gamma}\right)\right] d\varepsilon(t')\right) \tag{4-144}$$

where

Φ = fast neutron flux ($n/m^2 \cdot s$)

Ψ = correlation fluence (n/m^2)

γ = zero flux correlation time (s)

and other symbols have been previously defined.

New parameters introduced in Equation (4-144) can be given a physical interpretation without defining a detailed mechanistic model. The correlation fluence, Ψ, is the amount of radiation damage required to destroy most of the effect of prior strain on current strain rate; and the zero flux correlation time, s, is the time at the temperature required to anneal most of the effect of prior strain in zero flux. Since Equation (4-118) is an alternate form of Equation (4-144), the same interpretation can be applied to Equation (4-118).

CCSTRN Equations (4-123) and (4-124) are approximations derived from Equation (4-118). Equation (4-123) is obtained from Equation (4-118) by assuming

$$t\left(\frac{\Phi}{\Psi}+\frac{1}{\gamma}\right) \ll 1 \quad . \tag{4-145}$$

And integrating Equation (4-118) from an initial to a final time, t. Equation (4-124) uses the steady-state approximation to Equation (4-118), derived by setting the time derivative of Equation (4-118) equal to zero and solving for the steady-state creep rate. If the creep rate at the given final time of a time step interval is greater than or equal to the steady-state creep rate, Equation (4-123) is employed for the entire time interval. If the creep rate at the given final time of a time step interval is less than the steady-state creep rate, the time to steady-state is calculated with Equation (4-125) and Equation (4-124) is used to calculate the final strain from the assumption that the creep rate after the time interval given by Equation (4-125) has passed. The time interval to steady-state is found by solving the time derivative of Equation (4-123) for the time when the creep rate is equal to the steady-state creep rate.

Equations (4-123) and (4-124) contain a term, $\varepsilon_{boundary}$, which is the initial creep strain for any time step in which the temperature and stress are the same as the previous time step. For time steps in which the temperature, stress, or fast neutron flux has changed, Equation (4-118) implies that the creep rate should respond immediately to changes in the product AB (a function of stress and temperature); but the response of the creep rate to changes in the factor, $\Phi/\Psi + 1/\gamma$ (a function of flux and temperature) should be more gradual. A boundary condition is therefore required to make the initial creep rate of Equation (4-123) equal to the creep rate at the end of the prior step. The appropriate condition is:

For prior steps not in steady-state,

$$\varepsilon_{boundary} = APexp\ (-BP\Delta tp) + eP_{boundary}[1 - exp) -BP\Delta tP)] \ . \qquad (4\text{-}146)$$

For prior steps in steady-state,

$$\varepsilon_{boundary} = \frac{APBP}{\frac{\Phi P}{\Psi P} + \frac{1}{\gamma P} + BP} \qquad (4\text{-}147)$$

where AP, BP, ΔtP, $\varepsilon P_{boundary}$, ΦP, ΨP, and γP are equal to A, B, Δt, $\varepsilon_{boundary}$, Φ, Ψ, and γ during the previous time step.

Values for the parameters A and B at 644 K and stresses near 125 MPa have been determined from Hobson's out-of-reactor data. These data can also be used in conjunction with the modeling ideas just developed to find a minimum value for the zero flux correlation time, γ, at 644 K. The strains shown in Figure 4-27 show that a steady-state creep rate (a straight line plot for strain versus time) did not occur prior to 600 hours in either of the out-of-reactor experiments represented in the figure. Equation (4-125), with $\Phi = 0$ and Δt_{ss} at least as large as 600 hours, implies aγ of at least 6.8×10^6 seconds. This value was adopted as an interim estimate for γ at 644 K, since the strains calculated from Test 269-27 (test that simulated an axial gap in the fuel pellets) are consistent with steady-state creep after 600 hours.

The temperature-dependent factors in Equations (4-120) through (4-122) are interim estimates because they are based on the temperature dependence of tensile creep data. The data from Fidleris' tests, R-6 and Rx-14,[4.8-11] were selected to estimate the temperature dependence of B, γ, and Ψ because these tests were carried out at stress magnitude that closely approximates the magnitude of the stress in Hobson's experiments.

Figure 4-30 illustrates the steady-state creep rates reported by Fidleris for a stress of 138 MPa at several temperatures. The in-reactor data are at fast neutron fluxes of 6.8×10^{16} or 6.0×10^{16} n/m^2•s. The range of steady-state creep rates predicted by the model for creepdown at 644 K is also represented. A solid square is used to represent the steady-state creep rate seen in Hobson's experiment at a fast neutron flux of 5.4×10^{17} n/m^2 s. The slope of the tensile stress data at temperatures > 614 K ($1/T < 1.626 \times 10^3$) corresponds to a temperature-dependent factor of the form exp (-25,100/T) The in-reactor data < 615 K

correspond to a temperature-dependent factor of the form exp (-10,400/T). The temperature-dependent factors in Equations (4-120) through (4-122) are the most convenient way of forcing the steady-state creep rate implied by Equation (4-124) to correspond to the temperature-dependence shown by the Fidleris equation.

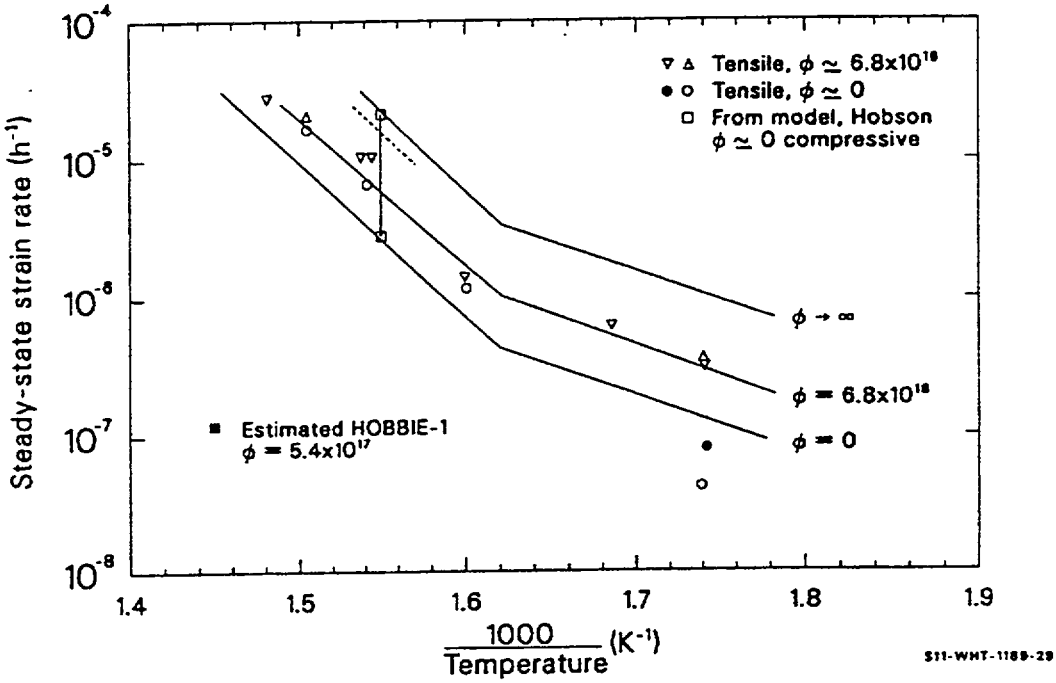

Figure 4-30. Steady-state creep rates reported by Fidleris for Tests R-6 and Rx-14 compared to model predictions for steady-state creepdown rates derived from these data.

The constants 2.9 x 10^6 and 6.967795 x 10^{16} in Equation (4-121) are the result of a least-squares fit to the steady-state creep rate data of Fidleris. As expected from the previous discussion, the resultant prediction of the steady-state creep rate for Hobson's in-reactor creep rate at 5.4 x 10^{17} n/m^2•s with a compressive stress is slightly too high. The predicted rate, s^{-1}, is shown in Figure 4-30 by the dashed line.

4.8.4 Model Uncertainty

Lack of an extensive data base for creep under compressive stress makes the assignment of uncertainty limits very tentative. The data of Stehle (illustrated in Figure 4-25) are the only other compressive stress data available. These data show creep strains of about half the magnitude of the model-predicted strains. Since these are the only appropriate data not used in developing the model, they were used to estimate fractional error of 0.6 and + 0.3 in strain at 644 K and 130 MPa stress. The remaining terms of the uncertainty estimate for the strain predicted by CCSTRN [Equations (4-126) and (4-127)] are simply engineering judgments that estimate 100% error when the stress differs from 130 MPa by more than 65 MPa or the temperature differs from 644 K by more than 60 K.

Equations (4-128) and (4-129), the expressions for the uncertainty of the stress calculated by CCSTRS, were derived from Equations (4-126) and (4-127) and the observation that the predicted strain is usually proportional to the fourth power of stress. The resultant uncertainty in stress expressed as a fraction of stress is one-fourth the fractional uncertainty in strain.

4.8.5 References

4.8-1 C. C. Dollins and F. A. Nichols, "Mechanisms of Irradiation Creep in Zirconium-Base Alloys," *Zirconium in Nuclear Applications*, ASTM-STP-551, 1974, pp. 229-248.

4.8-2 G. R. Piercy, "Mechanisms for the In-Reactor Creep of Zirconium Alloys," *Journal of Nuclear Materials, 2*, 1968, pp. 18-50.

4.8-3 J. R. MacEwen, "The Effect of Neutron Flux on Dislocation Climb," *Journal of Nuclear Materials, 54*, 1974, pp. 85-96.

4.8-4 F. A. Nichols, "Point Defects and the Creep of Metals," *Journal of Nuclear Materials, 69 and 70*, 1978, pp. 451-464.

4.8-5 F. A. Nichols, "On the SIPA Contribution to Irradiation Creep," *Journal of Nuclear Materials, 84*, 1979, pp. 207-221.

4.8-6 D. O. Northwood, "Comments on In-Pile Dimensional Changes in Neutron Irradiated Zirconium Base Alloys," *Journal of Nuclear Materials, 64*, 1977, pp. 316-319.

4.8-7 E. F. Ibrahim, "In-Reactor Creep of Zirconium Alloys by Thermal Spikes," *Journal of Nuclear Materials, 58*, 1975, pp. 302-310.

4.8-8 P. A. Ross-Ross and C. E. L. Hunt, "The In-Reactor Creep of Cold-Worked Zircaloy-2 and Zirconium-2.5 wt Niobium Pressure Tubes," *Journal of Nuclear Materials, 26*, 1968, pp. 2-17.

4.8-9 V. Fidleris, "Summary of Experimental Results on In-Reactor Creep and Irradiation Growth of Zirconium Alloys," *Atomic Energy Review, 13*, 1976, pp. 51-80.

4.8-10 E. D. Warda, V. Fidleris, and E. Teghtsoonian, "Dynamic Strain Aging During Creep of α-Zr," *Metallurgical Transactions, 4*, 1972/1973, pp. 302-316.

4.8-11 V. Fidleris, "Uniaxial In-Reactor Creep of Zirconium Alloys," *Journal of Nuclear Materials, 26*, 1968, pp. 51-76.

4.8-12 W. J. Duffin and F. A. Nichols, "The Effect of Irradiation on Diffusion-Controlled Creep Processes," *Journal of Nuclear Materials, 45*, 1972/1973, pp. 302-316.

4.8-13 D. S. Wood, "Dose Dependence of Irradiation Creep of Zircaloy-2," *Properties of Reactor Structural Alloys After Neutron or Particle Irradiation*, ASTM-STP-570, 1975, pp. 207-217.

4.8-14 D. S. Wood and B. Watkins, "A Creep Limit Approach to the Design of Zircaloy-2 Reactor Pressure Tubes at 275 °C," *Journal of Nuclear Materials, 41*, 1971, pp. 327-340.

4.8-15 E. Kohn, "In-Reactor Creep of Zr-2.5Nb Fuel Cladding," *Zirconium in the Nuclear Industry*, ASTM-STP-633, 1977, pp. 402-417.

4.8-16 E. R. Gilbert, "In-Reactor Creep of Reactor Materials," *Reactor Technology, 14*, Fall 1971, pp. 258-285.

4.8-17 H. Stehle et al., "Mechanical Properties of Anisotropy and Microstructure of Zircaloy Canning Tubes," *Zirconium in the Nuclear Industry*, ASTM-STP-633, American Society for Testing and Materials, December 1977, pp. 486-507.

4.8-18 M. L. Picklesimer, "Deformation, Creep, and Fracture in Alpha-Zirconium Alloys," *Electrochemical Technology, 4*, 1966, pp. 289-300.

4.8-19 G. E. Lucas and A. L. Bement, "Temperature Dependence of the Zircaloy-4 Strength Differential," *Journal of Nuclear Materials, 48*, 1975, pp. 163-170.

4.8-20 R. H. Chapman, *Characterization of Zircaloy-4 Tubing Procured for Fuel Cladding Research Programs*, ORNL/NUREG/TM-29, 1976.

4.8-21 D. O. Hobson and C. V. Dodd, *Interim Report on the Creepdown of Ziraloy Fuel Cladding*, ORNL/NUREG/TM-103, May 1977.

4.8-22 D. O. Hobson, *Quarterly Progress Report on the Creepdown and Collapse of Zircaloy Fuel Cladding for January-March 1977*, ORNL/NUREG/TM-125, July 1977.

4.8-23 D. O. Hobson, *Creepdown of Zircaloy Fuel Cladding-Initial Tests*, ORNL/NUREG/TM-181, April 1978.

4.8-24 D. O. Hobson, *Preliminary Analysis of Surface Displacement Results in the Creepdown Irradiation Experiment HOBBIE-1*, NUREG/CR-0810 and ORNL/NUREG/TM-310, June 1979.

4.8-25 H. Stehle et al., "Uranium Dioxide Properties for LWR Fuel Rods," *Nuclear Engineering and Design, 33*, 1975, pp. 230-260.

4.8-26 A. A. Bauer et al., *Progress on Evaluating Strength and Ductility of Irradiated Zircaloy During July-September 1975*, BMI-1938, September 1975.

4.8-27 C. Kittle, *Elementary Statistical Physics*, New York: John Wiley and Sons, Inc., 1958.

4.9 Plastic Deformation (CSTRES, CSTRAN, CSTRNI, CANISO, CKMN)

This section is a description of materials properties subcodes for cladding stress and plastic deformation. The subroutine CSTRES calculates instantaneous cladding stress as a function of plastic strain, strain rate, temperature, cold work, fast neutron fluence, and average oxygen concentration. The subroutine CSTRAN calculates instantaneous cladding strain as a function of strain rate, stress, temperature, cold work, fast neutron fluence, and average oxygen concentration. CSTRNI calculates the cladding strain at the end of a time step of specified length as a function of the initial strain, average stress during the time step, temperature, cold work, fast neutron fluence, and average oxygen concentration.

The stresses and strains used with CSTRES, CSTRAN, and CSTRNI are effective stresses and strains. The subcode CANISO provides coefficients of anisotropy for converting given stress and plastic strain components to effective stresses and strains. CANISO includes a preliminary model for the change in texture with deformation. The subcode CKMN provides the parameters for the cladding equation of state as a function of temperature, average oxygen concentration, fast neutron fluence, and cold work.

4.9.1 Summary

All input strain or stress components are assumed by MATPRO mechanical property routines to be true strain or true stress.[a] The basic equation used to relate stress and plastic strain is

$$\sigma = K\varepsilon^{n}\left(\frac{\dot{\varepsilon}}{10^{-3}}\right)^{m} \qquad (4\text{-}148)$$

where

σ = true effective stress (Pa)

ε = true effective plastic strain (unitless)

$\dot{\varepsilon}$ = rate of change of true effective plastic strain (s^{-1})

K,n,m = parameters which describe the metallurgical state of the cladding.

Equation (4-148) is the expression used in CSTRES to calculate effective stress.

The strain returned by CSTRAN is obtained from the solution of Equation (4-148) for strain. The strain returned by CSTRNI is obtained from the time integral of the strain-dependent factors of Equation (4-148), assuming stress is constant during the time interval

a. True strain equals the change in length divided by the length at the instant of change integrated from the original to the final length. True stress equals the force per unit cross-sectional area determined at the instant of measurement of the force.

$$\varepsilon_f = \left[\left(\frac{n}{m}+1\right)10^{-3}\left(\frac{\sigma}{K}\right)^{1/m}\Delta t + \varepsilon_i^{\left(\frac{n}{m}+1\right)}\right]^{\frac{m}{n+m}} \quad (4\text{-}149)$$

where

ε_f = true effective strain at the end of a time interval (unitless)

ε_i = true effective strain at the start of a time interval (unitless)

Δt = duration of the time interval (s).

Effective stress for use with the CSTRAN and CSTRNI subroutines is obtained from stress components and the equation

$$\sigma = [A1S(\sigma_1-\sigma_2)^2 + A2S(\sigma_2-\sigma_3)^2 + A3S(\sigma_3-\sigma_1)^2]^{1/2} \quad (4\text{-}150)$$

where

σ = effective stress (Pa)

$\sigma_1, \sigma_2, \sigma_3$ = principal axis stress components (Pa)

A1S,A2S,A3S= coefficients of anisotropy provided by the CANISO subcode.

Effective strain for use with the CSTRES code is obtained from strain components with the equation

$$d\varepsilon = \left[\frac{1}{A1EA2E + A2EA3E + A3EA1E}\right](A1E(A2Ed\varepsilon_1 - A3Ed\varepsilon_2)^2 + A2E(A3Ed\varepsilon_2 - A1Ed\varepsilon_3)^{(2)} \quad A3E(A1Ed\varepsilon_3 - A2Ed\varepsilon_1)^2)^{1/2} \quad (4\text{-}151)$$

where

$d\varepsilon$ = effective plastic strain increment

$d\varepsilon_1, d\varepsilon_2, d\varepsilon_3$= axial, circumferential, and radial strain component increments

A1E,A2E,A3E= coefficients of anisotropy provided by the CANISO subroutine.

Once effective stress and strain are known, along with the input values of either strain or stress components, the unknown components of either stress or strain can be obtained from the Prandtl-Reuss flow rule[4.9-1]

$$d\varepsilon_1 = \frac{d\varepsilon}{\sigma}[\sigma_1(A1E + A3E) - \sigma_2 A1E - \sigma_3 A3E] \quad (4\text{-}152)$$

$$d\varepsilon_2 = \frac{d\varepsilon}{\sigma}[-\sigma_1(A1E + \sigma_2(A1E + A2E) - \sigma_3 A2E)] \quad (4\text{-}153)$$

$$d\varepsilon_3 = \frac{d\varepsilon}{\sigma}[-\sigma_1 A3E - \sigma_2 A2E + \sigma_3(A3E + A2E)] \quad (4\text{-}154)$$

where all the terms have been previously defined.

As mentioned in conjunction with Equations (4-150) and (4-151), coefficients of anisotropy are provided by the CANISO subroutine. The information required by this subroutine is the temperature, the three principal components of plastic strain during a time interval, three constants related to the cladding basal pole distribution at the start of the time interval, and three constants related to the deformation history of the cladding prior to the time interval. For each time step, the subroutine updates the six constants required and provides the six coefficients of anisotropy required by Equations (4-150) through (4-154). Initial (no plastic deformation) values of the pole figure and deformation history constants will be discussed in conjunction with the following summary of the equations used in the CANISO subcode.

For undeformed cladding, with σ_1, σ_2, σ_3 of Equation (4-150) defined to be the axial, circumferential, and radial components of stress, the expressions used to find the stress anisotropy constants are

$$A1S = (1.5f_r - 0.5)\, g(T) + 0.5 \quad (4\text{-}155)$$

$$A2S = (1.5f_z - 0.5)\, g(T) + 0.5 \quad (4\text{-}156)$$

$$A3S = (1.5f_\theta - 0.5)\, g(T) + 0.5 \quad (4\text{-}157)$$

where

g(T) = a function which is 1.0 for temperatures < 1,090 K, 0 for temperatures > 1,255 K, and found by linear interpolation for temperatures between 1090 and 1,255 K.

f_r, f_z, f_θ = average of the squared cosine between the c-axis of grains in the cladding and the radial, axial, and tangential reference directions, respectively, weighted by the volume fraction of grains at each orientation. These averages can be obtained from a pole figure and the CTXTUR subroutine (f_r = COSTH2, f_z = COSF12 - CT2CF2, and f_θ = 1-COSTH2 - COSFI2 + CT2CF2 in the notation of the CTXTUR subroutine). Values of f_r, f_z, and f_θ for typical cladding textures are $f_r = 0.66$, $f_z = 0.06$, and $f_\theta = 0.28$.[4.9-2]

The change of the factors, f_r, f_θ, and f_z, of Equations (4-155) through (4-157) due to deformation is modeled with the following correlations

$$\Delta f'_r = -d\varepsilon_3 \, [-1.505T \, (0.00895)] \tag{4-158}$$

$$\Delta f'_\theta = -d\varepsilon_1 \, [-1.505T \, (0.00895)] \tag{4-159}$$

$$\Delta f'_z = -d\varepsilon_2 \, [-1.505T \, (0.00895)] \tag{4-160}$$

where

$\Delta f'_r, \Delta f'_z, \Delta f'_\theta$ = change in f_r, f_z, and f_θ due to deformation

T = 644 K, for temperature < 644 K, the temperature for > 644 temperature ≤ 1,090 K, 1,090 K for temperature > 1,090 K.

The strain anisotropy coefficients A1E, A2E, and A3E are given by Equations (4-155) through (4-160), with A1S, A2S, and A3S replaced by A1E, A2E, and A3E when the cladding temperature is below 650 K. However, limited data at temperatures above 800 K suggest initial strain anisotropy coefficients of 0.5 (the isotropic values). The description of high temperature strain anisotropy thus requires a separate set of f values, set initially at the isotropic values and changed during each time step by an amount given by Equations (4-158) through (4-160). The expressions for A1E, A2E, and A3E which are used to model this rather complex switching from texture-dependent to deformation-dependent strain anisotropy are

$$A1E = \frac{A1S + [(1.5f'_r - 0.5)g(T) + 0.5]\exp\left[\frac{(T-725)}{18}\right]}{\exp\left[\frac{(T-725)}{18}\right] + 1} \tag{4-161}$$

$$A2E = \frac{A2S + [(1.5f'_z - 0.5)g(T) + 0.5]\exp\left[\frac{(T-725)}{18}\right]}{\exp\left[\frac{(T-725)}{18}\right] + 1} \tag{4-162}$$

$$A3E = \frac{A3S + [(1.5f'_\theta - 0.5)g(T) + 0.5]\exp\left[\frac{(T-725)}{18}\right]}{\exp\left[\frac{(T-725)}{18}\right] + 1} \quad (4\text{-}163)$$

where f'_r, f'_z, and f_θ are deformation-dependent parameters set equal to 1/3 at zero deformation and changed like the parameters f_r, f_z, and f_θ in Equations (4-158) through (4-160).

Effects of cladding temperature, cold work, irradiation, in-reactor annealing, and oxidation on mechanical properties are expressed as changes in the strength coefficient, K; the strain hardening exponent, n; and the strain rate sensitivity exponent, m; of Equations (4-148) and (4-149). For fully annealed isotropic zircaloy-2 or zircaloy-4 cladding, the temperature and strain rate dependent values of m, n, and K are as shown below.

(1) Values of the strain rate sensitivity exponent, m[a]:

For $T \leq 730$ K,

$$m = 0.02 \ . \quad (4\text{-}164)$$

For $730 \leq T < 900$ K,

$$m = 2.063172161 \times 10^{1} + T\{-7.704552983 \times 10^{-2} + T[9.504843067 \times 10^{-5} + T(-3.860960716 \times 10^{-8})]\} \quad (4\text{-}165)$$

For $900 \leq T < 1{,}090$ K,

$$m = -6.47 \times 10^{-2} + 2.203 \times 10^{-4} T \ . \quad (4\text{-}166)$$

For $1{,}090 \leq T \leq 1{,}172.5$ K,

$$m = -6.47 \times 10^{-2} + 2.203 \times 10^{-4} T, \text{ for } \dot{\varepsilon} \geq 6.34 \times 10^{-3} s^{-1} \quad (4\text{-}167)$$

$$m = -6.47 \times 10^{-2} + 2.203 \times 10^{-4} T + 6.78 \times 10^{-2}\left(\frac{T-1090}{82.6}\right)\ln\left(\frac{6.34 \times 10^{-3}}{\dot{\varepsilon}}\right) \text{ for } \dot{\varepsilon} < 6.34 \times 10^{-3} s^{-1} \ . \quad (4\text{-}168)$$

For $1{,}172.5 < T < 1{,}255$ K,

a. Eight to ten significant figures are used in these expressions to minimize discontinuities.

$$m = -6.47 \times 10^{-2} + 2.203 \times 10^{-4} T, \text{ for } \dot{\varepsilon} \geq 6.34 \times 10^{-3} s^{-1} \quad (4\text{-}169)$$

$$m = -6.47\times10^{-2} + 2.203\times10^{-4}T + 6.78\times10^{-2}\left(\frac{1255 - T}{82.6}\right)\ln\left(\frac{6.34\times10^{-3}}{\dot{\varepsilon}}\right) \text{ for } \dot{\varepsilon} < 6.34\times10^{-3} s^{-1} \quad . \quad (4\text{-}170)$$

For $1{,}255 \leq T \leq 2{,}100$ K,

$$m = -6.47 \times 10^{-2} + 2.203 \times 10^{-4} T \quad . \quad (4\text{-}171)$$

(2) Values of the strain hardening exponent, n:

For $T < 1{,}099.0772$ K,

$$n = -9.490 \times 10^{-2} + T[1.165 \times 10^{-3} + T(-1.992 \times 10^{-6} + T9.588 \times 10^{-10})] \quad . \quad (4\text{-}172)$$

For $1{,}099.0722 \leq T < 1{,}600$ K,

$$n = -0.22655119 + 2.5 \times 10^{-4} T \quad . \quad (4\text{-}173)$$

For $T \geq 1{,}600$ K,

$$n = 0.17344880 \quad (4\text{-}174)$$

When the strain is $< n/(1 + m)$, the strain hardening exponent is modified to a larger value than the one given by Equations (4-170) through (4-172). The expression used to modify n for strains $< n/(1 + m)$ is

$$n' = \text{the smaller of ANL or } n^2/[(1 + m)\cdot \varepsilon] \quad (4\text{-}175)$$

where

ANL = 0.17 for $T \leq 730$ K; $0.056T - 11.218$ for $730 < T < 780$ K; or 0.95 for $T \geq 780$ K

n = the number given by Equations (4-170) through (4-172)

n = the revised number to be used with Equation (4-148) or (4-149) in place of n.

(3) Values of the strength coefficient, K:

For $T < 750$ K,

$$K = 1.17628 \times 10^9 + T\{4.54859 \times 10^5 + T[-3.28185 \times 10^3 + T(1.72752)]\} \quad . \tag{4-176}$$

For $750 \leq T < 1{,}090$ K,

$$K = 2.522488 \times 10^6 \exp(2.8500027 \times 10^6/T^2) \quad . \tag{4-177}$$

For $1{,}090 \leq T < 1{,}255$ K,

$$K = 1.841376039 \times 10^8 - T1.4345448 \times 10^5 \quad . \tag{4-178}$$

For $1{,}255 \leq T \leq 2{,}100$ K.

$$K = 4.3302 \times 10^7 + T[-6.685 \times 10^4 + T(3.7579 \times 10^1 - T7.33 \times 10^{-3})] \tag{4-179}$$

The changes in form of Equations (4-164) through (4-177) in various temperature ranges are caused by changes in the physical mechanism of the plastic deformation. At 700 to 900 K, the deformation becomes significantly strain-rate-dependent, the strength of the material begins to decrease rapidly with temperature, and strain hardening becomes relatively unimportant. This change is generally attributed to thermal creep at high temperature, but the specific deformation system change has not been identified. The 1,090 to 1,255 K region is the $\alpha + \beta$ phase region for zircaloy, and the region above 1,255 K is the β phase region for this material.

The change in the strain hardening exponent due to irradiation and cold-working of cladding is described by multiplying the value of n given in Equations (4-170) through (4-172) by

$$RIC = [0.847\exp(-39.2COLDW) + 0.153 + COLDW(-9.16\times10^{-2} + 0.229COLDW)] \exp\left(\frac{-\Phi^{1/3}}{3.73\times10^7 + 2\times10^8 COLDW}\right) \tag{4-180}$$

where

RIC = strain hardening exponent for irradiated and cold-worked material divided by the expression in Equations (4-170) through (4-172)

COLDW = effective cold work for strain hardening exponent (unitless ratio of areas). (Changes in the effective cold work as a function of time and temperature are modeled by the CANEAL subroutine discussed in Section 4.10.)

Φ = effective fast neutron fluence (neutrons > 1.0 MeV/m^2). (Changes in the effective fast neutron fluence are modeled by the CANEAL subroutine discussed in Section 4.10.)

The change in the strength coefficient due to irradiation and cold-working of the cladding is modeled with the expression

$$DK = (0.546\ COLDW + 9.76 \times 10^{-27}\Phi)\ K \tag{4-181}$$

where ΔK is the strength coefficient for irradiated and cold-worked material minus the expression in Equations (4-174) through (4-177) (Pa). The strain rate sensitivity exponent does not change as a function of irradiation or cold work.

Correlations for the changes in the strain hardening exponent, strength coefficient, and strain rate sensitivity exponent due to the oxidation of the cladding are

$$RNO = 1 + \left[1250 - \frac{1250}{\exp\left[\frac{(T-1380)}{20}\right] + 1}\right] Y \tag{4-182}$$

$$RKO = 1 + \left[1120 - \frac{990}{\exp\left[\frac{(T-1301.5)}{61}\right] + 1}\right] Y \tag{4-183}$$

and

$$RMO = \exp(-69Y) \tag{4-184}$$

where

RNO = strain hardening exponent for oxidized cladding divided by strain hardening exponent for as fabricated cladding

RKO = strength coefficient for oxidized cladding divided by strength coefficient for as fabricated cladding

RMO = strain rate sensitivity exponent for oxidized cladding divided by strain rate sensitivity exponent for as fabricated cladding

T = temperature (K)

Y = average oxygen concentration increase (kg oxygen/kg zircaloy). (Changes in oxygen concentration are modeled by the COBILD subroutine).

Estimates have been made for the expected error of the strength coefficient, strain hardening exponent, and strain rate sensitivity exponent. The expressions for these uncertainties are

$$UK = \begin{cases} 77\times10^{6} \text{ for } T < 700K \\ 110.43693\times10^{6} - T\,4.7767045\times10^{4} \text{ for } 700 \le T \le 800K \\ \dfrac{(\text{strength coefficient})}{3} \text{ for } T > 800K \end{cases} \quad (4\text{-}185)$$

$$Un = \begin{cases} 0.017 \text{ for } T < 700K \\ -2.8405405\times10^{-2} + 6.486864\times10^{-5}T \text{ for } 700 \le T \le 1255K \\ 0.053 \text{ for } T > 1255K \end{cases} \quad (4\text{-}186)$$

$$Um = \begin{cases} 0.01 \text{ for } T < 700K \\ -2.97992\times10^{-2} + 5.6856\times10^{-5} \text{ for } 700 \le T \le 900K \\ 0.16(\text{strain rate sensitivity exponent}) \text{ for } T \ge 900K \end{cases} \quad (4\text{-}187)$$

where

UK = expected error of the strength coefficient (fraction of value)

Un = expected error of the strain hardening exponent (fraction of value)

Um = expected error of the strain rate sensitivity exponent (fraction of value).

The following section is a review of the data used to derive the expressions summarized in this section Section 4.9.3 describes the development of the plastic deformation models, and Section 4.9.4 is a comparison of model predictions to data not used to develop the models. Uncertainties are discussed in Section 4.9.5.

4.9.2 Available Data

A number of references which discuss zircaloy plastic deformation are available.[4.9-2 to 4.9-37] However, many of the data are from uniaxial load elongation tests on poorly characterized material. Also, the basic data used to construct models are often not published. The critical data for analysis of cladding deformation stress and strain versus time in tests with biaxial stress using well characterized cladding are sparse. This section is a review of the theoretical results and data available for use in cladding plastic deformation models. The general features of zircaloy plastic deformation are reviewed first, followed by reviews of uniaxial and biaxial test data.

4.9.2.1 Modes of Deformation. Zircaloy has a hexagonal, close packed crystal structure at temperatures in the range from 300 to 1,090 K. At temperatures of 1,255 to 2,100 K, the alloy has a body-centered cubic structure. Since the structure changes, significant changes in the plastic deformation must also be expected in the temperature range 1,090 to 1,255 K. Moreover, the alpha (hexagonal), alpha + beta, and beta (body-centered cubic) phase boundaries change with increasing oxygen content. Thus, the temperatures at which one expects discontinuities in cladding plastic deformation change with oxygen content.

The alpha phase (at least in unirradiated zircaloy) is anisotropic. This means the texture (orientation of individual grains) of the material is important at temperatures below 1,090 K. Theories exist to deal with anisotropic plastic deformation[4.9-30,4.9-38] under varying stress-states, but they rely on the assumption that the physical process responsible for plastic deformation does not change significantly as a function of the stress state. That is, a single plastic potential[4.9-38] or a single stress-strain law[4.9-29] is assumed at each temperature. There is evidence that indicates that this is an oversimplification.[4.9-3,4.9-31] Both slip and twinning systems are expected to operate in zircaloy, and the operable system is related to the orientation of grains with respect to the applied stress. As multiaxial stress versus strain data become available, it is likely that different stress strain laws (equations of state) will be developed for each mode of deformation, along with conditions for specifying when each mode is active. There is not enough detailed biaxial data to develop equations of state for separate modes of deformation; therefore, an equation of state has been developed based on existing uniaxial data and compared to limited biaxial data to see if discrepancies exist. Analysis discussed in Section 4.9.3 of this report indicates that the discrepancies may be significant.

Modeling zircaloy plastic deformation is further complicated by the fact that deformation is caused by true stress, which is not measured in any of the tests reported because none of the investigators measured the minimum cross-sectional area of the sample during deformation. The problem was addressed by other experiments,[4.9-37] but zircaloy data from these tests were not included in the model.

4.9.2.2 Uniaxial Test Data. The low temperature part of the equation of state used in MATPRO for fully annealed cladding, Equation (4-148), in conjunction with Equations (4-172) through (4-179), is based primarily on data in Section VI of a review by Woods.[4.9-5] He reports strength coefficients and strain hardening exponents derived from load elongation tests at temperatures from 300 to 783 K. Strain rates of 1.25×10^{-2} and 5×10^{-4}/s were used in the tests, and cladding samples with several different annealing histories were studied. Reciprocal pole figures were provided to specify the texture of each cladding group, but these figures are not sufficiently detailed to allow an accurate characterization of the texture. Considerable scatter has no doubt been introduced into the data base because the details of the material texture are not accurately known and because models for cold work effects had to be used to try to account for the different annealing histories of the samples.

Ultimate strength data from Bauer[4.9-27] have been used to supplement the data from Woods for the low temperature equation of state. These data were from well characterized cladding,[4.9-39] but the full stress-strain curve was not published. To use these data, a stress-strain law of the form of Equation (4-148) had to be assumed.

Since neither Woods nor Bauer reported strain rate sensitivities, data from tests on zircaloy sheet specimens were used for the low temperature correlation for the strain rate sensitivity exponent, Equation (4-164). The values of m obtained with zircaloy-2 plate by Mehan and Wiesinger[4.9-6] and those reported for zircaloy-4 plate in the transverse direction by Lee and Backofen[4.9-9] were employed.

With two important exceptions, which will be discussed in the next subsection, all of the correlations for plastic deformation above 783 K are based on ultimate strength, uniform elongation, and strain rate sensitivity measurements by Chung, Garde, and Kassner[4.9-20] and on ultimate strength data reported by Brassfield.[4.9-7] Such data are not satisfactory for deriving an equation of state because (a) the form of the equation of state must be assumed to use the data and (b) even if the assumed form of the equation of state is correct, the parameters obtained from those data in the alpha phase may apply to a mode of deformation not active when biaxial stress is applied. The high temperature data just discussed were used in MATPRO because there have been so few publications on biaxial isothermal measurements of stress and strain versus time at high temperature.

Equations (4-180) and (4-181) for the effects of cold work and irradiation on plastic deformation are based primarily on a study by Bement.[4.9-8] The study was conducted with well characterized zircaloy-2 plates irradiated to fast neutron fluences of 10^{25} fast n/m^2. The entire load elongation curve was used to deduce values of the strength coefficient and strain hardening exponent. Unfortunately, specimen irradiation was conducted at 333 K and testing was at room temperature. It is, therefore, possible that irradiation at reactor operating temperature produces different results.[4.9-40] For that reason, the data from this study were compared with limited and less well characterized data from Cowan and Langford[4.9-12] and Howe and Thomas.[4.9-10] The latter data were obtained from material irradiated at reactor operating temperatures. The load elongation tests of Reference 4.9-10 and Reference 4.9-12 were conducted at room temperature and 573 K.

The most applicable data for modeling the effect of irradiation and cold work are the measurements of ultimate strengths, yield strengths, and uniform elongation reported by Bauer.[4.9-26,4.9-28] His measurements were taken with cladding irradiated in the Carolina Power and Light H. B. Robinson reactor to fast neutron fluences of 4 x 10^{25}n/m^2. Testing was performed at 644 K. Unfortunately, Bauer was unable to test unirradiated samples from the lot of tubing they used. Use of this data must therefore rely on nominal preirradiated values of ultimate strength.[4.9-28]

The models for the effect of cladding oxidation on plastic deformation are based on ultimate strength data from Rubenstein[4.9-11] and additional work by Chung, Garde, and Kassner.[4.9-23] The tensile strength data by Rubenstein were measured at temperatures in the range 300 to 644 K and oxygen concentrations up to 6,330 ppm. Unfortunately, neither load elongation curves nor values of uniform elongation were published.

Chung, Garde, and Kassner[4.9-23] published constants based on a fit of stress strain data. The temperature range (1,123 to 1,673 K) and oxygen concentrations (0.46 to 1.10 wt% oxygen) make the data unique. An approximate model was developed by reformulating correlations so that they could be used in the MATPRO package.

4.9.2.3 Biaxial Test Data. Tube burst tests provide strain versus time data that are usable for stress versus strain modeling of multiaxial stress states. These experiments are important because it is possible that a change in the deformation mode under multiaxial stress will lead to a completely different equation of state for relating stress and strain under biaxial stress.

The earliest attempt at providing data for a biaxial stress strain law is the work of Hardy.[4.9-34] Zircaloy-4 cladding tubes were heated in an inert environment, and both temperature and internal pressure were recorded. The important feature of these tests is that tests with similar initial pressures and heating rates were stopped by venting internal pressure before burst temperature occurred. The posttest diameter measurements from tests with the same input conditions provide a reasonable measure of strain during a typical test. Only the diametral expansion was reported, so only one component of strain can be obtained from these tests. Their primary value is for checking predicted diametral strain versus time. At least two components of strain are needed to construct an (effective stress)-(effective strain) expression.

Similar biaxial data have been provided by Chung[4.9-23,4.9-24] using a laser and high-speed camera. In most cases, only diameter versus time was reported; but the data are a valuable supplement to Hardy's measurements of diametral strain versus time. In a few cases,[4.9-24] both diameter and length versus time were reported. Unfortunately, those cases include only preoxidized cladding; and it has been shown[4.9-23] that the presence of an oxide changes the properties of the composite specimen considerably.

The most useful data available to date are measurements of cladding diameter and length versus time by Hann.[4.9-2] The cladding is well characterized, and experimental details are discussed The principal difficulty with using these data are possible local effects variations in temperatures and cladding wall thickness, which will cause the measured strain to be an average of local strains. The published data from two of the tests described in Reference 4.9-2 have been analyzed and are discussed in Section 4.9.3.

4.9.3 Model Development

The equation of state used in MATPRO to provide a description of zircaloy cladding plastic deformation under tensile stress is based on the Holloman relation

$$\sigma = K\varepsilon^n \qquad (4\text{-}188)$$

where

σ = true effective stress (Pa)

K = strength coefficient (Pa)

n = strain hardening exponent (unitless)

ε = true effective strain (unitless).

Holloman's equation was modified to include the effect of strain rate because this parameter was found to be more important than strain in high temperature, uniaxial stress tests. The resultant form of the equation of state is

$$\sigma = K\varepsilon^{n}\left(\frac{\dot{\varepsilon}}{10^{-3}}\right)^{m} \tag{4-189}$$

where

$\dot{\varepsilon}$ = rate of change of true effective strain (s^{-1})

m = strain rate sensitivity exponent (unitless).

Several more complex relations between stress and strain have been proposed,[4.9-18,4.9-20,4.9-30] and a few highly simplified equations have been successfully employed in limited temperature ranges.[4.9-32,4.9-34] Equation (4-148) was selected because it is efficient for code use and consistent with available data

The following subsections discuss the development of equations for the coefficients of anisotropy used to determine effective stress and strain from their components. Equations (4-164) through (4-179) form, n, and K as a function of temperature are developed in Section 4.9.3.2. Section 4.9.3.3 discusses Equation (4-180) and (4-181) for the change in n and K with cold work and irradiation. Finally, Equations (4-182) through (4-184) for the effect of oxidation on the equation of state are developed in Section 4.9.3.4.

4.9.3.1 Coefficients of Anisotropy. The model for the effects of texture is based on Hill's quadratic expression for plastic potential[4.9-38] [for principal axes, Equation (4-150)]. As Hill and several others have pointed out, the expression implies that the effect of tensile stress is the same as compressive stress. Since compressive and tensile stress of equal magnitude produce different strains in zircaloy,[4.9-3] Hill's theory is not sufficient to model plastic strain for all states of stress. The theory has been used because (a) it is compatible with the mechanics package of the FRAPCON and FRAP-T codes[4.9-1] and (b) there are not enough data to modify Hill's theory in the temperature range from 500 to 1,255 K.

The constants A1S, A2S, and A3S in Equation (4-150) have been assumed to be proportional to the texture factors defined in conjunction with Equations (4-155) through (4-157) and to correspond to isotropic material in the beta phase. The assumption is ad hoc and intended to reflect the general observation that effective stress is smaller when stress is applied in directions with heavy concentrations of basal poles. Its justification is that it reduces the scatter in measured values of cladding strength for material with different textures, as discussed in Section 4.9.3.2.

The appropriate texture factor to use to estimate each anisotropy constant was determined simply by considering uniaxial tests. For example, in a test with $\sigma_2 = \sigma_3 = 0$ and σ_1 = axial stress, Equation (4-150) becomes

$$\sigma = \begin{matrix} (A1S + A3S)^{1/2}\sigma_z \\ \left[\frac{3}{2}(f_r + f_\theta)\right]^{1/2}\sigma_z \\ \left[\frac{3}{2}(1 - f_z)\right]^{1/2}\sigma_z \end{matrix} \qquad (4\text{-}190)$$

where the symbols have been defined previously. For a texture with basal poles strongly concentrated in the axial direction, f_z could be nearly 1.0 and the effective stress small. For the small values of f_z more characteristic of cladding, the effective stress would be relatively large.

For a perfect crystal, the empirical constants A1S, A2S, and A3S would imply that there is no deformation at all in the basal pole direction. Since twinning is known to occur and allow deformation along the basal pole direction, the estimated values of A1S, A2S, and A3S can be expected to overestimate the effect of texture when the largest stress differences in the expression for effective stress

$$\sigma = [1.5f_r(\sigma_z - \sigma_\theta)^2 + 1.5f_z(\sigma_\theta - \sigma_r)^2 + 1.5f_\theta(\sigma_r - \sigma_z)^2]^{1/2} \qquad (4\text{-}191)$$

multiply small texture factors.

The uniaxial stress tests by Busby[4.9-18] agree well with both the effective stress predicted by Equation (4-191) and with the strain ratios predicted when A1E, A2E, and A3E in Equations (4-152) through (4-154) are presumed to be equal to the anisotropy coefficients just discussed for effective stress. However, an analysis of recent experimental data at 811 and 1,089 K has indicated that the anisotropy coefficients given in Equation (4-191) are not appropriate for a closed tube burst test in the temperature range 800 to 1,090 K. For these tests, strain anisotropy coefficients derived from the data are characteristic of isotropic material for small strain but change rapidly with increasing strain. A similar result has been reported by Stehle.[4.9-35]

It is likely that the change in the strain anisotropy is due to a change in the physical mechanism of plastic deformation that is, in turn, caused either by increased temperature or the biaxial stress state of the data. The data that could be used to tell whether the important difference between Busby's tests and later tests is the temperature or the stress state were not published at the time of model development. If the stress state changes the mechanism of plastic deformation, a second equation of state and a second set of anisotropy coefficients would be required to describe this second mode of deformation.

An attempt has been made to include the second mode of deformation by defining experimentally determined strain anisotropy coefficients that are different than the texture related stress anisotropy coefficients previously discussed. The experimental data used to define the high temperature strain anisotropy coefficients are measurements of length, diameter, and internal pressure versus time for isothermal cladding burst tests at 810 and 1,089 K by Hann.[4.9-2] With the incompressibility assumption, the data can be used to calculate the three components of strain as a function of the stress components. With the additional assumption that the deformation of these samples was symmetric, at least during the early part of the test, plastic strain components were calculated and compared to the predictions of

Equations (4-152) through (4-154) using the texture determined values for A1E, A2E, and A3E. These predicted results were totally inconsistent with the measured strain components. However, consistent results were obtained by assuming that the constants A1E, A2E, and A3E were all initially 0.5. Moreover, if the anisotropy coefficients are interpreted as texture coefficients, the change in the anisotropy coefficients with deformation was consistent with the general rule suggested by Busby (Reference 4.9-18), i.e., that "the basal planes of zircaloy tend to become aligned parallel to the direction of positive (tensile) strain and perpendicular to negative (compressive) strain."

Unfortunately, a direct solution for A1E, A2E, and A3E from the measured strain components and Equations (4-152) through (4-154) is not possible. The equations are not independent, since the sum of the strain increments is zero. However, the assumption that the coefficients of anisotropy are proportional to the volume average of some texture coefficients gives another independent equation

$$A1E + A2E + A3E = 1.5 \quad . \tag{4-192}$$

With this relation, it is possible, in principle, to solve two of Equations (4-152) through (4-154) and Equation (4-192) in terms of stress and strain components. However, the expressions for $d\varepsilon$ and σ are complicated functions, so an alternate approach, taking $d\varepsilon/\sigma$ as a fourth unknown, was used. With this approach, the expressions for two of the three unknowns A1E, A2E, and A3E in terms of a third and measured stress and strain components are Equation (4-192) and

$$\frac{d\varepsilon_\theta}{d\varepsilon_z} = \frac{A1E(\sigma_\theta - \sigma_z) + A2E(\sigma_\theta - \sigma_r)}{A3E(\sigma_z - \sigma_r) + A1E(\sigma_z - \sigma_\theta)} \quad . \tag{4-193}$$

The idea that the basal poles of zircaloy should tend to become aligned in the direction of compressive strain leads to the conclusion that A2E, the coefficient proportional to the axial concentration of basal poles, should change very little because the axial strain observed in closed tube burst tests is small. With this assumption and using Equation (4-192), the increase in A1E and the decrease in A3E are of equal magnitude. Substitution of

$$A1E = 1/2 + \delta \tag{4-194}$$

$$A2E = 1/2 \tag{4-195}$$

$$A3E = 1/2 - \delta \tag{4-196}$$

into Equation (4-193) allows δ (and thus A1E, A2E, and A3E) to be determined from measured quantities.

Figure 4-31 shows the results obtained for the two tests from Reference 4.9-2 at 810 and 1,089 K. The increase in the anisotropy coefficient that has been assumed proportional to the effective concentration of basal poles in the radial direction (A1E) is approximately proportional to the radial compressive strain

in each test. The rate of change appears to increase with temperature. The expressions for the change of anisotropy coefficients with compressive strain, Equations (4-158) through (4-160), were obtained by least-squares fits to the two sets of data shown in Figure 4-31, assuming a linear temperature dependence. Extrapolation of this correlation to 644 K predicts no significant departure of the coefficients A1E, A2E, and A3E from their initial values until strains of about 0.15 are produced. This is the approximate strain for which Busby reported significant departure in his tests.

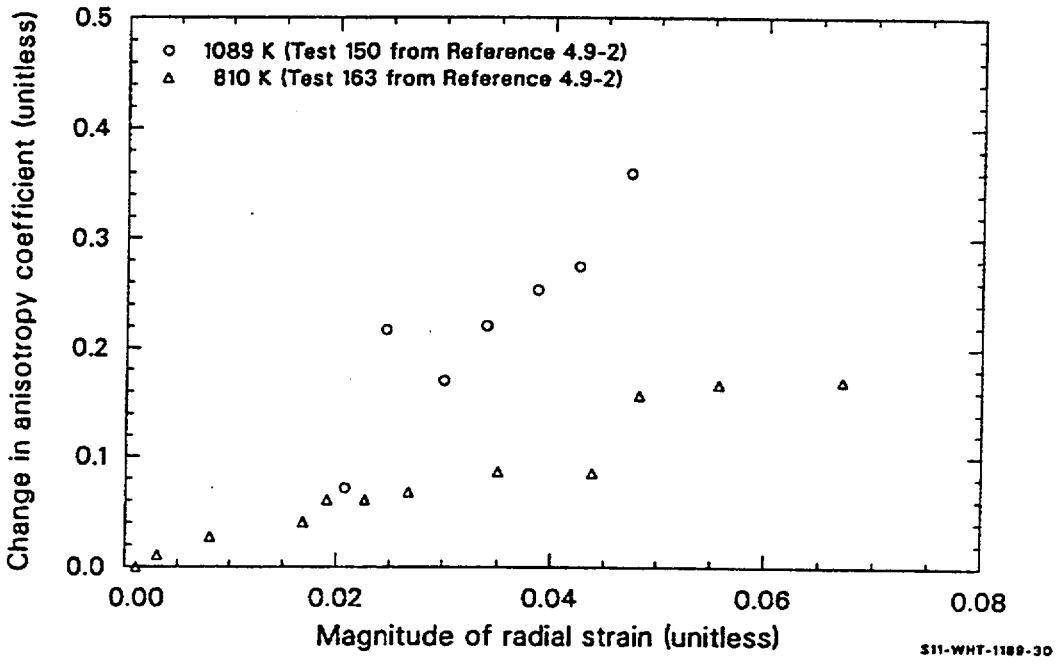

Figure 4-31. Increase of the strain anisotropy constant A1E as a function of radial compressive strain in two tests.

4.9.3.2 Plastic Deformation Parameters m, n, and K as Functions of Temperature. The strain rate sensitivity constant, m, of zircaloy-2 and zircaloy-4 was evaluated with data obtained from Reference 4.9-5, Reference 4.9-6, Reference 4.9-9, Reference 4.9-16, and Reference 4.9-20. The data are plotted in Figure 4-32. Most of the values of m at temperatures higher than 900 K were given in Reference 4.9-20 as a function of engineering strain for strain rate changes centered around 10^{-3}/s. No significant dependence on strain was indicated, so m is modeled without strain dependence. Outside the $\alpha - \beta$ phase transition region (taken as from 1,090 to 1,255 K), significant dependence of m on strain rate again was not observed. Within the $\alpha - \beta$ transition region and at strain rates below 6.34×10^{-3}, m was a strong function of the strain rate.

In the MATPRO plastic deformation models, values of m from data taken at temperatures below 730 K are approximated with a constant (m = 0.02), while data for temperatures above 900 K and outside the $\alpha - \beta$ phase transition region are modeled as a linear function of temperature. The value of m in the region from 730 to 900 K is modeled by a third-degree polynomial in temperature with the constants determined so that the values and slopes of the polynomial match the values and slopes of the expressions form outside the boundaries of the 730 to 900 K region. The values of m predicted by Equations (4-164) through (4-171) are illustrated in Figure 4-32, along with the data. The two points at 561 K are particularly interesting

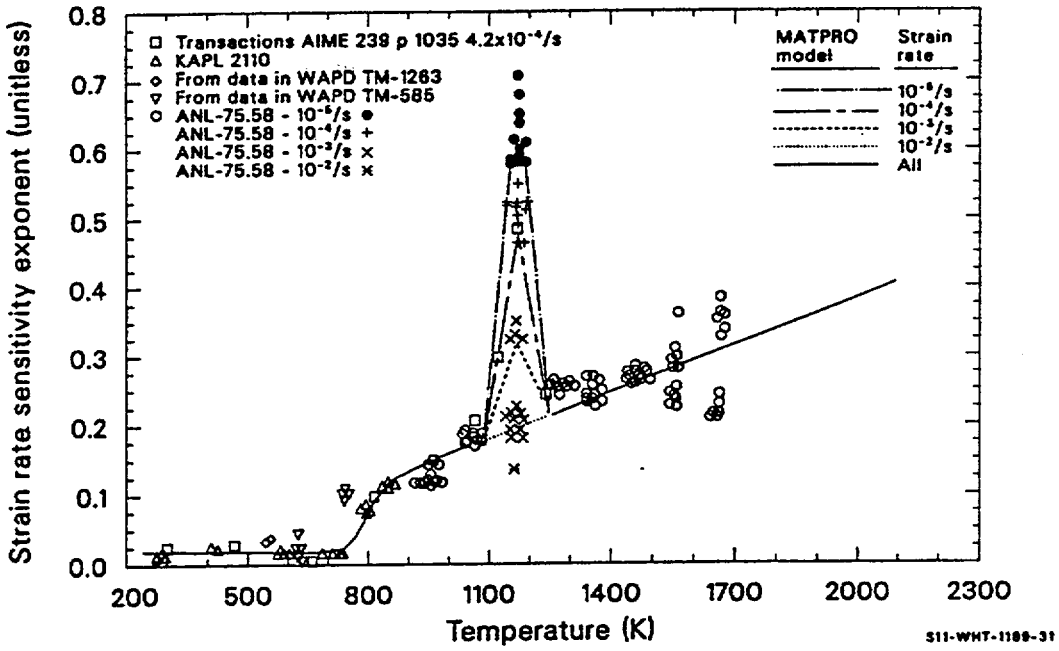

Figure 4-32. Strain rate sensitivity exponent as a function of temperature and strain rate.

because they are estimates based on high-strain-rate (4/s) tests with irradiated material. They do not appear to be significantly different from the values of m obtained at lower strain rates with unirradiated material.

Most of the values of m in the $\alpha - \beta$ transition region were also obtained from data presented in Reference 4.9-20. The strain-rate-dependent values measured at 1,173 K were assumed to reflect an additive increase in m due to the mixed phases. When the increase is plotted against the logarithm of the strain rate, the effect of varying strain rates on m can be closely approximated by a straight line of the form

$$\Delta m = 0.1253 + 0.1562 \log (10^{-3} s^{-1} / \text{STRAIN RATE}) \qquad (4\text{-}197)$$

which was obtained by a least-squares fit to the data. The fit is illustrated in Figure 4-33. For strain rates outside the range 10^{-5}/s to 6.34×10^{-3}/s, the change in m is taken to be equal to its value at the nearest point of this range.

In this model, it is assumed that m increases linearly from its value at the edges of the $\alpha - \beta$ transition region to a maximum at 1,172.5 K in the center of the region, as shown in Figure 4-32. Additional data on values of m as a function of temperature and strain rate in the $\alpha - \beta$ transition region will be required if this approximation is to be refined. However, the need for such refinement is questionable, at least until biaxial data confirm a similar effect.

Values of the strain hardening exponent, n, as a function of temperature from room temperature to 755 K are based on data from tensile tests on zircaloy-4 tubes.[4.9-5] The data and the values of n predicted by the MATPRO correlation Equations (4-172) through (4-174) are shown in Figure 4-34. At temperatures

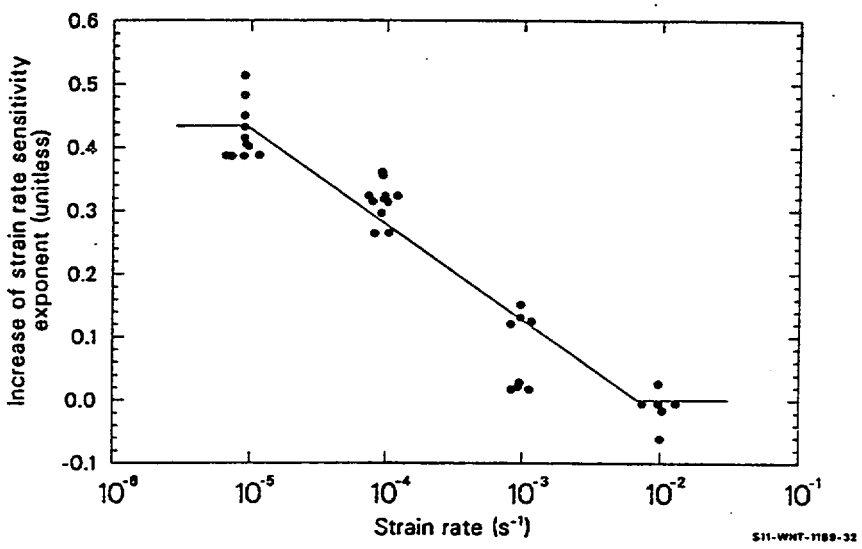

Figure 4-33. Increase of the strain rate sensitivity exponent at 1,173 K as a function of strain rate based on Chung, Garde, and Kassner's data.

above 850 K, the only datum from a full stress strain curve is the point from EPRI NP526.[4.9-2] This value was obtained by a double regression fit to data derived from EPRI Test 150. The majority of the estimates for the high temperature strain hardening exponent are simply the values of uniform strain reported by Garde.[4.9-20] Use of the uniform strain as an estimate is based on the theoretical result that the maximum force in a uniaxial test on a material which obeys Equation (4-148) will occur at a strain of n/(1 + m).

The very large value of n at 811 K was obtained from a double regression analysis of EPRI Test 163, which will be discussed in more detail later in this subsection. The large value of n is either due to an unfortunate feature of the double regression fitting technique or an indication that the stress-strain law for cladding plastic deformation is significantly different when biaxial (closed tube burst tests) rather than uniaxial stress drives the deformation.

Equations (4-176) through (4-179) for the strength coefficients, K, of fully annealed, isotropic cladding are based on uniaxial tests of cladding,[4.9-5,4.9-27] on a uniaxial plate test,[4.9-20] and on two closed tube burst tests.[4.9-2] For the low temperature data, the effects of varying amounts of cold work and stress relief in the tubing tested were removed prior to including the measured values of K in the data base. This was done by using the cladding annealing model discussed in Section 4.10 and the models for the effects of irradiation and cold work, which will be described in the next subsection. The effects of different strain rates were similarly removed with the model discussed in previous paragraphs of this section.[a]

The strength coefficients based on uniaxial tests of cladding were modified to apply to isotropic cladding using the empirical anisotropy coefficients discussed in the previous subsection. This was done by substituting values of effective stress from Equation (4-150) and values of effective strain from Equation (4-152) into the equation of state, Equation (4-148) to obtain

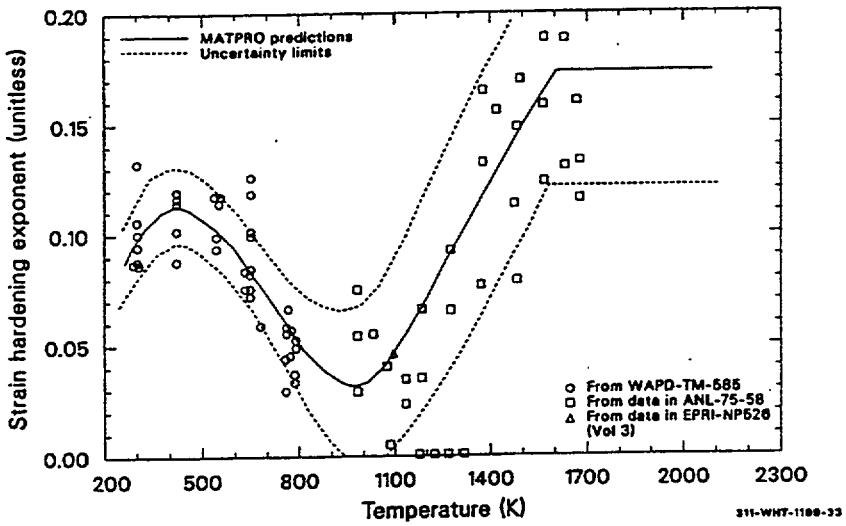

Figure 4-34. Base data, MATPRO prediction, and uncertainty estimate for strain hardening exponent of annealed tubes.

$$\sigma_z = \left[\frac{K}{(1.5f_r + 1.5f_\theta)^{\frac{(1+m+n)}{2}}}\right]\varepsilon_n^z\left[\frac{\dot{\varepsilon}_z}{10^{-3}}\right]^m \quad . \tag{4-198}$$

Thus, the isotropic strength coefficient is related to the strength coefficient determined in a uniaxial test by the expression

$$K = K_{\text{axial test}}\,(1.5f_r + 1.5f_\theta)^{1+m+n/2} \quad . \tag{4-199}$$

This approach is different than the usual practice of taking the uniaxial test as the equation of state.[4.9-41] The new approach reduces the scatter in values of K because the texture of the material being tested is considered.

---

a. Strain rate effects and annealing effects were removed from K by redefining K' (from the expression $\sigma = K'\varepsilon^m$)[4.9-5] as

$$K' = K\left[\frac{\dot{\varepsilon}}{10^{-3}s^{-1}}\right]^m$$

Then, the fractional change in K expected from varying amounts of cold work and annealing was removed to give values for the K of annealed tubing consistent with the model for the effects of cold work and annealing.

Unfortunately, values of f_r and f_θ were not given in Reference 4.9-5, so estimated values based on the texture factors were employed. The approximation that worked best to reduce the scatter in values of the strength coefficient was

$$f_r + f_\theta = 1 - [\text{axial (0.02) texture coefficient}]/4 \ . \qquad (4\text{-}200)$$

The factor of 1/4 was determined by requiring the sum of the axial, tangential, and radial (002) texture coefficients of Reference 4.9-5 to be approximately 1.5 (f factors sum to1).

The base data and the values of the strength coefficient predicted by the MATPRO correlation of the strength coefficient Equations (4-176) through (4-179) are shown in Figure 4-35. Discontinuities in the slope of the predicted strength coefficient as a function of temperature occur at 750, 1,090, and 1,255 K.

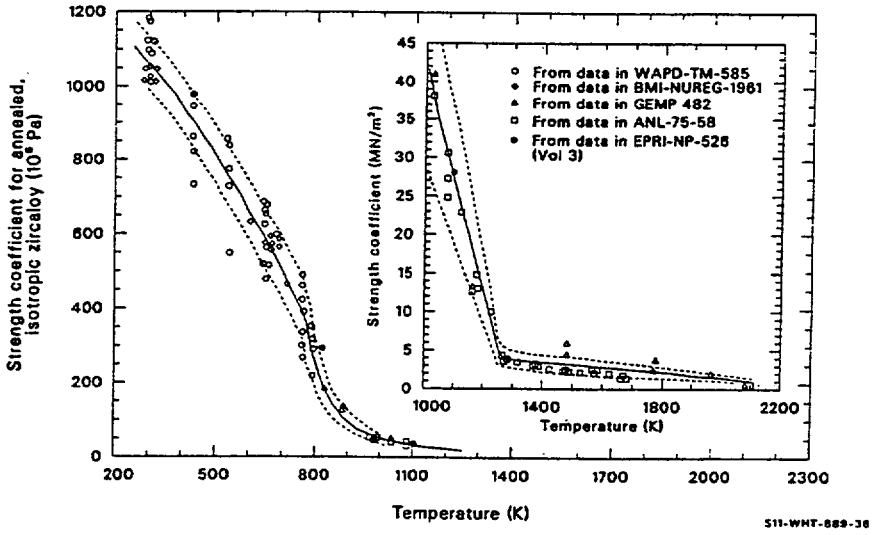

Figure 4-35. Base data, MATPRO prediction, and uncertainty estimate for strain coefficient of annealed, isotropic cladding.

Values of the strength coefficient from BMI-NUREG-1961,[4.9-27] GEMP-482,[4.9-7] and ANL-75-58[4.9-20] were calculated from ultimate tensile strengths (presumed equal to maximum engineering strength at constant engineering strain rate). To estimate $K_{\text{axial test}}$, the axial stress and strain rate are converted to their engineering equivalents,[a] the true strain at maximum engineering stress is found,[b] and this true strain is substituted into Equation (4-148) to find

a. Engineering stress = true stress x exp (true strain) inside the exp of the first equation, true strain rate = engineering strain rate x exp (true strain).

b. The true strain at maximum engineering stress with constant engineering strain rate is 1 = m/n.

$$K_{axialtest} = \frac{S_{max}\exp\left(\frac{n}{1+m}\right)}{\left(\frac{n}{1+m}\right)^{m}\left[\dot{e}\exp\left(-\frac{n}{1+m}\right)\times 10^{3}\right]^{m}} \quad (4\text{-}201)$$

where

S_{max} = maximum engineering stress (Pa)

$\dot{e}$ = engineering strain rate (s^{-1}).

This approach is not very satisfactory because it neglects possible necking of the test sample. It is used because true stress/true strain curves were not available.

The most important strength coefficient data shown in Figure 4-35 are the two values determined from data in EPRI NP-526, Volume 3.[4.9-2] These strength coefficients were determined with a least squares regression technique that found the values of K, n, and m of Equation (4-148) that best fit the measured values of the stress and plastic strain.[a]

As previously discussed, the anisotropy coefficients calculated from strain components did not agree with the anisotropy coefficients determined from the materials texture. An effort was made to construct a plastic deformation equation of state by assuming that the experimentally determined strain anisotropy coefficients were also the stress anisotropy coefficients. This approach leads to strength coefficients of 469 MPa at 810 K and 32.9 MPa at 1,089 K--results that differ from the uniaxial strength coefficients significantly. With this approach, a second equation of state is required; but there were only two tests available and no useful model could be produced. The approach was, therefore, abandoned; and it was assumed that stress anisotropy coefficients are different than strain anisotropy coefficients at high temperatures. The anisotropy coefficients determined from material texture were used for stress, and the experimentally determined strain anisotropy coefficients were retained for strain only. The corresponding values of strength coefficients were 360 MPa at 810 K and 27.9 MPa at 1,089 K--results consistent with the uniaxial strength coefficients.

The most plausible explanation of these results is that the kind of deformation assumed in Equation (4-191) does not occur because some other mode is activated first. The physical arguments for this explanation have been advanced by Picklesimer.[4.9-3] If the empirical anisotropy coefficients in Equation (4-183) are considered acceptable, then Picklesimer's ideas are confirmed by the fact that (a) the largest shear stress for $\sigma_\theta \approx 2\sigma_z$ and $\sigma \approx 0$ in Equation (4-191) is multiplied by a very small texture coefficient, f_z, and (b) the strength coefficients found when experimentally determined anisotropy coefficients are used to calculate effective stress are larger than those calculated for basal plane slip. The first fact means that basal plane slip is not likely in the EPRI tests because of the relationship between the applied stress and the material texture. The second fact means that the second mode of deformation will be seen only when the

a. Elastic strains were calculated with the CELAST model and subtracted from the total strain components.

effective stress for basal plane slip is low, because the second mode produces much less strain than the basal plane slip when the effective stresses for the two modes are equal.

Unfortunately, this interpretation cannot yet be exploited because the two sets of values for K, n, m, and the anisotropy coefficients are also the only values available to use to construct an equation of state for the second mode of deformation in the temperature range from 600 to 1,255 K The values of K obtained with effective stresses calculated from Equation (4-191) have thus been incorporated into the data base for MATPRO (after the 810 K value was corrected for cold work effects) to help force reasonable predictions even though the model is probably incomplete.

4.9.3.3 Irradiation and Cold Work Effects. Irradiation and cold work effects on cladding plastic deformation have been incorporated into the equation of state for plastic deformation by repeating the analysis discussed in Section 4.9.3.2 for uniaxial tests and noting the changes in the strain rate sensitivity exponent (m), the strain hardening exponent (n), and the strength coefficient (K) with varying amounts of cold work and irradiation. No change in the strain rate sensitivity exponent with irradiation or cold work was found, but the other two parameters did vary with both cold work and irradiation. The effect of cold work on K and n will be discussed first, followed by the effect of irradiation.

Strength coefficients from Reference 4.9-8 are plotted in Figure 4-36. Although texture effects are evident in annealed material and irradiation does tend to increase the strength coefficient slightly, the dominant correlation is a linear increase in the strength coefficient with cold work. A linear least squares fit yields the room temperature correlation

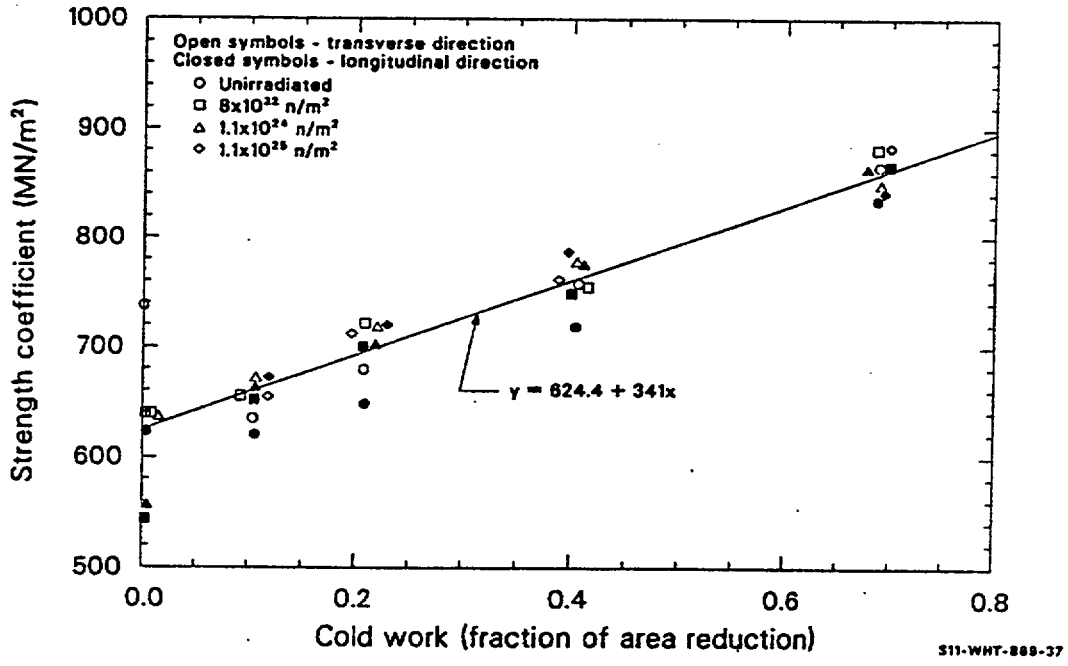

Figure 4-36. Data and least squares fit to strength coefficients as a function of cold work and irradiation at room temperature.

$$K' = 624.4 + 341\ CWK = 624.4\ (1 + 0.546\ CWK) \quad (4\text{-}202)$$

where

CWK = the cold work for strength coefficient

K' = strength coefficient at room temperature (MN/m^2).

To estimate the effect of temperature on this correlation, values of the strength coefficient determined from the limited data from Reference 4.9-10 and Reference 4.9-12 at temperatures of 553 and 573 K were also fit to a straight line, with the resultant correlation

$$K' = 373 + 238\ CWK = 373\ (1 + 0.64)\ CWK\ . \quad (4\text{-}203)$$

Comparison of the two results show that they are consistent with a temperature dependent expression of the form

$$K' = K\ (T)\ [1 + \text{constant}\ CWK] \quad (4\text{-}204)$$

where K(T) is the temperature dependent function describing the behavior of the strength coefficient of annealed zircaloy [Equations (4-176) through (4-179)]. The form of Equation (4-204) has, therefore, been assumed. The constant coefficient of the cold work is taken to be 0.546, as determined at room temperature, because the room temperature data exhibit much less scatter than the high temperature data taken from several different sources.

Figure 4-37 illustrates the effect of cold work and irradiation on the strain hardening exponent, n, as determined at room temperature in Reference 4.9-8. The strain hardening exponent of unirradiated material shown in Figure 4-37 can be described by the empirical relation

$$n = 0.11 \exp(-39.2\ CWN) + 0.03(CWN)^2 - 0.12(CWN) + 0.021 \quad (4\text{-}205)$$

where CWN is the effective cold work for the strain hardening exponent. This expression is essentially a decreasing exponential function for small values of cold work and a slowly increasing parabola for large values of cold work.

At higher temperatures, trends exhibited by the limited and scattered values of n (which have been obtained at 553[4.9-12] and 573K[4.9-10]) are consistent with the assumption that the fractional changes in n with cold work are similar to the fractional changes in n at room temperature. The following functional relationship is assumed in the present model

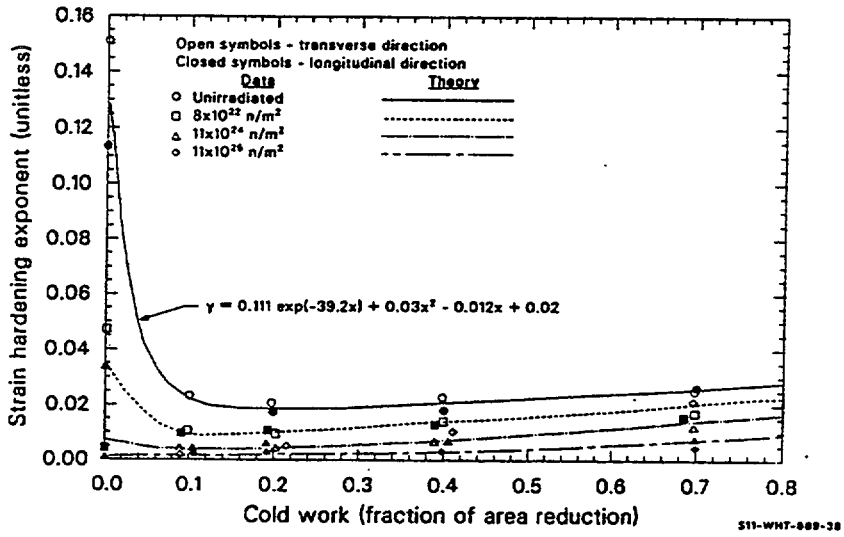

Figure 4-37. Data and analytical functions for strain hardening coefficient as a function of cold work and irradiation at room temperature.

$$n(T, \text{cold work}) = n(T)\frac{n(\text{cold work})}{n(\text{at 0 cold work})} \quad . \tag{4-206}$$

When the expression for n as a function of cold work given by Equation (4-205) is substituted into Equation (4-206), the following expression is obtained:

$$n = n(T)\frac{0.11\exp[-39.2(CWN)] + 0.03CWN^2 - 0.012CWN + 0.021}{0.132} \tag{4-207}$$

where n(T) is given by Equations (4-172) through (4-174).

The data from Reference 4.9-8 plotted in Figure 4-36 show little effect of irradiation on the strength coefficient. However, the irradiation of these samples were conducted at 333 K, and it is probable that irradiation at reactor operating temperature produces different results.[4.9-40]

The most applicable data for modeling the effect of irradiation on cladding are the measurements of ultimate strength and uniform elongation reported by Bauer.[4.9-26,4.9-28] Their measurements were taken with cladding irradiated in the Carolina Power and Light H. B. Robinson Reactor to fast neutron fluences of 4×10^{25} fast n/m^2. Testing was performed at 644 K. Unfortunately, they were unable to test unirradiated samples from the lot of tubing they used, so use of their data must rely on nominal preirradiated ultimate strengths.[4.9-28]

Bauer's data are most representative of in-reactor irradiation damage and are, therefore, used instead of the data from Reference 4.9-8 to find an expression for the effect of irradiation on temperature. Strength coefficients for irradiated cladding at 644 K were determined with Equation (4-201) and tensile test results given in Table I of Reference 4.9-26 (samples P8-20, P8-34, and P8-46). Equations (4-176) and (4-204) were then used to estimate the strength coefficient for annealed cladding and the cold work contribution to the strength coefficient (for typical cold work of 0.5) at 644 K. The difference between the strength coefficient of the irradiated material and the predicted strength coefficient of cold worked material is presumed to be due to irradiation effects. Furthermore, the effect of irradiation is assumed to be proportional to the fast neutron fluence. The second term of Equation (4-181) resulted from these assumptions.

At present, the best evidence in support of a linear dependence of K on fast neutron fluence is the fact that the small effect of irradiation on the samples of Reference 4.9-8 is not inconsistent with the predictions of Equation (4-181) for the relatively low fluences reported in that reference.

The effect of irradiation on the strain hardening exponent, n, is complex. Figure 4-37 shows that the fractional change in n due to irradiation at 333 K is large in annealed material and somewhat less in material that has been heavily cold worked. Furthermore, the effect of irradiation is highly nonlinear. Increasing amounts of irradiation produce continually decreasing changes in n.

These features are described empirically in the irradiation model by expressing the ratio of the value of n after irradiation to the value of n before irradiation as an exponential multiplier with a moderating cold work dependent term in the argument of the exponent. The strain hardening exponent of irradiated material is then

$$n = n\,(\text{unirradiated})\,\exp\left[-(\text{fluence})^{1/3}/(A + BCWN)\right] \qquad (4\text{-}208)$$

where

$$A = 3.73 \times 10^{7}\ (n/m^2)^{1/3}$$

$$B = 2.0 \times 10^{8}\ (n/m^2)^{1/3}$$

and n (unirradiated) is defined in Equation (4-207).

4.9.3.4 Effects of Oxygen. The effects of oxygen on cladding plastic deformation have been incorporated into the equation of state for plastic deformation by developing correlations for the changes in the strength coefficient, the strain hardening exponent, and the strain rate sensitivity exponent with increasing oxygen content. The derivation of the expressions for the change in the strength coefficient is presented first, followed by a discussion of the effects of oxygen on the strain hardening exponent and the strain rate sensitivity exponent.

4.9.3.4.1 *Effect of Oxygen Concentration on the Strength Coefficient*--There are no data that may be used directly to find the influence of oxygen on the strength coefficient. However,

data do exist that may be manipulated to yield this information. Because different types of data are available for high and low temperatures, different analytical techniques were used for these temperature ranges and the analyses are presented separately.

(1) Low Temperature Strength Coefficient Data. In the range 300 to 650 K, which includes typical LWR operating temperatures, the effect of oxygen concentration may be obtained from measurements of the change in the ultimate tensile strength (UTS) of zircaloy as a function of oxygen content. The true strain at maximum engineering stress, that is, the engineering stress at the onset of plastic instability in a tensile test on sheet specimens at constant strain rate, is given by Equation (4-201), which is rewritten here for convenience

$$K = \frac{S_{max}\exp\left(\frac{n}{1+m}\right)}{\left(\frac{n}{1+m}\right)^{m}(\dot{\varepsilon}\times 10^{3})^{m}} \qquad (4\text{-}209)$$

where S_{max} is the ultimate tensile strength in a tensile test (Pa). When ε was specified in the data, it was 10^{-3}/s. Since 10^{-3}/s is a typical value for ε in tensile tests, this value was assumed when not specified. In this case, Equation (4-209) reduces to

$$K = S_{max}\left[\frac{\exp\left(\frac{n}{m+1}\right)}{\left(\frac{n}{m+1}\right)^{n}}\right] . \qquad (4\text{-}210)$$

A paper by Rubenstein[4.9-11] gives values for the UTS as a function of oxygen concentration for temperatures ranging from about 300 to 650 K. For this range, MATPRO estimates an m of 0.02 for as received zircaloy. Therefore, m has very little effect on the value of K calculated with Equation (4-209) and can be neglected. The value for n predicted by MATPRO varies from 0.119 to 0.144 in this temperature range, causing the term $\exp(n)/n^n$ of Equation (4-210) (with m = 0) to vary from 1.45 to 1.53. If this term is replaced by 1.49 for all temperatures, the maximum error introduced is smaller than 3%, which is substantially less than the scatter in the data. Therefore, the strength coefficient in this temperature range has been calculated by simply multiplying the UTS by 1.49. Strength coefficients calculated in this way using data taken from Rubenstein are presented in Table 4-25. The lowest concentration for each temperature (9×10^{-3} weight fraction) was assumed to be the concentration of the as-fabricated zircaloy. With this information, the ratio K/K_o, where K_o is the strength coefficient of as received zircaloy, may be calculated; and these data are also shown in the table.

Table 4-25. Strength coefficient calculated with data of L. S. Rubenstein.

Temperature (K)	Oxygen content (weight fraction)	Ultimate tensile srength (MPa)	Calculated K (MPa)	K/K_o
297	0.0009	524	781	1.00
297	0.0018	616	918	1.18
297	0.0034	785	1,170	1.50
297	0.0063	949	1,414	1.81
422	0.0009	354	527	1.00
422	0.0034	544	811	1.54
422	0.0063	680	1,013	1.92
533	0.0009	266	396	1.00
533	0.0018	298	444	1.12
533	0.0034	361	538	1.36
533	0.0063	462	688	1.74
644	0.0009	227	338	1.00
644	0.0018	241	359	1.06
644	0.0034	283	422	1.25
644	0.0063	373	556	1.64

*(2) **High Temperature Strength Coefficient Data.*** All of the information used to model the effects of oxygen concentration on the high temperature plastic deformation of zircaloy was taken from a report by Chung, Garde, and Kassner,[4.9-23] of Argonne National Laboratory. Rather than reporting the stress associated with a given strain, however, the Argonne group made a computer fit of their data to a flow curve equation known as the Ludwik equation,[4.9-41]

$$\sigma = K\varepsilon^n + \sigma_0 \tag{4-211}$$

and reported only the parameters K, n, and σ_0 for many different strain intervals and oxygen concentrations. The additional variable, σ_0, will cause the stress, σ, resulting from Equation (4-211) for a given ε to differ from that of Equation (4-150) for the same K and n.

The Argonne curves generally start at strains of 0.0004, and their data are fit accurately to the Ludwik equation by dividing the flow curve into two or three strain intervals with different values of K, n, and σ_0 for each interval. There are scattered examples in the Argonne results, indicating that this approach may be inappropriate for small strains. In several of these cases, $\sigma < 0$. Since σ_0 can be interpreted as the yield stress,[4.9-41] a negative value indicates a physical inconsistency. To avoid these problems, the Argonne correlations were used only for strains greater than an arbitrarily chosen minimum of 0.002.

To get a base for a model, data were generated using Equation (4-211) and fit to Equation (4-150) (the Holloman equation). The strain interval (from 0.002 to the maximum reported strain) was divided into 20 equally spaced intervals for each temperature oxygen content combination. The Ludwik equations were then used to find a stress associated with each strain, and the resulting stress strain pairs were fit by the method of least squares to the Holloman equation. Only those tests where $\varepsilon = 10^{-3}$/s were used. This included 82 equations describing 60 different samples. The fluctuations in the resulting strength coefficient and the strain hardening exponent were much smaller for the Holloman equation than they were for the Ludwik equation.

For these derived data, the ratio (K/K_o) was calculated, as was done with the low temperature data. As with the Rubenstein data, (K/K_o) increases with oxygen concentration for all temperatures.

(3) Correlation for the Effect of Oxygen Concentration on the Strength Coefficient. Because little is known about the physical mechanism causing the strength coefficient of zircaloy to change with oxygen concentration, a model based on theory is not possible. An empirical fit to the data is, therefore, the approach chosen. In addition to fitting the data, the correlation should satisfy the obvious condition that $(K/K_o) = 1$ when $C = C_o$. A quite simple correlation that does this is

$$K/K_o = 1 + a(C - C_o) \qquad (4\text{-}212)$$

where

C = oxygen concentration (weight fraction)

C_o = oxygen concentration of as received zircaloy (weight fraction)

a = a function of temperature to be determined $(\text{weight fraction})^{-1}$.

An equation of the form of Equation (4-212) for each temperature was generated by a least squares fit technique using the data. The results are presented in Table 4-26.

Table 4-26. Rate of change of K/Ko with oxygen content.

Temperature (K)	a
297	160
422	178
533	137
644	115
1,123	89
1,173	95
1,223	343
1,273	541
1,323	676
1,373	891
1,673	1116

The ratio (K/K_o) derived from Equation (4-212) is plotted as a function of oxygen concentration for all temperatures used in Figure 4-38. The data from Table 4-26 are shown in the same figure. The six lowest temperatures are represented by a single line with a = 130 because they are too close together to be distinguishable.

The general characteristics of the temperature dependence of a are that it is relatively constant until about 1,200 K, rises rapidly between 1,200 and 1,400 K, and then begins to level off. The leveling off is based on only the data point at the highest temperature. However, there are too few data to justify a sophisticated correlation. A single function can be found which fits the data with acceptable accuracy over the entire temperature range, thus having the advantages of automatically avoiding discontinuities and fitting compactly into a computer routine. For $300 < T < 1{,}673$ K, the function is

$$a = 1120 - \frac{990}{\exp\left[\frac{(T - 1301.5)}{61}\right] + 1} \qquad (4\text{-}213)$$

Equation (4-213) is plotted as the function of temperature in Figure 4-39, where it is compared with the data from Table 4-26.

A comparison of the values of (K/K_o) predicted by Equations (4-212) and (4-213) with the data shows that the average percentage error is 12%. All the points except those at 1,123 and 1,173 K have

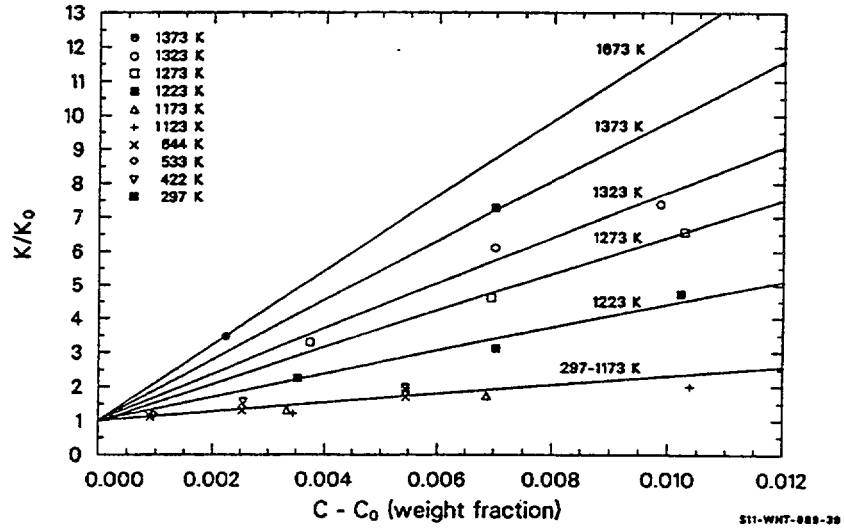

Figure 4-38. Calculated ratios of the strength coefficients of zircaloy, containing oxygen (K) and the strength coefficients of as fabricated zircaloy (K_0) as a function of oxygen concentration for several temperatures.

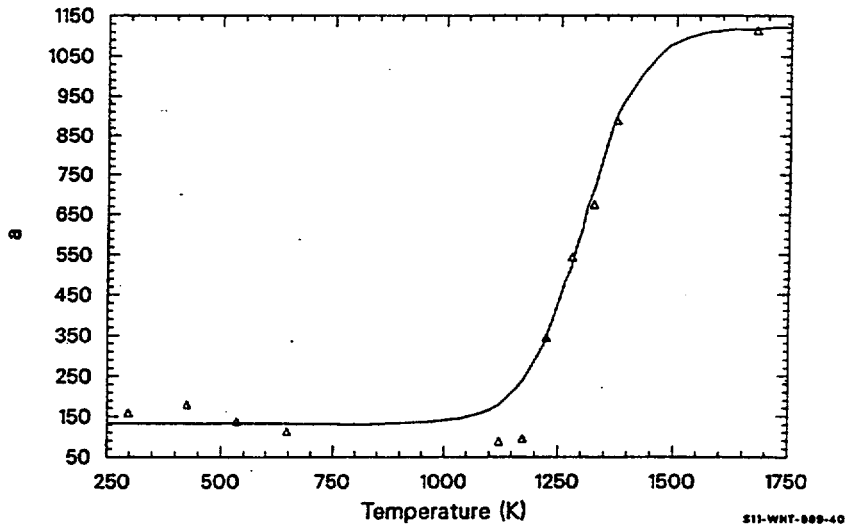

Figure 4-39. Calculated curve and data showing the rate of change of the zircaloy strength coefficient with oxygen content as a function of temperature.

percentage errors of this size or less. At these two temperatures, the average percentage error is 45%. These uncertainties can serve only as a rough guide in assessing the accuracy of the model, since they were calculated by comparing the correlation to its own data base.

4.9.3.4.2 ***Effect of Oxygen Concentration on the Strain Hardening***--The methods of development and the form of the equations used to correlate oxygen content with changes in the strain hardening exponent, n, are identical to those used for the analogous changes in the strength coefficient.

(1) High Temperature Strain Hardening Exponent Data. The only data available are those from Chung, which were all taken at high temperature.

(2) Correlation for the Effect of Oxygen Concentration on the Strain Hardening Exponent. The ratio(n/n_o) is modeled using the equation

$$n/n_o = 1 + b(C - C_o) \tag{4-214}$$

where b is a function of temperature to be determined. A fit of Equation (4-214) to the data gives the value for b listed in Table 4-27.

Table 4-27. Rate of change of n/n_o with oxygen content.

Temperature (K)	b
1,123	-19.0
1,173	4.9
1,223	-12.7
1,273	-11.1
1,323	340.0
1,373	244.3
1,673	1,245.0

The lines given by Equation (4-214) using the values of b listed in Table 4-27 are plotted in Figure 4-40 with their data bases.

The data presented in Table 4-27 and Figure 4-40 show considerable scatter. It is possible that this is a reflection of actual physical processes. Systematic oscillations in such things as the total strain at failure and the strain at maximum engineering stress have been repeatedly documented in the Argonne Quarterly Reports,[4.9-22,4.9-23 to 4.9-26] and these oscillations may be due in part to variations in the strain hardening exponent. More data are needed to accurately quantify these variations. Therefore, only the general

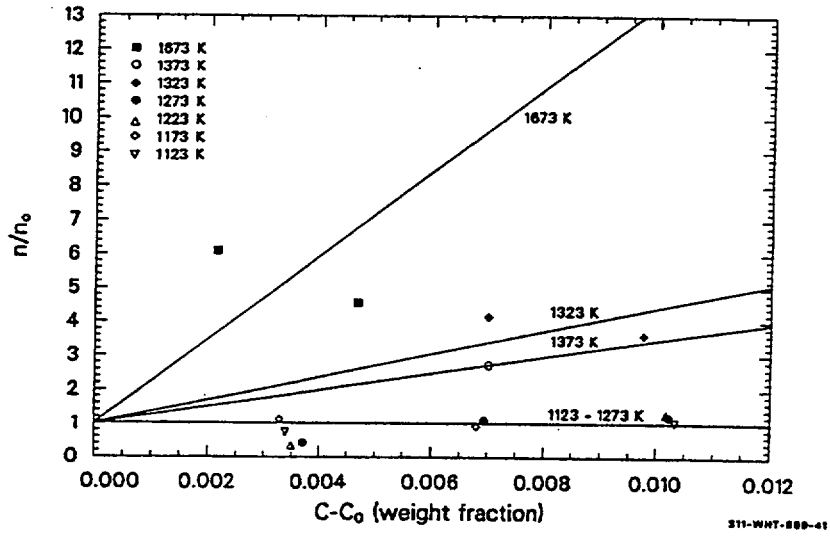

Figure 4-40. Calculated ratios of the strain hardening exponents of zircaloy containing oxygen (n) and the strain hardening exponents of as-fabricated zircaloy (n_0) as a function of oxygen concentration for several temperatures.

features of the coefficient b in Equation (4-214) are treated in the model. It is small below about 1,300 K, rises rapidly between 1,300 and 1,400 K, and then levels off about 1,500 K. The function used is

$$b = 1250 - \frac{1250}{\exp\left[\frac{(T-1380)}{20}\right] + 1} \qquad (4\text{-}215)$$

for $1{,}123 < T < 1{,}673$K.

Equation (4-215) is plotted in Figure 4-41, where it is compared with the data from Table 4-27.

At temperatures below 1,100 K, b calculated with Equation (4-215) is negligibly small, so that $(n/n_0) = 1$. This means that the strain hardening exponent is unchanged by the presence of oxygen. Therefore, the lower limit of the model may be extended down to operating temperatures without affecting the stress-strain laws now in MATPRO.

The uncertainty in the predictions of Equations (4-214) and (4-215) when compared with the data base is quite large. The one standard deviation limits are ± 42%. There are two data which are in error by more than 100%; but since the data indicate that the strain hardening exponent changes by a factor of five or more in some cases, the model is certainly better than entirely neglecting oxygen effects.

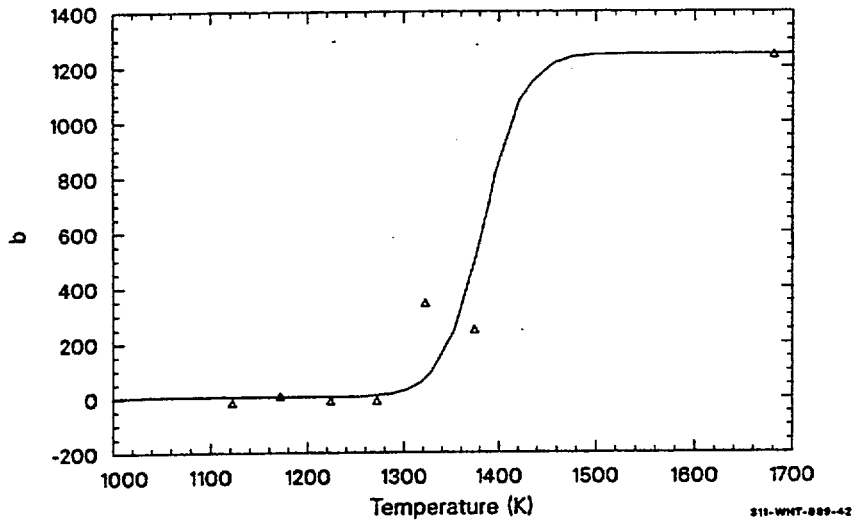

Figure 4-41. Calculated curve and data showing the rate of change of the zircaloy strain hardening exponent as a function of temperature.

4.9.3.4.3 ***Effect of Oxygen Concentration on the Strain Rate Sensitivity Exponent***–As with the strength coefficient and the strain hardening exponent, the data used for determining the effect of oxygen concentration on the strain rate sensitivity exponent of Equation (4-150) are taken from Chung. In this case, however, the data may be used directly, since they are consistent with the Holloman equation, Equation (4-150), as will be shown in the next subsection.

(1) Experimental Technique. Chung[4.9-19] measured m by quickly changing the strain rate during a stress strain test, causing a change in the stress, σ. If the change occurs rapidly, the strain itself does not change significantly during the transient, and m may be found from the equation

$$\left(\frac{\sigma_1}{\sigma_2}\right) = \left(\frac{\dot{\varepsilon}_1}{\dot{\varepsilon}_2}\right)^m \tag{4-216}$$

or

$$m = \frac{\ln\left(\frac{\sigma_1}{\sigma_2}\right)}{\ln\left(\frac{\dot{\varepsilon}_1}{\dot{\varepsilon}_2}\right)} \tag{4-217}$$

where

σ_1 = stress immediately before the transient (Pa)

σ_2 = stress immediately after the transient (Pa)

$\dot{\varepsilon}_1$ = strain rate before the transient (s^{-1})

$\dot{\varepsilon}_2$ = strain rate after the transient (s^{-1}).

Taking the logarithm of both sides of Equation (4-148) for two cases with different stresses and strain rates, but the same strain,

$$\ln(\sigma_1) = \ln(K) + n[\ln(\varepsilon)] + m(\ln(\varepsilon_1)) - m(\ln(10^{-3})) \quad (4\text{-}218)$$

$$\ln(\sigma_2) = \ln(K) + n[\ln(\varepsilon)] + m(\ln(\varepsilon_2)) - m(\ln(10^{-3})) \quad (4\text{-}219)$$

Subtracting Equation (4-219) from Equation (4-218) yields Equation (4-217)), so the strain rate sensitivity exponents measured by Chung may be used directly in Equation (4-148).

*(2) **High Temperature Strain Rate Sensitivity Exponent Data.*** The data were taken from two Argonne Quarterly Reports[4.9-22,4.9-22] and, as with the strain hardening exponent, cover the temperature range from 1,123 to 1,673 K. These data are shown in Figure 4-42, where m is plotted as a function of oxygen concentration for seven temperatures. The change in m is plotted as a function of oxygen concentration for seven temperatures. The changes in m with temperature reflect the changes predicted by MATPRO. The 1,173 K curve is anomalous because the as received zircaloy is in the alpha + beta transition phase region at this temperature.[a] It is evident that m decreases with increasing C in all cases; and each curve resembles an exponential decay, although the scatter in the data precludes quantification of the temperature dependence.

Only the ratio (m/m_o) as a function of concentration was modeled, as shown in Figure 4-43. The equation used was

$$m/m_o = \exp[-69(C - C_o)] \quad (4\text{-}220)$$

where m_o is the strain rate sensitivity constant for as received material. The number 69 in the argument of the exponent in Equation (4-220) was obtained by a least squares fit of the data to the equation.

---

a. This explanation will not suffice to explain the low values of m at 1,473 K, where the material remains in the beta region over the entire range of oxygen concentrations reported, as may be seen in the phase diagram taken from Chung.[4.9-23]

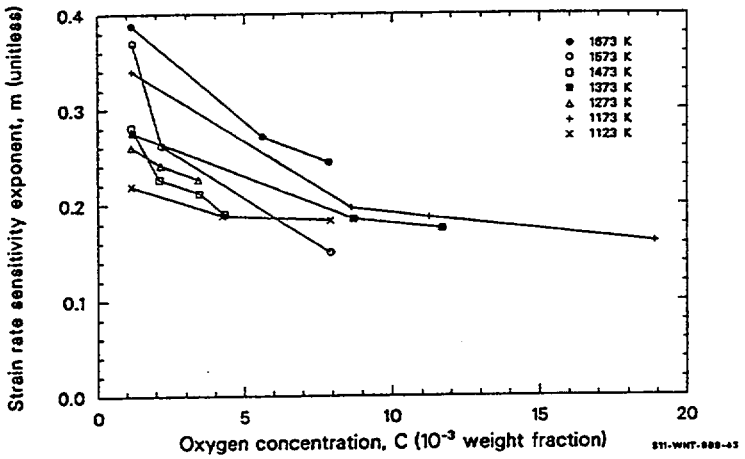

Figure 4-42. Strain rate sensitivity exponent, m, data as a function of oxygen concentration from Chung.

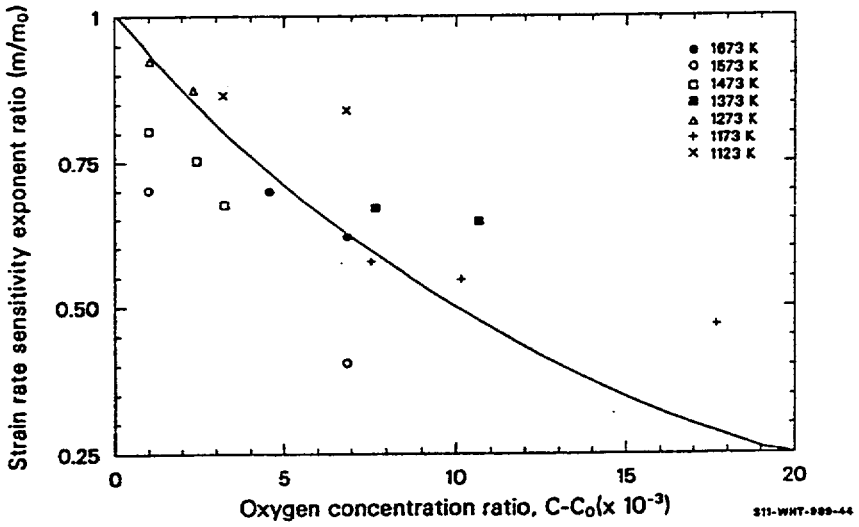

Figure 4-43. The ratio m/m_0 as a function of oxygen concentration showing Chung data and the line used to fit these data.

The quality of the fit of Equation (4-220) using Chung's values form$_0$ can be seen in Figure 4-43. Although a quantitative statement cannot be made at this time, the scatter may be partly the result of phase transitions which can occur even isothermally with changes in oxygen content (Figure 4-44). For example, at 1,123 K, m_0 is measured using material which is midway through the alpha plus beta transition phase; while the material at the highest oxygen concentration point at 1,123 K is oxygen stabilized, alpha-phase zircaloy. The fact that this point is quite far from the calculated curve may be a reflection of the failure to consider the effects of the phase transition.

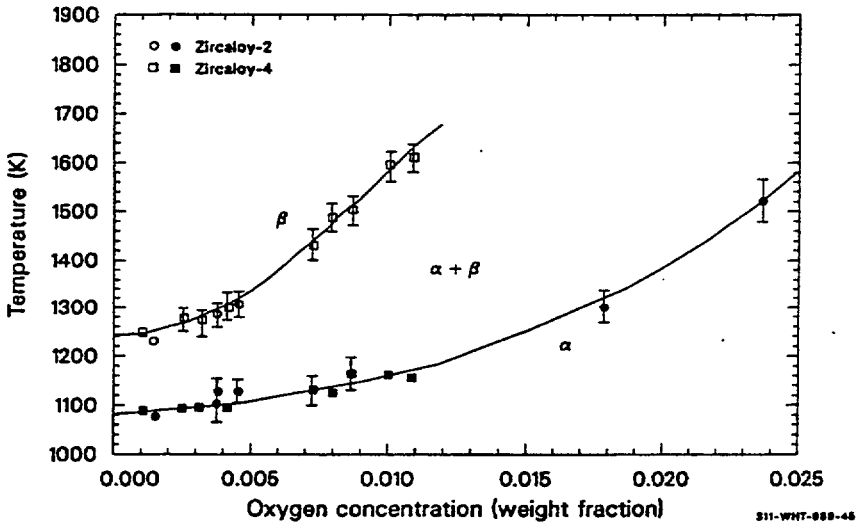

Figure 4-44. Zircaloy oxygen phase diagram, taken from Chung.

To include the 68% of the data that should fall within one standard deviation from the calculated line, the coefficient 69 of Equation (4-220) must be given quite large uncertainty limits, ± 40. The data lying below the calculated line in Figure 4-43, especially those for which $(C - C_0) = 10^{-3}$, contribute much to the uncertainty because they require particularly large values to make the curve drop abruptly enough from its starting point to pass through them.

4.9.3.4.4 ***Flow Curves Showing the Effect of Oxygen Concentration***–Three figures are presented in this section to show how oxygen concentration affects the plastic deformation portion of the stress strain curves predicted by MATPRO. Equations (4-212) through (4-215) and Equation (4-220) were used in conjunction with the MATPRO subroutines to generate these plots. All plots show two curves, one for as fabricated zircaloy ($C - C_0 = 0$) and one for zircaloy containing a total of about five times the as fabricated oxygen level ($C - C_0 = 0.005$ weight fraction). Unless otherwise specified, the as fabricated oxygen content, C_0, was assumed to be 0.0012 weight fraction.

Figure 4-45 shows the flow curves at 600 K, a temperature typical of PWR normal operation. The strain rate was taken as 10^{-3}/s, so that the strain rate dependence on oxygen content was not a factor. At

this temperature, Equations (4-214) and (4-215) predict a completely negligible change in n, the strain hardening exponent. The entire difference between the curves thus results from the change in K which, for these conditions, increases by a factor of 1.65.

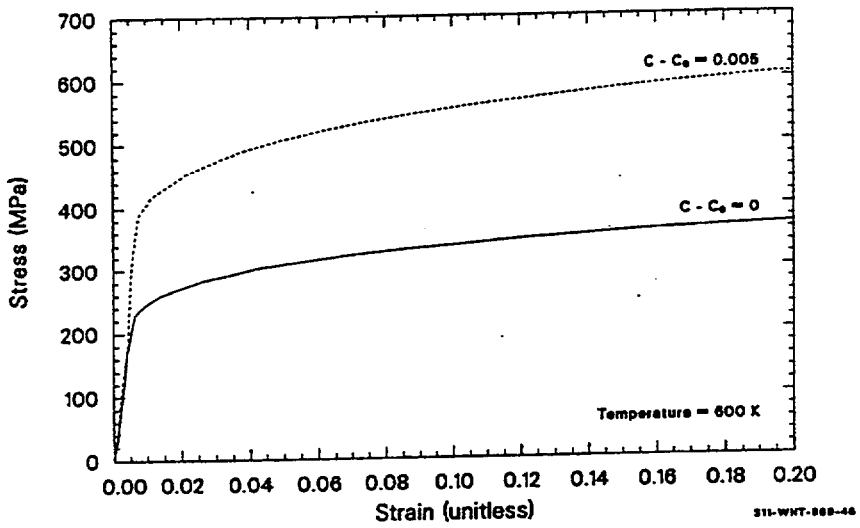

Figure 4-45. Stress as a function of strain at a strain rate of 10^{-3}/s for two oxygen concentrations at 600 K.

Figure 4-46 shows flow curves for conditions the same as those of Figure 4-45 except that the temperature is 1,400 K, which is characteristic of the temperature postulated for reactor transients, such as a loss of coolant or a power cooling mismatch. At this temperature, K increases by a factor of 5.8 and n by a factor of 5.6. Since the curve with $C = C_0 = 0$ is nearly flat except at very small strains, the increasing slope of the curve for $C - C_0 \neq 0$ is largely due to the change in n caused by the extra oxygen.

Figure 4-47 shows the stress required to cause a strain of 0.1 at various strain rates. This figure is included to illustrate the effect of oxygen concentration on the strain rate exponent. Nearly all of the difference between the oxidized and unoxidized cladding is caused by the change in the strength coefficient. Careful examination of the curves will show a slightly increasing separation between them as the strain rate increases. The separation of the curves increases by only 2.5% as the strain rate changes from 10^{-4} to 10^{-2}. However, under these conditions, if m were unchanged by oxygen concentration but K were affected, the increase would be 9.3%. In general, the effect of oxygen concentration on m is to increase $d\sigma / d\varepsilon$ for $\varepsilon < 10^{-3}$/s and to decrease $d\sigma / d\varepsilon$ for $\varepsilon > 10^{-3}$/s. For the strain rate range of Figure 4-47, approximately nine-tenths of the strain rates are greater than 10^{-3}/s; therefore, the net effect is a slope smaller than would be found if m were not a function of oxygen concentration. These observations must still be regarded as tentative, since Equation (4-188) was derived from data taken at strain rates close to 10^{-3}/s, and these data included large scatter.

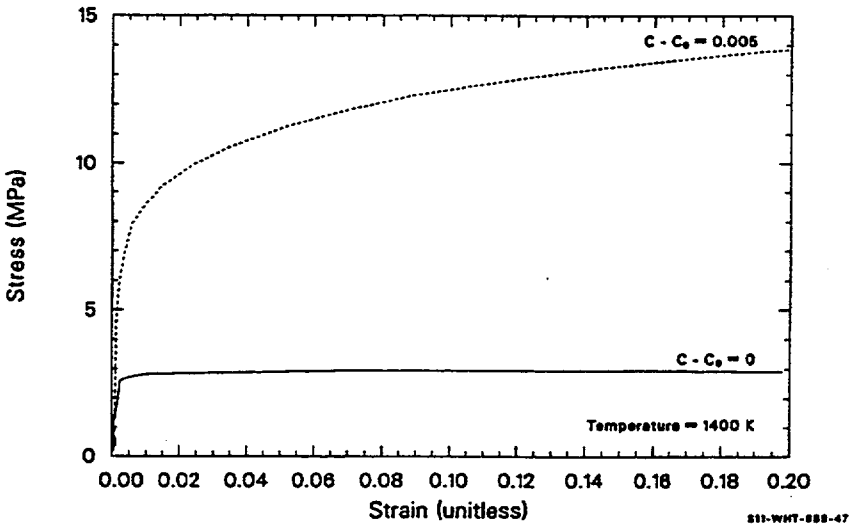

Figure 4-46. Stress as a function of strain at a strain rate of 10^{-3}/s for two oxygen concentrations at 1,400 K.

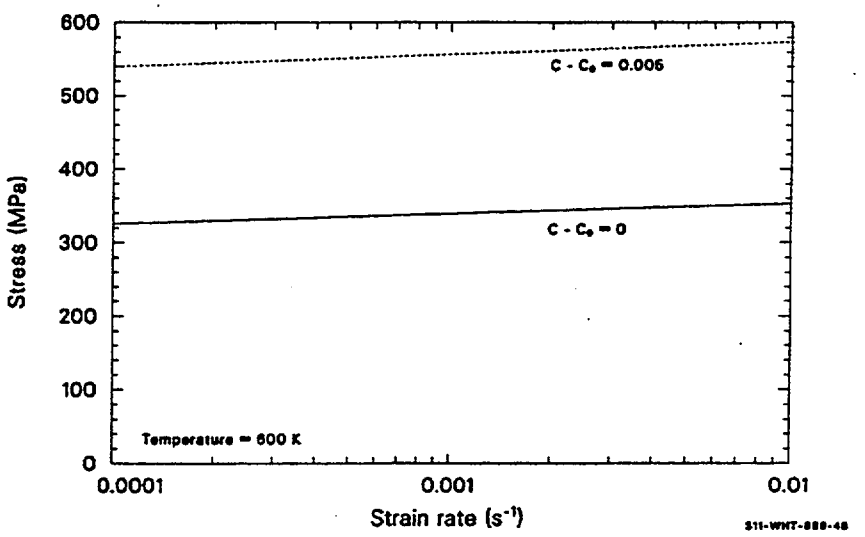

Figure 4-47. Stress as a function of strain at a strain rate of 0.1 for two oxygen concentrations at 600 K.

4.9.4 Comparison to Burst Test Data

The transient temperature tests by Hardy[4.9-34] discussed in Section 4.9.2 offer an opportunity to test the model at temperatures in the range 900 to 1,400 K. Figure 4-48 is a comparison of predicted versus measured strains for four of Hardy's tests at a heating rate of 25 K/s and initial pressures of 5.5, 2.8, 1.4, and 0.3 MPa. Since Hardy did not report the cladding texture, typical values were assumed ($f_r = 0.66$, $f_z = 0.06$, and $f_\theta = 0.28$).

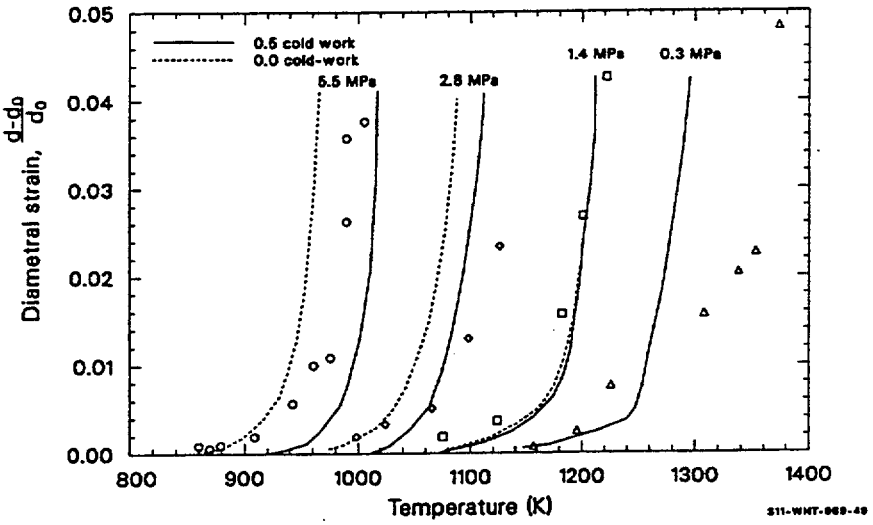

Figure 4-48. Measured diametral strain versus MATPRO predictions for two initial values of cold work in tests conducted by Hardy at heating rates of 25 K/s.

Details of the stress relief were also not reported, so two predicted strains are shown for each series--one for fully annealed material and one for a very light stress relief. With the exception of the highest temperature data (where slight oxidation due to residual water vapor in the vacuum chamber may have affected the experiment), the predictions are within ± 25 K of the experimental value.

It is somewhat surprising that a model based on uniaxial deformation and empirical texture coefficients stays within about 25 K of these biaxial data. Apparently, the temperature dependence of the strength coefficient for the second mode of deformation is similar to the temperature dependence of the mode observed with uniaxial tests. Inspection of the predicted strain curves and Hardy's data seems to confirm the different (large) strain hardening exponent found with the biaxial test by Hann. Strains are systematically underpredicted when they are small and tend to be overpredicted when they are large. It is also possible that the relatively large initial strain is caused by an as yet unmodeled annealistic deformation.

A more sensitive test is provided by a stress rupture experiment reported by Chung.[4.9-24] In this test, temperature and pressure were set at 1,023 K and 5.2 MPa. Chung's data and the MATPRO model

predictions for 1,023 and 1,048 K are shown in Figure 4-49. The model overpredicts cladding strength at 1,023 K, but the prediction at 1,048 K approximates Chung's data fairly well out to strains of 0.2, where ballooning becomes important.

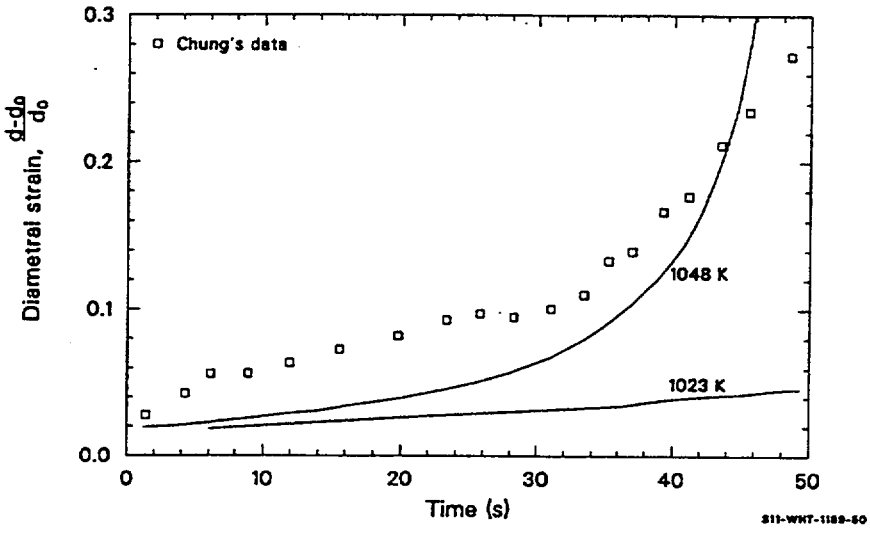

Figure 4-49. Measured diametral strain versus MATPRO predictions for Chung's test at 1,023 K and 5.2 MPa.

4.9.5 Uncertainties

Equations (4-185) through (4-187) for the expected error of the constants K, n, and m were obtained by comparing values predicted by Equations (4-164) through (4-179) with their own data base Two points should be emphasized for users of these expressions: (a) they are not standard errors, and (b) they do not apply to irradiated or oxidized material. Standard error was not used as a measure of uncertainty because the scatter in the data is a function of temperature. Use of a single standard error would lead to nonphysical predictions, such as negative strengths at high temperatures, and there are not enough data to define a more reasonable distribution than the Gaussian distribution of the usual standard error definition. The error estimates of Equations (4-158) through (4-172) seem to be consistent with the comparison to burst tests that were discussed in the previous section. That is, the error from Equations (4-164) through (4-179) (strength coefficient/3.0) is approximately equivalent to an error of 25 K. The limited burst test data also were found to be in error by 25 K.

4.9.6 References

4.9-1 L. J. Siefken, M. P. Bohn, S. O. Peck, and J. A. Dearien, *FRAP-T5: A Computer Code for the Transient Analysis of Oxide Fuel Rods*, NUREG/CR-0840, TREE-1281, June 1979.

4.9-2 C. R. Hann et al., *Transient Deformation Properties of Zircaloy for LOCA Simulation*, NP-526, Volume 3, March 1978.

4.9-3 M. L. Picklesimer, "Deformation, Creep and Fracture in Alpha-Zirconium Alloys," *Journal of Electrochemical Technology, 4*, July-August 1966, pp. 289-300.

4.9-4 P. L. Rittenhouse and M. L. Picklesimer, "Research on the Mechanical Anisotropy of Zircaloy-2," *Journal of Electrochemical Technology, 4*, July-August 1966, pp. 322-329.

4.9-5 C. R. Woods (ed.), *Properties of Zircaloy-4 Tubing*, WAPD-TM-585, December 1966.

4.9-6 R. L. Mehan and F. W. Wiesinger, *Mechanical Properties of Zircaloy-2*, KAPL 2110, February, 1961.

4.9-7 H. C. Brassfield, J. F. White, L. Sjodahl, and J. T. Bittel, *Recommended Property and Reaction Kinetics Data for Use in Evaluating a Light Water Cooled Reactor Loss of Coolant Incident Involving Zircaloy-4 or 304-SS-Clad UO_2*, GEMP-482, April 1968.

4.9-8 A. L. Bement, Jr., *Effects of Cold Work and Neutron Irradiation on the Tensile Properties of Zircaloy-2*, HW-74955, April 1963.

4.9-9 D. Lee and W. A. Backofen, "Superplasticity in Some Titanium and Zirconium Alloys," *Transactions of the Metallurgical Society of AIME, 239*, July 1967, pp. 1034-1040.

4.9-10 L. M. Howe and W. R. Thomas, "The Effects of Neutron Irradiation on the Tensile Properties of Zircaloy-2," *Journal of Nuclear Materials, 2*, 1960, pp. 248-260.

4.9-11 L. S. Rubenstein et al., "Effect of Oxygen on the Properties of Zircaloy-2," *Transactions of the American Society for Metals, 54*, 1961, pp. 20-30.

4.9-12 A. Cowan and W. J. Langford, "Effects of Hydrogen and Neutron Irradiation on the Failure of Flawed Zircaloy-2 Pressure Tubes," *Journal of Nuclear Materials, 30*, 1969, pp. 271-281.

4.9-13 C. C. Busby and K. B. Marsh, *High Temperature Deformation and Burst Characteristics of Recrystallized Zircaloy-4 Tubing*, WAPD-TM-900, January 1970.

4.9-14 D. O. Pickman, "Properties of Zircaloy Cladding," *Nuclear Engineering and Design, 21*, 1972, pp. 212-236.

4.9-15 G. F. Fieger and D. Lee, "Strength and Ductility of Neutron Irradiated and Textured Zircaloy-2," *Zirconium in Nuclear Applications*, ASTM-STP-551, 1973, pp. 355-369.

4.9-16 P. J. Crescimanno, *High Strain Rate Tensile Tests of Zircaloy at 550 °F* (LWBR Development Program), WAPD-TM-1263, February 1976.

4.9-17 Y. Miyamoto, Y. Komatsu, N. Nagai, "Mechanical Behavior of Zircaloy-2 Tubing Under Biaxial Stresses," *Journal of Nuclear Materials, 61*, 1976, pp. 53-65.

4.9-18 C. C. Busby and K. B. Marsh, *High Temperature, Time Dependent Deformation in Internally Pressurized Zircaloy-4 Tubing*, WAPD-TM-1043, October 1974.

4.9-19 H. M. Chung, A. M. Garde, and T. F. Kassner, *Light-Water-Reactor Safety Research Program: Quarterly Progress Report,* January-March, 1975, ANL-75-28, June 12, 1975.

4.9-20 H. M. Chung, A. M. Garde, and T. F. Kassner, *Light-Water-Reactor Safety Research Program: Quarterly Progress Report, April-June, 1975*, ANL-75-58, June 13, 1975.

4.9-21 H. M. Chung, A. M. Garde, and T. F. Kassner, *Light-Water-Reactor Safety Research Program: Quarterly Progress Report, July-September, 1975*, ANL-75-72, December 1975.

4.9-22 H. M. Chung, A. M. Garde, and T. F. Kassner, *Light-Water-Reactor Safety Research Program: Quarterly Progress Report, October-December, 1975*, ANL-76-15, March 1976.

4.9-23 H. M. Chung, A. M. Garde, and T. F. Kassner, *Light-Water-Reactor Safety Research Program: Quarterly Progress Report, January-March, 1976*, ANL-76-49, June 1976.

4.9-24 H. M. Chung, A. M. Garde, and T. F. Kassner, *Light-Water-Reactor Safety Research Program: Quarterly Progress Report, July-September, 1976*, ANL-76-121, December 1976.

4.9-25 H. M. Chung, A. M. Garde, and T. F. Kassner, *Light-Water-Reactor Safety Research Program: Quarterly Progress Report, January-March, 1977*, ANL-77-34, June 1977.

4.9-26 A. A. Bauer, L. M. Lowry, and J. S. Perrin, *Evaluating Strength and Ductility of Irradiated Zircaloy: Quarterly Progress Report April-June, 1976*, BMI-NUREG-1956, July 1976.

4.9-27 A. A. Bauer, L. M. Lowry, and J. S. Perrin, *Evaluating Strength and Ductility of Irradiated Zircaloy: Quarterly Progress Report July-September, 1976*, BMI-NUREG-1961, October 1976.

4.9-28 A. A. Bauer, L. M. Lowry, and J. S. Perrin, *Evaluating Strength and Ductility of Irradiated Zircaloy: Quarterly Progress Report October-December, 1976*, BMI-NUREG-1967, January 1977.

4.9-29 D. Lee et al., *Plasticity Theories and Structural Analysis of Anisotropic Metals--Zircaloys*, NP-500, May 1977.

4.9-30 O. D. Sherby and A. K. Miller, *Development of the Materials Code, MATMOD (Constitutive Equations of Zircaloy)*, NP-567, December 1977.

4.9-31 E. Tenckhoff, "Operable Deformation Systems and Mechanical Behavior of Textured Zircaloy Tubing," *Zirconium in Nuclear Applications*, ASTM-STP-551, 1974, pp. 179-200.

4.9-32 B. D. Clay and G. B. Redding, "Creep Rupture Properties of Alpha Phase Zircaloy Cladding Relevant to the Loss of Coolant Accident," *J. Br.Nucl. Energy Soc., 15*, 1976, pp. 253-256.

4.9-33 J. R. Stanbridge and B. A. Keen, "Strain in the Zircaloy Clad of Fuel Pins in Loss of Coolant Accidents," *J. Br. Nucl. Energy Soc., 16*, 1977, pp. 341-346.

4.9-34 D. G. Hardy, "High Temperature Expansion and Rupture Behavior of Zircaloy Tubing," *Topical Meeting on Water Reactor Safety, Salt Lake City, UT, March 26-28, 1973*, CONF-730304.

4.9-35 H. Stehle, H. Steinberg, and E. Tenckhoff, "Mechanical Properties Anisotropy and Microstructure of Zircaloy Canning Tubes," *Zirconium in the Nuclear Industry*, 1977, ASTM-STP-663, pp. 486-507.

4.9-36 K. H. Matucha and G. Dressler, "Yield and Fracture of Biaxially Stressed Zircaloy-4 Cladding Tubes at Room Temperature and at 400 °C," *Zirconium in the Nuclear Industry*, 1977, ASTM-STP-663, pp. 508-522.

4.9-37 C. S. Hartley, "Properties of Reactor Materials at Constant True Strain Rates," *Progress Report July 1, 1977-June 30, 1978*, NUREG/CR-0235, August 1978.

4.9-38 R. Hill, "A Theory of the Yielding and Plastic Flow of Anisotropic Metals," *Proceedings of the Royal Society of London, Series A, Mathematical and Physical Sciences, 193*, 1948, pp. 281-297.

4.9-39 R. H. Chapman, *Characterization of Zircaloy-4 Tubing Procured for Fuel Cladding Research Programs*, ORNL/NUREG/TM-29, July 1976.

4.9-40 D. R. Olander, *Fundamental Aspects of Nuclear Reactor Fuel Elements*, TID-26711-P1, 1976.

4.9-41 G. E. Dieter, *Mechanical Metallurgy*, New York: McGraw-Hill Book Company, Inc., 1976, pp. 28-32.

4.10 Annealing (CANEAL)

The equation of state for cladding plastic deformation described in Section 4.9 contains terms which are dependent on cold work and fast neutron fluence. This section is a description of a subcode that determines the thermal annealing of cold work and fast neutron fluence. The annealing is modeled with empirical rate equations, which are used to keep track of the remaining effective cold work and fast neutron fluence for use in the equation of state for cladding plastic deformation.

4.10.1 Summary

The CANEAL subcode requires input values of temperature at the start of a time step, an estimate of the rate of change of temperature during the time step, time step size, fast neutron flux, and start-of-step values of cold work and fast neutron fluence.

The expression used to find the ratio of effective cold work for the strength coefficient at the end of a time step divided by effective cold work at the beginning of an isothermal time step with temperature < 1,255 K is

$$FK = \exp\left[-1.504\left(1 + 2.2 \times 10^{-25}\,\Phi_{KO}\right)(t)\exp\left(-2.33 \times 10^{18}/T^{6}\right)\right] \quad (4\text{-}221)$$

where

FK = effective cold work for the strength coefficient at the end of a time step divided by effective cold work at the start of the time step

Φ_{KO} = effective fast neutron fluence for strength coefficient at the start of the time step (n/m^2)

t = time step size (s)

T = cladding temperature (K).

The effective fast neutron fluence for calculating the strength coefficient after an isothermal time step with temperature < 1,255 K is computed with the expression

$$\frac{10^{20}}{\Phi_K} = 2.49\times10^{-6}(t)\exp\left(\frac{-5.35\times10^{23}}{T^{8}}\right) + \frac{10^{20}}{\Phi_{KO}} \quad (4\text{-}222)$$

where Φ_K is the effective fast neutron fluence for the strength coefficient at the end of a time step (n/m^2).

For temperatures < 1,255 K, the expression used to find the ratio of effective cold work for the strain hardening exponent at the end of an isothermal time step to the effective cold work for strain hardening at the start of the time step is

$$FN = \exp\left[-12.032\left(1 + 2.2\times10^{-25}\Phi_{NO}\right)(t)\exp\left(\frac{-2.23\times10^{18}}{T^{6}}\right)\right] \quad (4\text{-}223)$$

where

FN = effective cold work for strain hardening exponent at the end of a time step divided by effective cold work for strain hardening exponent at the start of the time step

Φ_{NO} = effective fast neutron fluence for the strain hardening exponent at the start of the

time step (n/m^2).

For temperatures < 1,255 K, the effective fast neutron fluence for calculating the strain hardening exponent after an isothermal time step is computed with the expression

$$\frac{10^{20}}{\Phi_N} = 2.49\times10^{-6}(t)\exp\left(\frac{-5.35\times10^{23}}{T^8}\right)+\frac{10^{20}}{\Phi_{NO}} \tag{4-224}$$

where Φ_N is the effective fast neutron fluence for the strain hardening exponent at the end of a time step (n/m^2).

If the time step is not isothermal, Equations (4-221) through (4-224) must be modified to include the effect of varying temperature. The modification used is

$$\exp\left(\frac{-Q}{T^m}\right) = \exp\left(\frac{-Q}{TO^m}\right)\left[\frac{\exp\left[Q\left(\frac{dT}{dt}\right)t\left(\frac{m}{TO^{m+1}}\right)\right]-1}{Q\left(\frac{dT}{dt}\right)t\left(\frac{m}{TO^{m+1}}\right)}\right] \tag{4-225}$$

where

Q,m = the constants that appear in the isothermal expression

TO = temperature at the start of the time step (K)

dT/dt = average rate of change of temperature expected during the time step (K/s).

Expression (4-224) is exact for a constant rate of temperature change and is only an approximation for nonlinear temperature changes.

If the temperature during the time step is as high as 1,255 K, the effective cold works and fast neutron fluences are set equal to zero.

The following section is a discussion of the data that were available to use to develop annealing rate equations. The model development itself is presented in Section 4.10.3.

4.10.2 Available Data

Howe and Thomas[4.10-1] reported postirradiation annealing studies on annealed, 13.1% cold worked, and tempered 25.5% cold worked zircaloy-2 irradiated at 493 and 553 K with integrated fast neutron fluences of 3.6×10^{23} n/m^2 and 2.7×10^{24} n/m^2. Specimens were given 1 hour anneals in vacuum at various temperatures. The nominal room temperature ultimate stresses measured with these samples are listed in Table 4-28.

Table 4-28. Room temperature ultimate strengths of cladding annealed for 1 hour from Howe and Thomas.

Cold work (%)	Neutron fluence (n/m^2)	Annealing temperature (K)	Ultimate strength (MPa)
0	3.6×10^{23}	555	634
0	3.6×10^{23}	625	588
0	3.6×10^{23}	675	513
0	3.6×10^{23}	725	513
0	3.6×10^{23}	775	500
0	3.6×10^{23}	875	500
0	3.6×10^{23}	975	499
25.5	0	555	619
25.5	0	675	614
25.5	0	775	603
25.5	0	875	530
25.5	0	975	512
25.5	2.7×10^{24}	555	728
25.5	2.7×10^{24}	625	712
25.5	2.7×10^{24}	675	675
25.5	2.7×10^{24}	725	626
25.5	2.7×10^{24}	775	579
25.5	2.7×10^{24}	875	504
25.5	2.7×10^{24}	975	486

The data from irradiated annealed zircaloy-2 show that irradiation induced hardening in this material is completely annealed out after 1 hour at temperatures above 775 K and that most of the recovery occurs in the temperature range from 575 to 675 K. From their recovery data with 25.5% cold worked zircaloy-2, Howe and Thomas concluded that:

1. The recovery occurring in the temperature range 550 to 725 K is the annealing out of irradiation damage rather than cold work.

2. The irradiation damage in cold worked material is completely annealed out after 1 hour at approximately 725 K.

3. The recovery from 725 to 973 K for irradiated material is fairly similar to that for unirradiated material. However, there is an indication that the irradiated material recovers slightly faster.

Since the 1 hour anneals of Howe and Thomas represent times which are long compared to loss of coolant accident blowdown and refill times, the data were used only for general guidance and verification of the models developed from shorter annealing times reported by Bauer. In particular, the data support the ideas that (a) irradiation damage anneals before cold work and (b) irradiation damage affects the rate of annealing of cold work.

Bauer reported yield strengths, ultimate strength, uniform elongations (engineering strain at maximum load), and total elongations from annealing studies of both cold worked and irradiated cold worked zircaloy cladding material.[4.10-2,4.10-3] The unirradiated cold worked cladding was from a standard lot of tubing which has been characterized by Chapman.[4.10-4] The irradiated cladding was obtained from spent fuel rods irradiated in the Carolina Power and Light H. B. Robinson Plant to a fast neutron fluence of approximately 4.4×10^{25} n/m^2.

Ultimate strengths and uniform elongations obtained at 644 K and a strain rate of 0.025/minutes with the unirradiated cladding are listed in Table 4-29. With a heating rate of 5.6 K/s, most of the recovery of both strength and uniform elongation occurs between temperatures of 894 and 978 K. However, the recovery has barely started at 978 K when the heating rate is 27.8 K/s. Since the annealing times at temperature are short, the maximum temperature required to anneal these samples is considerably higher than the temperatures reported by Howe and Thomas.

Table 4-29. 644 K test results for unirradiated transient annealed cladding.[4.10-2]

Specimen number[a]	Heating Rate (K/s)	Maximum temperature (K)	Ultimate strength (MPa)	Uniform elongation (%)
As received	--	644	434.5	4.1
0781-8	5.6	811	434	4.1
0781-7	5.6	866	432	4.1
0781-6	5.6	894	409	4.8
0781-5	5.6	978	252	24.3
0781-4	27.8	811	434	3.6

Table 4-29. 644 K test results for unirradiated transient annealed cladding.[4.10-2] (Continued)

Specimen number[a]	Heating Rate (K/s)	Maximum temperature (K)	Ultimate strength (MPa)	Uniform elongation (%)
0781-3	27.8	866	438	3.3
0781-2	27.8	894	432	3.6
0781-1	27.8	978	422	4.6

a. The number 0781 is the rod number.

Table 4-30 and Table 4-31 are a summary of Bauer's measurements of ultimate strengths and uniform elongations of annealed irradiated tubing. The measurements were performed at 644 K and a strain rate of 0.025/minutes. The results in Table 4-30 were obtained with transient anneals similar to those used with the unirradiated tubing. Table 4-31 summarizes results from isothermal anneals similar to the anneals carried out by Howe and Thomas.

Table 4-30. 644 K test results for irradiated transient annealed cladding.[4.10-3]

Specimen number[a]	Heating rate (K/s)	Maximum temperature (K)	Ultimate strength (MPa)	Uniform elongation (%)
PB-20	--	644	622.8	4.10
PB-34	--	644	650.3	4.00
PB-46	--	644	660.9	2.80
H10-20	--	644	694.0	3.80
P4-50-55	0.6	700	674.0	2.10
P4-55-60	0.6	755	633.0	2.70
P4-89-1/2-94-1/2	0.6	811	574.5	2.30
P4-94-1/2-99-1/2	0.6	894	286.1	9.57
Pr-89-1/2-104-1/2	0.6	978	268.9	9.21
P4-111-116	5.6	700	653.0	2.00
P4-45-50	5.6	755	676.0	2.40
P4-35-3/4-46-3/4	5.6	811	595.2	2.35
Pr-70-3/4-75-3/4	5.6	866	349.3	2.94
Pr-75-3/4-80-3/4	5.6	894	313.7	4.77

Table 4-30. 644 K test results for irradiated transient annealed cladding.[4.10-3] (Continued)

Specimen number[a]	Heating rate (K/s)	Maximum temperature (K)	Ultimate strength (MPa)	Uniform elongation (%)
Pr-80-1/2-89-1/2	5.6	978	287.3	10.56
014-106-1/2-111-1/2	13.9	755	717.0	2.40
A8-120-3/4-125-3/4	13.9	811	652.7	2.27
P4-16-1/2-21-1/2	13.9	866	577.9	2.50
P4-21-1/2-26-1/2	13.9	894	456.2	2.16
P4-26-1/2-31-1/2	13.9	978	304.5	5.74
P4-65-70	27.8	755	671.0	2.10
A1-29-1/2-34-1/2	27.8	811	721.6	2.70
A8-105-3/4-110-3/4	27.8	866	671.0	2.70
A8-110-3/4-115-3/4	27.8	894	597.5	2.06
A8-115-3/4-120-3/4	27.8	978	348.2	3.49
P4-116-21	27.8	1,033	329.0	4.70
014-111-1/2-116-1/2	27.8	1,144	338.0	8.60
014-37-42	27.8	1,255	340.0	10.50

a. The letter and number, letter, or number before the first hyphen identifies the rod number; that is Rod P8, Rod P4-9, Rod 014, etc.

Table 4-31. 644 K test results for irradiated isothermally annealed cladding.[4.10-3]

Specimen number[a]	Temperature (K/s)	Time at temperature (minutes)	Ultimate strength (MPa)	Uniform elongation (%)
P8-20	644	--	622.8	4.10
P8-34	644	--	650.3	4.00
P8-46	644	--	660.9	2.80
H10-20	644	--	694.0	3.80
H10-5	700	60	615.9	3.35
H10-41	755	10	590.6	2.85
H10-17	755	60	556.2	3.06

Table 4-31. 644 K test results for irradiated isothermally annealed cladding.[4.10-3] (Continued)

Specimen number[a]	Temperature (K/s)	Time at temperature (minutes)	Ultimate strength (MPa)	Uniform elongation (%)
P4-60-65	811	1	560	2.90
A1-24-1/2-29-1/2	811	10	363.1	3.20
H10-18	811	30	371.1	5.10
A1-105-3/4-110-3/4	866	1	332.1	4.52
A1-99-104	866	5	311.4	8.03
H10-3	866	30	321.7	10.10
A1-110-3/4-115-3/4	894	1	308.9	7.90
H10-4	894	30	319.4	13.93
A1-116-1/2-121-1/2	978	1	305.6	7.67
H10-16	978	30	311.4	11.80

a. The letter and number before the first hyphen identifies the rod number; that is, Rod P8, Rod H10, and Rod A1.

The annealing behavior of the irradiated cladding is different than the behavior of the unirradiated material. Ultimate strengths obtained with irradiated material which had little or no annealing are substantially higher than the ultimate strengths of the unirradiated material. However, transient anneals that begin to affect the strength of cold worked material (5.6 K/s to 866 and 894 K or 27.8 K/s to 978 K) leave the irradiated material with strengths below the strengths of the unirradiated material after corresponding anneals. It is possible that these differences are due to the fact that the tubing does not come from the same lot, but a similar trend has been shown by the studies of Howe and Thomas on material from one lot. It has thus been concluded that irradiation for long times at reactor operating temperatures causes a significant increase in the strength of zircaloy cladding and enhances the annealing of the strength increase due to cold work.

Comparison of uniform elongation measurements with the unirradiated cladding (Table 4-29 and Table 4-30) shows that the effect of irradiation on this parameter is different than its effect on ultimate strength. The uniform elongation of the unannealed irradiated material is less than the uniform elongation of the unannealed unirradiated material, but there is no obvious increase in the rate of recovery from cold work effects because of the irradiation. Therefore, models that describe annealing by keeping track of effective cold work and effective fluence should be set up to use different values of these parameters for predicting strength and elongation.

The isothermal annealing effects reproduced in Table 4-31 are similar to those of Table 4-30 in that recovery of ultimate strength precedes recovery of uniform elongation. However, several additional

features of the annealing of cold-worked and irradiated zircaloy cladding become apparent from the isothermal data.

1. The four tests at 644 K show that approximately 10% sample to sample scatter should be expected in the measured values of strength. In particular, rod H10 shows consistently high strength. Variation on the order of a percent seems to be present in the uniform elongation data. Models for annealing will therefore have to emphasize general trends and avoid exact fits to individual measurements.

2. Irradiation effects on the strength of zircaloy cladding do not seem to saturate at the low fluences used by Howe and Thomas. The two 60 minute anneals show strengths at 644 K similar to the room temperature strengths measured after similar anneals by Howe and Thomas. If the tensile test data had been taken at similar temperatures, the cladding measured by Bauer would show considerably greater strength.

3. Time at temperature during annealing is less important for the irradiated material than for the unirradiated material. The exponential dependence on time of the model developed in Section 4.10.3 for annealing the effect of cold work on strength predicts that the log of the departure of strength parameters from their annealed values for two isothermal anneals that differ only in the time at temperature should be proportional to the reciprocal ratio of the annealing times. The major component of the increase of the strengths in Table 4-31 is much less dependent on time at temperature than this relation would imply.[a]

The net impression left by the data of Table 4-28 through Table 4-31 is that at least two different processes are important in the annealing of cold worked and irradiated cladding and that the annealing of the irradiation caused component follows a rate equation that is different than the rate equation for the cold work component. Data that could be used to model these separate processes (for example, annealing studies with one lot of material irradiated to several different fluences) were not available for use in the development of the annealing model for MATPRO. Therefore, the model developed in the next section is a strictly empirical attempt to reproduce the available data with a reasonably concise set of correlations. Also, there were no data for annealing rates at temperatures corresponding to the beta phase (temperature > 1,255 K).

4.10.3 Model Development

The approach used to develop the annealing models presented here was to develop a model for the annealing of cold worked cladding and modify it to fit data from cold worked and irradiated material in the alpha and alpha plus beta phase temperature range. The model for recovery kinetics in cold worked cladding is based on a result reported by Byrne.[4.10-5] He found that recovery[b] data frequently conform to the assumption that the rate of recovery of a property from its cold worked value is proportional to the instantaneous value of the property. If the property is the strength coefficient,[c] the rate equation for recovery is

a. For example, the 10- and 60-minute anneals at 775 K have ultimate strengths that are 279.2 and 244.8 MPa above the fully annealed ultimate strength sample H10-16. An equation with the exponential time dependence of Equation (4-221) would imply that the ratio of the logs of the two strengths should be 1/6, or 0.17. The ratio is 0.98.
b. A separate model for recrystallization kinetics was developed but not used because only limited recrystallization data were available.

$$dK/dt = -f_T (K - K_A) \quad (4\text{-}226)$$

where

K = strength coefficient of cold worked cladding (MPa)

t = time (s)

f_T = a temperature-dependent factor

K_A = strength coefficient of annealed cladding (MPa).

Since isothermal annealing data with unirradiated cold worked tubing are not available, the effect of temperature on the factor f_T in Equation (4-226) had to be determined from the limited transient annealing data of Table 4-29. The method used to do this is outlined as follows:

(1) The change of the factor f_T in Equation (4-226) is assumed to be represented by the expression

$$f_T = B \exp (Q/T^m) \quad (4\text{-}227)$$

where

B,Q,m = positive constants

T = temperature (K).

(2) Equation (4-226) is integrated over a very short (approximately isothermal) time interval to produce a differential expression for the change in strength coefficient

$$\frac{K_{final} - K_A}{K_{initial} - K_A} = \exp\left[-B(t_{final} - t_{initial})\exp\left(-\frac{Q}{T^m}\right)\right] . \quad (4\text{-}228)$$

(3) The long interval beginning at a temperature T_i, and ending at a temperature T_f is divided into η small intervals, and the temperature during any small interval is assumed constant. The net change in K is the product of η terms like Equation (4-228) for each interval

c. Since the change in the strength coefficient is modeled as a linear function of cold work, one can use cold work instead of the strength coefficient in this equation.

$$\frac{K_{final}-K_A}{K_{initial}-K_A} = \prod_{j=1}^{\eta}\exp\left[-B\left(\frac{t_{final}-t_{initial}}{\eta}\right)\exp\left(-\frac{Q}{T_j^m}\right)\right]$$
$$= \exp\left[-b\left(\frac{t_{final}-t_{initial}}{\eta}\right)\sum_{j=1}^{\eta}\exp\left(-\frac{Q}{T_j^m}\right)\right] \quad (4\text{-}229)$$

where T_j is the temperature during the j-th interval.

(4) When the temperature change is a linear function of time, T_j in Equation (4-229) can be obtained by interpolation between the initial and final temperatures. The linear interpolation,[a] a Taylor series expansion, and a power series summation yield

$$\sum_{j=1}^{\eta}\exp\left(-\frac{Q}{T_j^m}\right) = \sum_{j=1}^{\eta}\exp\left(\frac{-Q}{\left[T_f-\left(\frac{T_f-T_i}{2\eta}\right)-(\eta-j)\left(\frac{T_f-T_i}{\eta}\right)\right]^m}\right)$$
$$= \sum_{j=1}^{\eta}\exp\left(\frac{-Q}{\left[T_f-\left(\frac{T_f-T_i}{2\eta}\right)\right]^m}\left[1+\frac{m(\eta-j)\frac{(T_f-T_i)}{\eta}}{T_f-\left(\frac{T_f-T_i}{2\eta}\right)}+\ldots\right]\right) \quad (4\text{-}230)$$

$$= \exp\left(\frac{-Q}{\left[T_f-\left(\frac{T_f-T_i}{2\eta}\right)\right]^m}\right)\left[\frac{1-\exp\left(\frac{-m(T_f-T_i)Q}{\left[T_f-\left(\frac{T_f-T_i}{2\eta}\right)\right]^{m+1}}\right)}{1-\exp\left(\frac{-m(T_f-T_i)Q}{\eta\left[T_f-\left(\frac{T_f-T_i}{2\eta}\right)\right]^{m+1}}\right)}\right] \quad (4\text{-}231)$$

---

a. The interpolation may start with the final temperature as is done here

$$T_j = T_f-\left(\frac{T_f-T_i}{2\eta}\right)-(\eta-j)\left(\frac{T_f-T_i}{\eta}\right)$$

or it may start with the initial temperature so that

$$T_j = T_i+\left(\frac{T_f-T_i}{2\eta}\right)+j\left(\frac{T_f-T_i}{\eta}\right).$$

The second form was used for coding the annealing model because it yields a result in terms of the initial temperature.

(5) Equation (4-231) is substituted into Equation (4-229), and the limit as the number of short intervals approaches infinity($n \rightarrow \infty$) is determined. The resultant expression is

$$\frac{K_f - K_A}{K_i K_A} = \exp\left(-B\left[\exp\left(-\frac{Q}{T_f^m}\right)\right]\left[\frac{1-\exp\left(\frac{-Q(T_f-T_i)^m}{T_f^{m+1}}\right)}{\frac{Q(T_f-T_i)^m}{T_f^{m+1}}}\right](t_{final}-t_{initial})\right) \quad . \tag{4-232}$$

(6) Ultimate strengths and uniform elongations from Table 4-29 are used to determine the strength coefficient[a] after the various anneals described in this table.

(7) The strength coefficients of Step (6) are used to determine Q, B, and m. For the current MATPRO version, the values of K_f after the anneals to 866 and 978 K at 5.6 K/s were used with the value of K_i from the as-received material and Equation (4-232) to determine B and Q with assumed trial values of K_A between 364 and 442 MPa and assumed trial integral values of m between 1 and 9. Finally, the values of Q, B, K_i, K_A, and m for each trial were used in Equation (4-232) to predict K_f for the six anneals that were not already considered. The predictions were compared with the data. The trial values of K_A and m that most successfully predicted both the postanneal data and the as received strength coefficient (using the stress relief annealing schedule provided in Reference 4.10-4) were K_A = 406 MPa and m = 6. The value m = 6 and the values of Q and B which produced the successful predictions (Q = 2.33 x 10^{18} and B = 1.504) were therefore adopted for the model.

A procedure similar to the one described in the previous seven steps could be used to develop a model for the effect of cold work annealing on the strain hardening exponent. However, the complex form of the expression relating cold work and the strain hardening exponent would complicate the solution considerably. For the time being, the rate of annealing of effective cold work for the strain hardening exponent is assumed to be proportional to the rate of the effective cold work for the strength coefficient. The best fit was obtained with a value of B which is eight times as large as the B used for the strength coefficient.

The rest of this section describes the development of models for the annealing of cold worked and irradiated cladding. It was concluded in Section 4.10.2 that the principal features of the annealing data with irradiated cladding are:

1. Fast neutron fluence increases the rate of recovery from cold work effects.

2. The annealing kinetics of the irradiation caused increase in strength do not have the exponential time dependence that characterizes the recovery from cold work effects.

a. The procedure used to determine a strength coefficient from ultimate strength and uniform elongation data is discussed in Section 4.9.

Based on these conclusions, the first step in producing the model for the effect of annealing on the strength coefficient of irradiated cladding was to modify the model for cold work annealing to include the irradiation caused enhancement of the recovery of the strength coefficient from cold work effects. The modification of the cold work annealing model was based on the information in Table 4-32.[a] The first two columns identify the annealing tests, and the third column lists the strength coefficients calculated from the ultimate strengths and uniform elongations of Bauer's isothermal annealing tests (Table 4-31). The column entitled "Residual Strength Coefficient" is the strength coefficient minus the sum of the strength coefficient for annealed cladding and the contribution of cold work calculated with the unmodified model for cold work annealing. The column entitled CW/CW_0 is the initial cold work divided into the postanneal cold work predicted by the unmodified cold work annealing model. Comparison of the residual strengths and the column titled CW/CW_0 shows that the residual strength coefficient is negative whenever the cold-work is predicted to be partly annealed (CW/CW_0 in the range 0.4 to 0.8). The most reasonable interpretation of this feature is to assume that the irradiation enhances the rate of annealing of the cold work. The change required to model this effect is to replace the constant B in Equation (4-232) by a function which increases with increasing fluence. The expression adopted for the strength coefficient annealing model was

Table 4-32. Strength and residual strength coefficients after isothermal anneals.

Temperature (K)	Time at temperature (min)	Strength coefficient (Mpa)	Residual strength coefficient (MPa)	CW/CW_0
644	As received	750.7	191.7	1
644	As received	781.5	222.5	1
644	As received	763.4	204.4	1
644	As received	828.9	205.9	1
700	60	724.8	101.8	1
755	10	683.5	61.0	0.997
755	60	648.2	28.3	0.982
811	1	649.7	94.5	0.975
811	10	425.2	-100.1	0.780
811	30	460.8	-72.6	0.475
866	1	387.9	-125.1	0.700
866	5	417.2	-14.3	0.167
866	30	451.6	-0.9	0.000

a. A similar table was constucted from Bauer's transient annealing data. The transient data have no new information.

Table 4-32. Strength and residual strength coefficients after isothermal anneals. (Continued)

Temperature (K)	Time at temperature (min)	Strength coefficient (Mpa)	Residual strength coefficient (MPa)	CW/CW_o
894	1	411.3	-54.7	0.392
894	30	483.2	-30.7	0.000
978	1	406.0	0	0.002
978	30	452.5	0	0.000

$$B = 1.504\,[1 + 2.22 \times 10^{-25}]\,\Phi \qquad (4\text{-}233)$$

where

B = the rate constant in Equation (4-232)

Φ = fast neutron fluence (n/m^2).

Table 4-33 lists the information of Table 4-32 using the revised rate constant of Equation (4-233). The residual strength coefficients are close to zero for temperatures above 866 K and for the two long isothermal anneals at 811 K.

Table 4-33. Strength and residual strength coefficients with modified cold work annealing model.

Temperature (K)	Time at temperature (minutes)	Strength coefficient (MPa)	Residual strength coefficient (MPa)	CW/CW_0
644	As received	750.7	191.7	1
644	As received	781.5	222.5	1
644	As received	763.4	204.4	1
644	As received	828.9	205.9	1
700	60	724.8	101.8	1
755	10	683.5	65.8	0.969
755	60	648.2	54.7	0.827
811	1	649.7	239.9	0.025
811	10	425.2	19.2	0.000
811	30	460.8	8.3	0.000
866	1	387.9	-18.1	0.000
866	5	417.2	11.2	0.000
866	30	451.6	-0.9	0.000
894	1	411.3	5.3	0.000
894	30	483.2	30.7	0.000
978	1	406.0	0	0.000
978	30	452.5	0	0.000

The second step in producing a model for the effect of annealing on the strength coefficient of irradiated cladding was the derivation of expressions to describe the annealing of the residual strength coefficient. The expressions for the annealing of the residual strength coefficient are based on the values of this parameter presented in Table 4-33 and on residual strengths obtained with the transient test data of Table 4-30.

Table 4-34 and Table 4-35 are summaries of the strength coefficient and residual strength coefficients obtained with the transient test data. Table 4-34 groups the tests with equal maximum temperature together, and Table 4-35 groups tests with equal heating rates together. Several trends used to develop the model for the annealing of the residual strength coefficient are apparent from an inspection of Table 4-34 and Table 4-35.

Table 4-34. Strength and residual strength coefficients after transient anneals (tests with equal maximum temperature).

Heating Rate (K/s)	Maximum temperature (K)	Strength coefficient (MPa)	Residual strength coefficient (MPa)	CW/CW_o
As received	644	750.7	191.7	1
As received	644	781.5	222.5	1
As received	644	763.4	204.4	1
As received	644	828.9	205.9	1
0.6	700	758.5	199.5	1
5.6	700	732.4	173.4	1
0.6	755	728.8	169.7	0.999
5.6	755	769.4	210.4	1.0
13.9	755	816.5	257.5	1.0
27.8	755	755.4	196.4	1.0
0.6	811	651.8	111.0	0.881
5.6	811	676.5	119.5	0.987
13.9	811	739.7	181.5	0.995
27.8	811	830.7	272.1	0.997
5.6	866	405.5	-115.0	0.749
13.9	866	660.5	118.2	0.891
27.8	866	772.4	220.0	0.944
0.6	894	397.0	-9.0	0.000

Table 4-34. Strength and residual strength coefficients after transient anneals (tests with equal maximum temperature). (Continued)

Heating Rate (K/s)	Maximum temperature (K)	Strength coefficient (MPa)	Residual strength coefficient (MPa)	CW/CW_o
5.6	894	385.8	-79.7	0.389
13.9	894	514.9	4.0	0.685
27.8	894	681.8	149.2	0.828
0.6	978	370.1	-35.9	0.000
5.6	978	407.1	1.1	0.000
13.9	978	384.9	-22.4	0.009
27.8	978	411.6	-8.7	0.932
27.8	1,033	403.6	-2.4	0.001
27.8	1,144	458.7	52.7	0.000
27.8	1,255	481.1	75.1	0.000

Table 4-35. Strength and residual strength coefficients after transient anneals (test with equal heating rates).

Heating rate (K/s)	Maximum temperature (K)	Residual strength coefficient (MPa)
As received	644	191.7
As received	644	222.5
As received	644	204.4
As received	644	205.4
0.6	700	199.5
0.6	755	169.7
0.6	811	111.0
0.6	894	-9.0
0.6	978	-35.9
5.6	700	173.4
5.6	755	210.4
5.6	811	119.5

Table 4-35. Strength and residual strength coefficients after transient anneals (test with equal heating rates). (Continued)

Heating rate (K/s)	Maximum temperature (K)	Residual strength coefficient (MPa)
5.6	866	-115.0
5.6	894	-79.7
5.6	978	
13.9	755	257.5
13.9	811	181.5
13.9	866	118.2
13.9	894	4.0
13.9	978	-22.4
27.8	755	196.4
27.8	811	272.1
27.8	866	222.0
27.8	894	149.2
27.8	978	-8.7
27.8	1,033	-2.4
27.8	1,144	52.7
27.8	1,255	75.1

Inspection of the data in Table 4-35 shows that the residual strength coefficient does not anneal significantly in any of the tests with a maximum temperature of 755 K or less. All of the tests with maximum temperature of 978 K show essentially complete annealing. The tests with maximum temperatures of 811 K show varying amounts of annealing, but the effect of different heating rates (or, said another way, different times at temperature) on the residual strength coefficient is much less than one would expect from an expression with an exponential time dependence like Equation (4-232). If an equation of the form of Equation (4-232) were used to model the annealing of the residual strength coefficient, the ratio of the logs of the measured residual strength coefficients after two anneals to the same maximum temperature would be predicted to be proportional to the heating rates. The four residual strengths measured after anneals with a maximum temperature of 811 K (where annealing changes are greater than the scatter of the data) show significantly less dependence on heating rate. This observation is supported by the isothermal annealing data of Table 4-33, which also show relatively little dependence on the time at a given temperature.

When the transient data are grouped with equal heating rates together (Table 4-35), a very strong dependence of residual strength on maximum temperature is apparent. For all of the heating rates, the

annealing of the residual strength occurs over a range of maximum temperatures only about 75 K wide. Moreover, the center of this 75 K band is increased by only about 100 K when the heating rate is increased by a factor of 50.

The approach used to model the annealing of the residual strength coefficient was to assume that this component is not subject to the rate equation used for the annealing of cold work effects. The assumption is logical, not only because of the information in Table 4-33 and Table 4-34 but also because the probable cause of the residual strength coefficient is radiation damage--vacancies, interstitials, and dislocation loops--rather than cold work effects. To describe the annealing of the residual strength coefficient, an empirical rate equation which is a generalized form of Equations (4-226) and (4-227) was written[a]

$$dv/dt = -B \exp(-Q/T^m)\, y^P \tag{4-234}$$

where

y = irradiation contribution to the strength coefficient (MPa)

T = temperature (K)

t = time (s)

and B, Q, m, and P are positive constants to be evaluated by comparison to the residual strength coefficient data of Table 4-33 through Table 4-35. The procedure used with the rate equation for the annealing of cold work effects [Steps (2) to (5) after Equation (4-227)] was repeated with Equation (4-234) to produce a differential expression for the change in y during a time interval with a linear change in temperature. The differential expression is

$$\frac{1}{y_f^p - 1} = [p-1]B\left[\exp\left(-\frac{Q}{T_f^m}\right)\right]\left[\frac{1-\exp\left(\frac{-Q(T_f-T_i)^m}{T_f^{m+1}}\right)}{\frac{Q(T_f-T_i)^m}{T_f^{m+1}}}\right](t_f - t_i) + \frac{1}{y_i^p - 1} \tag{4-235}$$

where terms with subscripts i refer to initial values and terms with subscripts f refer to final values of the terms in Equation (4-234).

No completely analytical method to obtain a best fit of Equation (4-234) to the data has been found. However, several observations aided in finding values of B, Q, m, and P that provide a fit that is within the scatter of the data.

(1) The factor

a. Since the change in the strength coefficient due to irradiation is modeled as a linear function of fast neutron fluence, one could use the fast neutron fluence in place of the variable y. The net effect would be a change of the constant B.

$$\frac{1-\exp\left(\frac{-Q(T_f-T_i)^m}{T_f^{m+1}}\right)}{\frac{Q(T_f-T_i)^m}{T_f^{m+1}}} \qquad (4\text{-}236)$$

can be viewed as a correction for the fact that the temperature did not remain at T_f throughout the anneal. It is not relevant to the fundamental annealing properties of the cladding.

(2) Increasing m increases the effect of temperature on the change in y because the factor exp $[-Q/(T_f)^m]$ is more sensitive to temperature when m is larger.

(3) Increasing P decreases the sensitivity of the change in y to the time span $t_f - t_i$. This is most easily seen by noting that for large y_i, y_f is proportional to $(t_f - t_i) - 1/(P - 1)$. For large values of P, the 1/(P - 1)-th root of $t_f - t_i$ is relatively insensitive to $t_f - t_i$.

The residual strength data of Table 4-33 and Table 4-35 were fit by trying integral values of m and P and using pairs of residual strengths from Table 4-35 in conjunction with the average value of the as received residual strength (206 MPa) and Equation (4-235) to solve for trial values of Q and B. Predictions of Equation (4-235) with each trial set of m, P, Q, and B were then compared to all the residual strengths in Table 4-33 and Table 4-34. The best fit to the residual strength data was obtained with m = 8, P = 2, Q = 5.35×10^{23}, and B = 4.50×10^{-3}.[a]

Two trivial steps were required to convert Equation (4-235) to the form actually used in MATPRO subcodes.

1. The equation was transformed to an equivalent expression in terms of the initial temperature and heating rate. This transformation allows all the required input information to be parameters at the beginning of a time step. The transformation was carried out by using an alternate linear interpolation for temperature, as noted in conjunction with Equation (4-231).

2. The equation was modified to express the change in residual strength in terms of an effective fluence.

The expression for the rate of annealing of the effective fast neutron fluence for strain hardening [Equation (4-224)] was obtained by assuming that the rate of annealing of the effective fast neutron fluence for the strain hardening exponent is proportional to the rate of annealing of the effective fluence for the strength coefficient. The model development was complicated by the fact that the cladding used to construct the model experienced three periods at high temperature in addition to the actual annealing test.

1. The stress relief anneal

a. The 13.9-K/s anneals to 811 and 866 K were used to find these values of Q and B.

2. The 2-year in-reactor life of the rod

3. The normal thermal transients during postirradiation handling of the rods.[4.10-6]

The effective fast neutron fluence for the strain hardening exponent at the start of the actual annealing test can be estimated from Bauer's as received data (Table 4-30 or Table 4-31). A maximum effective fluence of 8.4 x 10^{22} n/m^2 (for zero effective cold work) was found. Since the measured fast neutron fluence was 4.3 x 10^{25} n/m^2, considerable annealing of the radiation damage component that determines the strain hardening exponent must be assumed either in-reactor or during postirradiation handling of the rods.

The constants used in Equation (4-224) were obtained by (a) assuming as received effective fast neutron fluences in the range 1 x 10^{21} to 8 x 10^{22} n/m^2; (b) determining a constant of proportionality between the annealing rates of effective fast neutron fluences for strength and strain hardening that yields a prediction consistent with the annealing data; and (c) checking the first two steps by applying the annealing model to the in-reactor history to see if the assumed as-received effective fast neutron fluence and annealing rate are consistent. Self consistent results were obtained with an as received effective fast neutron fluence for strain hardening of 2 x 10^{22} n/m^2 and a constant of proportionality of 1,000.

Since no data are available for beta phase annealing, an approximation is necessary. The effective cold works and fast neutron fluences are set equal to zero whenever the temperature is as high as 1,255 K, the approximate equilibrium phase boundary for beta zircaloy.

4.10.4 Comparison of Annealing Models to Data

Table 4-36 and Table 4-37 are comparisons of the predicted strength coefficients and strain hardening exponents to the data base used to construct the annealing models. The limited data for unirradiated cladding appear in Table 4-35. The cladding used in these tests had been 70% cold worked, then stress relieved according to schedules published by Chapman.[4.10-4] Equations (4-221) and (4-223) predict an effective cold work of 50% for the strength coefficient and 4% for the strain hardening exponent after the stress relief anneal. Both strength coefficient and strain hardening exponent are well predicted by the model.

Table 4-36. Comparison of model predictions of K and n with data base for unirradiated cladding.

Heating rate (K/s)	Maximum temperature (K)	Strength coefficient (MPa) from data--predicted		Strain hardening exponent from data--predicted	
As received	644	524	524	0.040	0.040
5.6	811	524	524	0.040	0.040
5.6	866	520	521	0.040	0.047
5.6	894	503	515	0.047	0.062

Table 4-36. Comparison of model predictions of K and n with data base for unirradiated cladding.

Heating rate (K/s)	Maximum temperature (K)	Strength coefficient (MPa) from data--predicted		Strain hardening exponent from data--predicted	
5.6	978	444	457	0.218	0.119
27.8	811	515	524	0.035	0.040
27.8	866	514	524	0.033	0.041
27.8	894	513	522	0.035	0.044
27.8	978	516	505	0.045	0.087

Table 4-37 and Table 4-38 compare model predictions for strength coefficients and strain hardening exponents with corresponding values derived from Bauer's measurements with cold worked and irradiated cladding. No annealing schedule has been published for this material, but published nominal preirradiation values[4.10-7] are consistent with the assumption that the annealing schedule was similar to the unirradiated cladding. Therefore, the effective cold works of 50% and 4% were also used to describe the irradiated cladding.

Table 4-37. Comparison of model predictions of K and n with data base for transient anneals of irradiated cladding.

Heating rate (K/s)	Maximum temperature (K)	Strength coefficient (MPa) from data--predicted		Strain hardening exponent from data--predicted	
As received	644	750.7	765.1	0.040	0.024
As received	644	781.5	765.1	0.039	0.024
As received	644	763.4	765.1	0.028	0.024
As received	644	828.9	765.1	0.037	0.024
0.6	700	758.5	764.6	0.021	0.024
0.6	755	728.5	721.3	0.027	0.024
0.6	811	651.8	574.1	0.023	0.029
0.6	894	397.0	442.7	0.091	0.092
0.6	978	370.1	409.9	0.088	0.100
5.6	700	732.4	765.1	0.020	0.024
5.6	755	769.4	759.9	0.024	0.024

Table 4-37. Comparison of model predictions of K and n with data base for transient anneals of irradiated cladding. (Continued)

Heating rate (K/s)	Maximum temperature (K)	Strength coefficient (MPa) from data--predicted		Strain hardening exponent from data--predicted	
5.6	811	76.5	706.2	0.023	0.025
5.6	866	405.5	598.7	0.029	0.030
5.6	894	385.8	547.0	0.047	0.041
5.6	978	407.1	441.0	0.100	0.083
13.9	755	816.5	762.9	0.024	0.024
13.9	811	739.7	736.9	0.022	0.024
13.9	866	680.5	660.5	0.025	0.026
13.9	894	514.9	511.6	0.021	0.031
13.9	978	384.9	482.9	0.056	0.071
27.8	755	755.4	764.0	0.021	0.024
27.8	811	830.7	750.2	0.027	0.024
27.8	866	772.4	700.6	0.027	0.025
27.8	894	681.8	662.1	0.026	0.027
27.8	978	411.6	532.3	0.034	0.054
27.8	1,033	403.6	476.4	0.046	0.074
27.8	1,144	458.7	439.7	0.083	0.081
27.8	1,255	481.1	428.7	0.100	0.084

Table 4-38. Comparison of model predictions of K and n with data base for isothermal anneals of irradiated cladding.

Heating rate (K/s)	Maximum temperature (K)	Strength coefficient (MPa) from data--predicted		Strain hardening exponent from data--predicted	
644	As received	750.7	765.1	0.040	0.024
644	As received	781.5	765.1	0.039	0.024
644	As received	763.4	765.1	0.028	0.024
644	As received	828.9	765.1	0.037	0.024
700	60	724.8	700.8	0.033	0.024
755	10	683.5	567.7	0.028	0.028
755	60	648.2	512.7	0.030	0.036
811	1	649.7	547.9	0.029	0.032
811	10	425.2	421.9	0.031	0.080
811	30	460.8	409.5	0.050	0.100
866	1	387.9	428.5	0.044	0.080
866	5	417.2	411.3	0.077	0.097
866	30	451.6	408.0	0.096	0.106
894	1	411.3	420.4	0.076	0.088
894	30	483.2	407.8	0.130	0.108
978	1	406.0	414.2	0.074	0.093
978	30	452.5	407.6	0.112	0.110

4.10.5 References

4.10-1 L. M. Howe and W. R. Thomas, "The Effect of Neutron Irradiation on the Tensile Properties of Zircaloy-2," *Journal of Nuclear Materials, 2*, 1960, pp. 248-260.

4.10-2 A. A. Bauer, L. M. Lowry, and J. S. Perrin, *Evaluating Strength and Ductility of Irradiated Zircaloy: Quarterly Progress Report, July-September 1976*, BMI-NUREG-1961, October 1976.

4.10-3 A. A. Bauer, L. M. Lowry, and J. S. Perrin, *Evaluating Strength and Ductility of Irradiated Zircaloy: Quarterly Progress Report, April-June 1976*, BMI-NUREG-1956, July 1976.

4.10-4 R. H. Chapman, *Characterization of Zircaloy-4 Tubing Procured for Research Programs*, ORNL/NUREG/TM-29, July 1976.

4.10-5 J. G. Byrne, *Recovery, Recrystallization and Grain Growth*, New York: The Macmillan Company, 1965.

4.10-6 A. A. Bauer, L. M. Lowry, and J. S. Perrin, *Progress on Evaluating Strength and Ductility of Irradiated Zircaloy During July-September 1975*, BMI-NUREG-1938, September 1975.

4.10-7 A. A. Bauer, L. M. Lowry, and J. S. Perrin, *Evaluating Strength and Ductility of Irradiated Zircaloy: Quarterly Progress Report, October-December 1976*, BMI-NUREG-1967, January 1977.

4.11 Mechanical Limits and Embrittlement (CMLIMT, CBRTTL)

Cladding deformation and failure under stress is characterized by several boundaries that define important changes in the physical response of the cladding to stress. This section is a description of these boundaries and the two subcodes used to model them The first subcode, CMLIMT, defines the elastic-plastic transition and cladding failure under tensile stress. The second subcode, CBRTTL, defines the amount of oxygen the cladding can absorb without becoming brittle.

4.11.1 Summary (CMLIMT)

Cladding mechanical limits are important to code predictions of both the number and shape of failed rods. This section describes expressions used to determine the most important limits, the elastic-plastic transition (yield) and cladding failure under tensile stress, as well as the ultimate engineering strength and the uniform elongation under uniaxial stress.

Failure expressions are related to the amount of detail the user chooses to consider in mechanical models. The fundamental failure criterion is derived for codes that model cladding plastic deformation without assuming azimuthally symmetric deformation. Alternate expressions are presented for less sophisticated codes that assume symmetric deformation, and one simplified correlation is presented for users who do not model plastic deformation at all.

The input parameters for the CMLIMT subcode are temperature, cold work, fast neutron fluences (> 1 MeV), average oxygen concentration, and strain rate. The equations used are

$$\text{true strain at yield} = \left[\frac{K}{E}\left(\frac{\dot{\varepsilon}}{10^{-3}}\right)^{m}\right]^{\frac{1}{(1-n)}} \tag{4-237}$$

$$\text{true yield strength} = \left[\frac{K}{E^{n}}\left(\frac{\dot{\varepsilon}}{10^{-3}}\right)^{m}\right]^{\frac{1}{(1-n)}} \tag{4-238}$$

$$\text{true strain at maximum load} = \frac{n}{1+m} \tag{4-239}$$

$$\text{true ultimate strength} = K\left(\frac{\dot{\varepsilon}}{10^{-3}}\right)^{m}\left(\frac{n}{1+m}\right)^{n} \tag{4-240}$$

where

K	=	strength coefficient (Pa)
E	=	Young's modulus (Pa)
$\dot{\varepsilon}$	=	true strain rate (s^{-1})
n	=	strain hardening exponent (unitless)
m	=	strain rate sensitivity constant (unitless).

K, n, and m are calculated with the subcode CKMN discussed in the description of CSTRES (Section 4.9), E is obtained by calling the function CELMOD (Section 4.6), and e is required input information.

Arguments are presented in Section 4.11.3 that demonstrate that cladding failure should be predicted by comparing the tangential component of true stress to the burst stress. Heating rate and strain rate do not affect this criterion, but irradiation and cold work increase it somewhat. The burst stress as a function of temperature is given by the following equations:

For $T \leq 750$ K,

$$\sigma_{\theta B} = 1.36K_A \ . \tag{4-241}$$

For $750 < T \leq 1{,}050$ K,

$$\sigma_{\theta B} = 46.861429K_A \exp\left(\frac{-1.9901087\times10^{6}}{T^2}\right) \ . \tag{4-242}$$

For $T > 1{,}050$ K,

$$\sigma_{\theta B} = 7.7K_A \ . \tag{4-243}$$

where

$\sigma_{\theta B}$	=	tangential component of true stress at burst (Pa)
K_A	=	strength coefficient for annealed cladding as determined with the MATPRO

CKMN subcode (Pa)

T = temperature (K).

For cold worked or irradiated cladding, the burst stress is increased by four tenths of the increase of the strength coefficient due to irradiation and cold work.

The standard error[a] of Equations (4-241) through (4-243) is

$$U\sigma_{\theta B} = 0.17\sigma_{\theta B} \quad (4\text{-}244)$$

where $U\sigma_{\theta B}$ is the standard error of $\sigma_{\theta B}$.

Section 4.11.2 is a review of the available data. Equations (4-237) through (4-242) are derived in Section 4.11.3, and alternate methods of applying Equation (4-241) are derived in Section 4.11.4.

4.11.2 Available Data

The data reported as yield points, strain at maximum load (uniform strain), and ultimate strength have been reviewed in conjunction with the description of the CSTRES code (Section 4.9). This subsection will review only the data used in development of the CMLIMT subcode failure criterion. The number of these data has been severely restricted by the requirement that they be sufficiently complete to allow an estimate of local stresses and strains at failure.

The most useful data have been produced by the Multirod Burst Test Program sponsored by the NRC. All of these data were obtained with internal heaters and an external steam environment. Heating rates varied from 0 to 28 K/s. Estimated burst temperatures, burst pressures, and burst strains (average circumferential elongation) have been published for a number of single rod tests.[4.11-1,4.11-2] In addition, calibrated photographs of cross-sections through the burst regions of some of the tests have been published.[4.11-2 to 4.11-5] These cross-sections were needed to estimate wall thickness at burst[b] for the calculation of local stress at failure. The other required information for the local stress analysis developed in Section 4.11.3 is an estimate of the axial radius of curvature at burst. This information was not published but could be estimated from side view photographs of the burst tubes.[4.11-6 to 4.11-8] Table 4-39 is a summary of the Multirod Burst Test Program Data used.

a. The standard error of a model is estimated with a set of data by the expression: (sum of squared residuals/number of residuals minus the number of constants used to fit the data)$^{1/2}$.

b. Most burst edges displayed one or more cleavage-like lines approximately 45 degrees from the radial direction. The wall thickness was measured adjacent to this line or, if the line could not be distinguished, 0.25 mm from the burst tear.

Table 4-39. Summary of multirod burst test data employed in CMLIMT.

Test no.	Burst temperature (K)	Differential pressure at burst (MPa)	Average circumferential strain (m/m)	Wall thickness at burst (mm)	Axial radius of curvature (cm)
PS-10	1,174[a]	6.000[a]	0.20[a]	0.079[c]	2.1[c]
PS-17	1,051[a]	12.130[a]	0.25[a]	0.176[c]	1.2[c]
PS-18	1,444[a]	0.772[a]	0.24[a]	0.111[d]	0.9[g]
PS-19	1,232[a]	2.590[a]	0.28[a]	0.079[c]	0.6[c]
SR-23	1,350[a]	0.960[a]	0.35[a]	0.164[e]	1.1[h]
SR-25	1,365[a]	0.960[a]	0.78[a]	0.077[e]	0.6[i]
SR-34	1,039[b]	5.820[b]	0.316[b]	0.109[b]	1.6[c]
SR-35	1,048[b]	4.470[b]	0.290[b]	0.073[f]	3.1[c]
SR-37	1,033[b]	13.560[b]	0.231[b]	0.263[f]	3.7[c]
SR-41	1,030[b]	9.765[b]	0.274[b]	0.199[b]	2.7[c]
SR-43	1,046[b]	7.620[b]	0.290[b]	0.179[b]	3.5[c]

a. 4.11-1.
b. 4.11-2.
c. From photographs sent by R. H. Chapman.
d. 4.11-3.
e. 4.11-4.
f. 4.11-5.
g. 4.11-6.
h. 4.11-7.
i. 4.11-8.

Data from tests by Hobson and Rittenhouse[4.11-9] were also employed. The Hobson-Rittenhouse tests were conducted using a radiant heating furnace on BWR cladding in an argon environment with heating rates from 5.6 to 56 K/s. There was no significant difference in the local failure stress predicted from the Hobson-Rittenhouse tests conducted in argon and that predicted from the tests in a steam environment. It is possible that longtime tests in steam will show a difference in local stress at failure. However, it is also possible that specimens that accumulate thick, oxygen rich layers before significant deformation occurs will show that the oxygen rich layers of the cladding rupture before the oxygen poor layers. In the latter case, oxidation would have a significant effect on the early (small strain) deformation but little effect on the stress at failure.

Table 4-40 is a summary of the data that were used from the tests of Hobson and Rittenhouse. Burst temperatures, wall thickness measurements, and the average circumferential elongation were obtained

from figures in Reference 4.11-9. Burst pressures were obtained by private communication from Chapman, and axial radii of curvature were estimated from samples sent by Hobson.

Table 4-40. Summary of data from the Hobson-Rittenhouse tests.

Test no.	Burst temperature (K)	Differential pressure at burst (MPa)	Average circumferential strain (m/m)	Wall thickness at burst (mm)	Axial radius of curvature (cm)
35	1,061	6.170	0.63	0.25	2.9
34	1,081	7.584	0.58	0.23	1.8
40	1,111	4.654	0.79	0.18	1.8
18	1,145	4.826	1.25	0.18	3.0
17	1,158	4.205	0.57	0.20	2.5
19	1,160	4.895	0.51	0.23	1.8
21	1,171	3.102	0.30	0.18	1.7
8	1,179	3.826	0.22	0.20	1.3
16	1,195	3.999	0.42	0.25	1.7
5	1,196	3.757	0.44	0.20	1.0
26a	1,205	3.068	0.27	0.28	1.8
27	1,213	2.241	0.55	0.15	1.1
15	1,214	2.275	0.41	0.18	1.1
37	1,215	2.344	0.40	0.18	1.4
26	1,220	3.033	0.53	0.13	1.5
9	1,235	1.448	0.43	0.20	2.7
28	1,253	1.413	0.85	0.18	2.8
11	1,299	1.434	0.68	0.25	1.5
32	1,302	0.745	0.93	0.25	2.1
29	1,432	0.676	0.92	0.23	2.5
36	1,440	0.827	0.50	0.23	1.5
4	1,472	0.689	1.11	0.20	2.5
36a	1,487	0.662	0.74	0.25	1.5

Table 4-41 is a summary of data obtained by Chung and Kassner[4.11-10] that were used in the development of the CMLIMT code. The burst temperature, differential pressure at burst, average circumferential strain, and axial radius of curvature were obtained from Reference 4.11-10. The wall thickness at burst was obtained from photographs of cross-sections from Chung by private communication. An important factor is that all of the samples in Table 4-41 were constrained by an internal mandrel, which applied an unknown axial stress to the cladding.

Table 4-41. Summary of data from the Chung-Kassner tests.

Test no.l	Burst temperature (K)	Differential pressure at burst (MPa)	Average circumferential strain (m/m)	Wall thickness at burst (mm)	Axial radius of curvature (cm)
AS-40	1,089	5.302	1.01	0.39	2.9
AS-36	1,310	0.558	1.11	0.26	2.9
AS-9	1,329	1.282	1.24	0.12	3.2
AS-5	1,348	1.334	1.02	0.42	1.6

None of the data mentioned so far were obtained from irradiated cladding or at temperatures below 1,000 K. The only available low temperature data with irradiated cladding were obtained from studies by Bauer, Lowry, Gallagher, Markworth and Perrin[4.11-11 to 4.11-13] on cladding obtained from the H. B. Robinson reactor. The data from Bauer's tests which have been used in the development of CMLIMT are presented in Table 4-42. Tests M12-16, M-12-4, and M12-15 were conducted on as received cladding; while Tests D9-7, D9-8, D9-13, and D9-14 were conducted on cladding that had been annealed. Wall thicknesses adjacent to the burst were obtained from unpublished photographs similar to Figure 7 of Reference 4.11-11. The axial radii of curvature in these tests have not been reported.

Table 4-42. Summary of data from the Bauer tests.

Test no.	Burst temperature (K)	Burst strength (MPa)	Average circumferential strain (m/m)	Wall thickness at burst (mm)
M12-16	477[a]	749.4	0.026	0.57
M12-4	644	659.1	0.052	0.60
M12-15	644	684.6	0.028	0.61
D9-7	644[b]	356.4	0.212	0.45
D9-8	644	350.9	0.204	0.46
D9-13	644	372.3	0.225	0.51
D9-14	644	367.5	0.292	0.48

a. From Reference 4.11-12. b. From photographs sent by Bauer and Lowry.

Two sources of in-reactor data were employed. One is the irradiation effects Test IE-5, conducted in the Power Burst Facility at the INEL.[4.11-14,4.11-15] The measured (Rod IE-19) internal pressure in this test was reported to be 5.2 MPa in excess of the coolant pressure, and the cladding temperature was estimated from microstructure studies to be near 1,100 K. The average circumferential elongation was reported to be 25%.[4.11-15] The wall thickness at burst was estimated to be 0.09 mm, using figures from the postirradiation examination results report;[4.11-15] and the axial radius of curvature was estimated to be approximately four times the rod diameter from the posttest side view in Reference 4.11-15.

The second source of in-reactor data is a series of tests in the FR2 reactor in Germany.[4.11-16] Complete data from three tests (A2.3, B1.2, and B1.3) were presented, but two of the cladding cross-sections showed evidence of contact with the shroud (burst edges rolled in). For that reason, only data from Test B1.2 were used. The average circumferential elongation, axial radius of curvature, burst pressure, and temperature for this test were taken from Reference 4.11-16 (0.249, 1.5 cm, 4.52 MPa, and 1,188 K).

The coolant pressure was assumed to be the typical value of 0.3 MPa quoted in Reference 4.11-16.

One out-of-pile test result from Germany[4.11-17] was used in developing the CMLIMT failure model. The test was performed in air (one atmosphere) with an internal heater. The burst temperature, internal pressure at burst, average circumferential strain, and wall thickness at burst (1,114 K, 7.1 MPa, 0.37, and 0.215 mm) were taken from Reference 4.11-17. The axial radius of curvature was estimated to be approximately three times the cladding radius at burst by inspection of x-ray photos of similar tests just prior to burst.

4.11.3 Model Development

The expressions used to describe the elastic-plastic transition (yield) do not correspond to the usual definition of yield (stress at 0.2% strain). In order to provide expressions that are consistent with code requirements for continuous stress-strain expressions, the yield point is taken to be the nonzero intersection of the stress-strain curves given by Hooke's law for the elastic region

$$\sigma = E\varepsilon \tag{4-245}$$

and by the modified power law used in CSTRES and CSTRAN for the plastic region

$$\sigma = K\varepsilon^{n}(\dot{\varepsilon}\times 10^{3})^{m} \tag{4-246}$$

where

σ = true stress (Pa)

E = Young's modulus (Pa)

ε = true strain (unitless)

K = strength coefficient (Pa)

n = strain hardening exponent (unitless)

$\dot{\varepsilon}$ = true strain rate (s^{-1})

m = strain rate sensitivity exponent (unitless).

Solution of these simultaneous equations gives the yield strain and yield strength described by Equations (4-237) and (4-238), respectively.

The point of maximum load in a one-dimensional stress test at constant engineering strain rate is found by converting the true stress and true strain rate in Equation (4-246) to their engineering equivalents

$$\sigma = (S) \exp(\varepsilon) \tag{4-247}$$

$$\dot{\varepsilon} = \frac{\dot{e}}{\exp(\varepsilon)} \tag{4-248}$$

where

S = engineering stress (Pa)

$\dot{e}$ = engineering strain rate (s^{-1}).

The derivative of S with respect to ε is zero at the true strain given by Equation (4-239), and the true stress at this strain is given by Equation (4-240).

The development of Equation (4-243) was preceded by a review of several different cladding failure criteria in use. Two previously used criteria, average circumferential elongation and engineering hoop stress, were rejected because they ignore the effect of local wall thinning and because this effect is now realized to vary considerably from test to test.[4.11-4,4.11-10,4.11-16] Two other possible criteria, strain rate at failure and strain-fraction rules (strain increment/strain at failure), were considered and rejected because these criteria would require a considerable collection of strain-versus-time data. Such a collection did not exist in the publicly available literature at the time the model was developed. The remaining criteria, local strain at failure and local stress at failure, were investigated with the data presented in Section 4.11.2.

Local strain at failure was determined using the measured wall thickness adjacent to the burst[a]

a. Since the material is not compressible, the sum of the axial and circumferential strains is ε_r.

$$\varepsilon_r = \ln\left(\frac{t_B}{t_0}\right) \tag{4-249}$$

where

ε_T = true radial strain at burst

t_o = initial cladding wall thickness

t_B = cladding wall thickness adjacent to burst.

Figure 4-50 is a plot of the local radial strains at burst versus temperature. The relevant observations are:

1. The scatter of the local strains at failure is much smaller than the scatter of the average circumferential strains at failure for these tests. The average strains are shown in Figure 4-51.

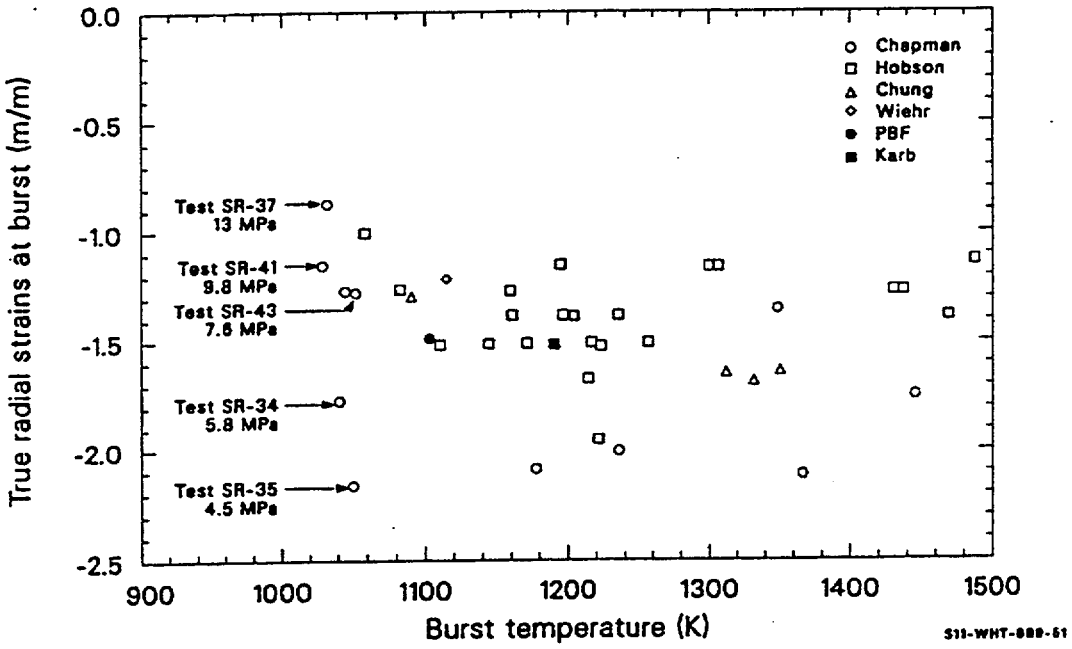

Figure 4-50. Local radial strains at burst versus temperature.

2. An important series of tests by Chapman (SR-37, SR-41, SR-34, and SR-35), with decreasing pressures and heating rates but similar heaters, burst temperatures, and average circumferential elongations, show a regularly decreasing wall thickness (more negative radial strain) with decreasing pressure. The Chapman data are identified by test number and burst pressure in Figure 4-50.

These observations suggest that the local stress is the common parameter of cladding about to burst. The data in the plot of local strains at failure versus temperature are scattered by neglected variations in

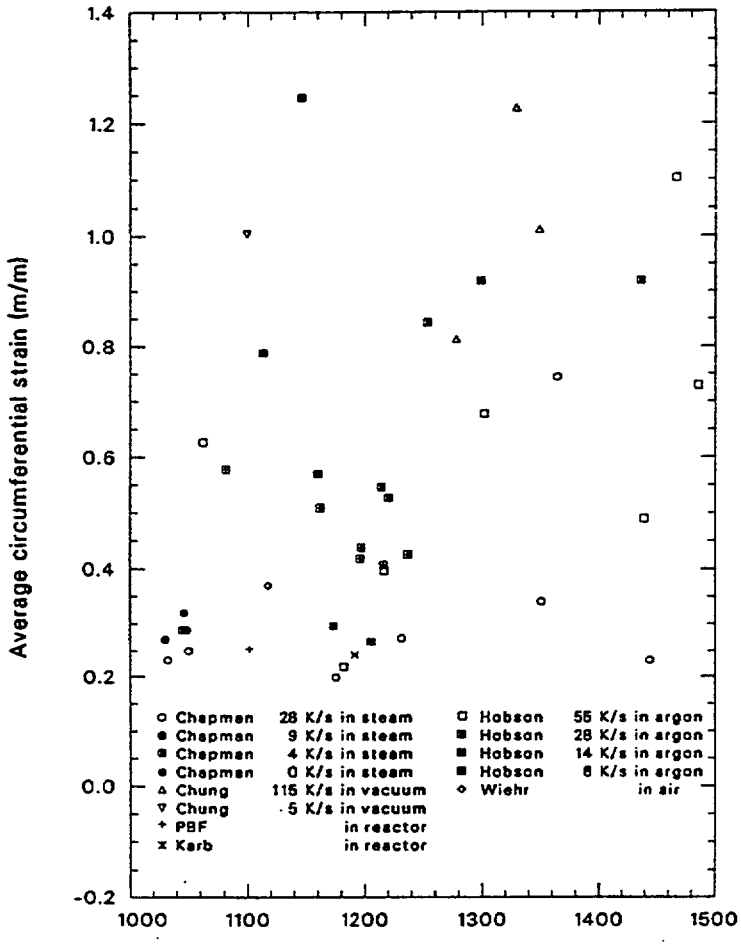

Figure 4-51. Average circumferential strains at failure versus temperature.

circumferential radii of curvature, axial radii of curvature, and burst pressure; and the data in the plot of average circumferential strains at failure are scattered further by circumferential variations in strain. More evidence for using stress as the failure criterion is provided by the observations that (a) failure cross-sections usually show a fracture surface or surfaces at 45° to the tangential direction and in the direction of maximum shear stress and (b) the fracture line is usually longitudinal. In cases where the fracture line is circumferential, there is good reason to suspect large axial stress components (Reference 4.11-10).

Local stresses at failure were estimated from the data presented in Section 4.11.2 and the equilibrium equation for a membrane element at the moment of failure[4.11-18]

$$\frac{\sigma_{ZB}}{r_Z} + \frac{\sigma_{\theta B}}{r_\theta} = \frac{P_B}{t_B} \qquad (4\text{-}250)$$

where

σ_{ZB} = axial stress at burst (Pa)

$\sigma_{\theta B}$ = tangential stress at burst (Pa)

P_B = difference between gas pressure and coolant pressure at burst (Pa)

r_z = axial radius of curvature at burst (m)

r_θ = circumferential radius of curvature at burst (m)

t_B = cladding thickness at burst (m).

Two approximations are needed to deduce $\sigma_{\theta B}$ from Equation (4-250) and the data presented in Section 4.11.2. The first approximation is that the azimuthal cross-section shortly before burst is approximately circular

r_θ = undeformed radius (1 + average circumferential strain). (4-251)

The second approximation is needed to estimate σ_{ZB}. The range of possible values for σ_{ZB} is severely limited by physical considerations. It must have been greater than the yield stress for significant ballooning to occur,[4.11-18] and it must have been less than $\sigma_{\theta B}$ for the failure to occur along an axial line. Since r_z is typically several times r_θ, the first term of Equation (4-250) is small; and any value of σ_{ZB} in the range between the yield stress and $\sigma_{\theta B}$ will estimate the first term of the equation with an uncertainty that is less than the uncertainty in the terms containing r_θ and t_B. The CMLIMT expression for failure stress was developed with the assumption that the axial and tangential stresses are nearly equal to burst because that assumption tends to underpredict $\sigma_{\theta B}$, while the assumption of Equation (4-251) tends to overpredict $\sigma_{\theta B}$.[a] The resultant expression for the tangential stress at burst is

$$\sigma_{\theta B} = \frac{P_B}{t_B}\left(\frac{1}{\frac{1}{r_z}+\frac{1}{r_\theta}}\right) . \quad (4\text{-}252)$$

Figure 4-52 is a plot of the local tangential failure stress obtained from Equation (4-252) and the data reviewed in Section 4.11.2. Approximate heating rates during burst are indicated to show that there is no systematic variation with heating rate. Comparison of the burst stresses obtained from Hobson's tests with both Chapman's tests and the two in-reactor data show that there is no significant effect of oxide films or alpha layers on the burst stress, at least at heating rates used in these tests. The most probable interpretation

a. Local ballooning will cause the actual value of r_θ to be less than the value predicted with Equation (4-250).

of this observation is the suggestion that the relatively thin oxide and alpha layers are cracked before the burst stress of the underlying beta layers is achieved.

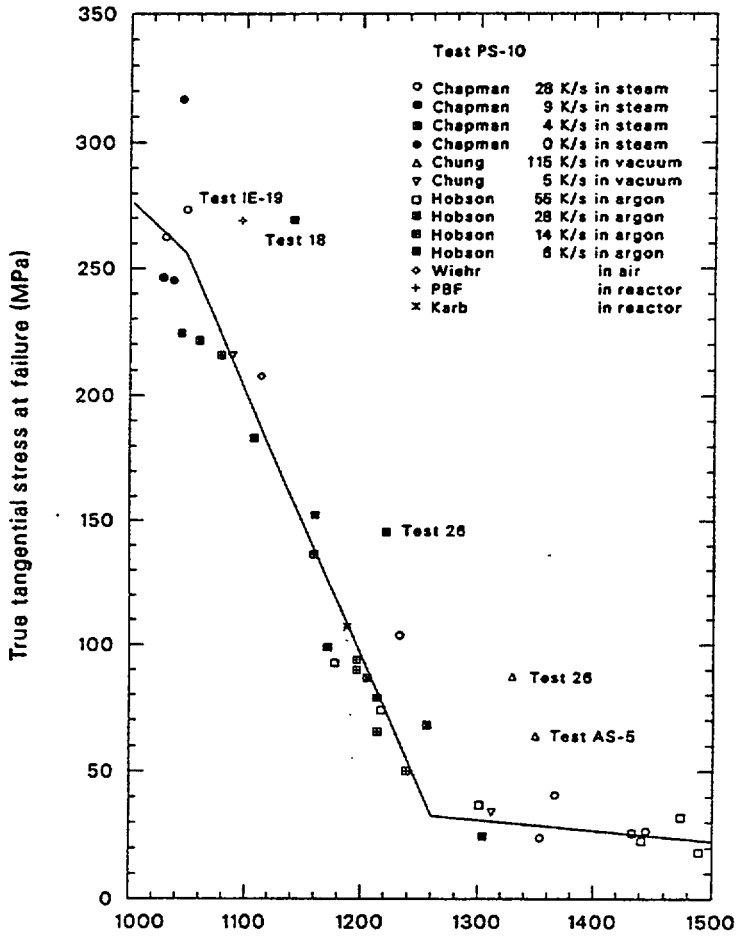

Figure 4-52. Local tangential stress at failure versus temperature.

Most of the burst stresses shown in Figure 4-52 are located near a curve that looks very similar to the plot of the strength coefficient for plastic deformation, which was obtained in Figure 4-35 of Section 4.9.3.2. The exceptions are not scattered randomly about the curve. They all lie above the curve. Upon closer inspection, it was noticed that the tests that yielded unusually high tangential burst stresses had some feature which caused one of the assumptions used in calculating tangential burst stress to be questionable. These features are discussed, test by test, in the next several paragraphs. The exceptional data are individually labeled in Figure 4-52.

In the PBF Test IE-5 (Rod IE-19), the maximum temperature of the cladding burst region was determined by metallography to be approximately 1,100 K. Postirradiation examination results[4.11-15] show that the maximum temperature of the fracture area was less than the maximum cladding temperature at

other azimuthal locations in the axial plane of the fracture. The interpretation given to this information in the postirradiation examination results report is that 1,100 K was also the burst temperature because no increase in temperature could have occurred on the protruding fracture tips. This conclusion may be slightly overstated. The Test Results Report[4.11-19] shows that the adjacent 45° thermocouple, which also protruded, experienced a 50 K temperature rise after the initial increase. It is therefore probably more realistic to estimate the burst temperature of the cladding in Rod IE-19 at 1,000 to 1,050 K.

Test PS-10 from Chapman's studies was performed with a heater which had an unusually large circumferential variation in temperature.[4.11-20] In this case, very local ballooning is likely; and Equation (4-251) is probably a poor approximation for the circumferential radius of curvature near burst. Because of the questionable validity of Equation (4-251) for this test and because of the large difference between the calculated burst stress of this test and several other data obtained at similar burst temperatures, this test was omitted from the CMLIMT failure analysis.

Test 18 from the Hobson-Rittenhouse series burst at a thermocouple temperature of 1,145 K, yet had an average circumferential strain characteristic of temperatures in the alpha phase. Moreover, the axial profile of this test is almost triangular (Reference 4.11-9). In all probability, the axial radius of curvature in Table 4-40 (estimated from the bottom half of the sample) is much too large. The test was therefore eliminated from the CMLIMT data base.

Test 26 from the Hobson-Rittenhouse series is the only sample in the entire test series that did not exhibit approximate mirror symmetry of wall thickness about a plane through the burst area and the cladding centerline. In this test, one half of the cross-section is essentially undeformed, and one half is uniformly thin. Thus, both the axial and circumferential radii of curvature estimated for this test are questionable; and the test was removed from the CMLIMT data base.

Tests AS-9 and AS-5 by Chung are the most difficult of all the data shown in Figure 4-52 to understand. One might assume that the constraining mandrel used in these tests caused a large axial stress that somehow perturbed the test; however, the argument given in conjunction with Equation (4-252) shows that the local axial stress near the failure area was between the yield and the burst stresses. Moreover, Test AS-36, which differed only in heating rate from AS-5 and AS-9, does not differ from the Hobson or Chapman tests that burst at similar temperatures. Tests AS-5 and AS-9 were tentatively removed from the CMLIMT data base solely because they differ markedly from the two tests by Chapman that were conducted in steam with an internal heater, two features that are believed to make Chapman's tests more representative of in-reactor cladding failure.

The remaining data shown in Figure 4-52 and reviewed in Section 4.11.2 were used to find an expression for the tangential burst stress at failure above 1,000 K. The failure stress was divided by the strength coefficient used with Equation (4-246), and the quotients were averaged. For the alpha phase data with burst temperatures above 1,000 K, the average quotient is 7.48 ± 0.91; for the alpha $\pm$ beta region, it is 7.54 ± 1.03; and for the beta phase, it is 8.14 ± 1.84. Since there is no significant variation of the quotient, the average obtained for the entire temperature range above 1,000 K, 7.70 ± 1.29, was used to produce Equations (4-243) and (4-244).

Equations (4-251) and (4-252)[a] were also used with the low-temperature data of Table 4-42 in an attempt to find low temperature failure stresses. In this case, the ratios of failure stress to strength

coefficient obtained were much smaller than those of the high temperature data 0.84 ± 0.03 for the annealed cladding and 0.80 ± 0.06 for the irradiated cladding. These ratios were not used for the CMLIMT failure stress correlation because the axial radii of curvature used to calculate them were assumed. Instead, the measured failure strains were used with Equation (4-246), an assumed strain rate sensitivity exponent of zero, and typical anisotropy coefficients[a] to calculate failure stresses consistent with Equation (4-244) and the measured strain. The approximation is more reasonable than guessing axial radii of curvature at low temperature because (a) the unknown strain rate at failure is unimportant at low temperature and (b) the stress strain curve at low temperature is very flat; (i.e., small uncertainties in stress are equivalent to large uncertainties in strain). The factor of 1.36 for annealed cladding and an increase of burst strength equal to four-tenths of the increase in the strength coefficient due to cold work or irradiation in Equation (4-241) reproduce the failure strains listed in Table 4-42. Equation (4-242) is simply an assumption contrived to extrapolate between the two regions where data are available without producing unreasonable predictions for failure strain in the temperature range where it is used.

4.11.4 Application of the Failure Criterion to Determine Cladding Shape After Burst

Equations (4-241) through (4-243) are sufficient to provide a complete description of both the time of cladding failure and the shape of failed cladding if they are used with an equation of state for plastic deformation and a mechanical code that models circumferential and axial variations in strain as a function of applied stress and time. The expressions derived in this section are intended as consistent alternatives to the direct use of Equations (4-241) through (4-243). They also illustrate the effect of deformation history on cladding shape after burst.

The first alternate expression is intended for use with codes like the FRAP-T5 ballooning subcode,[4.11-18] which treat asymmetric deformation but do not calculate local stress. The recommended test for failure is a comparison of wall thickness to the minimum wall thickness given by the following approximate expressions for the strain at failure in a azimuthally symmetric test:

$$\varepsilon_r = \varepsilon_{\theta SYM} \tag{4-253}$$

and

$$\varepsilon_{\theta SYM} = \ln\left(\frac{\sigma_{ZB} t_0}{2 P_B r_Z} + \left(\frac{t_0 \sigma_{\theta B}}{P_B r_0}\right)^{1/2} + \frac{1}{2}\left(\frac{\sigma_{ZB} t_0}{P_B r_Z}\right)^2\right) \tag{4-254}$$

where

ε_r = local true radial strain at failure (m/m)

a. The axial radius of curvature was assumed to be three times the circumferential radii of annealed cladding and infinite for the irradiated cladding.

a. The irradiated cladding was assumed to be isotropic when effective stress and strains were calculated, but the annealed cladding was assumed to have the typical anisotropy coefficients given in Section 4.10.

$\varepsilon_{\theta SYM}$ = true tangential strain at failure for azimuthally symmetric deformation (m/m)

σ_{ZB} = axial component of true stress at burst (Pa)

t_o = initial cladding wall thickness (m)

P_B = pressure differential across cladding at burst (Pa)

r_z = axial radius of curvature at burst (m)

$\sigma_{\theta B}$ = tangential component of true stress at burst (Pa) given by Equation (4-241) through (4-243)

r_o = initial cladding radius (m).

If ballooning is neglected ($r_z = \infty$), Equation ((4-254)) reduces to

$$\varepsilon_{\theta SYM} = \ln\left(\frac{r_{\theta B}}{S_{\theta B}}\right)^{1/2} \quad (4\text{-}255)$$

where $S_{\theta B}$ is the tangential component of engineering stress at burst (Pa). An outline of the derivation of Equation (4-254) follows:

1. Following Reference 4.11-21, the cladding deformation is considered to be composed of the strain for cylindrical deformation plus a perturbation due to ballooning. Axial strains for isotropic, closed-tube, cylindrical deformation are zero; and it is shown in Reference 4.11-21 that the change in axial strain due to a balloon with negligible tangential displacement is also zero. It is, therefore, reasonable to assume that the axial strain for typical bursts is small compared to the radial and tangential strains.

2. From the incompressibility relation (true strains sum to zero) and Step 1, the true radial strain equals the negative of the true tangential strain in an azimuthally symmetric burst test.

3. For an azimuthally symmetric burst test, the circumferential radius of curvature and the cladding thickness at burst are related to their initial values through the tangential strain

$$r_\theta = r_0 \exp(\varepsilon_{\theta SYM}) \quad (4\text{-}256)$$

$$t_B = t_0 \exp(-\varepsilon_{\theta SYM}) \; . \quad (4\text{-}257)$$

4. Substitution of Equations (4-256) and (4-257) into Equation (4-250) and a Taylor series expansion with

$$\frac{\sigma_{ZB}}{r_Z} \ll \frac{\sigma_{\theta B}}{r_\theta} \tag{4-258}$$

yields Equation (4-246) for $\varepsilon_{\theta SYM}$.

5. If the burst test does not have azimuthal symmetry, Equation (4-256) will overpredict the circumferential radius of curvature[4.11-18] and Equation (4-257) will overpredict the cladding wall thickness at failure. However, this is not a serious fault because the local deformation near failure is very rapid. The average strains, and thus the average elongation, will be only slightly underpredicted by using Equations (4-256) and (4-254) to predict strain at failure.

The second alternate set of expressions for determining cladding shape after failure and burst stress at failure are intended for codes that assume azimuthally symmetric cladding plastic deformation in spite of known temperature differences during the burst. An approximate expression for the effect of temperature variation on circumferential elongation was obtained by correlating to data taken at temperatures near 1,050 K.[4.11-10,4.11-22] The data and least-squares correlation used to describe them are shown in Figure 4-53. The least-squares expression obtained by fitting an exponential function to the data is

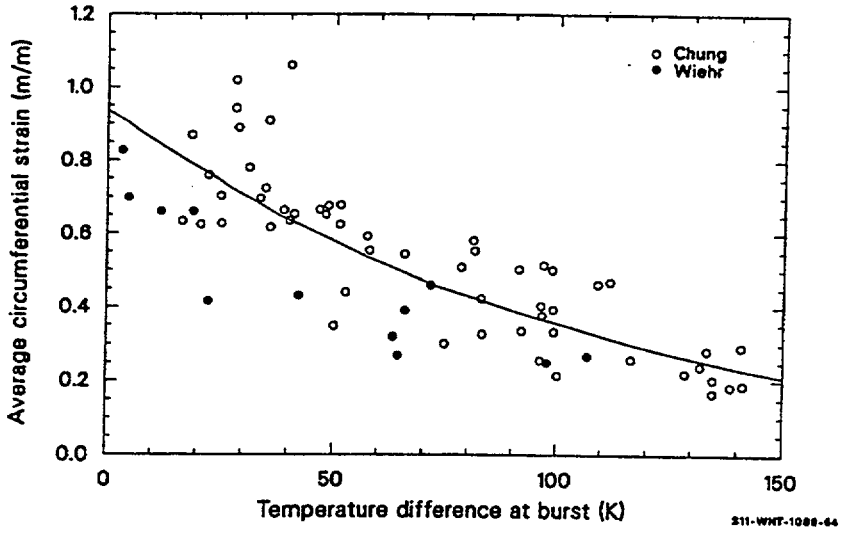

Figure 4-53. Base data and MATPRO correlation for effect of temperature variation on average circumferential elongation.

$$\varepsilon_\theta = -0.94\exp(-0.01\Delta T) \tag{4-259}$$

where

$$\bar{\varepsilon}_\theta = \frac{\text{Circumferential at burst} - \text{initial circumference}}{\text{initial circumference}}$$

ΔT = approximate temperature difference during burst (K).

If the 0.94 of Equation (4-257) is replaced by the more general expression of Equation (4-254), the resultant expression for the average circumferential elongation in a typical burst test near 1,050 K is

$$\bar{\varepsilon}_\theta = \left[\left(\frac{t_0 \sigma_{\theta B}}{P_B r_0}\right)^{1/2} - 1\right] \exp(-0.01\Delta T) \tag{4-260}$$

where ΔT is the estimated temperature variation around the circumference during burst (K) and the other symbols have been defined previously.

A mechanical model that assumes azimuthal symmetry cannot independently calculate the average circumference and the maximum stress of asymmetric deformation. However, it is possible to define an effective stress that is consistent with Equations (4-257) and (4-241). This effective burst stress is derived by considering the three cross-sections shown in Figure 4-54.

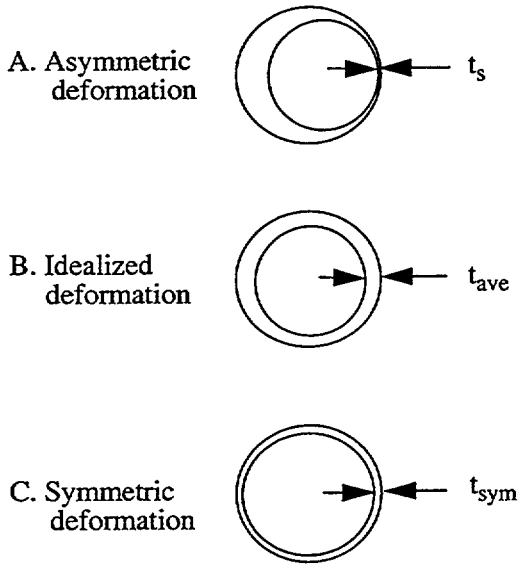

Figure 4-54. Schematic cross-sections of cladding at burst.

Figure 4-54A represents the actual asymmetric cladding with local thinning at a hot spot and relatively little deformation elsewhere. Figure 4-54B represents an idealized symmetric deformation modeled by analytical codes that do not consider asymmetric deformation. The circumferences of Figure 4-54A and Figure 4-54B are equal. Figure 4-54C represents a symmetrically deformed cladding with true stress equal to the maximum hoop stress of the actual asymmetric cladding.

The maximum tangential component of true stress of the asymmetric deformation is approximately

$$\sigma_{\theta B} = \frac{P_B r_a}{t_B} \tag{4-261}$$

where r_a is the radius of the cladding (m) and other symbols have been defined previously. The circumferential stress which will be used to predict the idealized deformation is

$$\sigma_{\theta B} = \frac{P_B r_a}{t_{ave}} \tag{4-262}$$

where t_{ave} is the wall thickness of the cladding predicted with idealized symmetric deformation (m). From Equations (4-261) and (4-262), the tangential stress at failure calculated with idealized deformation is related to the true burst stress by the equation

$$\sigma_{\theta B} = \sigma_{\theta B} \frac{t_B}{t_{ave}} \ . \tag{4-263}$$

The ratio t_B/t_{ave} in Equation (4-263) is related to the reduction in circumferential elongation at failure. Since the maximum true local stress of asymmetric deformation and the circumferential stress of symmetric deformation are both equal to the burst stresses,

$$\frac{P_B r_a}{t_B} = \frac{P_B r_{SYM}}{t_{SYM}} \tag{4-264}$$

where

r_{SYM} = radius of symmetrically deformed cladding (m)

t_{SYM} = wall thickness of symmetrically deformed cladding (m)

and the other terms were defined previously.

The incompressibility relations with the simplifying assumption that axial strain is less than radial or circumferential strain imply that the areas of the idealized and symmetrically deformed cladding are equal. This in turn implies

$$r_a t_{ave} = r_{SYM} t_{SYM} \tag{4-265}$$

Equations (4-264) and (4-265) can be combined to show

$$\frac{t_B}{t_{ave}} = \left(\frac{r_a}{r_{SYM}}\right)^2 . \tag{4-266}$$

The radii r_a and r_{SYM} are related to the circumferential elongation of A and C, (Figure 4-54)

$$r_a = r_0(1.0 + \varepsilon_\theta) \tag{4-267}$$

$$r_{SYM} = r_0(1.0 + \varepsilon_{\theta SYM}) = r_o \exp(\varepsilon_{\theta SYM}) \tag{4-268}$$

where r_o is the initial radius of the cladding.

Substitution of Equation (4-255) into Equation (4-268), Equations (4-267) and (4-268) into Equation (4-266), and the resultant expression into Equation (4-263) yields the following result for effective burst stress

$$\sigma_{\theta B} = S_{\theta B}(1 + \varepsilon_\theta)^2 \tag{4-269}$$

where $\sigma_{\theta B}$ is the effective burst stress to be used when azimuthally symmetric deformation is assumed in spite of known circumferential temperature differences.

The instability strain returned by CMLIMT is also determined with the correlation for typical strain distribution. The expression used in the CMLIMT subcode for instability strain is

$$\bar{\varepsilon}_{\theta l} = \max\left\{\begin{array}{c} 0.05 \text{ or} \\ \left(\frac{1.15Kt_0}{10^{2m_p}r_0}\right)^{1/2} - 1 \end{array}\right\} \exp\left(\frac{-\Delta T}{100}\right) \tag{4-270}$$

where

$\bar{\varepsilon}_{\theta l}$ = $\dfrac{\text{circumference at instability} - \text{initial circumference}}{\text{initial circumference}}$

P = pressure differential across cladding (Pa).

Equation (4-270) was derived by setting the true strain rate in Equation (4-246) equal to 10^{-1}/s and employing the following simplifying assumptions:

1. Isotropic texture coefficients and closed tube stress radios were assumed ($\sigma = 0.866\sigma_\theta$ and $\varepsilon = \varepsilon_\theta / 0.866$),

2. $\sigma_\theta = S_{\theta exq}(2\varepsilon_\theta)$,

3. Equation (4-259) relates average strain to symmetric strain at instability as well as at burst.

The third alternate expression for describing cladding failure is intended for users who choose to ignore all the details of the deformation history of the cladding. The quantity returned is a typical engineering burst stress obtained by correlating tests without regard for either the distribution of strain during the tests or the variation of pressure and temperature with time during the test. If the user is willing to accept the uncertainty associated with using typical burst stresses (pressure) for a given temperature, he can use this relation with all of the previous relations to determine typical average circumferential elongations as a function of burst temperature and the circumferential temperature variation during burst. The correlation used for typical engineering burst stresses is

$$\log_{10}(S) = 8.42 + T[2.78 \times 10^{-3} + T(-4.87 \times 10^{-6} + T\ 1.49 \times 10^{-9})] \quad (4\text{-}271)$$

where

S = typical engineering hoop stress at burst (Pa)

T = temperature at rupture (K).

Equation (4-271) was obtained by correlating engineering burst stress to burst temperature using data obtained from several sources.[4.11-9,4.11-23 to 4.11-29] Since all information about the local stress and strain has been ignored in producing this correlation, it provides only a typical engineering burst stress as a function of temperature.

Figure 4-55 shows typical average tangential strains as a function of temperature obtained by substituting typical engineering burst stresses from Equation (4-271), true stress at burst from Equation (4-241), and several assumed temperature differences during burst into Equation (4-260).

4.11.5 Summary (CBRTTL)

Cladding may fail because of embrittlement by oxygen. In embrittled cladding, failure occurs at low temperatures with no plastic strain. Several hypothetical reactor transients can cause cladding to reach the high temperature necessary for extensive oxygen diffusion. These transients include power cooling mismatch, reactivity insertion, and loss of coolant. In the cooling following these transients, the cladding will be subjected to thermal stresses that may cause its fragmentation. Therefore, oxygen embrittlement is an important safety consideration.

A model is presented in this report defining limits for the amount of oxygen that may diffuse into zircaloy without causing it to become embrittled. This model is restricted to outside oxidation.

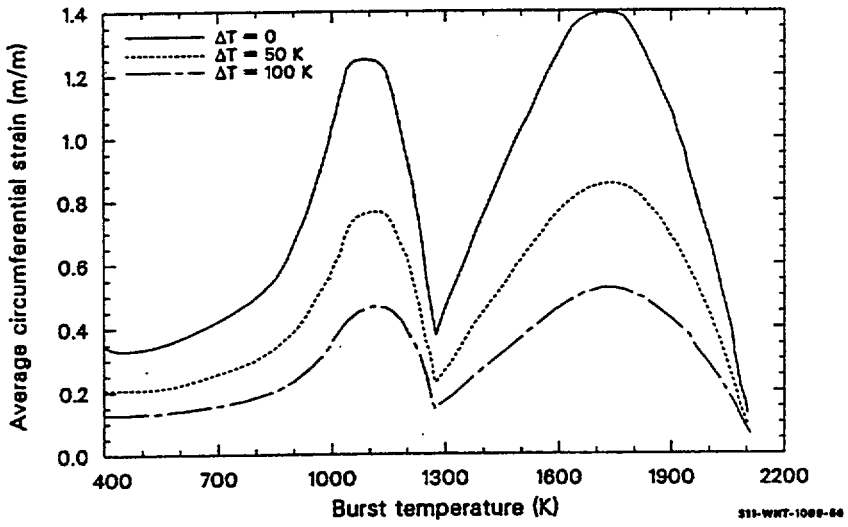

Figure 4-55. Typical average circumferential strains predicted by the MATPRO correlations for typical engineering burst stress, true burst stress, and typical strain distributions at three different temperature differences

The model deals with cladding that has reached a temperature of at least 1,244 K at least once in its lifetime. At this point, zircaloy has completed a phase transition from its low temperature, hexagonal, close packed structure, called the alpha phase, to a body centered cubic structure called the beta phase. This threshold is chosen because oxygen uptake increases exponentially with temperature and, for typical postulated transients, not enough oxygen to cause embrittlement will diffuse into the cladding until beta temperatures are reached. However, for transients lasting more than about one half hour at around 1,300 K, the model is not adequate. The model is divided into two parts to account for both fast and slow cooling rates.

For fast cooling rates (> 100 K/s) such as are found following film boiling, the cladding is characterized as embrittled if:

1. The oxygen concentration in the beta phase is greater than 90% of the saturation concentration at the beginning of the fast quench,

2. The average oxygen concentration in the beta phase exceeds 0.65 percent by weight, or

3. The maximum temperature exceeds 1,700 K.

The first two of these restrictions are of the type proposed by Pawel, of Oak Ridge National Laboratory (ORNL).[4.11-30] The last is based on data obtained at EG&G Idaho, Inc.[4.11-31]

During a LOCA transient, there are two cladding cooling rates. One is a rather slow rate during refill, and the other is a rapid rate due to quench. If the slow decrease brings the cladding below the temperature of the beta phase, it is this rate that is important for embrittlement. In these cases, the cladding is characterized as embrittled if 0.3 mm or more of the beta phase contains more than 1 wt% oxygen. This criterion is similar to one proposed by Chung, Garde, and Kassner.[4.11-32]

The inputs required by the model are the temperature and oxygen profiles in the beta phase zircaloy. At EG&G Idaho, Inc., these are found with the FRAP codes,[4.11-18,4.11-33] in conjunction with the COBILD high temperature oxidation subcode (see Section 4.15). When the oxygen concentration exceeds the limits defined above, the model indicates that the cladding is critically embrittled.

Section 4.11.3 contains a discussion of the literature reviewed. The model development is presented in Section 4.11.7, along with model data comparisons and a discussion of the uncertainty.

4.11.6 Literature Review

The paper by Pawel[4.11-30] is the basis for the part of CBRTTL describing fast-cooled cladding. The criteria presented by Pawel are modified based on in-pile data taken at the INEL.[4.11-31] The embrittlement criterion for slow cooled cladding is based on data taken from a recent series of reports from ANL.[4.11-32,4.11-34,4.11-35] These data sets are described in the following subsections.

4.11.6.1 Data for Fast Cooling. Data taken in-pile at the Power Burst Facility (PBF) reactor of EG&G Idaho, Inc., are extensively documented.[4.11-31] In this reactor, fuel rods about 3 feet in length but otherwise of typical PWR dimensions are brought into film boiling. The rods are externally pressurized with a pressure differential of at least 10 MPa. The oxidizing agent is steam, since data were taken from areas experiencing film boiling. The rods were oxidized under nonisothermal conditions. In some cases, the cladding temperature varied by as much as 800 K during a single experiment. An important feature of the PBF tests is that the source of heat was actual fuel pellets, which can relocate causing pellet-cladding thermal and mechanical interactions.

A major disadvantage of the PBF data base is that it is quite small. Competing embrittlement effects, such as chemical reactions at the inside surface from pellet-cladding interaction and aggressive fission products, present another difficulty. The fact that the PBF data conform well to Pawel's criteria developed from data taken out of pile,[4.11-36] where such competing effects are absent, suggests that this latter disadvantage may not be important and that oxygen uptake is the dominant embrittlement process.

4.11.6.2 Data for Slow Cooling. Many out of pile data were taken from recent reports by Chung, Garde, and Kassner.[4.11-32,4.11-34,4.11-35] The samples were 30 cm zircaloy tubes with inner and outer diameters typical of LWR cladding. About one-half of the tube length was filled with alumina (Al_2O_3) pellets to simulate the fuel. The experimental procedure was to heat the sample by induction heating to the test temperature from room temperature at 10 K/s. This temperature was held for the desired time period, after which the sample was cooled at 5 K/s to approximately 810 K and then rapidly quenched by bottom flooding with water. The tubes ruptured during the heating phase due to an initial internal pressure, typically about 7 MPa. During the entire experiment, a steam generator circulated steam at about 0.15 MPa

pressure past the specimen. After each experiment, the tubes were examined and classified in one of three ways:

1. Tubes that failed during the quench.

2. Tubes that survived quench but failed in normal handling required to remove them from the experimental apparatus.

3. Tubes that remained intact.

The ANL experiments provide a good test of the ability of zircaloy cladding, embrittled by nearly isothermal oxidation, to withstand the thermal shock of reflood after a hypothetical LOCA. The principal disadvantage of these tests is that the experiment environment may not apply the same stresses as cracked and relocated fuel.

4.11.7 Model Development

Ideally, a model for embrittlement by oxygen uptake would specify a maximum acceptable stress as a function of oxygen content in the cladding. The available data, however, are not amenable to such an approach because neither the stress nor the strain at failure are measured. For some cases, the stress or strain could be calculated; but this is clearly not possible for those rods which failed during normal handling at the ANL. Therefore, a more empirical process is used, wherein several commonly used embrittlement criteria are tested against the data and the most appropriate ones are subjected to sensitivity studies to determine the best boundary conditions.

Several embrittlement criteria are now in use or have been proposed. In this subsection, the more prominent ones are compared to the data. The COBILD code was used to calculate oxide layer thicknesses, oxygen uptake, and oxygen profiles in the beta phase.

4.11.7.1 Presently Used Acceptance Criteria. For reactor licensing purposes, the present oxidation limits for an acceptable emergency core cooling system are defined in the Code of Federal Regulations, Title 10, Section 50. The code specifies:

(a) That the peak cladding temperature must not exceed 2,200 °F (1,477.5 K)

(b) That the oxide thickness that would result if all oxygen uptake produced ZrO_2 (called the equivalent cladding reacted) must not exceed 17% of the original cladding wall thickness.

Both of these criteria have been shown to be conservative for out-of-pile tests[4.11-32,4.11-34] and inconsistent for in-pile tests.[4.11-31]

4.11.7.2 Fraction of Wall Thickness That is Beta Phase Criterion. Scatena[4.11-37] suggested an embrittlement criterion based on the quantity F_w, where

$$F_w = \frac{\text{remaining beta phase thickness}}{\text{original unoxidized wall thickness}} \quad . \tag{4-272}$$

If $F_w \leq 0.5$, the material is considered embrittled This criterion was not found to work well for either the out-of-pile or in-pile data, being conservative in both cases.

4.11.7.3 Argonne Impact Energy Criterion. In these tests, the tubes were treated as described in Section 4.11.6. In an effort to quantify the embrittlement, those rods that emerged intact from quenching and handling were subject to impact testing with a pendulum device. Impact energies of 0.03 and 0.30 J were used, causing additional rods to fail. However, unless an allowable impact energy is specified, classification of tubes shattered by impact as failed is not useful. If such energy is specified, an embrittlement model based on these data will become attractive.

4.11.7.4 ORNL Correlation of Embrittlement with Oxygen Content in the Beta Phase. Using data from a report by Hobson and Rittenhouse,[4.11-36] Pawel[4.11-30] arrived at two embrittlement criteria for zircaloy. He considered the cladding embrittled if the oxygen content of the beta phase exceeded 95% of the saturation content, or 0.7 wt%. This model, slightly modified, is used for fast-cooled cladding in this section. The saturation oxygen concentration is determined from a zircaloy-oxygen phase diagram published by Chung.[4.11-38]

4.11.7.5 Argonne Correlation of Embrittlement with Oxygen Content in the Beta Phase. Using a computer code developed at ANL, Chung[4.11-32] found an embrittlement criterion that fits their data very well. Their criterion states that the cladding will not be embrittled if there is at least 0.1 mm of beta with less than 1.0 wt% oxygen. The limits set by the ANL group are consistent with the conclusions of a more qualitative study by Sawatzky,[4.11-39] who states that the maximum temperature and total oxygen content have little or no effect on the tensile properties of zircaloy-4. Sawatzky used a maximum cooling rate of 160 K/s for about 10% of his samples; but the other 90% were cooled at rates of 21 K/s or less, so his conclusions apply primarily to slow cooled cladding. The ANL model is also modified and used for slow cooled cladding in this section.

4.11.8 Model for Fast Cooled Cladding

The Pawel criteria, slightly modified and with the additional limit that the peak cladding temperature must not exceed 1,700 K, are adopted for the fast-cooled cladding model. Physically, a percent saturation limit makes sense, at least qualitatively, because as the oxygen content of the beta phase approaches saturation, any local oxygen excess is relieved by the formation of brittle oxygen-stabilized alpha precipitates, often in the form of incursions originating in the normal alpha-phase layer and extending into the beta phase. The presence of these oxygen-rich alpha incursions is always associated with a loss of ductility. They may also form during cooling because as the temperature decreases, so does the oxygen solubility, often making the beta phase super-saturated with oxygen.

The criterion specifying a maximum oxygen weight fraction is needed because the diffusivity of oxygen also decreases with temperature. If the cooling rate is high enough, there will not be sufficient time for incursions to form during cooling and only those formed at high temperature will be present. Since the ductility of zircaloy decreases even without incursions as its oxygen content increases, there must be a critical oxygen concentration that causes embrittlement. The 1,700 K limit, although in contradiction to the conclusions of Sawatzsky,[4.11-39] was necessary to fit the data.

Pawel's limits of 95% saturation and 0.70 wt% oxygen were subjected to a brief sensitivity analysis to examine the effect of varying these limits. Combinations that were tried included 0.70 and 0.65 wt% and saturations of 90 and 95%. The results are shown in Figure 4-56, along with data from the Hobson-Rittenhouse experiment. The plot shows little to be gained by changing the limits. These criteria do not specify a single thickness for the beta layer necessary to retain ductility. However, for a given original wall thickness, it is possible to find a critical beta thickness as a function of temperature corresponding to the limits of this model. This thickness is usually expressed as a ratio

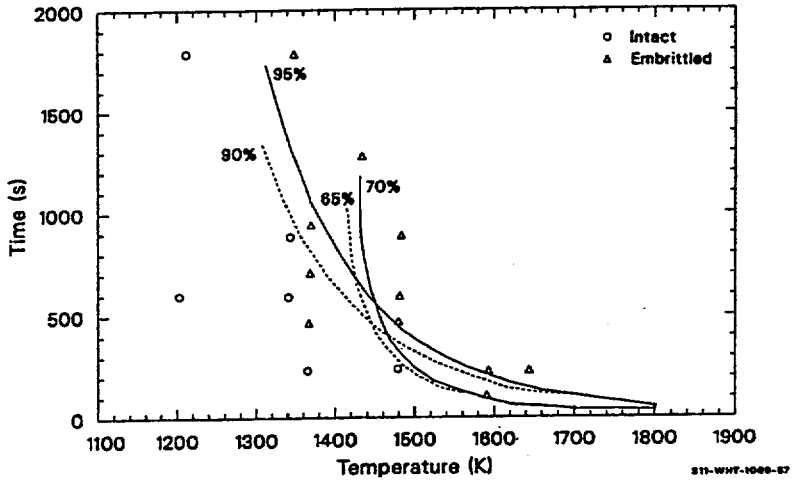

Figure 4-56. Hobson-Rittenhouse isothermal data for fast cooled cladding compared with the 0.65 and 0.70 wt% and the 90 and 95% filled criteria.

$$(F_W)_{crit} = \frac{\text{critical thickness of beta layer}}{\text{original unoxidized wall thickness}} \quad . \tag{4-273}$$

An $(F_w)_{crit}$ criterion corresponding to limits such as those specified by Pawel is particularly useful because it contains no explicit reference to time and may therefore be generalized to more realistic situations where the rod temperature changes. Time is still a necessary parameter to make the calculations; but, in the evaluation of the ductility, only the oxygen content and the temperature at a time are required. For this part of the model, the time and temperature used are those at the end of the last time temperature segment when the cladding was entirely in the beta phase. Figure 4-57, $(F_w)_{crit}$ is plotted as a function of

temperature. The solid lines are for 0.7 wt% and 95% filled, and the dashed lines are for 0.65 wt% and 90% filled. Also shown in the figure are data from the Hobson-Rittenhouse out-of-pile isothermal tests and the in-pile PBF nonisothermal tests. All the points, as well as the limiting lines, were calculated with the COBILD subcode. As with Figure 4-56, the data apply for a specific wall thickness, chosen here to be 0.60 mm to correspond to the PBF data. However, COBILD runs show that the limiting lines in Figure 4-57 move less than 1% when the wall thickness changes by as much as 40% from 0.60 mm.

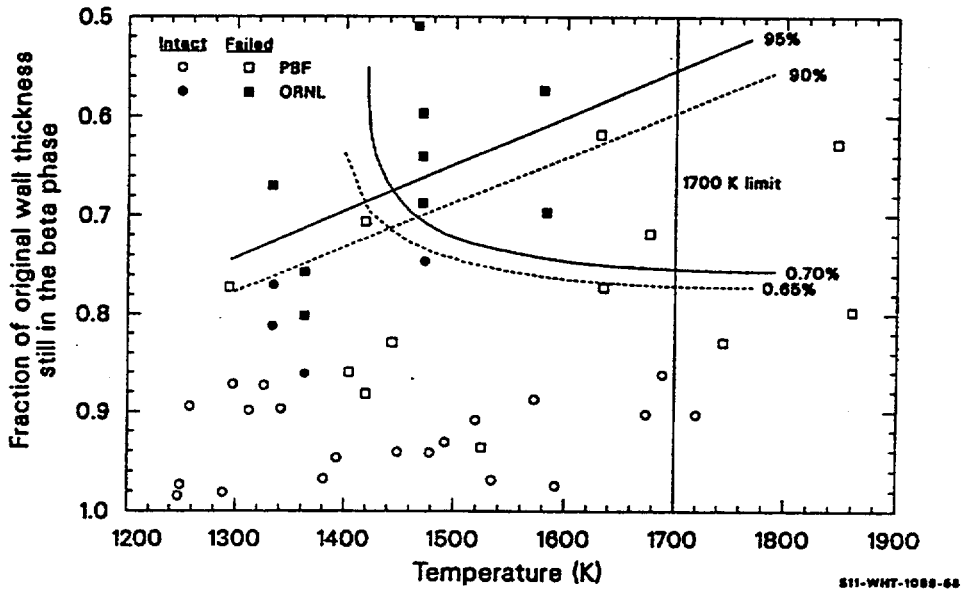

Figure 4-57. Hobson-Rittenhouse and PBF data for fast-cooled rods compared with the critical fractional wall thickness as calculated from the 0.65 and 0.70 wt% and the 90 and 95% filled criteria.

An obvious feature of these figures is that three in-pile rods failed when they apparently should not have. These rods were at temperatures of 1,405, 1,418, and 1,523 K. Postirradiation examination of the inner surface oxidation showed that these rods had a wall defect in the vicinity of the failure, allowing steam to enter. Hot zircaloy exposed to stagnant steam will absorb an abnormally large amount of hydrogen,[4.11-40] and the failures of these three rods show evidence of hydride influence.[4.11-31] These rods are therefore not deemed suitable examples of the simple failure by oxygen embrittlement.

It is clear from Figure 4-57 that the lower limits of 90% saturation and 0.65 wt% oxygen include more of the failed rods than do Pawel's original limits. Consequently, the model for fast-cooled cladding is considered embrittled if the oxygen content of the beta phase exceeds (a) 90% of the saturation content or (b) 0.65% of weight. A third criterion limiting the maximum cladding temperature to < 1,700 K is added to fit the highest temperature data.

The data are still too limited to consider this model final; however, the accuracy is encouraging, especially considering the differences in the experiments. The Hobson-Rittenhouse samples were oxidized

on both sides, out of pile, and quenched rapidly, while the PBF samples were oxidized primarily on the outside, in pile, and quenched slowly.

4.11.9 Model for Slow Cooled Cladding

Designation of this part of the model as being applicable to slow cooled cladding is slightly misleading; it is meant to apply during the prequench of a LOCA. As described in Section 4.11.2 of this report, Chung, Garde, and Kassner[4.11-32,4.11-34,4.11-35] have completed many out-of-pile tests of this sort and have developed an embrittlement criterion requiring at least 0.1 mm of cladding thickness with < 1 wt% oxygen. When the criterion was checked using COBILD, it was found that at least 0.3 mm with < 1 wt% oxygen are required to avoid failure by thermal shock. No reason for the difference between this and the ANL minimum thickness of 0.1 mm has been found. It possibly lies in the mechanics of the two codes. Until a comparison of the ANL code and COBILD can be performed, the criterion established with COBILD is recommended for use with the MATPRO package.

In Figure 4-58, this criterion is compared with the data. Only temperatures > 1,244 K are considered, since this is the lower range of validity for COBILD. Not all of the data are shown in the figure because many are coincident, or nearly so. Of the 146 intact rods, 16 (or 11%) are predicted to fail; and of the 57 failed rods, 4 (or 7%) are predicted to remain intact. In the entire data set, < 10% of the predictions are incorrect. Given the scatter in the data, this is considered acceptable accuracy.

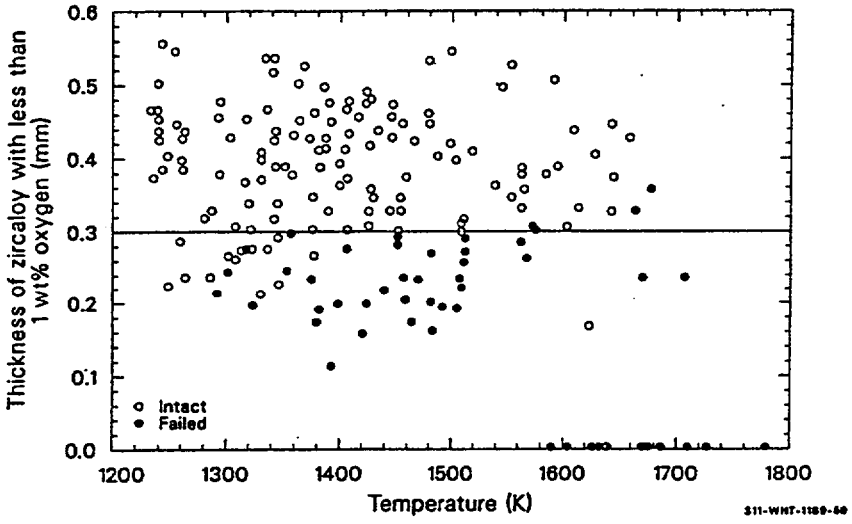

Figure 4-58. Comparison of the Argonne data for slow-cooled cladding with the criterion that at least 0.3 mm of zircaloy with less than 1 wt% oxygen is required to survive thermal shock.

Since all the tubes tested at ANL had a wall thickness of 0.635 mm, it is impossible to conclude whether 0.30 mm is the actual minimum thickness required to retain ductility or if there is some minimum F_W. The former is more reasonable on physical grounds because it seems logical that there should be a minimum thickness of ductile material necessary for ductility.

If the embrittlement criteria for fast-cooled rods are compared with the slow-cooled data, failure would be predicted in most cases, contrary to experimental observation. Similarly, the criterion used for the slow cooled rods almost never predicts a failure when compared to the fast-cooled data. These facts underscore the importance and complexity of cooling rate on the ductility of zircaloy at high temperature and further emphasize the importance of clearly specifying the cooling rate.

4.11.10 Model Uncertainties

A primary source of uncertainty for both models is in temperature measurement. For the Hobson-Rittenhouse data set, the temperature uncertainty is estimated by comparing the temperature reported for a given layer thickness with that calculated using isothermal oxidation kinetics published by Cathcart[4.11-41] for the same thickness. From this analysis, the root mean square of the temperature difference is about 50 K. A similar technique was used for the PBF and ANL data. Seiffert and Hobbins[4.11-31] also arrived at an uncertainty of about 50 K, while Chung[4.11-34] found an 85 K uncertainty. This technique should give a reasonable estimate because Cathcart's correlations are based on a careful analysis of his own data. This analysis shows the data to have a high degree of consistency, and the major error in measurement should be the temperature, the layer thickness being much easier to obtain with accuracy.

There is another potentially important source of systematic error in the ANL data. They were presented in graphical rather than tabular form. A digitizer was used to obtain numerical values. The data were generally plotted as the logarithm of the time versus reciprocal temperature, so larger errors result for long times or high temperatures. By repeating the digitizing from the same plots, the uncertainties listed in Table 4-43 were found.

An idea of the effect of errors for fast cooled cladding may be obtained by examining Figure 4-55. For slow-cooled cladding, a sensitivity analysis is required to find what change in beta phase thickness with less than 1% oxygen content would result from the given uncertainties. Such an analysis has not been carried out.

Table 4-43. Uncertainties in digitized Argonne data.

Temperature (K)	ΔTemperature (K)	Time (s)	ΔTime (s)
1,250	16	10^2	2.50
1,650	28	10^4	2.50

4.11.11 References

4.11-1 R. H. Chapman, *Multirod Burst Test Program Quarterly Progress Report for April-June 1977*, ORNL/NUREG/TM-135, December 1977.

4.11-2 R. H. Chapman, J. L. Crowley, A. W. Longest and E. G. Sewell, *Effect of Creep Time and Heating Rate on Deformation of Zircaloy-4 Tubes Tested in Steam With Internal Heaters*, ORNL/NUREG/TM-245 and NUREG/TM-74, October 1978.

4.11-3 R. H. Chapman, *Multirod Burst Test Program Quarterly Progress Report for April-June 1976*, ORNL/NUREG/TM-74, January 1977.

4.11-4 R. H. Chapman, *Multirod Burst Test Program Quarterly Progress Report for July-December 1977*, ORNL/NUREG/CR-0103, June 1978.

4.11-5 R. H. Chapman, *Multirod Burst Test Program Quarterly Progress Report for January-March 1978*, NUREG/CR-0225, ORNL/NUREG/TM-217, August 1978.

4.11-6 R. H. Chapman, *Multirod Burst Test Program Quarterly Progress Report for January-March 1976*, ORNL/NUREG/TM-36, September 1976.

4.11-7 R. H. Chapman, *Multirod Burst Test Program Quarterly Progress Report for October-December 1976*, ORNL/NUREG/TM-95, April 1977.

4.11-8 R. H. Chapman, *Multirod Burst Test Program Quarterly Progress Report for January-March 1977*, ORNL/NUREG/TM-108, May 1977.

4.11-9 D. O. Hobson and P. L. Rittenhouse, *Deformation and Rupture Behavior of Light Water Reactor Fuel Cladding*, ORNL-4727, October 1971.

4.11-10 H. M. Chung and T. F. Kassner, *Deformation Characteristics of Zircaloy Cladding in Vacuum and Steam Under Transient-Heating Conditions: Summary Report*, NUREG/CR-0344, ANL-77-31, July 1978.

4.11-11 A. A. Bauer, L. M. Lowry, and J. S. Perrin, *Evaluating Strength and Ductility of Irradiated Zircaloy: Quarterly Progress Report for January-March 1976*, BMI-NUREG-1948, March 1976.

4.11-12 A. A. Bauer, W. J. Gallagher, L. M. Lowry, and A. J. Markworth, *Evaluating Strength and Ductility of Irradiated Zircaloy: Quarterly Progress Report for July-September 1977*, BMI-NUREG-1985, October 1977.

4.11-13 A. A. Bauer, W. J. Gallagher, L. M. Lowry, and A. J. Markworth, *Evaluating Strength and Ductility of Irradiated Zircaloy: Quarterly Progress Report for October-December 1977*, NUREG/CR-0026, BMI-1992, January 1978.

4.11-14 D. W. Croucher, *Behavior of Defective PWR Fuel Rods During Power Ramp and Film Boiling Operation*, NUREG/CR-0283, TREE-1267, February 1979.

4.11-15 T. F. Cook, S. A. Ploger, and R. R. Hobbins, *Postirradiation Examination Results for the Irradiation Effects Test IE-5*, TREE-NUREG-1201, March 1978.

4.11-16 E. H. Karb, "Results of the FR-2 Nuclear Tests on the Behavior of Zircaloy Clad Fuel Rods," *6th NRC Water Reactor Safety Research Information Meeting, Gaithersburg, MD, November 7, 1978.*

4.11-17 K. Wiehr and H. Schmidt, *Out-of-Pile Versuche zum Aufblahvorgang von Zirkaloy Hullen Ergenbnisse aus Vorversuchen mit verkurzten Brennstabsimulatoren*, KfK 2345, October 1977.

4.11-18 L. J. Siefken, M. P. Bohn, S. O. Peck, and J. A. Dearien, *FRAP-T5: A Computer Code for the Transient Analysis of Oxide Fuel Rods*, TREE-1281, NUREG-CR-0840, June 1979.

4.11-19 D. W. Croucher, T. R. Yackle, C. M. Allison, and S. A. Ploger, *Irradiation Effects Test Series IE-5 Test Results Report*, TREE-NUREG-1130, January 1978.

4.11-20 R. H. Chapman, *Multirod Burst Test Program Quarterly Progress Report for October-December 1975*, ORNL/NUREG/TM-10, May 1976.

4.11-21 J. M. Kramer and L. W. Deitrich, *Cladding Failure by Local Plastic Instability*, ANL-77-95, December 1977.

4.11-22 K. Wiehr et al., *Jahreskolloquim 1977 des Projekts Nukleare Sicherheit.*

4.11-23 C. C. Busby and K. B. Marsh, *High Temperature Deformation and Burst Characteristics of Recrystallized Zircaloy-4 Tubing*, WAPD-T-900, January 1970.

4.11-24 D. G. Hardy, "Burst Testing of Zircaloy Cladding from Irradiated Pickering-Type Fuel Bundles," *Symposium on the Effects of Radiation on Substructure and Mechanical Properties of Metal and Alloys, Los Angeles, CA, June 25-30, 1972*, ASTM-STP-529, 1973, pp. 415-435.

4.11-25 M. F. Osborne and G. W. Parker, *The Effect of Irradiation on the Failure of Zircaloy-Clad Fuel Rods*, ORNL-3626, January 1972.

4.11-26 D. O. Hobson, M. F. Osborne, and G. W. Parker, "Comparison of Rupture Data from Irradiated Fuel Rods and Unirradiated Cladding," *Nuclear Technology, II*, August 1971.

4.11-27 D. G. Hardy, "The Effect of Neutron Irradiation on the Mechanical Properties of Zirconium Alloy Fuel Cladding in Uniaxial and Biaxial Tests," *Symposium on Irradiation Effects on Structural Alloys for Nuclear Reactor Applications, Niagara Falls, Canada, June 29-July 1, 1970*, ASTM-STP-484, 1971, pp. 215-216.

4.11-28 W. J. Landford, "Metallurgical Properties of Cold Worked Zircaloy-2 Pressure Tubes Irradiated Under CANDU-PHW Power Reactor Conditions," *Symposium on Irradiation Effects on Structural Alloys for Nuclear Reactor Applications, Niagara Falls, Canada, June 29-July 1, 1970*, ASTM-STP 484, 1971, pp. 259-286.

4.11-29 W. R. Smalley, *Saxton Core II Fuel Performance Evaluation Material*, WCAP-3385-56, September 1971, pp.4-84,4-65; W. R. Smalley, *Evaluation of Saxton Core III Fuel Materials Performance*, WCAP-3385-57, July 1974, pp. 3-69, 3-132, 3-134.

4.11-30 R. E. Pawel, "Oxygen diffusion in Beta Zircaloy During Steam Oxidation," *Journal of Nuclear Materials, 50*, 1974, pp. 247-258.

4.11-31 S. L. Seiffert and R. R. Hobbins, *Oxidation and Embrittlement of Zircaloy-4 Cladding from High Temperature Film Boiling Operation*, TFBP-TR-292, October 1978.

4.11-32 H. M. Chung, A. M. Garde, and T. F. Kassner, *Light Water Reactor Safety Research Program: Quarterly Progress Report for January-March 1978*, ANL-78-49, p. 56.

4.11-33 G. A. Berna et al., *FRAPCON-1: A Code for the Steady-State Analysis of Oxide Fuel Rods*, CDAP-TR-78-032-R1, November 1978.

4.11-34 H. M. Chung, A. M. Garde, and T. F. Kassner, *Light-Water Reactor Safety Research Program: Quarterly Progress Report, for July-September 1977*, ANL-78-3, January 1978, pp. 47-75.

4.11-35 H. M. Chung, A. M. Garde, and T. F. Kassner, *Light-Water Reactor Safety Research Program: Quarterly Progress Report, for October-December 1977*, ANL-78-25, May 1978, pp.31-44.

4.11-36 D. O. Hobson and P. L. Rittenhouse, *Embrittlement of Zircaloy-Clad Fuel Rods by Steam During LOCA Transients*, ORNL-4758, January 1972.

4.11-37 C. J. Scatena, *Fuel Cladding Embrittlement During a Loss-of-Coolant Accident*, NEDO-10674, General Electric, October 1972.

4.11-38 H. M. Chung, A. M. Garde, and T. F. Kassner, *Light-Water Reactor Safety Research Program: Quarterly Progress Report for January-March 1976*, ANL-76-49.

4.11-39 A. Sawatzsky, "Oxygen Embrittlement of Zircaloy-4 Fuel Cladding," *6th Water Reactor Safety Research Information Meeting, Gaithersburg MD, November 6, 1978.*

4.11-40 C. Roy, "An Experiment to Clarify the Effect of Dissolved Oxygen on the Terminal Solubility of Hydrogen in Zirconium," *Journal of Nuclear Materials, 13*, 1964.

4.11-41 J. V. Cathcart et al., *Zirconium Metal Water Oxidation Kinetics VI Reaction Rate Studies*, ORNL/NUREG-17, August 1977.

4.12 Cyclic Fatigue (CFATIG)

The subcode CFATIG provides preliminary estimates of material constants in a format compatible with the use of fracture mechanics to model the effect of cyclic fatigue as described in the following equations.

4.12.1 Summary

High-cycle (nominally elastic strain) fatigue uses material constants in an equation of the following form:

For $\Delta K \geq 9.5 \times 10^6$ MN/m$^{1.5}$,

$$dl/dN = B\,(\Delta K)^m \quad . \tag{4-274}$$

And for $\Delta K < 9.5 \times 10^6$ MN/m$^{1.5}$,

$$dl/dN = 0 \tag{4-275}$$

where

dl/dN = the change in crack length per cycle (m/cycle)

ΔK = the stress intensity range (MN/m$^{1.5}$)

B,m = material parameters returned by the CFATIG code.

The exponent m is

$$m = 15 - 12 \exp(-\Phi/10^{24}) \tag{4-276}$$

where Φ is the fast neutron fluence (n/m^2).

The parameter B in Equation (4-274) is computed from the following expressions for fast neutron fluences less than 10^{25} n/m^2:

$$B = 2 \times 10^{-11} \{ 15.5311432^{12[\exp(-\Phi/10^{-24})-1]} \} \quad . \tag{4-277}$$

For fast neutron fluences of 10^{25} n/m^2 or more,

$$B = 1.0165786 \times 10^{-25} \quad . \tag{4-278}$$

Low-cycle (plastic strain) fatigue uses material constants intended for use in the equation proposed by Tomkins.[4.12-1]

$$\frac{dl}{dN} = K(\Delta\varepsilon)^{1/\alpha}l \tag{4-279}$$

where

$\Delta\varepsilon$ = plastic strain amplitude (unitless)

l = crack length (m)

α, K = material parameters.

The value returned by CFATIG for the dimensionless material parameter K is 10.7, and the value for α is 0.6. ($1/\alpha = 1.67$).

4.12.2 Basis for High-Cycle Fatigue Material Constants

Constants for the description of high-cycle crack propagation are based on data taken by Rao[4.12-2] and preliminary measurements by Walker and Kass.[4.12-3] (stress versus number of cycles to failure) data reported by O'Donnell and Langer[4.12-4] are not incorporated into the model because the effect of varying initial crack sizes is not known.

Rao's measurements of crack growth rates as a function of stress intensity (from Figure 4 of Reference 4.12-2) are reproduced in Table 4-44. The parameter m in Equation (4-274) is equal to the slope of a plot of log dl/dN against log ΔK. The value of m obtained from a least-squares fit to a plot of the data of Table 4-44 is 3.3.

Table 4-44. Crack growth rate versus stress intensity range from Rao.

Stress intensity range ($MN/m^{1.5}$)	Crack growth rate (10^{-8}m/cycle)
20.5	4.0
25.5	11.3
31.6	22.1
37.4	37.8
45.3	69.2
54.9	134.5
20.5	9.4

Table 4-44. Crack growth rate versus stress intensity range from Rao. (Continued)

Stress intensity range ($MN/m^{1.5}$)	Crack growth rate (10^{-8}m/cycle)
25.5	22.4
31.6	42.5
37.4	71.4
45.3	116.7
54.9	203.8

The preliminary data of Walker and Kass (Figure 9 of Reference 4.12-2) were analyzed with the same approach used for the data of Rao. The straight line used by Walker and Kass to summarize data from unirradiated samples is equivalent to a value of m = 2.8 in Equation (4-274).

Walker and Kass also reported crack growth rates from eleven samples which received fast neutron fluences from 5 to 19 x 10^{24} n/m^2. A linear least-squares fit to a [log (stress intensity) versus log (crack growth rate)] plot of these measurements suggests that a value of m = 15.7 in Equation (4-274) would yield the best description of irradiated zircaloy.

The exponential form of Equation (4-276) is an estimate relating the values of m = 3 for unirradiated zircaloy and m = 15 for zircaloy irradiated to a fast neutron fluence of 10^{25} n/m^2. A decreasing exponential is typical of the change of material constants with fluence.

Value of the parameter B for unirradiated zircaloy were determined by substituting measurements of crack growth rate and stress intensity range into Equation (4-274) with m = 3. Values of B determined from the two sets of data shown in Table 4-44 were averaged to obtain 12.7 and 6 x 10^{-30} or stress intensities in $N/m^{1.5}$. Two additional estimates for B were obtained by repeating the solution of Equations (4-277) and (4-278) with Rao's measurements of crack growth rates at constant stress intensity (Figure 9 of Reference 4.12-2). Analysis of data from these two samples yielded B = 19.3 x 10^{-30} and B = 16 x 10^{-30}. A fifth estimate for B in unirradiated zircaloy was obtained using the Walker and Kass summary of their data with unirradiated material. Their straight line fit corresponds to a value of B = 48 x 10^{-30}.

The only data used to find B for irradiated zircaloy are the eleven measurements of crack growth rate and stress intensity factor range by Walker and Kass discussed earlier in this section The average value of B from these data and Equation (4-274) with m = 15 was B = 10^{-25}.

The expression used to model B [Equation (4-277)] is a fit to the average of the five estimates for B at zero fast neutron fluence and the one value of B at fluences on the order of 10^{25} n/m^2. The functional dependence of B on fast neutron fluence is an estimate based on the data at zero and 10^{25} n/m^2. The value

of B for fluences between 10^{24} and 10^{25} n/m^2 has been determined to cause the predicted value of crack growth rate to remain constant at stress intensity factors of 15.531432 MN/m$^{1.5}$.

The value ΔK_{min} = 9.5 MN/m$^{1.5}$ in Equation (4-274) is based on a test by Rao at this stress intensity range. No change in crack length was observed in this test.

4.12.3 Basis for Low-Cycle Fatigue Material Constants

The values returned for the material parameters in Equation (4-279) are based on the data and analysis of Pettersson.[4.12-5] Pettersson has shown that Equation (4-279) can be integrated and expressed in the form of the Coffin-Manson relationship

$$\Delta E = CN_f^{-\alpha} \tag{4-280}$$

where

ΔE = plastic strain range

N_f = number of cycles to failure

C, α = material parameters.

The constant α in Equation (4-280) is the same material parameter as the constant a in Equation (4-279). Pettersson shows that the constant C in Equation (4-280) is related to the material constant K of Equation (4-279) by the following expressions:

for uniaxial straining,

$$C^{1/\alpha} = \frac{\ln\left(\frac{l_f}{l_0}\right)}{K} = \frac{4.83}{K} \tag{4-281}$$

for bend tests,

$$C^{1/\alpha} = \frac{1}{K}\int_{\frac{l_0}{t}}^{\frac{l_f}{t}} \frac{dX}{X(1-X)^{1/\alpha}} = \frac{6.26}{K} \tag{4-282}$$

where

l_o = the initial crack length (m)

l_f = the final crack length (m)

t = the specimen thickness (m).

The constants α and log C, which Pettersson reports from fits to his data, are listed in Table 4-45, along with the constant K obtained from Equation (4-282).

Table 4-45. Low-cycle fatigue material parameters.

Fast fluence $(n/m)^2$	Material parameter, α (unitless)	log C (unitless)	Material parameter, K (unitless)
0	0.60	1.87	10.3
1.3×10^{24}	0.64	1.96	11.7
2.6×10^{24}	0.56	1.75	10.1
Average	0.6	--	10.7

4.12.4 References

4.12-1 B. Tomkins, "Fatigue Crack Propagation - An Analysis," *Philosophical, 18*, 1968, p. 1041.

4.12-2 V. S. Rao, *High-Cycle Fatigue Crack Growth of Two Zirconium Alloys*, AE-486, March 1974.

4.12-3 T. J. Walker and J. N. Kass, "Variation of Zircaloy Fracture Toughness in Irradiation," *Zirconium in Nuclear Applications*, ASTM-STP-551, 1974, pp. 328-254.

4.12-4 W. J. O'Donnell and B. F. Langer, "Fatigue Design Basis for Zircaloy Components," *Nuclear Science and Engineering, 20*, 1, 1964

4.12-5 K. Pettersson, "Low-Cycle Fatigue Properties of Zircaloy Cladding," *Journal of Nuclear Materials, 56*, 1975, pp. 91-102.

4.13 Collapse Pressure (CCLAPS)

The subcode CCLAPS was produced to aid in the prediction of cladding collapse into axial gaps between fuel pellets. It is based on a correlation developed by Hobson,[4.13-1] which predicts collapse pressure for temperatures between 590 and 700 K. This version of the subcode does not apply to the description of high temperature (900 K) collapse or waisting of cladding into pellet to pellet gaps, which has been observed during power cooling mismatch (PCM) accident tests.[4.13-2]

4.13.1 Model Development

The required input parameters for the function CCLAPS are cladding temperature (K), the largest pellet to pellet gap in the node considered (m), and the room temperature midwall diamond pyramid hardness number (DPH) of the cladding. An additional input argument, pellet-to-cladding gap size (m) is not used by this version of the model but is included in the argument list to allow for future improvement of the model. The function returns the pressure at which collapse is predicted by Hobson's correlation.

When measured values of hardness for the particular lot of tubing under consideration are not available, it is suggested that the user input Hobson's measured values. These were reported[4.13-3] as follows: for 80% cold worked and 775 K stress relieved material, hardness equals 238 DPH; for fully recrystallized material, hardness equals 180 DPH.

The expression for collapse pressure derived by Hobson[4.13-1] is

$$P = 6895\left[15660 + \frac{G}{2.17\times10^{-4}G - 4.57\times10^{-7}} - 183H + 0.729H^2 - 7.40\times10^{-4}H^3 - 3762T\right] \quad (4\text{-}283)$$

where

P = collapse pressure (Pa)

G = pellet to pellet gap (m)

H = room temperature midwall hardness (DPH)

T = test temperature (K).

Hobson's correlation is based on out-of-pile tests with unirradiated cladding and pellet-to-cladding gaps of 0.20 mm (0.008 in.). Some tests were conducted with other pellet-to-cladding gaps sizes[4.13-3] but were not included in the data base of the correlation.

4.13.2 References

4.13-1 D. O. Hobson, *Quarterly Progress Report on the Creepdown and Collapse of Zircaloy Fuel Cladding Program Sponsored by the NRC Division of Reactor Safety Research for April-June 1976*, ORNL/NUREG/TM-52, October 1976.

4.13-2 J. B. Ferguson (ed.), *Quarterly Technical Progress Report on Water Reactor Safety Programs Sponsored by the Nuclear Regulatory Commission's Division of Reactor Safety Research for October-December 1976*, TREE-NUREG-1070, April 1977, p.37.

4.13-3 D. O. Hobson, *Quarterly Progress Report on the Creepdown and Collapse of Zircaloy Fuel Cladding Program Sponsored by the NRC Division of Reactor Safety Research for January-March 1976*, ORNL/NUREG/TM-51, October 1976.

4.14 Meyer Hardness (CMHARD)

The routine CMHARD calculates Meyer hardness as a function of cladding temperature.

4.14.1 Model Development

One of the parameters required for calculating fuel-to-cladding contact conductance is hardness. As the contact pressure between the two surfaces increases, the points of contact enlarge due to localized plastic deformation and the solid-to-solid thermal conductance is improved. The Meyer hardness is used by Ross and Stoute[4.14-1] in their heat transfer correlation as an indication of the hardness of resistance to deformation of the softer (zircaloy) material.

The Meyer hardness number is a measure of indentation hardness and is defined in conjunction with Meyer's law,

$$L = ad^n \tag{4-284}$$

where

L = load

d = the diameter of impression at the surface of a specimen in a static ball test

n = the Meyer work hardening coefficient

a = a material constant.

The Meyer hardness number (MH) is defined as $4L/\pi d^2$. Other hardness numbers are available (Brinell, Rockwell, etc.), and conversion from one to another is possible. However, the routine CMHARD was created to provide information required by the Ross and Stoute gap conductance model.

Meyer hardness numbers for temperatures from 298 to 877 K were taken from Peggs and Godin.[4.14-2] A regression analysis of the reciprocal of the Meyer hardness values versus the log of temperature was used to obtain the analytical expression used in CMHARD. The correlation used is given by

$$MH = \exp\{2.6034 \times 10^{1} + T\{-2.6394 \times 10^{-2} + T[4.3502 \times 10^{-5} + T(2.5621 \times 10^{-8})]\}\} \tag{4-285}$$

where

MH = Meyer hardness (N/m^2)

T = temperature (K).

Figure 4-59 illustrates the correlation and its data base. The Meyer hardness decreases rapidly with increasing temperature, beginning at 2×10^9 MPa at room temperature and decreasing to 2×10^8 MPa at 875 K The hardness is presumed to continue its rapid rate of decrease at temperatures above 875 K. The minimum Meyer hardness number of zircaloy cladding is 1.0×10^5 N/m^2.

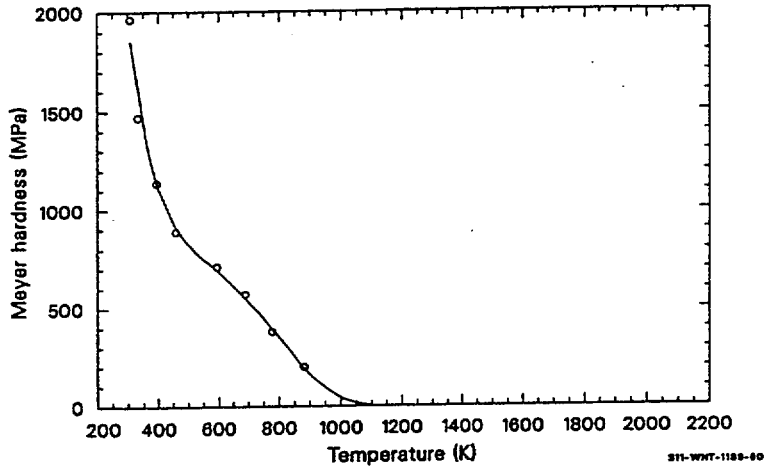

Figure 4-59. Values of the CMHARD correlation and its data base

4.14.2 References

4.14-1 A. M. Ross and R. L. Stoute, *Heat Transfer Coefficient Between UO_2 and Zircaloy-2*, AECL-1552, June 1962.

4.14-2 I. D. Peggs and D. P. Godin, "The Yield Strength-Hot Hardness Relationship of Zircaloy-4," *Journal of Nuclear Materials, 57*, 1975, pp. 246-248.

4.15 Zircaloy Oxidation in Water and Steam (CORROS, COBILD, COXIDE, COXWTK, COXTHK)

The oxidation of zircaloy cladding is an important subject because the thermal and mechanical properties of oxidized zircaloy are significantly different than the unoxidized properties. Moreover, the oxidation is highly exothermic. It can proceed rapidly enough at high temperatures to cause the reaction heat to significantly influence temperatures.

4.15.1 Summary

Low temperature (523 to 673 K) oxidation is modeled with the CORROS subcode, and high-temperature (1,273 to 2,100 K) oxidation is modeled with the COBILD, COXIDE, COXWTK and COXTHK subcodes. These codes provide information for other MATPRO subcodes, which describe the mechanical properties of zircaloy containing oxygen. This information includes oxygen concentrations, layer thicknesses, and the linear heating rate due to the zirconium-water reaction.

Oxide layer thickness is the only quantity calculated by the CORROS subcode. No other layers are found in zircaloy oxidized at 523 to 673 K.

COBILD, a FORTRAN adaptation of the BASIC BUILD5 code by Pawel, of Oak Ridge National Laboratory, calculates high-temperature oxygen concentrations, layer thicknesses, and the heating rate due to the zirconium steam reaction. The temperature at the beginning and end of a time step and the time step duration are required input information. The time step is divided into five substeps. During each substep, the average temperature obtained from a linear interpolation of the input temperatures is used with the isothermal correlations that are discussed below.

Calculations in COXIDE are isothermal. The input time step is not divided, and the temperature provided is assumed to be the average temperature for the entire step. Also, the oxygen concentration calculations of COBILD are not carried out in COXIDE.

COXWTK and COXTHK provide only oxidation rate constants for the high temperatures. The rate constants are provided in separate subcodes so that they are available for use with routines that calculate the coupled effects of oxidation heat, temperature, and geometry.

4.15.1.1 Low Temperature Oxidation (CORROS). The subroutine CORROS returns an expression for the thickness of the oxide layer on zircaloy cladding during typical reactor operation at temperatures of 523 to 673 K. Required input values are temperature at the outer surface of the oxide, initial oxide film thickness, length of time at the given temperature, type of reactor (BWR or PWR), heat flux across the oxide layer, and zircaloy oxide thermal conductivity.

Cladding oxidation during normal LWR operation occurs in two stages, depending on the oxide thickness and to some extent on the temperature of the oxide. For thin oxides, the rate of oxidation is controlled by the entire oxide layer. When the oxide layer becomes thicker, a change of the outer portion occurs; and further oxidation is controlled by the intact inner layer. The transition between stages is described in terms of thickness of the oxide layer at transition:

$$X_{TRAN} = 7.749\times10^{-6}\exp\left(-\frac{790}{T}\right) \qquad (4\text{-}286)$$

where

X_{TRAN} = thickness of the oxide layer at transition point (m) (typically 1.9×10^{-6} m thick)

T = temperature of the oxide-metal interface (K).

Values of the thickness of the oxide layer on the outside of the cladding are given by Equations (4-287) through (4-289) for pre-transition and post-transition oxide films.

For pre-transition oxide films:

$$X_{PRE} = \left[4.976\times10^{-9}(At)\exp\left(-\frac{15660}{T}\right)+X_0^3\right]^{1/3} . \quad (4\text{-}287)$$

For post-transition oxide films when X_o, the initial oxide thickness, is less than X_{TRAN}:

$$X_{POST} = 82.88A(t-t_{TRAN})\exp\left(-\frac{14080}{T}\right)+X_{TRAN} . \quad (4\text{-}288)$$

When X_o is greater than the transition thickness:

$$X_{POST} = 82.88(At)\exp\left(-\frac{14080}{T}\right)+X_0 \quad (4\text{-}289)$$

where

X_{PRE} = thickness of the oxide layer when a pre-transition oxide film exists (m)

A = a parameter describing enhancement of the cladding oxidation rate in a reactor environment. Typical reactor coolant chemistry, temperatures, and flux levels result in a value of A = 1.5 and 9 for a PWR and BWR, respectively. However, the factor is a function of temperature, as discussed in Section 4.15.3. A value for A is determined by correlations in the subcode using user specification of BWR or PWR chemistry with an input parameter ICOR.

t = time at temperature (days)

T = temperature of the oxide metal interface calculated by the subcode from the input value of the temperature at the outer oxide surface, the heat flux across the oxide, and the thermal conductivity of the oxide layer (K).

X_o = initial thickness of the cladding oxide layer (m). (This term can be approximated as $X_o = 0$ for etched cladding, but it becomes important if extensive prefilming has occurred or if oxidation is carried out in several steps which take place at different temperatures or in different coolant chemistries.)

X_{POST} = thickness of the oxide layer when the oxide film is in the post-transition state (m)

t_{TRAN} = time of transition between states (pre- and post-transition). [This time is calculated in the subcode from the inverse of Equation (4-287)].

X_{TRAN} = thickness of the oxide layer at the transition point (m) [Equation (4-286)].

4.15.1.2 High Temperature Oxidation (COBILD, COXIDE, COXWTK, COXTHK). For the high temperature range (1,273 to 2,100 K), neither the heat flux nor the coolant chemistry has an important influence on the extent of oxidation. At these reactor operating temperatures, the coolant has become steam; and oxidation proceeds much more rapidly than at normal LWR operating temperatures. Zircaloy normally has a body-centered cubic structure in this temperature range, called the beta phase, but the presence of oxygen causes two other possibilities. If the oxygen concentration is greater than about 0.25 weight fraction, one of several zirconium dioxide structures is formed. For oxygen weight fractions around 0.04, a hexagonal, close-packed phase called oxygen stabilized alpha zircaloy is formed. Thus, high-temperature oxidation of zircaloy in steam produces three layers: the ductile inner beta layer with minimal dissolved oxygen, an intermediate oxygen-stabilized alpha-zircaloy layer, and a zirconium-dioxide layer near the zircaloy steam interface.

When zircaloy cladding is exposed not only to steam on its outer surface but also to firm contact with uranium dioxide on the inside surface, three distinct inside layers are formed as oxygen and uranium diffuse into the cladding. A schematic cross-section of a fuel rod with fuel and pellet in contact is shown in Figure 4-60. The layers shown in this figure are

ZrO_2 = a zirconium dioxide layer formed by the metal water reaction

α-Zr(O) = an oxygen stabilized alpha zircaloy layer formed with oxygen from the coolant

β = a beta zircaloy layer with some dissolved oxygen

α-$Zr(O)_a$ = oxygen stabilized alpha zircaloy layer formed with oxygen from the fuel

α-$Zr(O)_b$ = oxygen stabilized alpha zircaloy layer formed with oxygen from the fuel

(U,Zr) = a thin layer of zircaloy uranium alloy.

COBILD works in time steps. At the start of each time step, it should be supplied with quantities including the duration of the time step, the temperature at the beginning and end of the step, the original unoxidized cladding dimensions, the thickness of the various layers and their oxygen concentrations, and the total oxygen uptake at the beginning of the timestep. After updating or recalculating several of these to conform to conditions at the end of the time step, it returns values for each of them.

The equations used to model the growth of the outside layers exposed to steam are all of the form

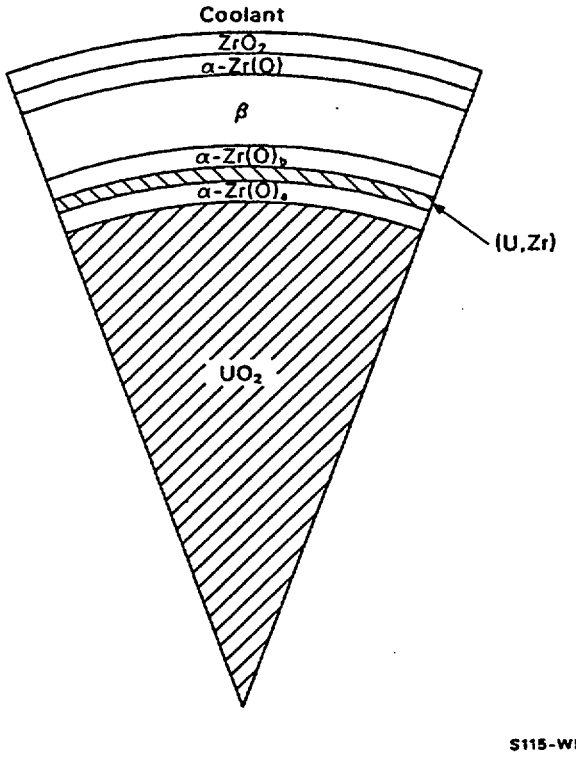

Figure 4-60. Idealized schematic of a uranium dioxide pellet in contact with the cladding, showing the layered structure.

$$Z_f = (Z_i^2 + 2A_e^{-B/T}\Delta t)^{0.5} \quad (4\text{-}290)$$

where

Z_i = initial value of oxidation parameter (ZrO_2 thickness, oxygen stabilized α-Zr thickness, or oxygen weight gain at the beginning of a time step

Z_f = final value of oxidation parameter at the beginning of time step

T = temperature of the oxide layer (K)

Δt = time step (s)

A,B = rate constants.

Table 4-46 lists the rate constants used with Equation (4-290) to model the various oxidation parameters for steam oxidation. In all cases, the model assumes that there is sufficient steam to provide the

indicated weight gain. The parabolic rate constants for the α-Zr(O) thicknesses in this table are not valid when the beta zircaloy layer becomes small.

Table 4-46. Rate constants for oxidation by steam.

Parameter	A	B
ZrO_2 thickness (m)		
For temperature ≤ 1,853 K	1.126×10^{-6} m^2/s	1.806×10^4 K
For temperature > 1,853 K	1.035×10^{-6} m^2/s	1.6014×10^4 K
α-Zr(O) thickness (m)	7.60×10^{-6} m^2/s	1.983×10^4 K
Weight gain per unit surface area (kg/m^2)		
For temperature ≤ 1,853 K	1.680×10^1 $(kg/m^2)^2/s$	2.006×10^4 K
For temperature ≥ 1,853 K	5.41×10^0 $(kg/m^2)^2/s$	1.661×10^4 K

Equation (4-290) is also used to model the growth of the inside of the α-$Zr(O)_a$ and α-$Zr(O)_b$ layers. For these layers, the growth rate is modeled as zero unless there is pellet cladding contact. For those time steps when there is pellet-cladding mechanical interaction, the constants given in Table 4-47 are used with Equation (4-290) to calculate the layer thickness.

Table 4-47. Rate constants for oxidation by UO_2.

Parameter	A	B
α-$Zr(O)_a$ thickness (m)	1.6×10^{-5} m^2/s	2.47×10^4 K
α-$Zr(O)_b$ thickness (m)	3.5×10^{-5} m^2/s	2.21×10^4 K

The expression used to calculate the rate of heat generation due to the exothermic oxidation of zircaloy by steam is

$$P = 1.15\times10^{8}\frac{R_0(W_f - W_i)}{\Delta t} \qquad (4\text{-}291)$$

where

P = rate of heat generation per unit length (W/m)

R_o = cladding outside radius without oxidation (m)

W_f = mass gain per unit surface area due to oxidation at end of time step (kg/m^2)

W_i = mass gain per unit surface area due to oxidation at start of time step (kg/m^2).

COBILD calculations for the oxygen profiles are completed after the oxide and alpha surface layer thicknesses are determined. The remaining beta thickness is divided into eight sections (nine nodes), and the oxygen concentrations are calculated with the expression

$$C(X, t+\Delta t) = C(X, t) + \frac{D\Delta t}{\Delta X^2}[C(X+\Delta X, t) - 2C(X, t) + C(X-\Delta X, t)] \quad (4\text{-}292)$$

where

$C(X,t)$ = oxygen concentration at position X and time t (kg/m^3)

D = diffusion constant of oxygen in zircaloy (m^2/s) [see Equation (4-293)]

ΔX = one-eighth of the beta layer thickness (m).

The diffusion constant is found with a correlation of experimental data versus temperature

$$D = 2.63\times10^{-6}\exp\left(-\frac{14200}{T}\right) . \quad (4\text{-}293)$$

In solving Equation (4-292) for oxygen concentrations, it is assumed that the concentration at the alpha beta interface (the first node) is always the saturation concentration for beta zircaloy,[a] that diffusion of oxygen into the beta region does not begin until the temperature is greater than 1,239 K, and that the initial oxygen concentration throughout the as fabricated metal is 0.0012 weight fraction.

The oxygen profiles calculated with Equation (4-292) are used to calculate the average mass of oxygen added to the beta layer. The expression used is

$$F = \frac{M}{6490B} - 0.0012 \quad (4\text{-}294)$$

where

F = oxygen weight fraction in the beta layer in excess of the as-fabricated content (dimensionless)

M = total oxygen in beta layer per unit surface area (kg/m^2)

a. Equations (4-315) through (4-317) are used to determine this concentration.

B = thickness of beta layer (m).

Since the oxygen weight fraction in the alpha phase is nearly constant at 0.047, no calculation is necessary for this parameter. It is simply listed in the COBILD code.

Section 4.15.2 is a review of the literature on zircaloy oxidation. The models that have just been presented are developed in Section 4.15.3. Section 4.15.4 is a description of the zircaloy oxidation subcodes, and references are listed in Section 4.15.5.

4.15.2 Zircaloy Oxidation Literature and Data

The review of oxidation data is divided into separate discussions of low and high-temperature data.

4.15.2.1 Low Temperature Oxidation (CORROS). Investigators generally agree[4.15-1,4.15-2] that oxidation of zirconium alloys by water in the temperature range from 573 to 673 K proceeds by the migration of oxygen vacancies from the oxide metal interface through the oxide layer to the oxide coolant surface (and the accompanying migration of oxygen in the opposite direction). The vacancies at the metal oxide surface are generated by the large chemical affinity of zirconium for oxygen. Although the rate of oxidation is controlled in part by vacancy migration, the process of oxygen transfer from coolant to metal is not complete until the vacancy is annihilated by an oxygen ion at the oxide coolant surface. It is thus reasonable to expect the complex array of both bulk oxide properties effects and surface (coolant chemistry) effects that are reported in the literature.

Well-characterized data for out-of-pile oxidation are available from numerous experiments. The principal features of these data are:

a. There is a transition between initial oxidation kinetics and later oxidation kinetics. The transition is a function of temperature and oxide layer thickness.

b. The pre-transition oxidation rate is time dependent and inversely proportional to the square of the oxide thickness.

c. The post-transition oxidation rate of a macroscopic surface is constant.

Detailed mechanisms to explain the time dependencies of zircaloy oxidation have not been established in the literature.[4.15-3,4.15-4] Proposed mechanisms are discussed in conjunction with the models developed in Section 4.15.3.

Empirical relations based on out of pile data are published in Reference 4.15-2. These relations are as follows:

$$\text{pre-transition oxidation} = (27.1 \pm 0.8)\times 10^{3} t^{1/3} e^{\left(-\frac{5220}{T}\right)} \qquad (4\text{-}295)$$

$$\text{post-transition oxidation} = (23.0 \pm 0.7)\times 10^{8} t e^{\left(\frac{14400}{T}\right)} \quad (4\text{-}296)$$

$$\text{weight gain at transition} = (123 \pm 4) e^{\left(\frac{790}{T}\right)} \quad (4\text{-}297)$$

where

oxidation = weight gain (mg/dm^2)

T = temperature (K)

t = time (days).

The correlations were reported to be accurate to $\pm$ 4%.

In-reactor oxidation is not successfully predicted by Equations (4-295) through (4-297). This oxidation is enhanced by physical mechanisms that are not completely clear. It is known that the enhancement is different in BWR environments than in PWR environments and that the enhancement is more pronounced at the lower end of the 573 to 673 K temperature range. An adequate data base for a careful prediction of oxidation enhancements in reactor environments is not available in spite of several past studies, which have concentrated on the effects of dissolved oxygen,[4.15-5,4.15-6] fast neutron flux,[4.15-6] fast neutron fluence,[4.15-7] and gamma irradiation.[4.15-8]

4.15.2.2 High Temperature Oxidation. Many of the complications observed with low temperature oxidation are absent at high temperatures. The use of parabolic kinetics to describe the total oxygen uptake by zircaloy from steam and the ZrO_2 and oxygen-stabilized alpha layers has been extensively documented by experimenters in several countries. In the United States, there has been a series of reports from ORNL[4.15-9,4.15-10] and from Worcester Polytechnic Institute.[4.15-11] There have been similar reports by Urbanic in Canada,[4.15-12] Leistikow in Germany,[4.15-13] and Kawasaki in Japan.[4.15-14] The only published data above 1,853 K are the measurements by Urbanic and Heidrick[4.15-15] at temperatures between 1,320 and 2,120 K. These data show a discontinuity in the oxidation rate at about 1,853 K. Since this temperature is near the monoclinic-to- cubic transformation of the oxide, it is suspected that the change in oxidation rate is due to the oxide structure change. No discontinuity was observed in the oxygen-stabilized α-Zr(O) layer, and none would be expected because the growth rate of this layer is controlled by the rate of oxygen diffusion into the beta-phase zircaloy. Urbanic and Heidrick calculate rate constants from the slope of the linear portion of a plot of their $(\text{weight gain})^2$ data versus time.

Several papers have been published describing the UO_2-Zr reaction responsible for the inside α-Zr(O) layers observed when cladding contacts UO_2 fuel. Hofmann and Politis[4.15-16] have published a particularly useful article. Other important papers are by Mallet[4.15-17] and Rooney and Grossman.[4.15-18] These investigators agree that a layered structure exists next to the fuel and that the inner surface reaction

layer farthest from the UO_2 is oxygen stabilized alpha zirconium. Next, a (U,Zr) alloy is found, which is primarily uranium. The different authors disagree in their description of this (U,Zr) alloy, and there is a further difference among them about the oxygen-stabilized alpha layer adjacent to the fuel.

An attempt to model the UO_2-Zr reaction analytically has been made by Cronenberg and El-Genk.[4.15-19] However, their analysis deals only with the diffusion of oxygen from the fuel and describes the resulting oxygen gradients in both the fuel and the zirconium. Their model has the advantage of being based largely on first principles, but it does not give the detail observed experimentally by the other investigators.

4.15.3 Model Development

Oxidation of materials that form a protective oxide layer is frequently found to conform to the assumption that the rate determining process is the diffusion of oxygen atoms across the oxide.[4.15-20] In this case, the rate of oxygen diffusion across the oxide layer is given by Fick's law

$$J_x = -D\frac{\partial N}{\partial X} \tag{4-298}$$

where

J_x = flux of oxygen atoms (atoms/m^2•s)

D = a function of temperature (m^2/s)

N = concentration of oxygen atoms (atoms/m^3)

X = direction perpendicular to the oxide surface (m).

If the concentration of oxygen atoms at both surfaces of the oxide surface is fixed, Equation (4-298) implies that the rate of formation of the oxide thickness will be inversely proportional to the oxide thickness

$$\frac{dy}{dt'} = \frac{D(N_s - N_i)}{Cy} \tag{4-299}$$

where

y = oxide layer thickness (m)

t' = time (s)

N_s = concentration of oxygen atoms at oxide surface (atoms/m^3)

N_i = concentration of oxygen atoms at oxide metal interface (atoms/m^3)

C = concentration of oxygen atoms in the oxide layer (atoms/m^3).

Integration of this equation from $y = Z_i$ at $t' = 0$ to $y = Z_f$ at $t' = \Delta t$ yields the parabolic time dependence of Equation (4-290), which is observed experimentally for high temperature oxidation.

4.15.3.1 Low Temperature Oxidation (CORROS). The fact that low temperature oxidation does not obey a parabolic time dependence implies that oxygen diffusion across the oxide is not the rate-controlling step. However, a slight extension of the derivation of the parabolic oxidation produces a result consistent with the measured time dependence of zircaloy corrosion. As mentioned at the beginning of Section 4.15.2.1, the migration of oxygen from the oxide surface to the metal-oxide interface may actually be caused by the migration of oxygen vacancies from the oxide metal interface through the oxide layer to the oxide-coolant surface. If the vacancies have a long lifetime, their migration should obey Fick's law. If the vacancies have a lifetime that is short compared to the time required to diffuse across the oxide layer, the flux of vacancies arriving at the oxide-coolant surface will be proportional to the inverse of the time, $t_{diffusion}$, required for a vacancy to diffuse to the oxide-coolant surface. Since this time is proportional to the square of the average diffusion distance $t_{diffusion} \alpha y^2$, the vacancy flux arriving at the oxide-coolant surface, and thus the rate of oxidation, should be proportional to the inverse of the square of the oxide thickness that the vacancies must cross.

From the physical arguments of the last paragraph, the vacancy lifetime limited rate of oxide growth should be $dy/dt' = M/y^2$, where M is not a function of time or oxide thickness. Integration of the rate equation from $y = X$ at $t' = 0$ to $y = X$ at $t' = t$, gives $X = (3Mt + X_0^3)^{1/3}$, which is the observed result. If the vacancy concentration at the metal oxide surface is assumed to be given by an expression of the form $M = R \exp(-T_o/T)$, where R and T_o are constants and T is the temperature of the interface, the resultant expression for pre-transition oxidation is

$$X = \left[(3Rt)\exp\left(-\frac{T_0}{T}\right) + X_0^3\right]^{1/3} . \qquad (4\text{-}300)$$

Post-transition oxidation is viewed in this section as a series of pre-transition modes. An inner oxide layer shown schematically in Figure 4-61, with thickness that varies as a function of surface position, is presumed to control the rate of oxidation until this inner layer grows to the transition thickness. At this time, the inner layer changes to an outer layer that does not affect the oxidation rate and growth of a new inner layer begins. The representation is adopted because it successfully relates pre-transition and post-transition oxidation rates for out-of-pile data.

If the representation with an inner oxide film of varying thickness is correct, the rate controlling inner part of the oxide layer should join the outer layer at a thickness approximately equal to the transition

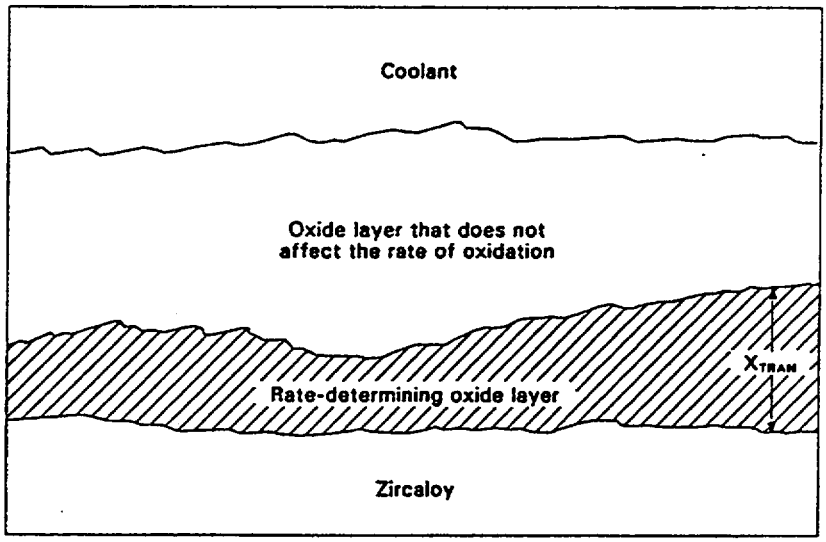

Figure 4-61. Schematic of post-transition oxide, showing an intact, rate-determining layer of varying thickness, with another oxide layer that does not affect the oxidation rate.

thickness but at a time determined by local conditions. After several cycles, the growth rates of the inner oxide layer at different locations on the surface of a macroscopic oxide film will be out of phase; and the rate of growth of the entire surface film at any time (which is what is observed in most experiments) will be the time-average rate of growth at any one place on the surface:

$$\frac{dy}{dt_{\text{surface average}}} = \frac{X_{TRAN}}{t_{TRAN_o}} = \frac{3R\exp\left(-\frac{T_0}{T}\right)}{X_{TRAN}^2} \tag{4-301}$$

where

y = oxide layer thickness (m)

X_{TRAN} = thickness of the oxide layer at transition (m)

t_{TRAN_o} = time necessary for an oxide film to grow from almost zero thickness to the transition thickness, according to Equation (4-288) (s)

T = temperature (K)

T_o = constant (K)

R = constant (m^3/day).

Since the post-transition oxidation is viewed as being a series of pre-transition modes that are separated by local loss of the inside oxide film, one would expect to obtain the pre-and post-transition oxidation rates with a single set of constants. In fact, the empirical constants determined by Van der Linde[4.15-2] for the pre-and post-transition oxidation rates [Equations (4-295) and (4-296)] can be reproduced with a single set of parameters, T_0 = 14,080 K, R = 1.659 x 10^{-9} m^3/day, and X_{TRAN} = 7.749 x 10^{-6}m exp (-790/T). Oxidation rates obtained using these constants and Equations (4-300) and (4-301) are within the ± 4% error reported by Van der Linde for oxidation rates obtained using Equations (4-295) and (4-296).

Changes in oxidation due to in-pile chemical effects are incorporated into the present model with an enhancement factor, A, which describes a multiplicative in-pile enhancement of the out-of-pile oxidation rate due to an increased supply of oxygen ions. The explanation of an increased supply of oxygen ions[4.15-8] was adopted over an alternate explanation, which suggests that in-pile corrosion enhancement is due to irradiation damage of the oxide layer,[4.15-21,4.15-22] because the former can be modeled by a simple change in the rate constant while the latter would require adding a new mechanism to the model. There are no definitive experiments to indicate which approach is correct.

Rate equations for in pile oxidation are thus:

For the pre-transition regime,

$$\frac{dX}{dt_{pre}} = \frac{AR\exp\left(-\frac{T_0}{T}\right)}{X^2} \quad . \tag{4-302}$$

For the post-transition regime,

$$\frac{dX}{dt_{post}} = \frac{3AR\exp\left(\frac{-T_0}{T}\right)}{X_{TRAN}^2} \tag{4-303}$$

where the terms of the equations have been previously defined.

The integrated forms of these equations are:

$$X_{PRE} = \left[3ARt\exp\left(-\frac{T_0}{T}\right) + X_0^3\right]^{1/3} \tag{4-304}$$

and

$$X_{POST} = \frac{3AR(t - t_{TRAN})\exp\left(-\frac{T_0}{T}\right)}{X_{TRAN}^2} + X_{TRAN} \quad (4\text{-}305)$$

if X_0 is less than X_{TRAN}. If X_0 is greater than X_{TRAN},

$$X_{POST} = \frac{3AR(t_{exp})\exp\left(-\frac{T_0}{T}\right)}{X_{TRAN}^2} + X_0 \quad . \quad (4\text{-}306)$$

An interesting result (and a good test of the theory if time-dependent in-reactor data become available) is the fact that the rate enhancement factor A does not result in a linear change in the oxide thickness for pre-transition films. That is, although the oxidation rate is enhanced by factor A, the pre-transition oxide film thickness at a given time is merely $A^{1/3}$ as thick as it would have been without the in-pile enhancement. Since the post-transition oxidation is linear in time, both the rate and change in oxide thickness at a particular time are enhanced by factor A.

The metal-oxide temperature is computed from the temperature at the outer oxide surface, the heat flux across the oxide surface, and the thermal conductivity of the oxide layer by the expression

$$T = T_c + Q\left(\frac{X}{KO2}\right) \quad (4\text{-}307)$$

where

T	=	temperature of the oxide-metal interface (K)
T_c	=	temperature of the outer surface of the oxide (K)
Q	=	heat flux across the oxide layer (W/m^2)
X	=	oxide layer thickness (m)
KO2	=	thermal conductivity of the oxide layer (W/m + K).

Since the term Q(X/KO2) normally is a small correction to the temperature of the outer oxide surface, the correction to the temperature is approximated with an iteration. For the first step, X is

approximated as the initial oxide thickness. The oxide thickness is then computed with Equation (4-304), (4-305), or (4-306), and the resultant value is inserted for X in Equation (4-307).

Expressions for the enhancement factor, A, were obtained by correlating BWR and PWR data to temperature. Values of the enhancement factor for BWRs shown in Figure 4-62 were proposed in Reference 4.15-22 and Reference 4.15-23. The point attributed to Megerth is the average value, A = 9, found necessary to obtain a reasonable fit of the model developed here to the oxidation data presented in Reference 4.15-24 and Reference 4.15-25. The analytical expression used in CORROS to represent these BWR enhancement factors in the temperature range $500 < T < 673$ K is

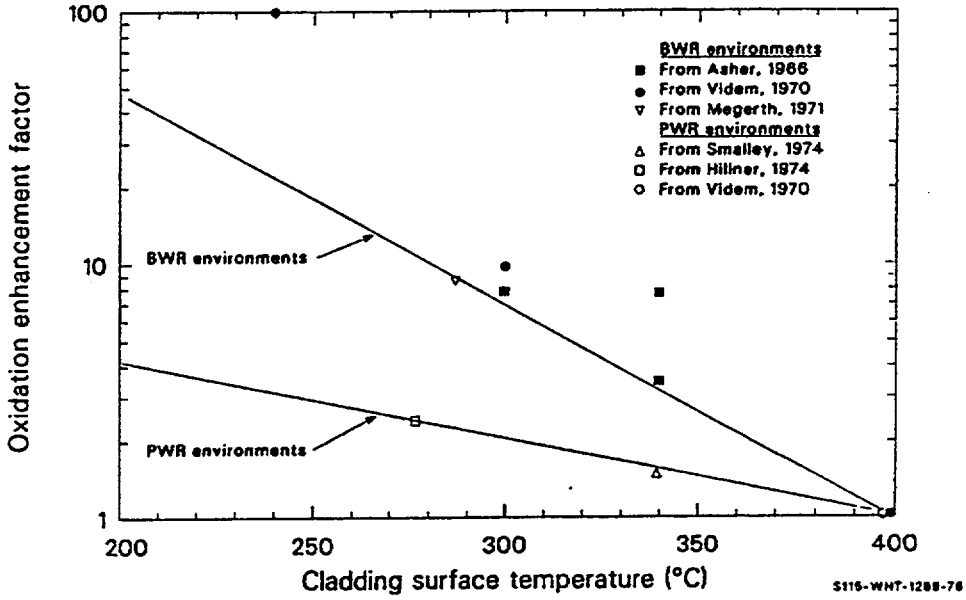

Figure 4-62. Estimates of enhancements over out-of-pile oxidation rates when cladding is irradiated in typical BWR and PWR environments.

$$A = 4.840\times10^{5}\exp(-1.945\times10^{-2}T_c) \qquad (4\text{-}308)$$

where

A = the enhancement factor

T_c = the temperature at the outer oxide surface (K).

Enhancement factors have been reported to be about 2.4[4.15-26] for zircaloy-2 rods in the Shippingport PWR. A fit of Equation (4-288) to values of oxide thickness reported in Reference 4.15-255 agreed with this value. A similar fit of the equation to values reported from Saxton PWR rods[4.15-27,4.15-28] resulted in a

value of A = 1.5. These values are also plotted in Figure 4-62. The relatively small value of A in PWR environments (which do not contain dissolved oxygen in the bulk coolant) is consistent with the picture of enhanced oxygen atom and ion supply rates due to ionization of dissolved oxygen. As in the case of BWR environments, the straight line sketched between these points is used by CORROS to estimate the enhancement in a typical PWR environment. The equation for $500 < T < 673$ K is

$$A = 1.203 \times 10^{2} \exp(-7.118 \times 10^{-3} T_c) \quad (4\text{-}309)$$

where

A = the enhancement factor

T_c = the temperature at the oxide coolant surface (K).

The predictions of the model developed in this section are compared with the values reported for individual samples in Figure 4-63 through Figure 4-65. There is considerable scatter in the data from individual rods, with maximum measured values of oxide thickness as large as twice the average values. In some cases, such as the Shippingport data of Figure 4-63, variations are generally consistent with the idea that temperature variations are responsible. In other cases, such as the Saxton data of Figure 4-64, variations are not explained solely by temperature variation; and the cause is probably related to local variations in coolant quality or chemistry caused by nucleate boiling or to contaminants. Similarly, variations in the coolant along the BWR rods could contribute to the large scatter in the BWR data of Figure 4-65. Note that the duration of the pre-transition period varies considerably in Figure 4-63 through Figure 4-65. Figure 4-63 and Figure 4-64 refer to PWRs with relatively low oxidation rate enhancements. However, the temperature is higher in the case of Figure 4-64, producing a shorter pre-transition period due to more rapid oxidation. Figure 4-65 refers to a BWR with low temperatures but a large oxidation enhancement factor (9 in this case). This results in a long pre-transition period so that the relatively rapid post-transition oxidation is predicted to start late for the BWR.

4.15.3.2 High Temperature Oxidation (COBILD, COXIDE). The COBILD and COXIDE subcodes were adapted from another code, BUILD5, written by Pawel, of Oak Ridge National Laboratory. Although BUILD5 was written in the computer language BASIC and the MATPRO codes are in FORTRAN, the computational techniques are similar. COBILD and COXIDE have been expanded to include oxidation of the cladding on the inside surface by oxygen released from the fuel. The oxygen weight fraction in the beta phase and the linear power generation from the metal-water reaction are also calculated in COBILD and COXIDE but not BUILD5.

The correlations for ZrO_2 thickness, α-Zr(O) thickness, and weight gain due to steam reaction between 1,239 and 1,853 K were taken from Cathcart,[4.15-9,4.15-10] because Cathcart's expressions give the best fit to the pooled data from all the sources mentioned in Section 4.15.2.[a] A comparison with data of the ZrO_2 thicknesses calculated with Cathcart's equation is shown in Figure 4-66. A similarly good fit is

a. Cathcart recommends these correlations only to 1,773 K. The authors extrapolated to 1,853 K, where the data of Urbanic and Heidrick suggest a discontinuity.

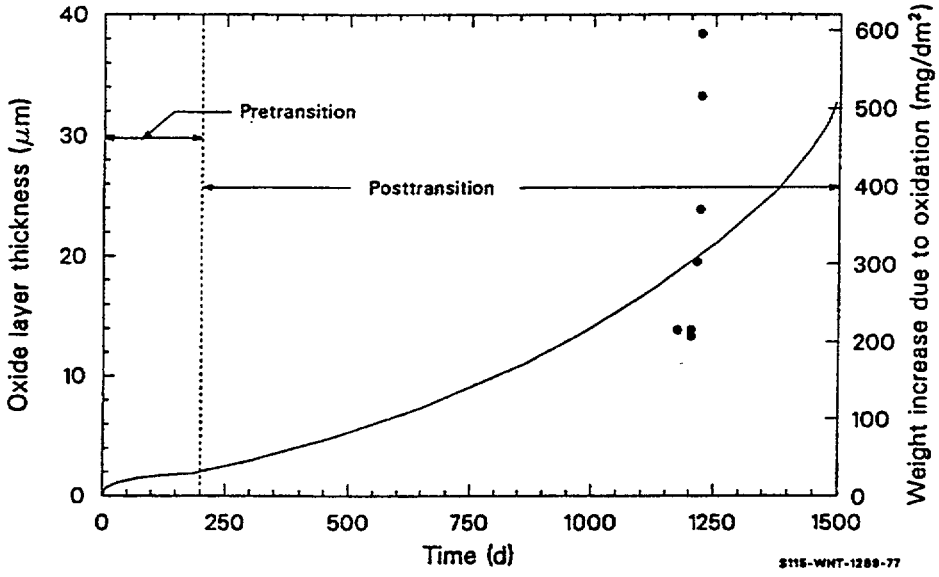

Figure 4-63. Comparison of the predicted oxide layer thickness with the base data from average values of six Shippingport zircaloy-2 rods in a PWR environment at 277 °C.

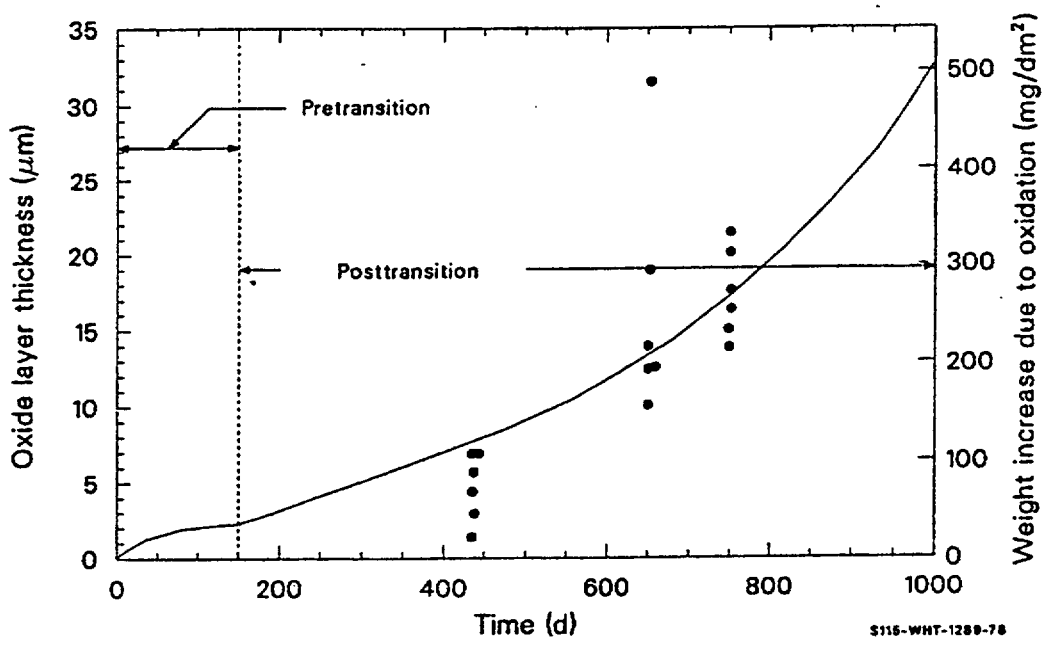

Figure 4-64. Comparison of the predicted oxide layer thickness with the base data from Saxton zircaloy-4 rods in a PWR at 340 °C.

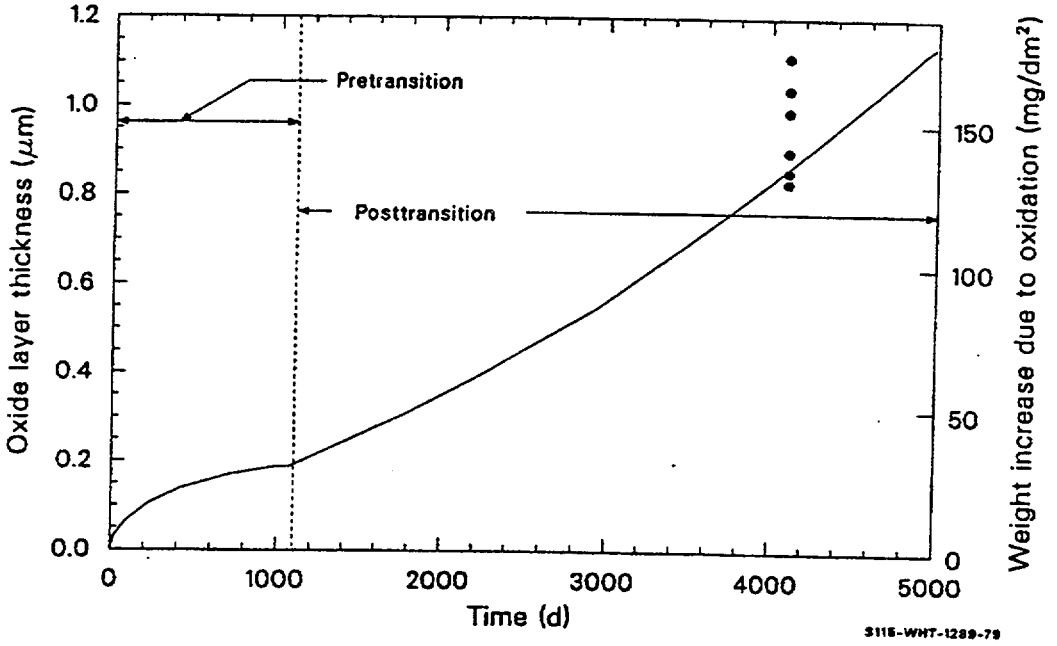

Figure 4-65. Comparison of the predicted oxide layer thickness with the base data from zircaloy-2 rods irradiated in the Vallecitos and Dresden BWRs at 286 °C.

obtained when the alpha thickness and weight gain correlations are compared with the data. Rate constants for temperatures between 1,853 and 2,100 K were taken from Urbanic and Heidrick.[4.15-15] In order to convert the correlations for zircaloy consumed given by Urbanic and Heidrick to oxygen consumed, the parabolic rate constant for zircaloy consumed was multiplied by the square of the ratio of oxygen consumed to zircaloy consumed given in Equation (4-310).

Cathcart has thoroughly analyzed the uncertainty in his measurement.[4.15-29] In an earlier report[4.15-30] he reported joint 90% confidence levels for the rate constants [A exp (-B/T)] of Table 4-46. The word "joint" is used to indicate the uncertainty of the rate constant as a whole rather than uncertainties in the parameters A and B separately. His conclusions are presented in Table 4-48. These uncertainties are recommended for use with the oxidation codes in the temperature range where Cathcart's correlations are used.

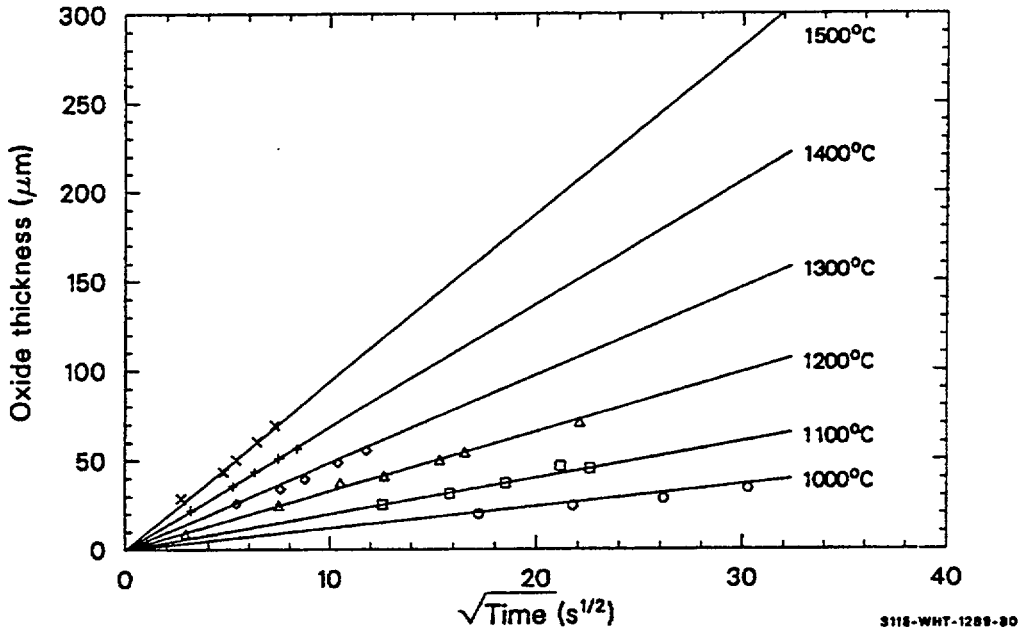

Figure 4-66. Comparison of calculated (solid lines) and measured ZrO_2 thickness for six temperatures.

Table 4-48. 90% joint confidence intervals for the parabolic rate constants for oxide layer growth, alpha layer growth, and total oxygen uptake.

	Percent deviation from expected value		
	1,323 K	1,523 K	1,773 K
Oxide	+4.9	+2.5	+4.3
Layer	-4.7	-2.4	-4.1
Alpha	+12.1	+6.1	-10.1
Layer	-10.8	-5.8	-9.2
Oxygen	+3.4	+1.7	+3.0
Uptake	-3.3	-1.7	-2.9

The numbers given in Table 4-48 are for isothermal oxidation only. There are no comparable statistics available for time dependent problems, largely because of the difficulty in obtaining reliable temperature measurements under transient conditions.

The standard error[a] of the weight gain correlation of Urbanic and Heidrick with respect to its own data base is 0.49 kg/m^2.

Only the linear portions of the entire data curves shown in Figure 4-67 were used by Urbanic and Heidrick to determine the high temperature correlation. Since these data did not pass through the origin, the resulting offset is the main contributor to the standard error.

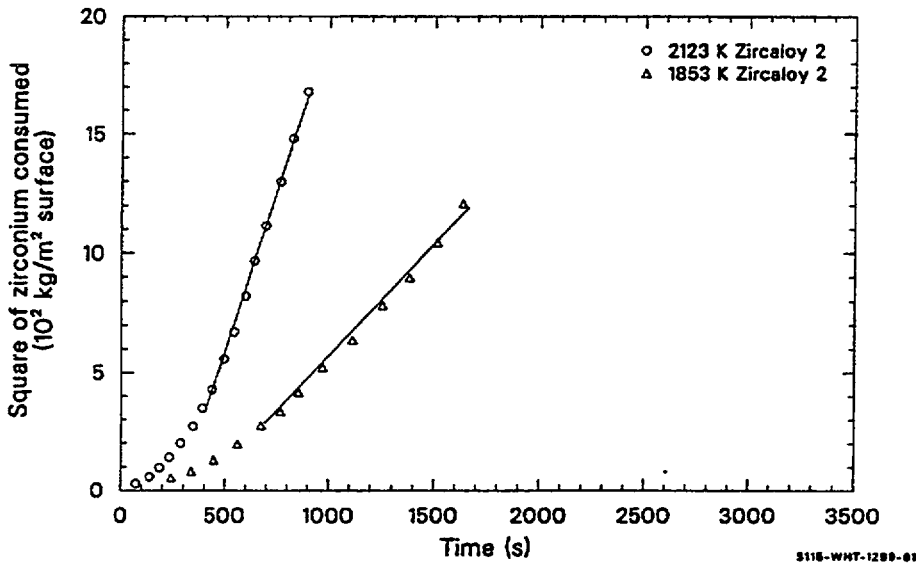

Figure 4-67. Data used by Urbanic and Heidrick to determine high temperature zircaloy oxidation rates.

The layers of alpha zircaloy on the inside cladding surface of unruptured cladding are caused by zircaloy-UO_2 interaction. The model for cladding oxidation by UO_2 is taken from Hofmann's results[4.15-16] for two reasons. His time and temperature data base is wider than that of Grossman and Rooney or of Mallet, and Hofmann gives correlations which can be integrated to become part of the high-temperature oxidation subcodes.

---

a. The expression used to calculate the standard error, σ, is

$$\sigma = \sum_{i=1}^{n} \frac{(C_i - M_i)^2}{n-1}$$

where

C_i = calculated weight gain

M_i = measured weight gain

n = number of data used.

In Figure 4-68, Hofmann's correlations for the α-Zr(O) layers are compared with his data; and the data are presented in Table 4-49. The standard deviations of the correlations with respect to their own data bases are ± 18% for $Zr(O)_a$ for T < 1,600 K and ± 16% for $Zr(O)_b$ for T < 1,760 K.

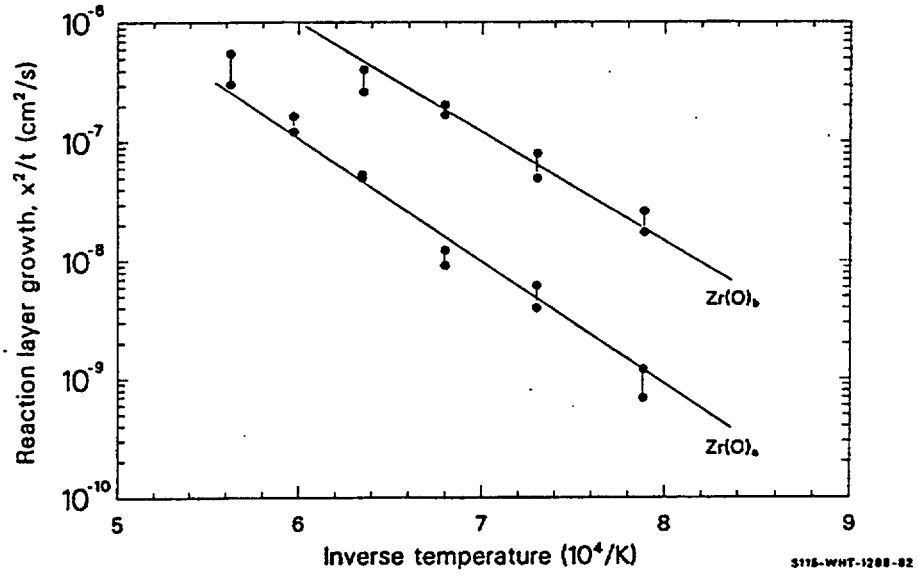

Figure 4-68. Growth of Zr(O) and $Zr(O)_b$ layers as a function of temperature from Hofmann and Politis.[4.15-16]

Table 4-49. Time temperature layer thickness data from Hoffman's[4.15-16] out of pile experiments.

	Depth of reaction layers (mm)		
Temperature (°C)	**Time (min)**	**$Zr(O)_a$**	**$Zr(O)_b$**
1,000	10	7	41
1,000	20	10	50
1,000	30	12	61
1,000	60	22	80
1,100	10	16	67
1,100	20	28	100
1,100	30	32	95
1,100	60	38	136

Table 4-49. Time temperature layer thickness data from Hoffman's[4.15-16] out of pile experiments.

	Depth of reaction layers (mm)		
Temperature (°C)	**Time (min)**	**$Zr(O)_a$**	**$Zr(O)_b$**
1,200	6	19	79
1,200	10	25	114
1,200	20	34	157
1,200	30	44	198
1,200	60	70	270
1,300	3	32	90
1,300	6	48	108
1,300	10	50	130
1,300	20	84	241
1,300	30	82	240
1,400	3	53	116
1,400	6	70	110
1,400	10	96	156
1,400	20	152	--
1,500	3	90	76
1,500	61	18	--
1,500	10	162	--
1,500	20	290	--

Calculations of the rate of heat generation are based on the heat of reaction of zirconium, 6.45×10^6 J/kg of zirconium converted to ZrO_2 by steam.[4.15-31] Since the weight fraction of oxygen in ZrO_2 is 0.26, the ratio of zirconium consumed to oxygen added is

$$\frac{\Delta Zr}{\Delta W} = \frac{1 - 0.26}{0.26} \tag{4-310}$$

where

ΔZr = mass of zirconium per unit surface area consumed by oxidation during the given

time increment (kg/m^2)

ΔW = mass gain per unit surface area due to oxidation during a given time increment (kg/m^2).

The mass of zirconium consumed per unit length for a cylindrical rod is the mass per unit surface area times the circumference. The rate of heat generation per unit length is thus

$$P = \frac{0.74\Delta W}{0.26\,\Delta t} 2\pi R_0 6.45\times10^6 \frac{J}{m} \quad . \tag{4-311}$$

This expression is equivalent to Equation (4-291).[a]

Figure 4-69 is a plot of P versus temperature for a fuel rod with an initial radius $R_0 = 6.25 \times 10^{-3}$ m. Several initial oxide thicknesses are shown, and a time step of 1 second is assumed in each case. The exponential increase in power with temperature is evident, as is the proportional relation between instantaneous power and reciprocal oxide thickness.

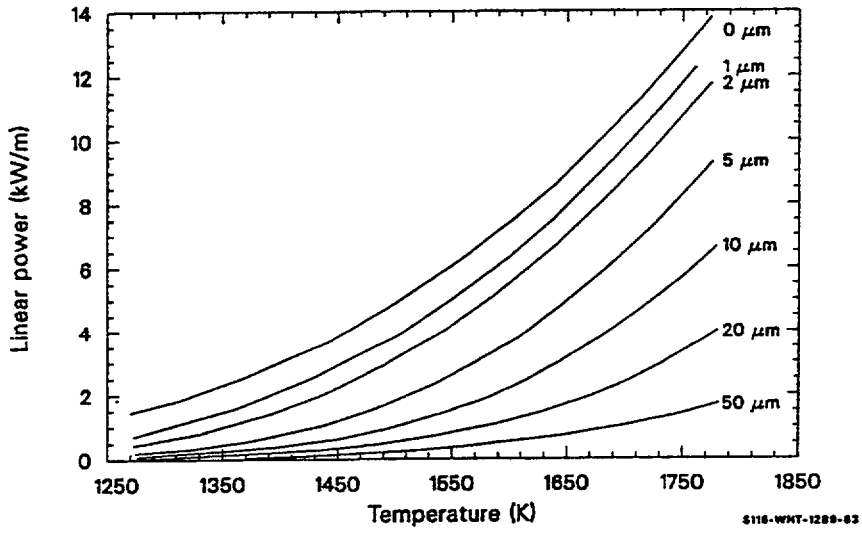

Figure 4-69. Linear power generation for a rod of initial diameter of 1.25×10^{-2} m as a function of temperature for various initial oxide thicknesses.

Equation (4-311) may underpredict the oxidation heating rate because it uses the heat released in the reaction

a. The derivation of Equation (4-311) uses the oxygen weight gain rather than the ZrO_2 thickness correlation because some of the oxygen consumed appears in the α-Zr(O) and beta layers.

$$2H_2O + Zr \rightarrow 2H_2 + ZrO_2 + Q \ . \qquad (4\text{-}312)$$

With $Q = 6.5 \times 10^6$ J/kg of zircaloy reacted, Q is smaller by nearly a factor of two than Q_1, the heat released in the following reaction:

$$Zr + O_2 \rightarrow ZrO_2 + Q_1 \qquad (4\text{-}313)$$

where Q_1 is 1.204×10^7 J/kg of zircaloy reacted.[4.15-32]

The difference arises because Equation (4-312) includes the heat required for the endothermic dissociation of water reaction

$$2H_2O + Q_2 \rightarrow 2H_2 + O_2 \ . \qquad (4\text{-}314)$$

The dissociation described by Equation (4-314) must take place either at the oxide-to-coolant interface or within the coolant itself. The oxygen thus liberated then diffuses through the oxide layer and combines with the zircaloy at the metal-to-oxide interface according to Equation (4-313). It is clearly Q_1 and not Q that causes the cladding to heat. However, Q_2 must ultimately come from the rod as well, cooling it. In a closed system, Equation (4-312) would be adequate. A problem can arise because the system is not strictly closed. As an example, dissociation may occur near one rod, cooling it, and oxidation may occur within an adjacent rod, heating it. The assumption made here is that these processes average out and Equation (4-312) is satisfactory.

COBILD calculations for the oxygen profile in the beta region, Equation (4-292) are taken directly from a computer code described by Pawel.[4.15-33] Equation (4-293), the diffusion constant used in the oxygen profile calculation, is from Perkins[4.15-34,4.15-35] (converted from oxygen 18 to oxygen 16); and the following correlation is used to determine the saturation concentration of oxygen in beta zircaloy.

For $T < 1{,}239$ K,

$$CS = 0.0012 \ . \qquad (4\text{-}315)$$

For $1{,}239 \leq T < 1{,}373$ K,

$$CS = [-0.0042807 + (T/392.46 - 3.1417)^{1/2}]/100 \ . \qquad (4\text{-}316)$$

For $T \geq 1{,}373$ K,

$$CS = (T-1081.7)/(4.91157 \times 10^4) \quad (4\text{-}317)$$

where CS is the saturation concentration of oxygen in beta zircaloy (weight fraction).

Equation (4-294), the expression used to calculate the oxygen weight fraction in the beta layer, is derived easily. To find the ratio of oxygen to zircaloy, the total oxygen per unit surface area in the beta region is divided by the product of the density of zircaloy (6,490 kg/m^3) and the beta layer thickness. The weight fraction of as-fabricated zircaloy, 0.0012, is subtracted to find the excess oxygen.

4.15.4 Description of the CORROS, COBILD, COXIDE, COXWTK, and COXTHK Subcodes

The first calculation is a check of the input parameters to determine the appropriate value of the error index. If impossible input parameter values are detected, no further calculations are attempted. If one of the input temperatures is below 1,239 K, only that portion of the time step above 1,239 K is used.

The input pellet-cladding interface pressure is checked to see if there is pellet cladding mechanical interaction during the given time step. If there is interaction, the cladding will be treated as two one-sided oxidation problems with steam supplying the outside source of oxygen and fuel providing the inside source of oxygen. The input initial cladding thickness is thus multiplied by 0.5.

Next, the step-average heat up rate, average temperature, beta saturation concentration, and diffusion constant for oxygen in beta zircaloy are calculated. The input time step size is divided by five to determine a substep size for later calculations, and the initial oxygen weight gain is saved because it will be needed to calculate the power of the oxidation reaction.

The next two sections of the program interpolate to find beta phase concentrations of oxygen if there has been a change from pellet-cladding mechanical interaction to no interaction, or vice versa. The input parameter IP2 is used to determine the prior step status and is updated to indicate current step status in the process.

Initialization of the dimensioned quantities AA(1) to AI(1) at the initial beta-phase oxygen concentrations in the nine outside nodes is performed next. If there is no pellet-cladding mechanical interaction, these nine nodes span the entire beta layer. If there is interaction, the nine nodes span the outer half of the beta layer. The switch IP2 determines which of these cases is present. IP is set equal to zero to indicate that the nine outer nodes are being modeled, since the same coding may later be used to model the nine inside nodes.

The initial thickness of the beta layer being modeled is determined by subtracting the outside alpha layer thickness and two-thirds of the oxide layer thickness from the initial thickness of the region under consideration. The factor of two thirds is found by equating the mass per unit surface area of the oxide to the sum of the zircaloy and oxygen masses that produced the oxide:

$$\rho_{ZrO_2}X = \rho_{Zr}Y + 0.26\rho_{ZrO_2}X \quad (4\text{-}318)$$

where

X	=	oxide layer thickness (m)
Y	=	thickness of zircaloy consumed to make the oxide (m)
ρ_{zr}	=	density of zircaloy (kg/m^3) = 6,490
ρ_{ZrO_2}	=	density of zircaloy oxide (kg/m^3) = 5,820.

The constant 0.26 represents the mass fraction of oxygen in the oxide. Solution of Equation (4-318) for the ratio Y/X yields the required ratio. If the nine nodes under consideration span the entire cladding beta region (IP2 = 0 for no contact), the inside alpha layer thicknesses are also subtracted.

An iteration over five substeps is used to calculate the oxide layer thickness, outside alpha layer thickness, and weight gain due to oxidation by steam. Each substep is assumed to be isothermal, and the temperature is determined by linear interpolation of the input temperatures.

The two layer thicknesses are used to calculate the end of step thickness of the beta zircaloy layer spanned by the outside nine nodes. This thickness is stored as the variable AL80 for possible later addition to the beta thickness spanned by nine inside nodes.

Next, the change in the beta layer is compared with one-eighth of the initial layer. If the change is greater than one-eighth of the initial beta layer, the following message is printed: "DECREASE IN BETA LAYER IS GREATER THAN 1/8 INITIAL LAYER..., TIME STEP TOO LARGE OR BETA LAYER TOO DEPLETED." Also, the error index is changed to one. Physically, the condition implies either that the time step is too long or that the beta layer is nearly completely converted to alpha-zircaloy.

A second check is made to determine if the finite-difference equation of Pawel, Equation (4-292), will be stable. If this condition is violated, the following message is printed: "DIFFUSION IS OCCURRING TOO RAPIDLY FOR COBILD TO ACCURATELY CALCULATE OXYGEN CONCENTRATIONS." Also, the input parameter index is set equal to one.

Since the beta layer boundary moves during the time step, the input oxygen concentrations will not apply to the positions of the nodes at the end of the time step. Thus, two calculations are used to find the oxygen concentration in the beta layer. First, it is assumed that the alpha beta interface jumps immediately to its end-of-step position. A parabolic interpolation is used to find the start of step concentrations at the end of step positions. In the second part of the calculation, Equation (4-292) is applied over five small substeps but always at the end of step positions.

Simpson's rule is used to integrate the oxygen concentrations over the beta layer width in order to find the net oxygen. The net oxygen is stored as AQ20 for possible addition to the net oxygen in the region spanned by the nine inside nodes.

The final concentrations, AA(6) to AI(6), are stored as the output variables AA0 to AI0.

If there is no pellet-cladding interaction, the outer nine nodes span all of the beta layer so the calculation of oxygen concentrations in the beta layer is complete. In this case, the percent saturation, average oxidation power, and average oxygen concentration in the beta layer are calculated and the COBILD calculation is complete.

If there is pellet-cladding interaction, the sequence of calculations for the oxygen concentration is repeated for the inside nine nodes of the beta layer before the percent saturation, average oxidation power, and average oxygen concentration in the beta layer are calculated.

The COXIDE logic is similar to the COBILD logic, but the calculations of oxygen concentration in the beta phase have been omitted.

4.15.5 References

4.15-1 E. Hillner, *Hydrogen Absorption in Zircaloy During Aqueous Corrosion, Effect of Environment*, WAPD-TM-411. November 1964.

4.15-2 A. VanderLinde, *Calculation of the Safe Life Time Expectancy of Zirconium Alloy Canning in the Fuel Elements of the Nero Reactor*, RCN-41, July 1965.

4.15-3 B. Cox, "Comments on the Paper 'The Influence of Oxide Stress on the Breakaway Oxidation of Zircaloy-2 by D. H. Bradhurst and P. M. Heuer," *Journal of Nuclear Materials, 41*, 1970, p. 96.

4.15-4 D. H. Bradhurst and P. M. Heuer, "Reply to Comments by B. Cox on 'The Influence of Oxide Stress on the Breakaway Oxidation of Zircaloy-2," *Journal of Nuclear Materials, 41*, 1971, p. 101.

4.15-5 A. B. Johnson, Jr., "Effects of Nuclear Radiation on the Corrosion, Hydriding, and Oxide Properties of Six Zirconium Alloys," *Applications Related Phenomena for Zirconium and Its Alloys*, ASTM-STP-458, 1969, pp. 301-324.

4.15-6 W. A. Burns, *Effects of Fast Neutron Irradiation, Fabrication History, and Water Oxygen on the Environmental Behavior of Zirconium Alloys*, BNWL-88, 1965.

4.15-7 A. B. Johnson, Jr., and J. E. Irvin, *Radiation-Enhanced Oxidation of Zircaloy-2 in pH-10 LiOH and pH-10 NH_4OH*, BNWL-463, 1967.

4.15-8 L. Lunde and K. Videm, "Effects of Surface Treatment on the Irradiation Enhancement of Corrosion of Zircaloy-2 in HBWR," *Zirconium in Nuclear Applications*, ASTM-STP-551, 1974, pp. 514-526.

4.15-9 J. V. Cathcart, *Quarterly Progress Report on the Zirconium Metal-Water Oxidation Kinetics Program Sponsored by the NRC Division of Reactor Safety Research for April-June 1978*, ORNL/NUREG/TM-41, August 1976.

4.15-10 J. V. Cathcart, *Quarterly Progress Report on the Zirconium Metal-Water Oxidation Kinetics Program Sponsored by the NRC Division of Reactor Safety Research for October-December 1976*, ORNL/NUREG/TM-87, February 1977.

4.15-11 R. G. Ballinger, W. G. Dobson, and R. R. Bierderman, "Oxidation Reaction Kinetics of Zircaloy-4 in an Unlimited Steam Environment," *Journal of Nuclear Materials, 62*, November 1976, pp. 213-220.

4.15-12 V. F. Urbanic, "Method for Estimating the Exposure Time and Temperature for Zircaloy Oxidation in Steam," *Journal of Nuclear Materials, 59*, 1976, pp. 90-94.

4.15-13 S. Leistikow et al., "Untersuchen zur Hochtemperature-Wasserdampf-Oxidation von Zircaloy-4 Hullrohen," *PBS Halbjahresbericht 1976/2*, KfK 2435, February 1977.

4.15-14 S. Kawasaki et al., *Reaction of Zircaloy Cladding with Steam Under Simulated Loss-of-Coolant Accident Conditions*, JAERI-M-6181, July 1975.

4.15-15 V. F. Urbanic and T. R. Heidrick, "High Temperature Oxidation of Zircaloy-2 and Zircaloy-4 in Steam," *Journal of Nuclear Materials, 75*, 1978, pp. 251-261.

4.15-16 P. Hofmann, and C. Politis, "Chemical Interaction Between UO_2 and Zry-4 in the Temperature Range Between 900 and 1,500 °C," *Fourth International Conference on Zirconium in the Nuclear Industry, Stratford-upon-Avon, England, June 26-29, 1979.*

4.15-17 M. W. Mallet et al., *The Zirconium-Uranium Dioxide Reaction*, BMI-1210, July 1975.

4.15-18 D. M. Rooney, and L. N. Grossman, *Interfacial Reaction Between UO_2 and Zircaloy-2*, GEAP-4679, April 1965.

4.15-19 A. W. Cronenberg, and M. S. El-Genk, *An Assessment of Oxygen Diffusion During UO_2--Zircaloy Interaction*, TREE-NUREG-1192, January 1978.

4.15-20 W. Jost, *Diffusion in Solids, Liquids, Gases*, NewYork: Academic Press Inc., 1972, p. 341.

4.15-21 D. H. Bradhurst, P. J. Shirvington, and P. M. Heuer, "The Effects of Radiation and Oxygen on the Aqueous Oxidation of Zirconium and its Alloys at 290 °C," *Journal of Nuclear Materials, 46*, 1973, p. 53.

4.15-22 R. C. Asher et al., "Effects of Radiation on the Oxidation and Hydrogen Absorption of Zirconium Alloys in Steam," *Electrochemical Technology, 4*, 1966, p. 231.

4.15-23 K. Videm, "Properties of Zirconium Base Cladding Materials Corrosion and Hydrogen Pickup," *Advanced Course on Limiting Aspects of Fuel Element Performance in Water Cooled Power Reactors at the Institute for Atomenergi in Kjeller, Norway, August 24-28, 1970.*

4.15-24 F. H. Megerth, C. P. Ruiz, and U. E. Wolff, *Zircaloy-Clad UO_2 Fuel Rod Evaluation Program*, GEAP-10371, June 1971.

4.15-25 H. E. Williamson et al., *AEC Fuel Cycle Program Examination of UO_2, Fuel Rods Operated in the VBWR to 10,000 MWD/TU*, GEAP-4597, 1965.

4.15-26 E. Gillner, "Corrosion and Hydriding Performance in Zircaloy Tubing after Extended Exposure in the Shippingport PWR," *Zirconium in Nuclear Applications*, ASTM-STP-551, 1974, pp. 449-462.

4.15-27 W. R. Smalley, *Saxton Core II Fuel Performance Evaluation, Part I: Materials*, WCAP-3385-56, 1971.

4.15-28 W. R. Smalley, *Saxton Core III Fuel Materials Performance*, WCAP-3385-57, 1974.

4.15-29 J. V. Cathcart, *Quarterly Progress Report on the Zirconium Metal-Water Oxidation Kinetics Program Sponsored by the NRC Division of Reactor Safety Research for January-March 1976*, ORNL/NUREG/TM-17, May 1976.

4.15-30 J. V. Cathcart, *Quarterly Progress Report on the Zirconium Metal-Water Oxidation Kinetics Program Sponsored by the NRC Division of Reactor Safety Research for July-September 1976*, ORNL/NUREG/TM-62, December 1976.

4.15-31 L. Baker and L. C. Just, *Studies of Metal-Water Reactions at High Temperatures-III, Experimental and Theoretical Studies of the Zirconium Water Reaction*, ANL-6548, May 1962.

4.15-32 S. Malang, *SIMTRAN I-A Computer Code for the Simultaneous Calculation of Oxygen Distributions and Temperature Profiles in Zircaloy During Exposure to High Temperature Oxidizing Environments*, ORNL-5083, November 1975.

4.15-33 R. E. Pawel, "Diffusion in a Finite System with a Moving Boundary," *Journal of Nuclear Materials, 49*, January 1974, pp. 281-290.

4.15-34 R. A. Perkins, *Zirconium Metal Water Oxidation KineticsII, Oxygen-18 Diffusion in Beta Zircaloy*, ORNL/NUREG/TM-19, 1976, p. 33.

4.15-35 R. E. Pawel, R. A. Perkins, R. A. McKee, J. V. Cathcart, G. J. Yurek, and R. E. Druschel, "Diffusion of Oxygen in Beta-Zircaloy and the High Temperature Zircaloy Steam Reaction," *Zirconium in the Nuclear Industry*, ASTM-STP-663, 1977, pp. 119-133.

4.16 Cladding Hydrogen Uptake (CHUPTK)

This subroutine calculates the average weight fraction of hydrogen in zircaloy cladding during typical reactor operation at temperatures of 523 to 650 K. Required inputs are: as-received hydrogen concentration in the cladding, initial fuel water content, fuel pellet diameter, type of cladding (zircaloy-2

or zircaloy-4), cladding inside and outside diameters, type of reactor (BWR or PWR), oxide thickness at the start and end of the current time step, temperature at the oxide-coolant interface, heat flux, zirconium oxide thermal conductivity, and the average weight fraction of hydrogen in the cladding at the start of the current time step.

4.16.1 Summary

The average weight fraction of hydrogen in zircaloy cladding during steady-state conditions is

$$H = H_o + H_1 + H_c \tag{4-319}$$

where

H = net weight fraction of hydrogen in the cladding (ppm)

H_o = initial concentration of hydrogen in the cladding due to impurities introduced during manufacturing and autoclaving (ppm). Typical values are 8 to 30 ppm[4.16-1,4.16-2]

H_1 = concentration of hydrogen in the cladding due to internal outgassing of water absorbed by the fuel (ppm)

H_c = concentration of hydrogen in the cladding due to absorption of hydrogen from the coolant (ppm).

H_o is an input parameter. H_1 is calculated by the routine using the input values for parts per million water vapor in the fuel, the input cladding dimensions, and the input fuel pellet diameter. CHUPTK assumes that all the hydrogen from the water vapor in the fuel is picked up by the cladding.

The primary consideration in determining H is the determination of H_c. Analytical expressions for H_c are divided into three parts: Equation (4-320) for oxide films thinner than the transition thickness,[a] Equation (4-321) for oxide films equal to the transition thickness at some point in the current time step, and Equation (4-322) for oxide films greater than the transition thickness during the current time step. In these equations, the variable H_c has been converted from a fraction of the oxide's oxygen increase to units of average parts per million by weight in the cladding.

$$H_{cf} = \left[\frac{(9\times10^5)d_o}{d_o^2 - d_i^2}\right]\frac{B}{8A}(X_f - X_i) + H_{ci} \tag{4-320}$$

a. Oxide film growth is discussed in conjunction with the description of the cladding oxidation subcode, CORROS. The terms pre- and post-transition refer to two different stages in the growth of the oxide film. A transition between the two stages occurs when the oxide film has added approximately 30 mg of oxide per dm^2 of oxide surface.

$$H_{cf} = \left[\frac{(9\times10^5)d_o}{d_o^2 - d_i^2}\right]\left[\frac{B}{8A}(X_f - X_i) + \frac{C}{8A}(X_f - X_{TRAN})\right] + H_{ci} \quad (4\text{-}321)$$

$$H_{cf} = \left[\frac{(9\times10^5)d_o}{d_o^2 - d_i^2}\right]\frac{C}{8A}(X_f - X_{TRAN}) + H_{ci} \quad (4\text{-}322)$$

where

H_{cf} = weight fraction of hydrogen added to the cladding from the coolant at the end of the current time step (ppm by weight)

H_{ci} = weight fraction of hydrogen added to the cladding from the coolant at the start of the current time step (ppm by weight)

d_o = cladding outside diameter (m)

d_i = cladding inside diameter (m)

B = fraction of hydrogen liberated by the reaction with the coolant that is absorbed by the cladding during pre-transition oxidation. The value of B is a function of the input parameters ICOR (BWR or PWR chemistry) and ICM (zircaloy-2 or zircaloy-4). Values of B for zircaloy-2 are 0.48 in a PWR environment and 0.29 in a BWR environment. For zircaloy-4, B = 0.12

C = fraction of hydrogen liberated by the reaction with the coolant that is absorbed by the cladding during post-transition oxidation. The value of C is a function of the input parameter ICM (zircaloy-2 or zircaloy-4). The value of C for zircaloy-2 is 1.0. For zircaloy-4, C = 0.12

A = a parameter describing the enhancement of the oxidation rate of the cladding in the reactor environment. The parameter is discussed in conjunction with the description of the cladding oxidation subcode, CORROS. The value for A is determined in the subcode by user specification of BWR and PWR chemistry with the input parameter ICOR

X_i = oxide layer thickness at the start of the current time step (m)

X_f = oxide layer thickness at the end of the current time step (m)

X_{TRAN} = oxide layer thickness at the transition point (typically, 2×10^{-6} m). The value of X_{TRAN} is calculated by the CHUPTK subcode using the expression developed for CORROS (Section 4.15) and the input information.

The approach and general physical picture used to model hydrogen uptake are summarized in Section 4.16.2. Section 4.16.3 develops the basic out-of-pile model, and Section 4.16.4 generalizes the basic model so that it describes in-pile hydrogen uptake.

4.16.2 Background and Approach

It is generally agreed[4.16-3,4.16-4] that oxidation of zirconium alloys by water in the temperature range from 523 to 673 K proceeds by the migration of oxygen vacancies in the oxide layer. Change and physical size considerations imply that the mechanism of introduction of hydrogen into the zirconium metal through an oxide film is by entry of neutral hydrogen atoms into oxygen vacancies in the lattice. (H_2 is too large and H^+ is too positive.) The constant ratio of absorbed hydrogen to oxygen taken up by the cladding (the 'pickup fraction') is explained as having been determined by the competition between possible subsequent reactions of the atomic hydrogen created by corrosion. (The atomic hydrogen can combine to form a gas or enter a surface vacancy in the oxide lattice.)

In this approach, the close relationship between the hydrogen weight gain and the oxygen weight gain from the coolant is viewed as a consequence of the fact that the oxygen and hydrogen usually come from a common source (the water molecule) and are transported to the metal by a common carrier (oxygen vacancies). The hydrogen pickup fraction is determined by the composition of the coolant-oxide surface. In particular, it is suspected that nickel oxide from the nickel in zircaloy-2 absorbs atomic hydrogen at the surface of the oxide and thereby enhances the fractional hydrogen uptake for zircaloy-2.

4.16.3 Out-of-Pile Basis for the Model

The in-pile model is based primarily on out-of-pile data because well characterized data on hydrogen uptake as a function of time and temperature have been published only for out-of-pile corrosion. At least two plausible suggestions for a hydrogen uptake model can be presented from the approach discussed in Section 4.16.2. According to both of these suggestions, the dependent variable is the ratio of the corrosion liberated hydrogen to oxygen absorbed by the metal, although the independent variables differ. A brief, summary of the two models, and a third less probable model, follows.

4.16.3.1 Simple Probabilistic Hydrogen Pickup Model. In this model, the fraction of released hydrogen absorbed by the oxide surface is assumed to be proportional to the rate of appearance of oxide vacancies at the oxide coolant interface. In the discussion of the cladding oxidation model, CORROS, it is shown that the vacancies appear at a rate proportional to the inverse of the square of the oxygen weight gain during the pre-transition phase of oxidation. During the post-transition phase of oxidation, the surface averaged rate of appearance of oxide vacancies is constant and proportional to three times the inverse of the square of the weight of the oxide layer at transition. This model ignores any details of the surface chemistry involved in the absorption of atomic hydrogen by the oxide vacancies.

4.16.3.2 Surface-Controlled Hydrogen Pickup Model. In this model, the fraction of released hydrogen absorbed by the oxide surface is a constant determined by the metallurgy of the oxide surface. The model assumes that the effect of absorption of atomic hydrogen is dominant in the capture of hydrogen by the oxide film's outer surface.

4.16.3.3 Diffusion-Controlled Hydrogen Pickup Model. It is also conceivable that the time rate of hydrogen input into the metal is controlled by some as-yet-unconsidered independent diffusion process. In the case of diffusion-controlled hydrogen uptake, the net time rate of hydrogen pickup is proportional to the inverse thickness of the oxide layer.

The rate equations implied by the three alternate pictures are summarized in Table 4-50. Pre-transition expressions were formulated simply by writing down the mathematical equivalent of the descriptions above. Post-transition expressions for the hydrogen pickup fraction were derived by replacing powers of X (proportional to the oxide thickness) in the pre-transition expressions with powers of X averaged over a rate-determining oxide thickness that randomly varies from zero to the transition thickness of the oxide film. A discussion of the post-transition oxide film and this approach to describing post-transition rates is included in the description of the cladding oxidation subcode CORROS in Section 4.15.

Table 4-50. Rate equations for hydrogen uptake.

Pre-transition rates	Post-transition
(1) Simple probabilistic pickup fraction determination	
$dH/dX = G/X^2$	$dH/dX = G/X^2_{ave} = 3G/X^2_{TRAN}$
(2) Surface-controlled pickup fraction determination	
$dH/dX = P$	$dH/dX = P$
(3) Diffusion-controlled time rate	
$dH/dX = Q/X$	$dH/dX = Q/X_{ave} = 2Q/X_{TRAN}$
where	
H = hydrogen weight gain(mg/dm^2)	
X = oxygen weight gain (mg/dm^2, corresponds to oxide thickness)	
t = time at temperature	
$^{X}TRAN$ = the transition weight of the oxide layer (mg/dm^2)	
X^2_{ave} = the average of X^2 with values of X distributed at random between 0 and the transition thickness, X_{TRAN} (mg/dm^2)	
X_{ave} = the space average of X with values of X distributed at random between 0 and the transition thickness (mg/dm^2)	
G,P,Q = constants	

When the three very different expressions for hydrogen uptake obtained with these models were integrated and compared with the pre-transition data of Tables 7 and 9 of Reference 4.16-3, the pre-

transition data for zircaloy-2 and zircaloy-4 were found to conform best to the assumption that the rate is surface-controlled. The surface-controlled model is therefore used.

Comparison of experimental pre-transition and post-transition hydrogen pickup fractions[4.16-3] for zircaloy-2 show that the post-transition rate is about twice the pre-transition rate. For zircaloy-4, the pre- and post-transition rates are similar. The reason for this difference between zircaloy-2 and-4 is not well understood but may be related to the presence of nickel, which absorbs atomic hydrogen in zircaloy-2.

The simple surface-controlled hydrogen pickup model of Table 4-50 has, therefore, been modified slightly.

For pre-transition,

$$\frac{dH}{dX} = \frac{B}{8} \quad . \tag{4-323}$$

For post-transition,

$$\frac{dH}{dX} = \frac{C}{8} \tag{4-324}$$

where B and C are determined by the oxide surface metallurgy of the particular alloy and 8 accounts for the different weights of hydrogen and oxygen in water so that dH/dX = 1/8 for complete pickup.

4.16.4 Generalization to an In-Pile Model

Prediction of in-pile corrosion is complicated because important variables (local temperature and reactor chemistry) are not always reported and because data on the time-dependence of corrosion are limited. Enhancement of the hydrogen uptake factors by the reactor environment is treated by determining the value of the pickup fractions B and C for each reactor environment. Changes in the rate of hydrogen picked up caused by changes in the oxidation rate are described with the parameter A, which is discussed in conjunction with the oxidation model, CORROS. Thus, separate parameters are specified to describe the separate processes involved in determining the total rate of hydrogen uptake.

The basic equations for the fraction of hydrogen pickup with respect to the amount of oxygen pickup (dH/dX) are discussed at the end of Section 4.16.3 [Equations (4-323) and (4-324)]. Those equations reference out-of-pile oxidation. For in-pile pickup, the enhancement factor A must again be used. It is presumed that the effect that enhances the oxidation rate in the reactor does not enhance the rate of hydrogen uptake. Thus, the enhancement of the oxidation rate by a factor A will decrease the fractional hydrogen uptake by a factor 1/A.

The rate equations for in-pile oxidation and for fractional pickup of hydrogen are summarized in Equations (4-325) and (4-326) for both pre- and post-transition regimes.

For the pre-transition in-pile regime,

$$\frac{dH}{dX} = \frac{B}{8} \quad . \tag{4-325}$$

For the post-transition in-pile regime,

$$\frac{dH}{dX} = \frac{C}{8} \quad . \tag{4-326}$$

Integration of Equations (4-325) and (4-326) and conversion of the integrated forms from weight gains to oxide thickness and parts per million hydrogen by weight leads to Equations (4-320) through (4-322).

An out-of-pile value of the parameter B has been determined in Reference 4.16-4 (from unpublished data) to be B = 0.33 for zircaloy-2. For zircaloy-4, a value of B = 0.12 was obtained from Figure 12 of Reference 4.16-3. The result is consistent with a value of 10% recommended by Reference 4.16-4.

When values of B were fit to the average hydrogen pickup values for the zircaloy-4 rods of the Saxton reactor,[4.16-5,4.16-6] an average value of B = 0.104 $\pm$ 0.04 was obtained. Thus, the out of pile determined value of B = 0.12 is apparently adequate for zircaloy-4 rods in PWRs. Since no data on zircaloy-4 cladding in a BWR are available, the PWR value, B = 0.12, is returned for the unlikely case of zircaloy-4 in a BWR. Values of B obtained by fitting the zircaloy-2 PWR hydrogen pickup reported in Reference 4.16-2 were B = 0.48 $\pm$ 0.07, while a fit to the BWR hydrogen pickup data on the zircaloy-2 rods of Reference 4.16-7 produced B = 0.29 $\pm$ 0.06. Since the PWR environment has an overpressure of hydrogen and it is known that hydrogen overpressures enhance the out-of-pile pickup fraction,[4.16-7] it is suggested that the difference in PWR and BWR values for B with zircaloy-2 is an effect of the different environments.

4.16.5 References

4.16-1 F. H. Megerth, C. P. Ruiz, and U. E. Wolff, *Zircaloy-Clad UO_2 Fuel Rod Evaluation Program*, GEAP-10371, June 1971.

4.16-2 E. Hillner, "Corrosion and Hydriding Performance of Zircaloy Tubing after Extended Exposure in the Shippingport PWR," *Zirconium in Nuclear Applications*, ASTM-STP-551, 1974, pp. 449-462.

4.16-3 E. Hillner, *Hydrogen Absorption in Zircaloy During Aqueous Corrosion, Effect of Environment*, WAPD-TM-411, November 1964.

4.16-4 A. VanderLinde, *Calculation of the Safe Life Time Expectancy of Zirconium Alloy Canning in the Fuel Elements of the Nero Reactor*, RCN-41, July 1965.

4.16-5 W. R. Smalley, *Saxton Core II Fuel Performance Evaluation, Part I: Materials*, WCAP-3385-56, July 1971.

4.16-6 W. R. Smalley, *Saxton Core III Fuel Materials Performance*, WCAP-3385-57, July 1974.

4.16-7 H. E. Williamson et al., *AEC Fuel Cycle Program Examination of UO_2 Fuel Rods Operated in the VBWR to 10,000 MWD/TU*, GEAP-4597, 1965.

4.17 Young's Modulus and Poisson's Ratio (CELMDR)

Subroutine CELMDR will return temperature dependent values for Young's modulus and a constant value of 0.30 for poisson's ratio. Subroutine CELMDR[4.17-1] does not account for fast neutron fluence, cold work, or oxygen concentration as does subroutine CELMOD. Young's modulus, Y (Pa), is calculated in the following manner:

If $T \leq 1090$ K,

$$Y = 1.088 \times 10^{11} - (5.47 \times 10^{7})\, T \ . \tag{4-327}$$

If $1090 \text{ K} < T \leq 1240$ K,

$$Y = 4.912 \times 10^{10} - 4.827 \times 10^{7}\,(T - 1090) \ . \tag{4-328}$$

If $1240 \text{ K} < T$,

$$Y = \text{maximum of} \begin{cases} 1.0 \times 10^{10} \\ 9.21 \times 10^{10} - (4.05 \times 10^{7})T \end{cases} \tag{4-329}$$

where,

T = temperature (K).

4.17.1 Reference

4.17-1 D. L. Hagrman et al., *MATPRO-Version 11 (Revision 1), A Handbook of Materials Properties for Use in the Analysis of Light Water Reactor Fuel Rod Behavior*, NUREG/CR-0497, February 1980.

4.18 Zircaloy and Zirconium Heats of Fusion (PHYPRP)

The heat of fusion of zircaloy depends to some extent on its composition and the extent of oxidation. Brassfield[4.18-1] has suggested that the heat of fusion of zircaloy-4 differs little from that of zirconium and list the heat of fusion of zirconium as 20.5 kJ/mol. However, Quill[4.18-2] lists the heat of fusion of zirconium as 23 kJ/mol with uncertainty. The routine PHYPRP returns Brassfield's listed heat of fusion for zirconium of 2.25×10^5 J/kg.

4.18.1 References

4.18-1 H. C. Brassfield et al., *Recommended Property and Reactor Kinetic Data for Use in Evaluating a Light-Water-Coolant Reactor Loss-of-Coolant Incident Involving Zircaloy-4 or 304-SS-Clad UO_2*, GEMP-482, April 1968.

4.18-2 L. L. Quill, *Chemistry and Metallurgy of Miscellaneous Material, Thermodynamic, National Nuclear Energy Series, IV*, 19B, New York: McGraw-Hill Book Company, Inc., 1950.

4.19 Zirconium Transformation Temperature (PHYPRP)

Pure zirconium isothermally transforms from the α phase to the β phase at 1,135 K.[4.19-1] The routine PHYPRP returns 1,135.15 K for the zirconium transformation temperature when the variable, CTRANSZ, is called.

4.19.1 Reference

4.19-1 B. Lustman and F. Kerze, *The Metallurgy of Zirconium*, New York: McGraw-Hill Book Company, Inc., 1955.